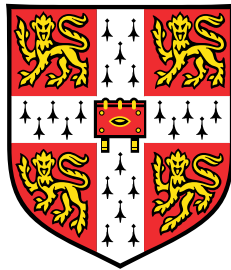


**Investigation of performance and the
influence of environmental conditions
on strip detectors for the
ATLAS Inner Tracker Upgrade**



Christoph Thomas Klein

Department of Physics
University of Cambridge

This dissertation is submitted for the degree of
Doctor of Philosophy

Für meine Eltern Barbara und Burkhard, und meine Schwester Carolin, für all eure Unterstützung.

Declaration

I hereby declare that except where specific reference is made to the work of others, the contents of this dissertation are original and have not been submitted in whole or in part for consideration for any other degree or qualification in this, or any other university. This dissertation is my own work and contains nothing which is the outcome of work done in collaboration with others, except as specified in the text and acknowledgements. This dissertation contains fewer than 60,000 words including summary/abstract, tables, footnotes and appendices, but excluding table of contents, photographs, diagrams, figure captions, list of figures/diagrams, list of abbreviations/acronyms, bibliography and acknowledgements.

Christoph Thomas Klein
July 2019

Abstract

Investigation of performance and the influence of environmental conditions on strip detectors for the ATLAS Inner Tracker Upgrade

Christoph Thomas Klein

With the upgrade of the Large Hadron Collider (LHC) to the High-Luminosity LHC (HL-LHC) scheduled for installation in 2024, the Inner Detector will be replaced with the new all-silicon ATLAS Inner Tracker (ITk) to maintain tracking performance in this high-occupancy environment and to cope with the increase of approximately a factor of ten in the integrated radiation dose. The outer four layers in the barrel and six disks in the end-cap region will host strip modules, built with single-sided strip sensors and glued-on hybrids carrying the front-end electronics necessary for readout.

The strip sensors are manufactured as n-in-p strip sensors from high-resistivity silicon, which allow operation even after the fluences expected towards the end of the proposed lifetime of the HL-LHC. Prototypes of different sensor designs have been extensively tested electrically as well as in testbeam setups, yielding generally satisfactory results, but also revealing ongoing challenges. During electrical sensor evaluation many prototype sensors are found to not comply with specifications for stable long-term operation. This outcome was attributed to the influence of humidity, which has been subsequently investigated in great detail and will have lasting consequences for sensor production and module assembly. Repeated measurements on continuously biased sensors revealed a decrease in tracking performance and increased charge-sharing due to the accumulation of charges in the Si-SiO₂ interface. The dynamics of this effect and how it will affect operation of the finished ITk have been examined with a novel approach using the time-development of inter-strip quantities and trap energy level characterisation in SiO₂ with Deep-level Transient Spectroscopy (DLTS).

Acknowledgements

“I hereby declare that the contents of this dissertation are original.” – that much is true. But it does by no means suggest that I achieved all of this on my own. Therefore, now is the time to thank some people who helped me out along the way, performed measurements together with me, or simply made life in Cambridge and Selwyn College more exciting.

First of all, I would like to thank my supervisor Dr. Bart Hommels for his excellent guidance and patience whenever I asked him for “just a minute” of his time to clarify some questions or discuss results. I also thank the head of the Cambridge HEP group Prof. Valerie Gibson, who together with Dr. Hommels made it possible for me to continue my research in Cambridge as a PhD student after my Erasmus year. The masters of the electronics universe in the form of Richard Shaw and Saevar Sigurdsson were a great support when it came to developing new setups and circuit boards, and for sharing their vast knowledge and various tricks. In addition, I would also like to thank my ATLAS and non-ATLAS colleagues in the HEP group who created the friendly, yet professional work environment that I truly enjoyed.

Apart from colleagues in Cambridge, I also worked closely with other students and senior researchers from the ITk Strips community. Most notably were the close connections with Prof. Thomas Koffas, Dr. John Keller, Robert Hunter, and Steven Lee from Carleton University, Ottawa, who had valuable advice when trying to tackle the ongoing challenges with the prototype sensors, and gave helpful feedback during the development of the automated electrical testing procedures. Another group of people I very much like to thank are those from the ITk Strips testbeam community. Not only did we have very productive testbeam campaigns, but while passing the time during long shifts in the testbeam hut, it also turned out that all people in that group tend to have a similar preference for good, albeit sometimes weird, music. In particular, I would like to thank Edoardo Rossi, whom I bothered with a lot of questions about the testbeam reconstruction software. For the testbeam campaigns I participated in, I have received funding from the European Union’s Horizon 2020 research and innovation programme under grant agreement No. 54168.

There are and there were a lot of people who made life in Cambridge so enjoyable throughout these years, so to anyone I forget to mention, I would like to thank all of you. This list of people includes my friends Harvey, Pablo, and Afnan, as well as everyone else in the Selwyn College MCR, for all the unforgettable events we had. In addition, there are to those in the Cambridge University Gymnastics Club and in the Athletics Club, who helped me in letting my mind relax after work and at the same time keeping me physically fit. Regarding sports, I also give thanks to everyone in the

Selwyn College Boat Club and everyone in our mixed “Splashy” crew for all the great rowing sessions and exciting races. In particular, a big thanks to my good friend Peter, who not only was part of my Cambridge rowing experience, but who also helped proof-reading this thesis.

In this last year in Cambridge, I am very grateful for meeting Klara. The time I was able to spend with you helped me through the stressful times, in particular during the final stretch while writing this thesis. Finally, I would not have been able to arrive at this point without the constant support from my parents and sister, as well as the rest of my family. The things you have done to help me throughout the years are simply immeasurable, therefore I just want to tell you: thank you, for everything.

A common mistake that people make when trying to design something completely foolproof is to underestimate the ingenuity of complete fools.

Douglas Adams
The Hitchhiker’s Guide to the Galaxy

Table of contents

List of figures	xv
List of tables	xix
1 Introduction	1
2 The LHC and ATLAS experiment: present and future	3
2.1 The Standard Model	4
2.1.1 Physics beyond the Standard Model	5
2.1.2 Physics benchmark studies	6
2.2 The Large Hadron Collider	9
2.3 The ATLAS detector	10
2.3.1 The ATLAS Inner Detector	12
2.4 The HL-LHC and ATLAS ITk upgrade	15
2.4.1 The ITk Strip Detector	17
3 Silicon tracking detectors	21
3.1 Energy loss of particles in matter	21
3.1.1 Heavy ionising particles	21
3.1.2 Electrons	24
3.1.3 Photons	25
3.1.4 Multiple scattering	26
3.2 Vertex and momentum measurement	27
3.3 Silicon detectors	30
3.3.1 Silicon sensors	31
3.3.2 Detector readout	35
3.4 Signal formation in silicon detectors	36
3.5 Radiation damage	39
4 Evaluation of prototype ITk Strip Sensors	43
4.1 Large area sensor design	44

Table of contents

4.2	Sensor technical specifications and evaluation	49
4.3	Instrumentation	51
4.4	Planarity of sensors	56
4.5	Bias voltage dependence of sensor properties	57
4.5.1	Sensor leakage current	57
4.5.2	Bulk capacitance	60
4.5.3	Coupling capacitance and implant resistance	65
4.6	Inter-strip measurements	66
4.6.1	Inter-strip capacitance	66
4.6.2	Inter-strip resistance	68
4.7	Punch-through Protection	70
4.8	Strip tests	71
4.9	Measurements of leakage current stability	76
4.9.1	Changes in IV behaviour	78
4.10	Evaluation of irradiated full-size sensors	78
4.11	Production Quality Control	83
4.12	Summary and conclusions	85
5	Anomalous sensor breakdown and the dependence on environmental conditions	87
5.1	Influence of mechanical stress on leakage current	88
5.1.1	Inducing controlled sensor bow	88
5.1.2	Breakdown characteristics	89
5.1.3	IV characteristic of sensors under mechanical stress	91
5.1.4	Summary and referral to further studies	93
5.2	Humidity dependence of breakdown voltage	94
5.2.1	Breakdown imaging	95
5.2.2	Humidity dependent breakdown characteristic	96
5.2.3	Sensor reconditioning treatments	101
5.3	Device simulations	103
5.3.1	Synopsis Sentaurus TCAD suite	103
5.3.2	Modelling ITk Strip Sensors	105
5.3.3	Sensor breakdown in device simulations	107
5.4	Summary and consequences for future sensor handling	110
6	Tracking reliability and the effects of long-term operation	111
6.1	Shift of C_{is} under long-term biasing	111
6.2	Characterisation of long-term biasing effects on the sensor surface	117
6.2.1	Surface states at the oxide interface	118
6.2.2	CV characteristic of an equivalent MOS structure	120

6.2.3	Oxide and interface charge effects	124
6.2.4	Substrate bias effects	126
6.2.5	Summary and explanation of observed behaviour	127
6.3	TCAD simulation of the ITk Strip Sensor surface	130
6.4	The ITk Strips testbeam setup	133
6.4.1	The EUDET telescope	134
6.4.2	Testbeam facilities	138
6.4.3	Track reconstruction and data analysis	140
6.5	Tracking reliability of sensors under long-term operation	141
6.5.1	Testbeam results of un-irradiated modules	142
6.5.2	Testbeam results of an irradiated module	146
6.6	Deep-level transient spectroscopy	147
6.6.1	Principle of capacitance DLTS	147
6.6.2	DLTS transient analysis for ITk Strip Sensors	150
6.6.3	DLTS setup and procedure	154
6.7	Charge trapping dynamics at the ITk Strip Sensor surface	155
6.7.1	Temperature dependence of charge trapping	155
6.7.2	Humidity dependence of charge trapping	160
6.8	Summary and conclusions	164
6.8.1	Consequences for ITk operation	165
7	Summary, conclusion, and outlook	167
	References	171

List of figures

2.1	Particle content of the Standard Model with respective interactions and masses [6, 7]	4
2.2	Leading order Feynman diagrams for H production at the LHC [17]	6
2.3	HH production diagrams with and without self-coupling [17]	7
2.4	Representative Feynman diagrams for $VVjj$ production in electroweak processes [17]	7
2.5	Performance plots showing the difference between the new ATLAS ITk and current Inner Detector [17, 18]	8
2.6	Overview of the CERN accelerator complex [21]	9
2.7	Operation and upgrade schedule of the LHC [22]	10
2.8	Cut-away view of the ATLAS detector [1]	11
2.9	Cut-away view of the ATLAS Inner Detector [1]	12
2.10	3D drawing showing a particle traversing the different Inner Detector components in the barrel regions [1]	13
2.11	An SCT barrel and end-cap module [35]	14
2.12	Schematic layout of the ITk Pixel and Strip Detector [17]	16
2.13	Exploded view of a short-strip barrel module and picture of a short-strip prototype module [17]	17
2.14	Picture of the corner of an ATLAS12 prototype sensor	18
3.1	Energy loss of a muon as a function of $\beta\gamma$ in copper absorber [41]	22
3.2	Landau distribution of the energy loss rate of a m.i.p. in silicon with varying thickness [41]	24
3.3	Fractional energy loss of e^\pm per radiation length and photon total cross section in lead as functions of incident energy [41]	25
3.4	Incident particle undergoing multiple Coulomb scattering in a material [7]	26
3.5	Sketch of a simple vertex detector (figure adapted from [29])	28
3.6	Schematic view of a two-layer hybrid strip detector module [29]	30
3.7	p-n junction in position space: dopant concentration, space charge density, electric field strength and electric potential [52]	32
3.8	Illustrated punch-through effect and depletion region below guard rings with potential of surfaces and edges [48]	35

List of figures

3.9	Schematic circuit of a typical AC-coupled front end cell [48]	36
3.10	Illustration of a number of electrodes in the presence of a moving charge whose path and instantaneous velocity are known (figure redrawn from [51])	37
3.11	Change of the absolute effective doping and full depletion voltage of a 300 μm thick silicon sensor versus the fluence [55]	40
4.1	Schematic cross-section of a sensor	44
4.2	Prototype sensor fabrication wafer layout [66]	47
4.3	Different types of electrical and their corresponding visual defects detectable with a full strip test [71]	50
4.4	Schematic circuit of the auto balancing bridge capacitance measurement method [72]	52
4.5	Photos of the coordinate measurement machine and automatic wire bonder	53
4.6	Alessi probe station and instruments used for strip sensor studies at Cambridge	54
4.7	Example net bow measurement of a full-size barrel sensor and histogram of maximum bow of all tested sensors	56
4.8	IV curves of all ATLAS12A sensors	58
4.9	IV curves of ATLAS17LS sensors and histogram of leakage current at $V_{\text{bias}} = -600\text{ V}$	59
4.10	CV curves of ATLAS12 sensor batches	60
4.11	CV curves of ATLAS17LS sensor batches	61
4.12	Frequency dependence of the bulk capacitance of an ITk Strip Sensor for various bias settings	62
4.13	Distribution of the effective doping concentration	63
4.14	Distribution of the effective doping concentration of all A12 and A17 sensors	64
4.15	Frequency dependence of the measured coupling capacitance and implant resistance of an ITk Strip Sensor	65
4.16	Conceptual diagram of the inter-strip capacitance measurement setup [66]	66
4.17	Example of normalised inter-strip capacitance versus V_{bias} for a prototype strip sensor	67
4.18	Frequency dependence of the inter-strip capacitance of an ITk sensor	67
4.19	Conceptual diagram of inter-strip resistance measurement [66]	68
4.20	Example plots of sourced current and induced voltage during R_{is} measurements as well as R_{is} versus V_{bias} measured on various A12 and A17 sensors	69
4.21	PTP measurements on a select sample of sensors	70
4.22	Conceptual diagram of full strip test setup [66]	72
4.23	Comparison between strip test results obtained with a single needle and a probecard	73
4.24	Summarised striptest results for all tested sensors	75
4.25	Leakage stability measurements of various sensors with exemplary results of their long-term behaviour	76
4.26	IV and CV curves of irradiated ATLAS12 sensor batches	79
4.27	Equivalent circuit of a simple R-C model representing a partially depleted sensor [52]	80

4.28	Frequency dependence of the bulk capacitance of an irradiated A12 sensor	81
4.29	Leakage current stability measurement of irradiated ATLAS12 main sensors	82
5.1	Simulated mechanical stress of an end-cap R0 module [75]	88
5.2	Metrology profile of a glass plate flexed on the metal jig	89
5.3	Testing procedure used to determine the influence of mechanical stress on the IV characteristic	90
5.4	IV measurements of a sensor for illustrating different breakdown characteristics . . .	90
5.5	Development of $V_{\text{breakdown}}$ for sensors during different stages of mechanical stress test sequence	92
5.6	Image of breakdown location within the guard ring region of a sensor	95
5.7	Image of breakdown locations within the strips region of a sensor	96
5.8	IV curves of a ATLAS17 sensor during during a measurement sequence with varying humidity	97
5.9	Time development of I_{leakage} during a stability measurement with varying RH	98
5.10	Development of $V_{\text{breakdown}}$ for a sensor with varying relative humidity	99
5.11	RH dependence of breakdown for a sensor with already low $V_{\text{breakdown}}$ and a sensor with special passivation	100
5.12	Results of bake-out treatment for sensors with captured breakdown location	102
5.13	Example of a modelled AC-coupled readout strip of an n-in-p microstrip sensor. . . .	104
5.14	Simulated surface electric field of a sensor in the bond pad region	108
5.15	Simulated surface electric field of a sensor at the sensor edge	109
6.1	Changes to C_{is} under long-term biasing	112
6.2	Time dependence of measured C_{is} values when biasing the sensor at V_{const}	113
6.3	Changes to IV characteristics and time dependence of I_{leakage} under long-term biasing	113
6.4	Recorded recovery of C_{is} hysteresis of an unbiased sensor	114
6.5	Dependence of saturation values during C_{is} hysteresis on applied V_{const}	115
6.6	Frequency dependence of C_{is} hysteresis for values measured at $V_{\text{bias}} = -250 \text{ V}$	115
6.7	Comparison of C_{is} hysteresis feature of ATLAS07 sensors with p-stop and p-spray . .	116
6.8	Schematic cross section of an inter-strip region (not to scale) showing the different contributions towards C_{is}	117
6.9	Energy band diagram of an oxide/semiconductor interface with p-type substrate for different oxide charge conditions [85]	119
6.10	Si/SiO ₂ interface under depletion and inversion conditions indicating the surface potential and the space charge width [85]	121
6.11	Energy band diagram of a MOS system prior to and after contact [85]	123
6.12	Ideal capacitance versus gate voltage characteristic of a MOS capacitor [85]	124
6.13	Charges associated with thermally oxidized silicon [87]	124

List of figures

6.14	CV characteristic of a MOS capacitor for increasing values of fixed oxide charge [85]	125
6.15	Band diagram of a MOS structure with interface states at inversion and the change of the CV characteristic [85]	126
6.16	Comparison of energy band diagrams for a p-type Si/SiO ₂ interface at inversion point without and with reverse bias [85]	127
6.17	Simulated changes in the electrostatic potential of the inter-strip region under constant bias	131
6.18	Simulation of hysteresis in C_{is} measurements	132
6.19	Schematic setup of the EUDET beam telescopes used for ITk Strip Detector testbeam campaigns	133
6.20	MAPS schematic cross section [90]	134
6.21	Pictures of prototype modules evaluated in testbeam campaigns	135
6.22	Acetal box used at DESY and MPI cooling box for low-temperature testbeam measurements at CERN SPS testbeam	136
6.23	Principle of TLU operation [95]	137
6.24	Schematic view of the testbeam generation at the DESY II testbeam facility [100]	138
6.25	EUDET-type beam telescopes at DESY II testbeam facility [100]	139
6.26	ACONITE telescope at the CERN SPS testbeam	140
6.27	Overview of the modular EU Telescope software framework [107]	141
6.28	Efficiency versus threshold curve of the R0 module at the DESY testbeam campaign from 2017	143
6.29	Average cluster size versus threshold for the R0 module at the DESY testbeam campaign from 2017	144
6.30	Efficiency and average cluster size versus threshold for one of the long-strip modules and the modules which constituted the double-sided R0 module at the DESY testbeam campaign from 2018	145
6.31	Efficiency and average cluster size versus threshold of the irradiated R0 module	146
6.32	Schematic procedure of C-DLTS measurements to evaluate trap level characteristics in an n-in-p silicon device [54, 108]	149
6.33	Temperature dependence of C_{is} at a constant V_{bias}	155
6.34	DLTS transients	156
6.35	Example of the Inverse Laplace Transform for a capacitance transient	158
6.36	Arrhenius plots obtained from C_{is} transients in dry conditions	159
6.37	DLTS transients taken in ambient conditions	161
6.38	Arrhenius plots obtained from C_{is} transients in ambient conditions	162
6.39	Humidity dependence of DLTS transients	163

List of tables

2.1	Comparison of current ATLAS Inner Detector and future ATLAS Inner Tracker [37]	15
2.2	Overview of the different types of silicon strip sensors for the ITk Strip Detector [17]	18
3.1	List of symbols used in the Bethe-Bloch formula Eq. 3.1 and subsequent equations [41]	23
4.1	Overview of ATLAS12 and ATLAS17 prototype sensor batches	48
4.2	Comparison of V_{FD} , D , and N_{eff} of sensors before and after irradiation	80
4.3	List of ITk microstrip sensor specifications [17]	83
5.1	List of symbols used in the device simulation formulas [80]	105
5.2	Input parameters for TCAD simulations of ATLAS12 prototype sensors	106
6.1	Characteristic quantities of the insulator-semiconductor and MOS structure in ATLAS12 prototype sensors	128
6.2	Calculated shift of V_T at selected V_{bias} for ATLAS12 prototype sensors	129
6.3	Summary of investigated prototype modules in this work	136
6.4	Summary of characteristic time constants and interface trap concentration of recorded DLTS transients in dry conditions	157
6.5	Summary of activation energy and effective cross section in dry conditions	160
6.6	Summary of characteristic time constants and interface trap concentration of recorded DLTS transients in ambient conditions	160
6.7	Comparison of relative fitted decay curve amplitudes for dry and ambient DLTS	161

Chapter 1

Introduction

There are many big questions in life which science strives to answer. From “Where do we come from?” and “What are we made of?” to “What will happen in the future?”, natural science is divided into many fields which seek their own tiny bit of the answers to those fundamental questions. The same is true for particle physics, which – maybe more than others – always seems on the verge of giving an ultimate answer to the fundamental building blocks and interactions of matter in our universe. This is achieved with the help of exceedingly larger accelerators and more precise collider experiments, which are used to analyse particle scattering and decays at energies and collision rates which, at their time, are unprecedented to date. But one important question is often overlooked in the shadows of those large machines: “How do we get to the point that we can detect all of this?”

Detectors for ionising particles and photons are commonly used in many research fields as well as today’s technology. In particle physics experiments, detectors are employed to measure the energy, momentum, and trajectory of traversing particles, thus allowing an identification of events. Especially in the case of particle colliders, the position of primary and secondary vertices is of utmost importance to determine the underlying physics of the decay.

The LHC, a large proton-proton collider approved in 1994, is currently the major research tool for particle physics and was commissioned in 2009. ATLAS is one of the main experiments that are installed on this accelerator. Since the effectiveness of the LHC will saturate within around 8 years of operation due to statistical limitations, a strategy has been devised to upgrade the LHC and all partaking experiments towards the high-luminosity LHC (HL-LHC) in 2022 in order to maximise the output by increasing the integrated luminosity by one order magnitude from 300 fb^{-1} to 3000 fb^{-1} .

In the ATLAS experiment, the Inner Detector is situated closest to the interaction point and consists of the Pixel Detector as the innermost layers, followed by the Semiconductor Tracker (SCT), and the Transition Radiation Tracker (TRT). Following the LHC upgrade, likewise, the strip detectors in the upgraded SCT – the ATLAS *Inner Tracker* (ITk) – must operate in an environment where sensors and electronics are exposed to fluences of high-energy ionising particles which are one magnitude larger. The result would be that increasing radiation damage degrades performance of the detector components. For that reason, alternative and more radiation hard detector materials and

Introduction

elaborate layout structures have been investigated for the upcoming upgrade. Moreover, in view of the proposed lifetime of several years, all components have to fulfil strict mechanical and technical specifications and therefore prototypes have to undergo a rigorous testing procedure to assure the quality and longevity of the specified properties. In order to maintain a satisfactory sensor performance during the foreseen lifetime, the design of the ITk Strip Sensors is based on the best-known radiation tolerance technology and long-term reliability to date.

This thesis presents the physical and experimental principles with regard to the application of the testing procedures used in the studies of the electrical properties of prototype sensors for the ITk Strip Detector upgrade, their results and impact on detector operation, as well as detailed investigations into ongoing challenges.

Following this introduction, Chapter 2 outlines the LHC and ATLAS experiment in their current form as well as giving details about the future upgrade which involves replacing the current ATLAS Inner Detector with the new ITk. In Chapter 3 the principles of the interaction and consequently detection of particles in a tracking detector are briefly discussed in addition to the basic functionality of a semiconductor detector. This includes an explanation of the consequences of radiation damage on sensor performance and ways to counter this.

Chapter 4 deals with the details of the prototype sensors and the experimental setups used for the testing procedures. The results of a detailed evaluation conducted on more than 160 prototype sensors are shown in the same chapter, also including the outcome of measurements performed on sensors after irradiation. As long-term reliability is one of the key factors in detector development for an experiment with such a long lifetime, the sensors used in tracking detectors have to fulfil strict requirements in terms of the stability of their electrical characteristics. One of the main outcomes of the sensor evaluation, however, is that this is one point where shortcomings can still be seen with unexpected electrical breakdown of current prototypes. Therefore, further investigations into the breakdown characteristics of sensors and their dependence on factors such as mechanical stress and humidity of the testing environment were conducted, the results of which are presented in Chapter 5. Unfortunately, an anomalous breakdown of sensors is not the only unexpected behaviour observed during the extensive testing. Simply by operating devices for longer periods of time important properties can be altered which have a potentially significant impact on the tracking reliability. This phenomenon is studied in Chapter 6, using electrical tests as well as testbeams at accelerator facilities. The dynamics of the observed effects have subsequently been examined using a novel application of Deep-Level Transient Spectroscopy, which not only yielded a characterisation of their time-development with regards to temperature dependence, but performing the same tests at different humidity levels also allowed a first quantification of the impact of humidity.

Chapter 2

The Large Hadron Collider and ATLAS experiment: present and future

Starting with J. J. Thomson's discovery of the electron in 1897, there has been a rapid development in our understanding of the fundamental building blocks of the universe. Particle physics experiments are addressing these questions by using a variety of sources, such as cosmic rays or particle accelerators, to investigate the production and decay processes of exotic particles, i.e. unstable particles not found in nature under normal circumstances. The current state of knowledge is summarised in the theory framework of the Standard Model of Particle Physics.

Until 2012, however, the particle content of the Standard Model was still incomplete, with no evidence of the Higgs boson from previous accelerator experiments. The experiments to finally discover this particle were ATLAS [1] and CMS [2] based on collisions in the Large Hadron Collider at CERN [3]. But even with the discovery of Higgs boson [4, 5] and the success of the Standard Model, there have already been findings of physics processes beyond the Standard Model, in particular in neutrino experiments. There is also a necessity for Standard Model extensions to explain results from astrophysical observations with regards to Dark Matter. To tackle these challenges, a large upgrade of the Large Hadron Collider and the detector experiments has been scheduled, with the preparation for the upgrade of the ATLAS Inner Detector in particular being the basis for this thesis.

This chapter serves as a brief presentation of the physics case for the high-luminosity upgrade of the Large Hadron Collider and an overview of the current ATLAS experiment and its new Inner Tracker. The physics included in the Standard Model and beyond will be described in Section 2.1. This also includes a brief look at important physics benchmarks of the upgraded ATLAS experiment. An outline of the collider and specifically the ATLAS experiment will be given in the successive Sections 2.2 and 2.3. Lastly, details of the upgrade and related detector requirements will be given in Section 2.4.

2.1 The Standard Model of Particle Physics

The *Standard Model* (SM) of Particle Physics is the theoretical basis for the interaction of elementary particles through three of the four known *fundamental forces*.

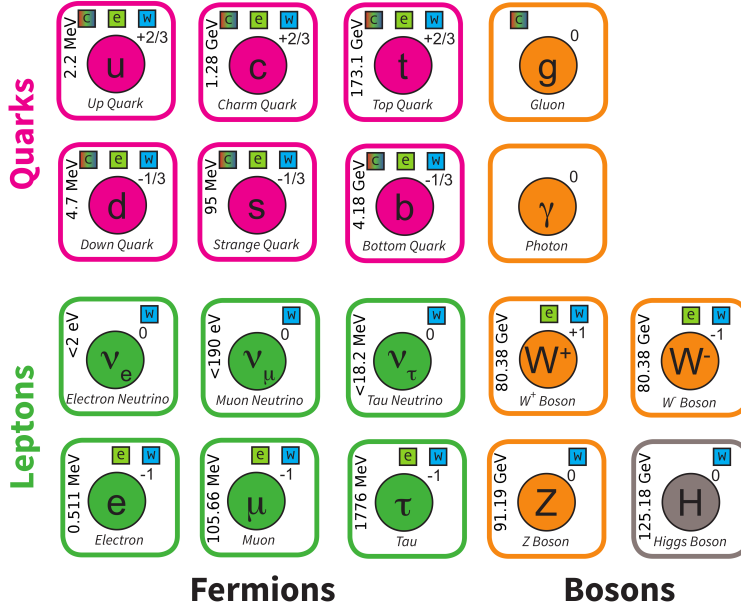


Fig. 2.1: Particle content of the Standard Model divided into fermions (leptons and quarks) and gauge bosons. The upper right numbers are the electrical charge and the small boxes indicate the possible modes of SM interactions (c: colour, e: electromagnetic, w: weak) [6]. The numbers on the left are the respective particle masses in natural units [7].

The particle content of the Standard Model (see Fig. 2.1) is divided into half-integer-spin *fermions*, which do not have any internal structure and are thus fundamental, and integer-spin mediator *bosons* for interactions via the fundamental forces. For fermions the SM further distinguishes between six *leptons* and six *quarks* depending on their interactions. Either is arranged into three *flavour* generations containing a pair differing in electrical charge Q by one elementary charge e . The leptons are grouped into the three charged leptons, *electron* e^- , *muon* μ^- , and *tau* τ^- , each with an integer negative charge $Q = -e$, as well as the neutral corresponding *neutrinos* ν . Quarks carry fractional charges of $Q = 2/3e$ or $-1/3$ and are known as the *up* u , *down* d , *strange* s , *charm* c , *bottom* (or *beauty*) b , and *top* t . Each fermion has a corresponding *antiparticle* with opposite electrical charge and other quantum numbers. In contrast to leptons, which can be found or produced as free particles, quarks are *confined* to appearing in bound states (*hadrons*) either containing three quarks (*baryons*) or a quark-antiquark pair (*mesons*).

The fundamental forces which are part of the Standard Model are the *strong* interaction, mediated by the *gluon* g , and the *electroweak* interaction. Due to the *electroweak symmetry breaking*, the latter manifests itself in nature as the separate *electromagnetic* interaction, mediated by the massless photon γ , and the *weak* interaction, which is mediated by the massive W^\pm and Z^0 bosons.

In order to preserve local gauge invariance, the masses of the W and Z bosons have to be dynamically generated as part of the electroweak symmetry breaking, as masses may not be explicitly attributed in the Standard Model [8–10]. The theoretical process by which the weak gauge bosons acquire their experimentally observable mass [11–14], is described by the *Higgs mechanism* [15, 16] and results in an additional coupling to a universal field, called the Higgs field, which is mediated by the massive, scalar *Higgs boson* H . The generation of fermion masses can also be described by the Higgs mechanism, where for each massive fermion f the additional mass-dependent *Yukawa coupling* y_f is introduced, which is directly proportional to the fermion mass.

2.1.1 Physics beyond the Standard Model

Despite the completion of the particle content of the Standard Model with the discovery of the Higgs boson and its overall success in predicting experimentally verifiable quantities, like coupling constants or branching ratios, without significant discrepancies, it is still no all-encompassing theory.

One major flaw of the SM is the omission of one fundamental force, *gravitation*. While gravitational interaction can also be described in a quantum field theory, its gauge boson, the *graviton*, cannot be detected in microscopic particle interaction due to its weak coupling. However, on a macroscopic scale it is the dominant force, e.g. in astrophysics.

One other problem originates from the neutrino sector. In the last three decades *neutrino oscillation* has been observed in reactor, solar, atmospheric, and accelerator neutrinos, which requires them to be massive particles, whereas in the SM neutrinos are massless.

Probably the biggest weakness of the current SM, is the discrepancy with astrophysical observations, such as non-baryonic matter which only interacts via gravitation and is commonly referred to as *Dark Matter*. Likewise, the potential for *baryogenesis* and *leptogenesis* incorporated in the SM is insufficient and cannot explain the matter-antimatter asymmetry in the universe.

One potential extension of the SM is *supersymmetry* (SUSY). SUSY models introduce additional supersymmetric partners to the fermions and bosons in the SM, thus extending its particle content and possible interactions. In addition, a stable SUSY particle would be a *weakly interacting massive particle* (WIMP), which is a potential candidate for Dark Matter. However, as of now there has been no evidence for SUSY particles in any accelerator experiments and therefore the search for them is one of the main challenges for the Large Hadron Collider and any future collider experiments.

To find a gateway towards physics beyond the Standard Model in collider experiments often involves the observation of interactions which are forbidden in the Standard Model, and therefore only very rarely occurring, or the precise measurement of quantities to search for discrepancies with SM predictions. For both of these it is necessary to maximise the integrated luminosity either in order to have a chance of recording rare interactions or to minimise the statistical uncertainties of the measured quantities. To increase the integrated luminosity by one order of magnitude is the purpose of the high-luminosity upgrade of the LHC.

2.1.2 Physics benchmark studies

The installation of the new tracking system and the high luminosity after the upgrade will have a large impact on particle analyses. A variety of benchmark analyses have been selected to validate the performance of the new Inner Tracker, for example in terms of b -tagging, pile-up rejection, and lepton identification [17].

One such process is the production of a Higgs boson via *vector-boson fusion* (VBF) which subsequently decays into $WW^{(*)}$ (see Fig. 2.2). VBF has the second highest contribution towards Higgs production, after *gluon-gluon fusion* (ggF), and the signature of such an event is the production of forward/backward jets with large dijet invariant mass. Those forward jets are used for tagging and a large signal-to-background ratio can be achieved: depending on the angular coverage of the ITk due to the need of b -jet veto to reject $t\bar{t}$ background, and the track confirmation for jets to prevent pile-up jet misidentification.

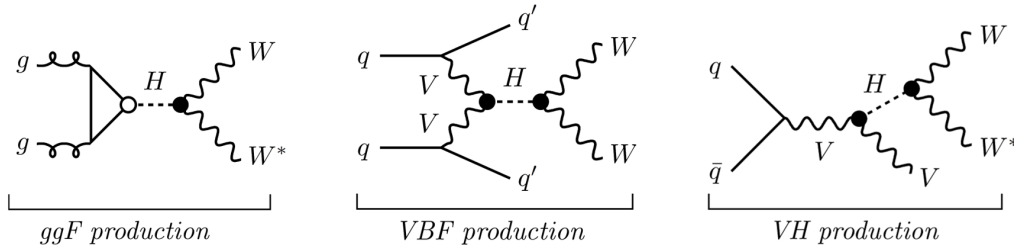


Fig. 2.2: Leading order Feynman diagrams for H production at the LHC. The processes are (from left to right) gluon-gluon fusion, vector-boson fusion, and production in association with a massive vector boson (*Higgsstrahlung*) [17].

After the discovery of the Higgs, a large part of the future effort related to it will consist of precise quantifications of its various coupling strengths, as they are related to multiple processes within the Standard Model. Given its total production cross section [7], after 10 years of operation the HL-LHC will have produced more than 100 million Higgs bosons, thus allowing the study of even very rare decays and search for deviations from the SM. One such channel would be $H \rightarrow \mu^+ \mu^-$, which will benefit from the prospective improvement in p_T resolution of the central tracker region for precise invariant mass reconstruction of the μ -pair.

A closer look into electroweak symmetry breaking and whether the Higgs boson is responsible for it, necessitates the measurement of *Higgs self-coupling* and therefore HH production and decay channels (Fig. 2.3). However, since the decay into $b\bar{b}$ has the largest branching fraction of Higgs decays, most analyses will have to consider at least one particle of the Higgs pair to decay into it, e.g. $b\bar{b}b\bar{b}$ or $b\bar{b}\gamma\gamma$, hence posing high requirements with respect to b -tagging capabilities. As such, the different HH channels are also part of the benchmark studies for the ITk.

One other measurement of interest is the *vector-boson scattering* (VBS, Fig. 2.4) through same-sign $W^\pm W^\pm$ production. The Standard Model Higgs limits the amplitude of the $VV \rightarrow VV$ interactions

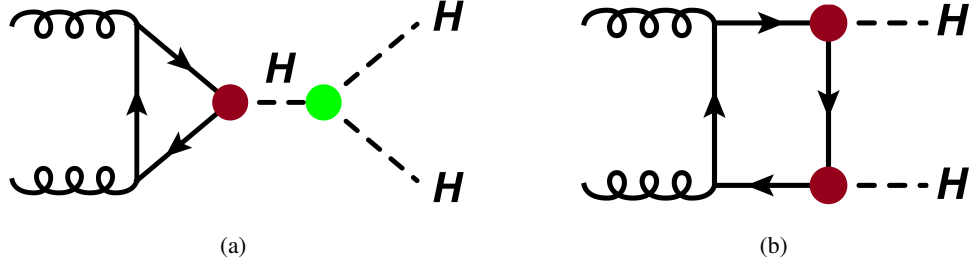


Fig. 2.3: HH production diagrams with (a) and without (b) self-coupling [17].

from infinitely increasing with centre-of-mass energy of the diboson system in the TeV scale. The expected precision depends largely on the angular coverage and tracker layout as it is responsible for vetoing jet signals from pile-up and additional leptons. This measurement is also sensitive towards deviations from the SM as VBS could be additionally mediated via new physics processes.

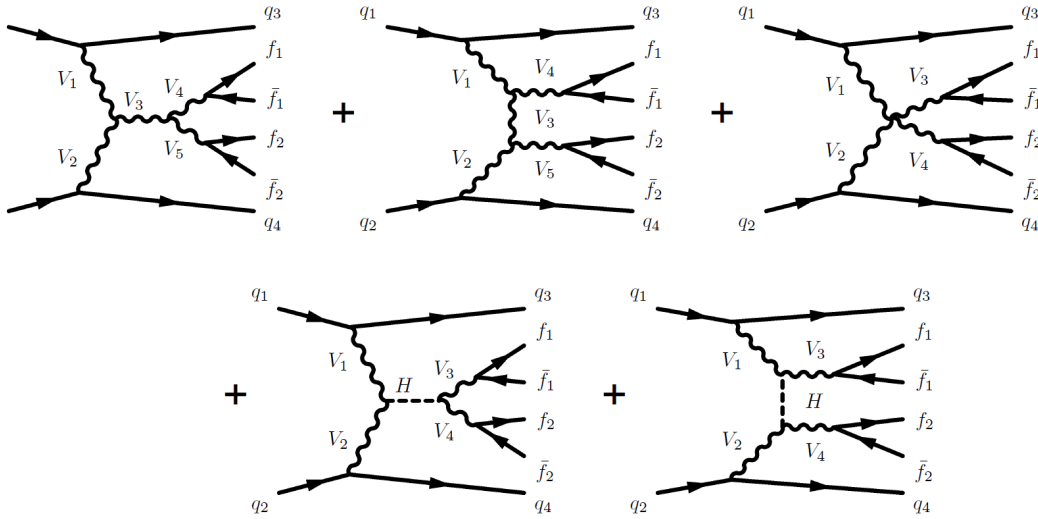


Fig. 2.4: Representative Feynman diagrams for $VVjj$ production in electroweak processes including VBS topology. The lines are labelled with quarks (q), vector bosons ($V = W, Z$), Higgs bosons (H), and general fermions (f) [17].

Likewise, sensitivity for physics beyond the Standard Model (BSM) can be achieved by a search for $t\bar{t}$ resonances. Those could be produced from decays of heavy bosons in the TeV region like Z' , present in many BSM theories. At increasingly higher masses, the quark pair would be highly boosted and hence the b -tagging capabilities of collimated jets in the ITk is very important.

Fig. 2.5 displays and summarises a few select parameters which are crucial to many of these ITk benchmark studies and compares them to the current Inner Detector, e.g. b -tagging or lepton track reconstruction. The shown plots also include the radiation lengths and nuclear interaction lengths of incident particles which is important for the performance of the tracker, but also for the other detector sub-systems (see Sections 3.1.2, 3.1.3, and 3.1.4).

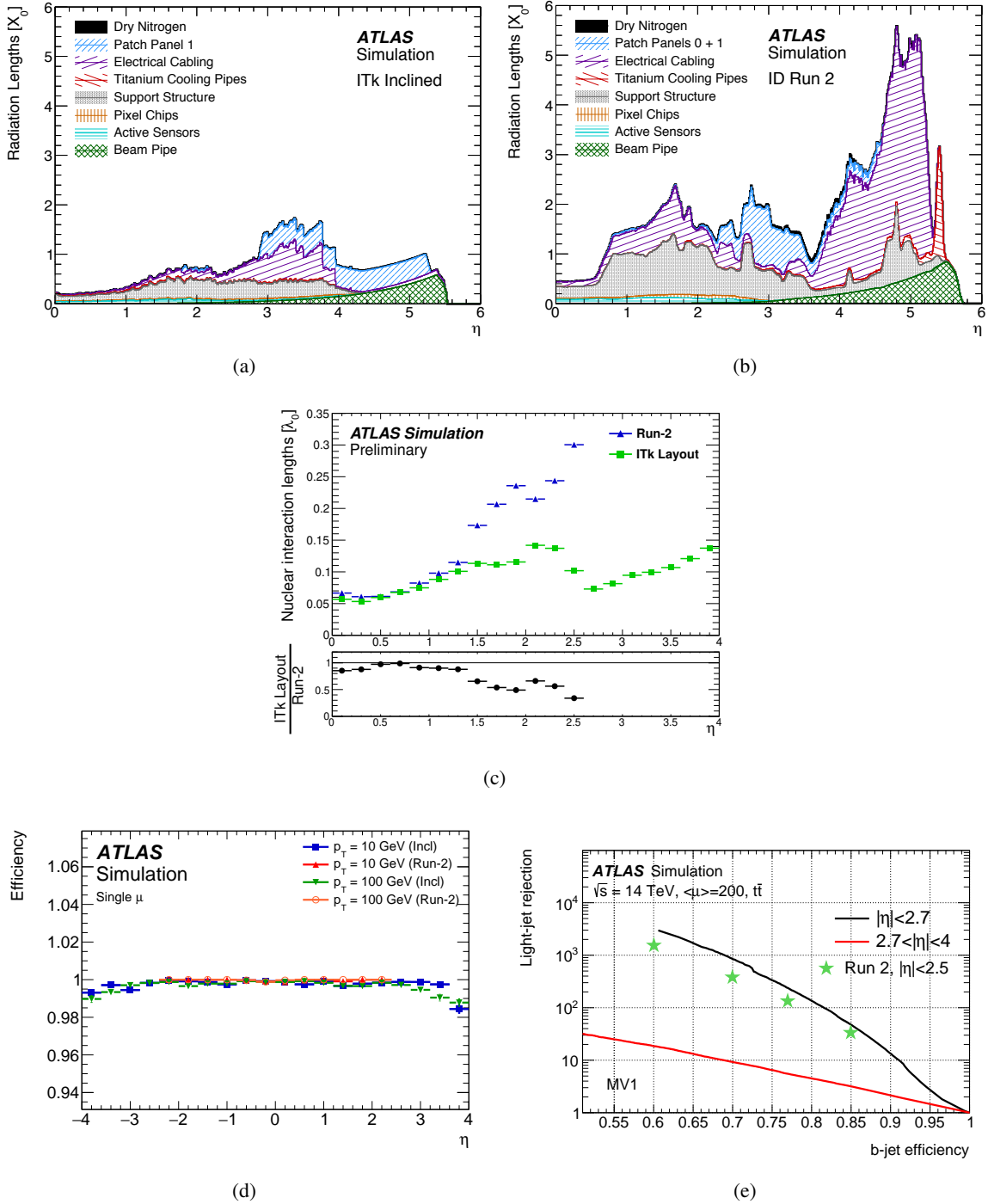


Fig. 2.5: Radiation lengths X_0 versus the rapidity η for (a) the ATLAS ITk, (b) the current Inner Detector, and (c) the nuclear interaction lengths seen by incident particles. (d): reconstruction efficiency of single muons in $t\bar{t}$ events versus η . (e): performance of the MV1 b -tagging algorithm in different η regions for the ITk layout and during Run II [17, 18].

2.2 The Large Hadron Collider

The *Large Hadron Collider* (LHC) at CERN [3] has been built to lead to new discoveries in the frontiers of the Standard Model of particle physics and beyond with its unprecedented energy and luminosity. Inside the LHC, two bunches of protons (p) will collide in intervals of 25 ns (*bunch-crossing*) with centre-of-mass energies up to 14 TeV at a design luminosity of $\mathcal{L} = 10^{34} \text{ cm}^{-2}\text{s}^{-1}$. The LHC can also collide heavy ions, in particular lead nuclei (Pb), with 5.5 TeV per nucleon pair, at a design luminosity of $\mathcal{L} = 10^{27} \text{ cm}^{-2}\text{s}^{-1}$.

The high interaction rates, radiation doses, particle multiplicities and energies, as well as the requirements for precision measurements have set new standards for the design of particle detectors. Two general purpose detectors, ATLAS (the acronym for *A Toroidal LHC Apparatus*, [1]) and CMS (*Compact Muon Solenoid*, [2]), have been built for probing p-p and Pb-Pb collisions. ATLAS and CMS are complemented by two more specialised detectors, LHCb (*Large Hadron Collider beauty*, [19]) as a forward detector with emphasis on investigating bottom- and charm-quark physics and ALICE (*A Large Ion Collider Experiment*, [20]) with the main focus on studying the Quark-Gluon Plasma through Pb collision.

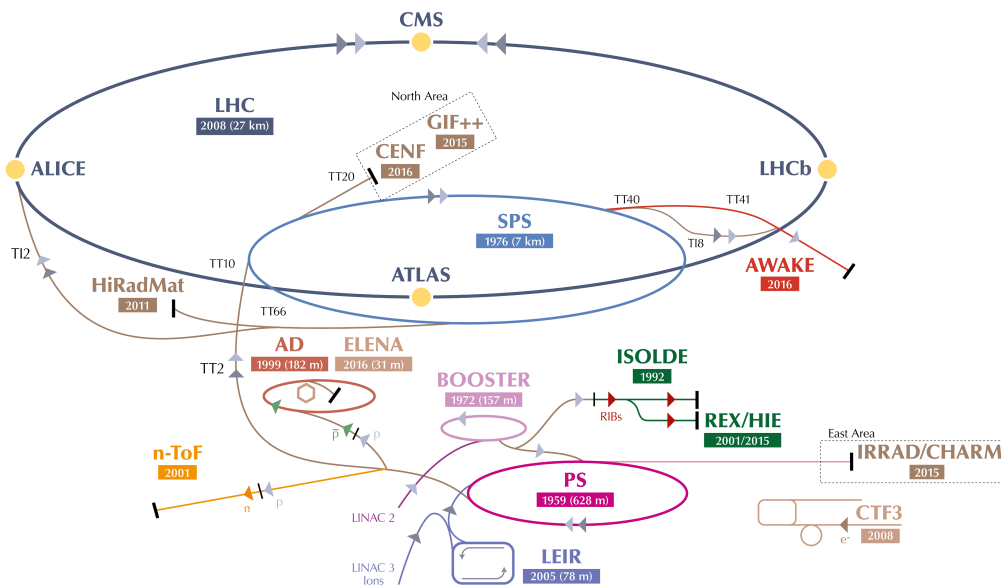


Fig. 2.6: Overview of the CERN accelerator complex showing the LHC as the last ring in a chain of particle accelerators. The smaller machines are used in the LHC injection chain to accelerate particles to their final energies before entering the LHC ring and also provide beams to many smaller experiments as well as irradiation and testbeam sites [21].

When using protons, the LHC is injected with accelerated particles following the injection chain (see Fig. 2.6) of *Linac2* (accelerated to energies of 50 MeV), *Booster* (1.4 GeV), *Proton Synchrotron* (PS, 25 GeV), and *Super Proton Synchrotron* (SPS, 450 GeV). The accelerator ring of the LHC itself

The LHC and ATLAS experiment: present and future

consists of two beam pipes and has a circumference of 26.7 km. 1232 superconducting dipole magnets, cooled down to 2 K with peak magnetic fields of 8 T, keep the proton bunches on their circular track, 393 quadrupole magnets are used to focus the beams, and 688 additional sextupole magnets are employed to correct the momentum drift resulting from the focussing.



Fig. 2.7: Operation and upgrade schedule of the LHC [22].

The operation schedule of the LHC (see Fig. 2.7) is divided into multiple runs interrupted by *Long Shutdowns* (LS) during which accelerator and detector maintenance as well as upgrades are performed. Run I was conducted at energies of 7 TeV and 8 TeV. The main goal of that run was the discovery of the Higgs boson, which has been unsuccessful in previous accelerators. After the end of the first Long Shutdown (LS1) in early 2015 the centre-of-mass energy of protons was increased to 13 TeV while also reaching the LHC design luminosity. At the time this thesis is written, Run II has just concluded a few months earlier and LS2 has started, which, among others, involves major upgrades of the ALICE and LHCb experiments. LS3, starting at the end of 2023, will mark the beginning of Phase-II of LHC operation with a major performance upgrade of the accelerator towards high luminosity and the replacement of several major detector components. More details on this will be given in Section 2.4.

2.3 The ATLAS detector

The ATLAS detector, shown in Fig. 2.8, is a cylindrical multi-purpose detector with a width of 44 m, a height of 25 m, and a weight of 7000 t [1]. It is composed of three main sub-systems with the innermost layers being the *Inner Detector* [23, 24], a charged particle tracker described in detail below. Situated outside the Inner Detector is the calorimetry system, which is divided into a liquid Argon (LAr) electromagnetic sampling calorimeter [25] and a hadronic calorimeter [26] comprised of steel-scintillator-tiles in the barrel region and LAr in the end-caps. Located in the outermost layer is the muon system [27], consisting of drift tubes as well as resistive-plate, cathode-strip, and thin-gap chambers, all of which are within a toroidal magnetic field [28].

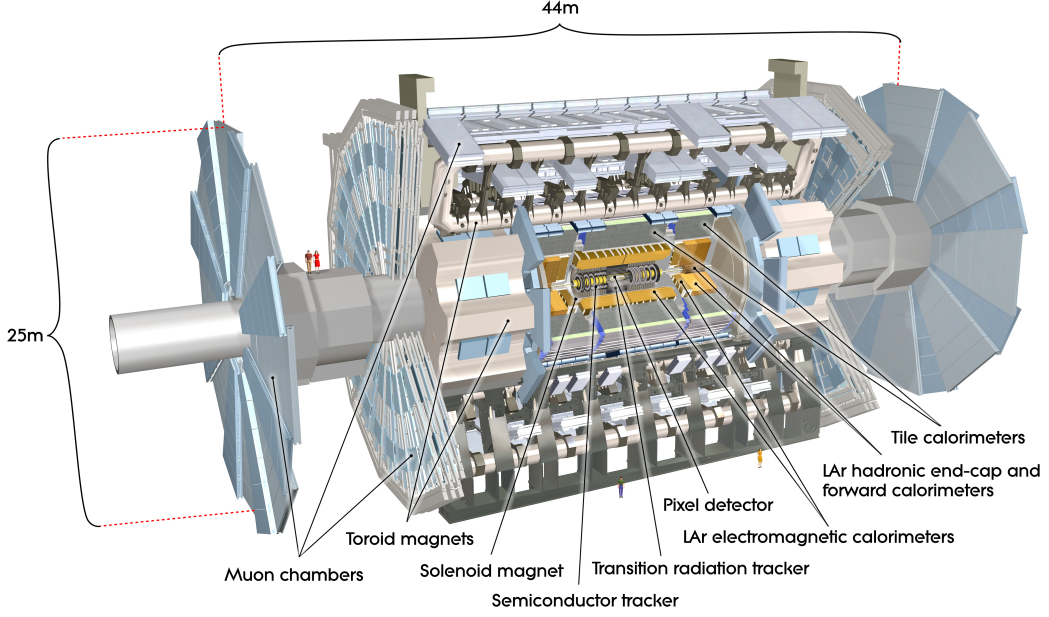


Fig. 2.8: Cut-away view of the ATLAS detector with its sub-systems marked [1].

In the ATLAS coordinate system the z -axis is defined along the beam axis, the x - y plane of a Cartesian coordinate system is transverse to the beam direction, chosen such that the x -axis is pointing towards the centre of the LHC ring and y in upwards vertical direction. Track properties are often given in the azimuthal angle ϕ and distance $R = \sqrt{x^2 + y^2}$ in the xy -plane and the polar angle θ . Another useful quantity, which is often used instead of θ is the *pseudorapidity* η , defined as $\eta = -\ln \tan(\theta/2)$. The pseudorapidity is approximately the same as the *rapidity* $y = 1/2 \cdot \ln[(E - p_z)/(E + p_z)]$ (E and p_z being the energy and z -component of the particle momentum 4-vector, respectively), which in Lorentz-transformations has the advantage of being additive and used in the case of massive objects such as jets. As such, detector layout and segmentation are often given in η rather than θ . The *transverse momentum* (p_T) and *energy* (E_T), as well as the *missing transverse energy* (\cancel{E}_T or E_T^{miss}) are defined in the x - y plane. Furthermore, the distance ΔR in the pseudorapidity-azimuthal angle space is defined as $\Delta R = \sqrt{\Delta\eta^2 + \Delta\phi^2}$.

The ATLAS detector sub-systems are segmented into a cylindrical barrel region around the interaction point at $z = 0$ and an end-cap region for tracks with larger $|\eta|$, which is further away from the interaction point and perpendicular to the beam direction. In the current ATLAS detector the tracking system covers the range $|\eta| \leq 2.5$, the EM and hadronic calorimetry $|\eta| \leq 3.2$ with an additional forward hadronic calorimeter $3.1 \leq |\eta| \leq 4.9$, and the muon spectrometer $|\eta| \leq 2.7$.

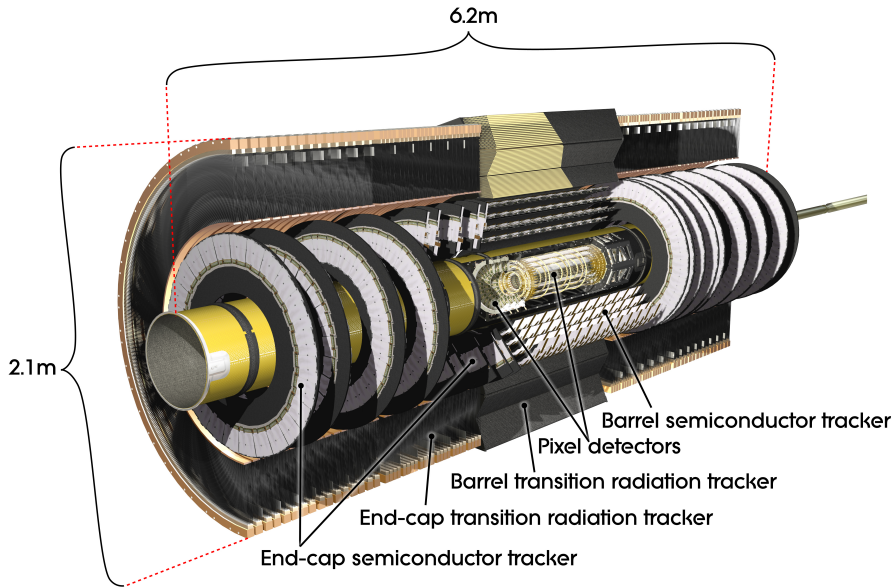


Fig. 2.9: Cut-away view of the ATLAS Inner Detector with its three sub-detectors in the barrel and end-cap region marked [1].

2.3.1 The ATLAS Inner Detector

The *ATLAS Inner Detector (ID)*, displayed in Fig. 2.9, is designed as the tracking and vertexing sub-system of the experiment. It combines the innermost *Pixel Detector*, microstrip detectors of the *Semi-Conductor Tracker (SCT)*, and tracking straw tubes of the *Transition Radiation Tracker (TRT)* for precise measurements of primary and secondary vertices. The Pixel Detector and the SCT cover a pseudorapidity range of $|\eta| \leq 2.5$ and the TRT works within $|\eta| \leq 2.0$.

One of the main goals of ATLAS is the discovery of the Higgs boson and precision measurements of its properties, this results in some stringent requirements for the ID [29]. The momentum resolution of isolated leptons has to be at least $\sigma_{p_T}/p_T \approx 0.1$ for p_T in the TeV range and a reconstruction efficiency for high- p_T tracks of more than 95% or 90% for isolated leptons and those within jets respectively. This is particularly important since the reliable determination of lepton charge in high- p_T tracks is necessary for measuring charge asymmetries arising from the decay of heavy gauge bosons [1]. To allow such precision momentum resolution the curvature of charged particle tracks in the homogeneous magnetic field of a 2 T solenoid is determined. The ID also has to yield an impact parameter resolution of better than $20\mu\text{m}$ in the transverse plane and $100\mu\text{m}$ in longitudinal direction. A more exhaustive account of the different deciding factors for the performance and resolution of vertex detectors will be given in Section 3.2. In addition, the material budget has to be as low as possible to minimise multiple scattering and photon interaction (see Sections 3.1.3 and 3.1.4) and the lifetime, which is limited by radiation damage in the collider environment, must be longer than the total operation period (see Section 3.5 for more details on radiation damage).

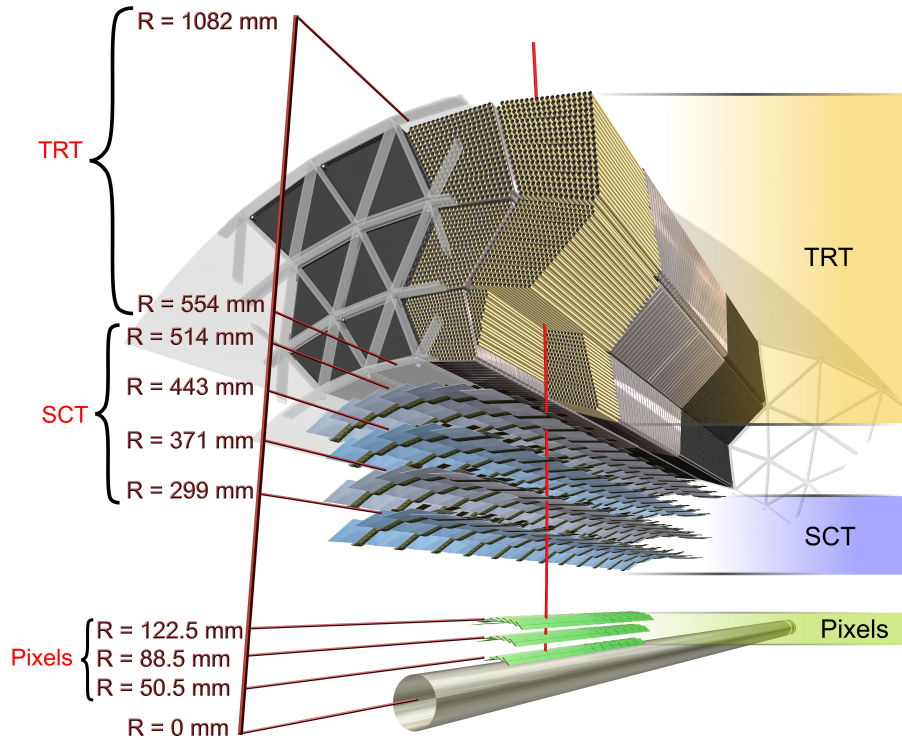


Fig. 2.10: 3D drawing showing a particle traversing the different Inner Detector components in the barrel regions. The particle exits the beam pipe and then subsequently traverses three pixel layers, four SCT microstrip double layers, and approximately 36 axial straws of the TRT [1].

Originally, the ATLAS Pixel detector [30] was composed of 1744 pixel modules on three barrel layers and 2×3 discs in the end-cap region with a total of approximately 80 million readout channels in about 2 m^2 active area. Pixel modules have three main components: one n^+ -in-n silicon pixel sensor as active material with most pixels being $50 \times 400 \mu\text{m}^2$ in size, 16 Front-End (FE) readout chips, and a flex hybrid holding the control chip, circuits for low and high voltage distribution as well as data connections. During the first Long Shutdown of the LHC (LS1) 2013-2014 an additional pixel layer, the Insertable B-Layer (IBL) [31], has been installed in order to mitigate the effects of module failure due to increasing radiation damage (see Section 3.5) and improve the vertexing performance with regards to secondary vertexes in B-Physics. Thanks to a new beam pipe with a smaller radius the IBL could be placed as the new innermost layer at distance of 33.4 mm from the interaction point. In addition to revised planar pixel sensors, 25% of IBL modules were built with then newly developed 3D pixel sensors.

The SCT [32] consists of high-resolution single sided p^+ -in-n silicon strip modules with AC-coupled readout. In total the SCT consists of 4088 modules arranged in four barrel layers and 2×9 end-cap disks, for an overall silicon surface area of 63 m^2 . An example of both barrel and end-cap modules can be seen in Fig. 2.11 and a more detailed description of the strip modules follows below.

The LHC and ATLAS experiment: present and future

In the TRT[33, 34], the transition radiation emitted by charged particles when passing through the boundary between materials with differing dielectric constant is detected. The tracker itself consists of drift tubes with a diameter of 4 mm, combined into 73 layers in the barrel and 160 straw planes in the end-caps. The intensity of the transition radiation depends of the Lorentz factor $\gamma = E/m$, thus heavier particles radiate less transition radiation than lighter particles at the same energy. Using this dependency and discriminating the signal with two different thresholds in the readout electronics, the TRT can distinguish electrons from heavier particles such as π mesons and as such combines particle tracking and identification. In the barrel, polypropylene fibres are interlaced in order to create transition radiation, while polypropylene radiator foils are used in the end-caps.



Fig. 2.11: An SCT barrel (a) and end-cap module (b) with descriptions of its components [35].

The ATLAS Semi-Conductor Tracker modules

In the barrel region each sensor has 768 strips with a pitch of $80\mu\text{m}$ which are implanted on $300\mu\text{m}$ thick substrate, fabricated using a $4''$ wafer process. A barrel module is made of four sensors with two sensors each connected as daisy-chain pairs and glued on either side of a thermally conductive baseboard. In the end-cap region sensors have 768 radial strips of constant azimuth resulting in a pitch from $56.9\mu\text{m}$ to $90.4\mu\text{m}$. Apart from the active strips, there are also an additional two strips, one on each edge of the sensor, at bias potential to define the electric field at the sensor edge (*field-shaping strips*). The strip pitch was chosen by taking into account the limits imposed on vertexing precision from the solenoid B-field, the expected particle momenta, and multiple scattering contributions, while at the same time being in accordance with the required granularity, digitising precision, particle occupancy, and noise performance.

Barrel and end-cap modules are equipped with flex-hybrids holding twelve readout ASICs [1], which provide 128 binary readout channels. The modules themselves are mounted in individual support structures. On the one hand, their purpose is to provide mechanical support and rigidity in addition to sensor cooling. On the other hand, they are also equipped with electrical connections to power supplies for the sensors and chips as well as data connections for readout.

2.4 The High-Luminosity LHC and ATLAS Inner Tracker upgrade

Over the course of its operation since the start-up in 2010, the LHC and its associated experiments have been the primary facilities for studying fundamental questions at the energy frontier in particle physics, culminating in the discovery of the Higgs boson ([4, 5]). In order to continue the scientific programme over the next two decades, a series of upgrades of the accelerator have been planned out, ultimately resulting in the *high-luminosity phase* of the LHC (HL-LHC, [36]). The major performance upgrades will lead to a 5 to 7 \times increase in instantaneous luminosity and an accumulated integrated luminosity for proton-proton collisions of 3000 fb $^{-1}$ [17]. Apart from the order of magnitude more in data collected than prior to the HL-LHC, the number of inelastic proton-proton collisions per bunch-crossing (*pile-up*) would increase from an average of $\langle\mu\rangle = 23$ up to ~ 200 [17].

The current ATLAS Inner Detector will have reached the end of its lifespan by the time of the HL-LHC upgrade, scheduled to be installed in 2024 (*Phase-II*) [17]. Also, the current ATLAS ID technology would be rendered inoperable with the increased luminosity, associated data rate, and radiation damage after the upgrade. The reason being, firstly, that the ID Pixels and SCT were only designed to be operable after the accumulated radiation damage corresponding to the integrated luminosity until the end of Run III. Operation beyond that point would lead to increased leakage current and risk of thermal runaway, exceeding the capacities of both the cooling system and the power supplies, as well as further problems with the readout chips. Secondly, the current bandwidth between the ID front-end electronics and their corresponding *readout driver buffers* (RODs) is insufficient to be used in the HL-LHC due to its saturation limit being well below the prospective instantaneous luminosity. Lastly, an average pile-up of $\langle\mu\rangle \sim 200$ would compromise pattern recognition and track-finding efficiency along the increase in detector occupancy and result in a 100% occupancy of the TRT.

Therefore the Inner Detector will be replaced with the new all-silicon *ATLAS Inner Tracker* (ITk) [17] composed of the inner *Pixel Detector*, consisting of 5 barrel layers and 4 end-cap ring

Tab. 2.1: Comparison of current ATLAS Inner Detector and future ATLAS Inner Tracker [37].

		Inner Detector		Inner Tracker	
		barrel	end-cap	barrel	end-cap
pixel detector	$ z $ range [m]	< 0.4	0.5 - 0.7	0.7(0.8)/ $< 1.2(1.3)$	0.8 - 3.0
	radius range [mm]	51 - 123	89 - 150	39 - 271	80 - \approx 320
	silicon area [m 2]	1.4	0.7	5.1	3.1
	number of layers	3	3	5	varying
strip detector	$ z $ range [m]	< 0.7	0.9 - 2.7	< 1.4	1.5 - 3.0
	radius range [mm]	299 - 514	275 - 560	405 - 1000	385 - \approx 980
	silicon area [m 2]	34.4	26.7	105	60
	number of layers	4	9	4	6

layers, and the outer *Strip Detector*, with 4 barrel cylinders and six disks on each side. A layout of one quadrant of the ITk is shown Fig. 2.12.

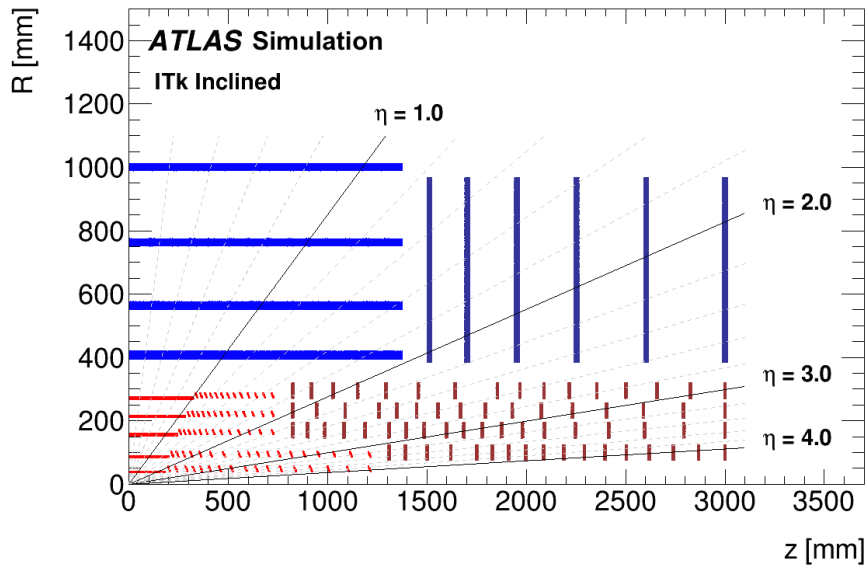


Fig. 2.12: Schematic layout of the ITk Pixel (red) and Strip Detector (blue) with only one quadrant and only active detector elements shown. Vertical elements are end-cap disks and while the strip detector only has one end-cap with 6 disks, the pixel end-cap is divided into individual ring layers. The horizontal axis is the axis along the beam line with zero being the interaction point. The vertical axis is the radius measured from the interaction point. The outer radius is set by the solenoid magnet [17].

The entire tracker layout has to be optimised for its performance in environments where decay products at high momentum can have a separation smaller than a single detector element, even at larger radii such as the position of the strips. As such, the design of the entire detector has to guarantee good tracking performance, despite densely clustered tracks, that is consistent with the physics goals of ATLAS at the HL-LHC. One way to ensure this is by using the charge information in the finely granulated pixel detector layers, as already successfully done in Runs I and II. This ensures accurate track separation even in a high pile-up environment and also illustrates the role of the additional pixel layers in the ITk design, not least in the form of redundancy in case of module failures.

Other requirements include correctly identifying photon conversions. This is mainly of importance to achieve maximum acceptance for events with final state photons, particularly where, even at the HL-LHC, final data will be statistics limited (for example $HH \rightarrow b\bar{b}\gamma\gamma$). For this reason, electrons from photon conversions need to be reconstructible with good efficiency for radii within the pixel layers. In addition, the performance of the b-tagging versus light-jet rejection should match the performance of the current detector despite the presence of 200 pile-up events. As such, the $R\phi$ and z granularity of the innermost pixel layers must be optimised for light-jet rejection in the jet p_T range around 150 GeV, thus the z pitch of the pixels will be reduced to 50 μm compared to 250 μm in the current ID Pixels. The Strip layout should be optimised towards minimal hit sharing in dense jets.

In the following section a more detailed description of the ITk Strip Detector will be given as the research presented in this thesis has been conducted in conjunction with it.

2.4.1 The ITk Strip Detector

The total silicon area of the ITk Strip Detector will be $\sim 165 \text{ m}^2$ and will cover the pseudorapidity range $\eta \leq 2.5$, the same as the current SCT (see Tab. 2.1). The mechanical structural elements, also called *local supports*, in the barrel region are 392 *staves* populated with 14 modules on each side of a stave and 32 *petals* in each disk which hold nine double-sided modules, respectively. The local support provides mechanical rigidity and support for the modules as well as common electrical, optical, and cooling services needed for operation. This is unlike the ID strip modules where cooling and mechanical support were provided for each module separately. The interface of power and data links to electronics outside the detector are *End-of-Substructure* (EoS) cards placed at one end of each respective stave or petal. Staves and petals in turn are loaded onto *global structures* within common mechanics for both the ITk Pixel and Strips components [17].

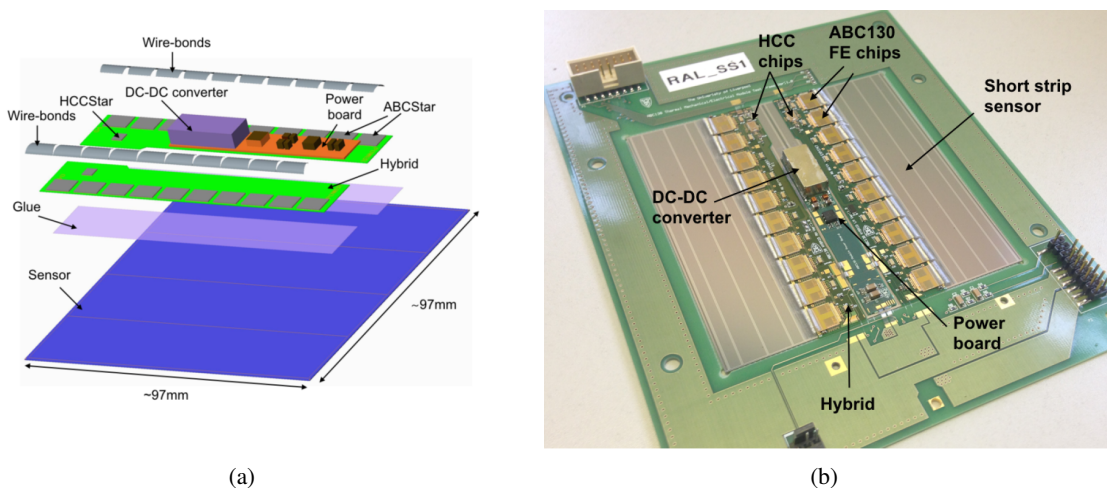


Fig. 2.13: (a): Exploded view of a short-strip barrel module with its components denoted. (b): Picture of a short-strip prototype module in its testframe [17].

Modules for the ITk Strip Detector are composed of one sensor and one or two PCBs (*hybrids*) hosting the readout ASICs (*ABCStar* and *HCCStar*), glued directly onto the sensor. The power board provides switchable sensor HV bias, delivers power to the front-end readout ASICs using DC-DC conversion and monitors environmental conditions. Sensor strips are connected to the ASIC channels via aluminium wire-bonds and similarly all signal connections on the hybrids are realised using wire-bonds. An exploded view of the design of a strip module as well as a picture of an actual prototype module is shown in Fig. 2.13 as an example.

ITk strip sensors are single-sided n^+ -in-p sensors with rectangular shape in the barrel region and wedge shape with curved edges at constant radius in the end-cap. In the barrel, the active silicon area

Tab. 2.2: Overview of the different types of silicon strip sensors for the ITk Strip Detector with their number of segments, total number of channels per sensor, and respective strip pitch [17].

Sensor type	Number of strip segments	Number of channels	pitch [μm]
Barrel sensors			
short-strip (SS)	4	5120	75.5
long-strip (LS)	2	2560	75.5
End-cap sensors			
R0	4	4360	73.5 - 84.0
R1	4	5640	69.0 - 81.0
R2	2	3076	73.5 - 84.0
R3	4	3592	70.6 - 83.5
R4	2	2052	73.4 - 83.9
R5	2	2308	74.8 - 83.6

is divided in either 2 or 4 rows (also referred to as *segments*) with equidistant pitch for each row. The strip length of sensors in the inner barrel layer is half the length of outer layer sensors. They are referred to as *short-strip* (SS) and *long-strip* (LS) sensors, respectively. For end-cap sensors there are six different layouts with radially oriented strips, named R0 to R5 depending on their proximity to the beam pipe. Due to the conical shape of end-cap sensors, the equidistance of their pitch is realised in terms of an angular strip pitch, rather than parallel strips as is the case for barrel sensors, resulting in small variations in the Cartesian distance between strips within each segment. An overview of the different types of sensors is given in Tab. 2.2.

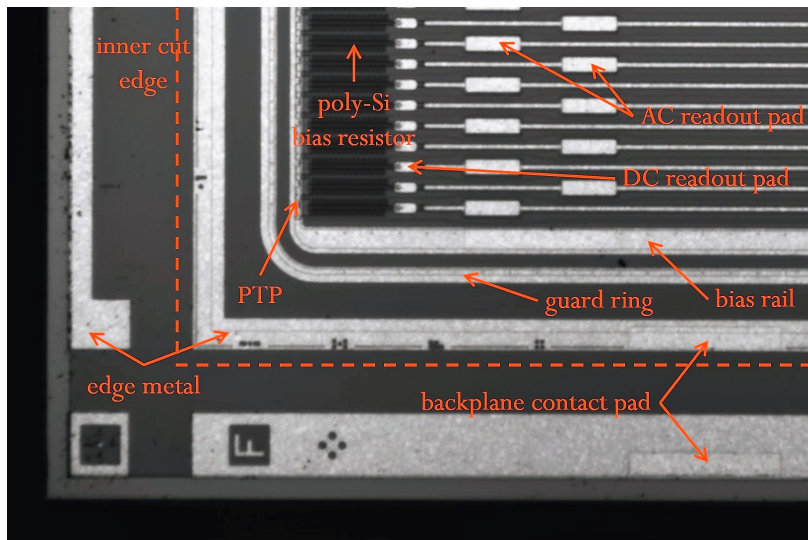


Fig. 2.14: Picture of the corner of an ATLAS12 prototype sensor containing reference to all relevant structures. The shown sensor is an “Outer Cut” type, whereas the final layout will contain “Inner Cut” sensors with reduced edge metal and therefore inactive region, indicated by the dashed line.

The active sensor area is surrounded by three aluminium rings on top of their respective implants. The innermost ring is the *bias rail* with an n^+ implant which is connected to all n^+ strip implants through poly-silicon bias resistors. The outermost ring and its underlying p^+ implant is connected to the backplane in order to define the sensor volume and to prevent the diced edge from developing a high electric field. The middle ring lies on top of an additional n^+ implant and acts as a floating *guard ring* (see Section 3.3.1). Top metal layer strips are AC-coupled to the strip implants through a thin insulating layer, with a p-spray layer or p-stop traces running in between along the full length for strip isolation (see Section 4.1). The top sensor layer is passivated with openings for probing and wire-bonding. Multiple iterations of prototype sensors for extensive testing have been manufactured by Hamamatsu Photonics (HPK) [38–40], a picture of the corner of one is shown in Fig. 2.14. More details on the inner structure of the sensors and their mechanical and electrical properties will be given in Chapter 4.

Chapter 3

Silicon tracking detectors

The detection of particles is a fundamental aspect, not only of high-energy physics, but also in many appliances in everyday life. Throughout the years, silicon, through its widespread availability and usage in the modern electronics industry, has become the standard material for tracking detector application.

The principles of particle detection with emphasis on silicon strip sensors are presented in the following: firstly, Section 3.1 describes the energy loss of different types of particles in matter. Secondly, the basics of vertex measurements in Section 3.2 is described. The properties and characteristics of silicon sensors as they are used in detectors are presented in Section 3.3. Sections 3.4 and 3.5 illustrate the charge carrier transport in tracking detectors with a focus on signal formation in silicon detectors and the influence of radiation damage on detector operation.

3.1 Energy loss of particles in matter

The processes by which particles deposit energy when traversing matter largely depend on the type of particle and its energy, outlined in Sections 3.1.1 and 3.1.2. In the case of tracking detectors in particle collider experiments, vertexing and track reconstruction rely on signals generated by charged particles. While photon interaction, as described in Section 3.1.3, has to be taken into account as an unwanted process in a pure tracker, most uncharged particles like neutrons deposit energy, mostly via scattering at nuclei, but the cross section of which is very small hence it is usually neglected in tracking detectors. However, in a similar manner, scattering processes also have a negative impact on tracking precision, which is further detailed in Section 3.1.4.

3.1.1 Heavy ionising particles

Assuming a charged particle traversing the material, the predominant energy loss happens via ionisation and excitations of the material, resulting in (quasi-)free charge carriers in the vicinity of the trajectory. To measure the induced charge, these charge carriers can be extracted by an external

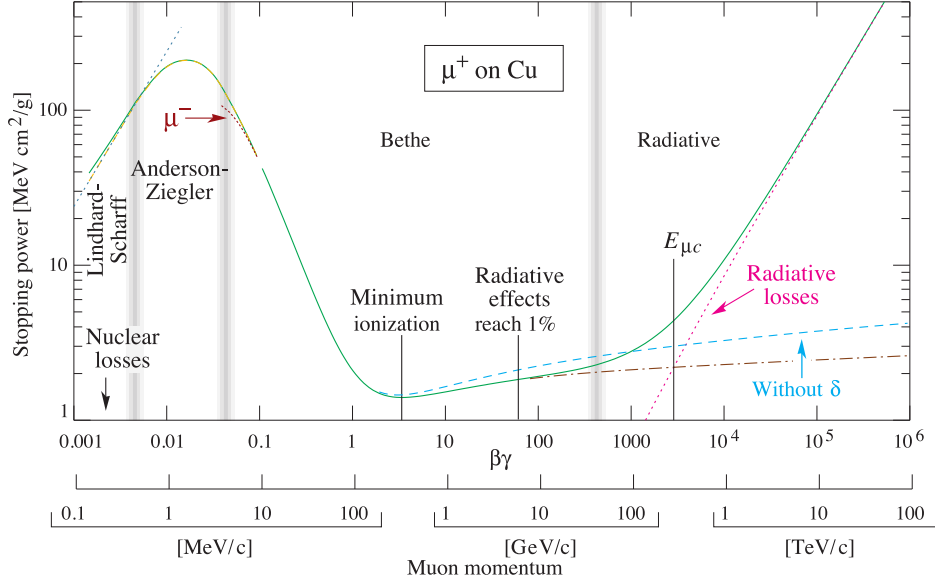


Fig. 3.1: Energy loss of a muon as a function of $\beta\gamma$ in copper absorber, illustrating the average energy loss according to Eq. 3.1. Boundaries between different approximations for several regions of kinetic energy are indicated by vertical lines [41].

electric field or light from the de-excitation can be detected. The quantum mechanical process for relativistic particles was first described by Bethe and Bloch [42, 43], determining the average of the energy transfer E for heavy particles of mass $M^2 \gg m_e^2 + 2m_e E$ as follows

$$-\left\langle \frac{dE}{dx} \right\rangle = K_z^2 \frac{Z}{A} \frac{1}{\beta^2} \left[\frac{1}{2} \ln \frac{2m_e c^2 \beta^2 \gamma^2 T_{max}}{I^2} - \beta^2 - \frac{\delta(\beta\gamma)}{2} \right]. \quad (3.1)$$

A list of symbols used here and in the following is given in Tab. 3.1.

The average energy loss is usually normalised to the mass density ρ (in g/cm^3) of the material, thus rendering the equation essentially independent of the material, since the ionisation energy only contributes logarithmically and the Z/A ratio is approximately $\frac{1}{2}$. The average energy loss for different $\beta\gamma$ is illustrated in Fig. 3.1 in the case of μ traversing copper.

Regarding the energy loss for small $\beta\gamma \lesssim 0.1$, the Bethe-Bloch formula is not yet valid, indicating other dominant processes in the interaction. For $\beta\gamma$ beyond the maximum, the $1/\beta^2$ -term in Eq. 3.1 dominates, hence yielding a steep fall in the average energy loss resulting in a minimum at $\beta\gamma \approx 3 \dots 4$ with $\langle dE/dx \rangle_{min} \approx 1.5 \text{ MeV cm}^2/\text{g}$ irrespective of the detector material. This minimum is often referred to as a hypothetical *minimum ionising particle* (m.i.p.), which is often used as the quantification of the detector response with no need for a specific particle. For higher $\beta\gamma$ the slow rise is proportional to $\ln(\beta\gamma)$, being further reduced for highly relativistic particles by the attenuation factor $\delta(\beta\gamma)$ in Eq. 3.1, such that the average loss only rises to values between 10% to several 10% above the minimum. A more detailed description of the energy loss of charged particles as well as

Tab. 3.1: List of symbols used in the Bethe-Bloch formula Eq. 3.1 and subsequent equations [41].

Symbol	Description
$\beta = v/c$	velocity of the traversing particle in units of the speed of light c
$\gamma = \frac{1}{\sqrt{1-\beta^2}}$	Lorentz factor
I	average ionisation energy of the material
T_{max}	maximum kinetic energy transfer to a free electron in a single collision
z	charge of the particle in units of the elementary charge e
Z, A	atomic number and atomic mass respectively
$m_e \simeq 511 \text{ keV}/c^2$	electron mass
$K = 4\pi r_e^2 m_e c^2 N_A$	$\simeq 0.307 \text{ MeV cm}^2/\text{g}$; here g is the unit of mass, gram
$r_e = \frac{e^2}{4\pi\epsilon_0 m_e c^2}$	classical electron radius
ϵ_0	permittivity of free space

photons can be found in the respective chapter of the ‘‘Review of Particle Physics’’, published by the Particle Data Group (PDG) [41].

Since energy loss is a statistical process and the Bethe-Bloch formula only describes the average value, the actual distribution of the total deposited energy has to be taken into account. Due to the fact that many of the individual scattering processes only lead to a small energy deposition with respect to the maximum possible kinetic energy transfer T_{max} , the total deposited energy ΔE is highly skewed for a small number of interactions, i.e. thin material. The probability distribution of energy deposition in thin absorbers is described by a *Landau-Vavilov distribution* [44, 45]

$$L(\lambda) = \frac{1}{\pi} \int_0^{\infty} e^{-u \ln(u) - u\lambda} \sin(\pi u) du \quad , \quad (3.2)$$

with

$$\lambda = \frac{\Delta E - (\Delta E)_{\text{m.p.v.}}}{\xi} \quad \text{and} \quad \xi = \frac{K}{2} z^2 \frac{Z}{A} \frac{1}{\beta^2} \rho d \quad , \quad (3.3)$$

where d is the thickness of the material and

$$(\Delta E)_{\text{m.p.v.}} = \xi \left[\ln \left(\frac{2m_e c^2 \beta^2 \gamma^2}{I} \right) + \ln \left(\frac{\xi}{I} \right) + j - \beta^2 - \delta(\beta\gamma) \right] \quad (3.4)$$

denotes the most probable value of the total energy deposition with $j = 0.2$ according to [46]. The Landau distribution for a m.i.p. traversing silicon with varying thickness is illustrated in Fig. 3.2. The asymmetric behaviour of the skewed distribution is apparent, whereas the average energy deposition $\langle \Delta E \rangle / d = \langle dE/dx \rangle$ remains constant, as described by the Bethe-Bloch formula Eq. 3.1. Moreover, it can be shown that while dE/dx is independent of thickness, $(\Delta E)_{\text{m.p.v.}}/d$ scales $\propto \ln d$.

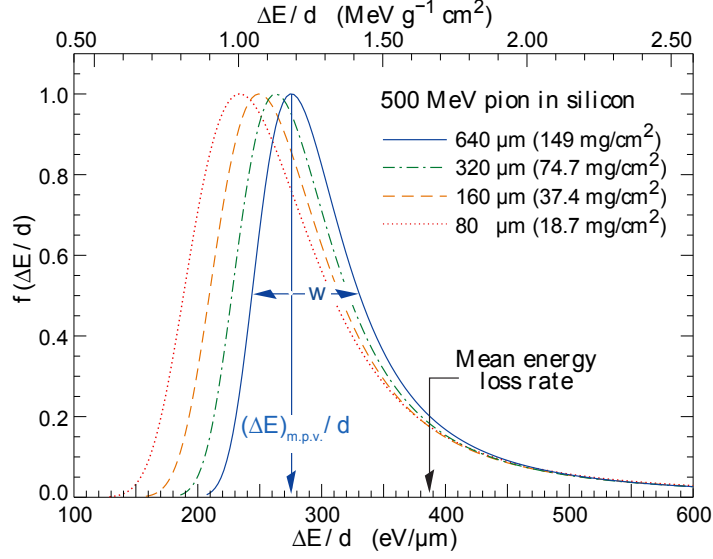


Fig. 3.2: Landau distribution, described by Eq. 3.2, of the energy loss rate ΔE of a m.i.p. in silicon with varying thickness d and normalized to d . The average value, as obtained from the Bethe-Bloch formula, is independent of absorber thickness as indicated, only the most probable value changes [41].

The transition from thin to thick material is defined by the parameter

$$\kappa = \frac{\xi}{T_{max}} \quad , \quad (3.5)$$

with $\kappa \rightarrow 0$ describing thin absorbers. $\kappa \rightarrow \infty$ indicates the case of thick absorbers, for which the distribution of the total deposited energy becomes Gaussian, due to the central limit theorem by interpreting thick absorbers as multiple thin layers. The transition case between thin and thick material has also been described in the work [45] by Vavilov.

3.1.2 Electrons

In contrast to heavy ionising particles, the additional energy loss of incident electrons or positrons due to *bremsstrahlung* in the electric field of the nuclei of the absorber material, as described in [47], cannot be neglected, leading to a correction term in addition to the Bethe-Bloch formula. But, as shown in Fig. 3.3(a), the general behaviour of energy loss due to ionisation in the valid energy region remains the same

$$\left(\frac{dE}{dx}\right)_{tot.} = \left(\frac{dE}{dx}\right)_{ion.} + \left(\frac{dE}{dx}\right)_{rad.} \quad . \quad (3.6)$$

Since the energy loss of electrons due to bremsstrahlung is proportional to the energy E of the traversing particle and the proportionality constant only depends on material and particle properties,

the process can be described by

$$-\left(\frac{dE}{dx}\right)_{rad.} \equiv \frac{E}{X_0} \quad (3.7)$$

The *radiation length* X_0 is a material property which combines the proportionality constants of energy loss via bremsstrahlung. It is the length after which the incident energy E_0 of an electron is reduced to E_0/e by bremsstrahlung losses.

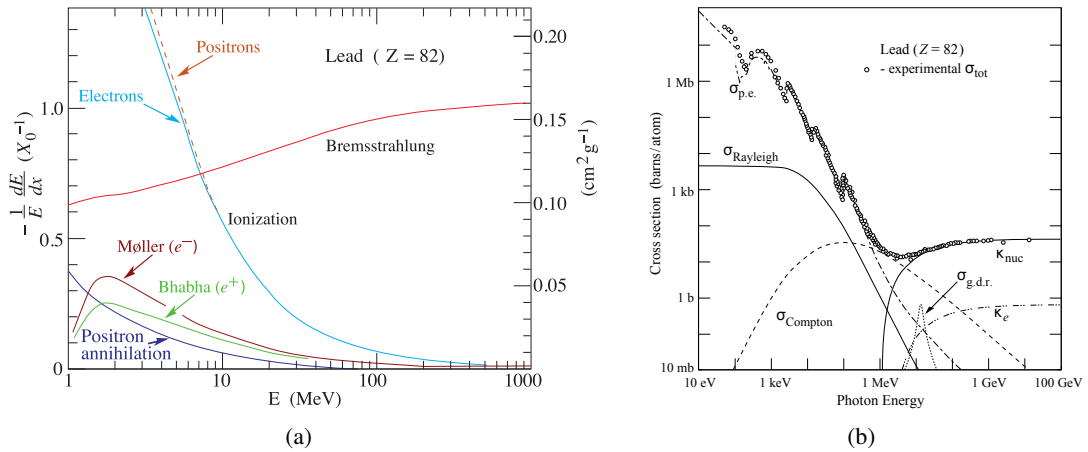


Fig. 3.3: (a) Fractional energy loss of e^\pm per radiation length and (b) photon total cross section in lead as functions of incident energy, showing the contributions of different processes [41].

3.1.3 Photons

The interaction of photons with an absorber material is substantially different in comparison to charged particles. There are three dominating processes which can occur depending on the energy of the incident photon and summarised in Fig. 3.3(b):

photo-absorption: For photon energies close to but larger than the binding energy of shell electrons in the material, the photon is completely absorbed by the electron which in turn becomes a free charge carrier with a kinetic energy equal to the difference of photon and binding energy.

Compton scattering: If the photon energy is well above the binding energy, the photons scatter off the shell electrons, which can be considered quasi-free, with a fraction of the photon energy transferred to the electron.

pair-creation: Photons with an energy exceeding twice the electron mass can create electron-positron pairs in the field of the nucleus of the absorber.

In the case of high-energy physics, only pair-creation has to be taken into account for the components of tracking and vertex detectors. Pair-creation is an overall unwanted process for these devices,

because of the additional tracks increasing the channel occupancy in the tracking detector, which is especially problematic in the case of a hadron collider with an already highly occupied detector. Moreover, measurements of the photon properties in subsequent detector components, such as an electromagnetic calorimeter, may be altered, since it is more difficult to reconstruct the properties from the added tracks. Due to the similarities between the processes of bremsstrahlung and pair-creation, the *mean free path* λ of photons also depends on the radiation length of the material

$$\lambda = \frac{9}{7}X_0 \quad . \quad (3.8)$$

Therefore, having low overall X_0 in the detector is important to reduce pair-creation.

3.1.4 Multiple scattering

Apart from energy loss due to ionisation and excitation according to the Bethe-Bloch formula or contributions from bremsstrahlung, another process that ultimately affects position and momentum resolution is elastic scattering off nuclei within the traversed material, illustrated in Fig. 3.4. The result is a total *scattering angle* θ from a large number of small, individually independent deviations, described by the *Rutherford formula*, when passing through a material of thickness x , depending on its radiation length X_0 . This process is called *multiple scattering* and the distribution of θ can be approximated by a Gaussian with mean zero and standard deviation [7]

$$\sigma_\theta = \frac{13.6 \text{ MeV}}{\beta c p} \sqrt{\frac{x}{X_0}} [1 + 0.038 \ln(x/X_0)] \quad . \quad (3.9)$$

In particular, multiple scattering can limit the measurement precision for tracks of particles with low momentum p or velocity β due to the inverse proportionality between those parameters and σ_θ .

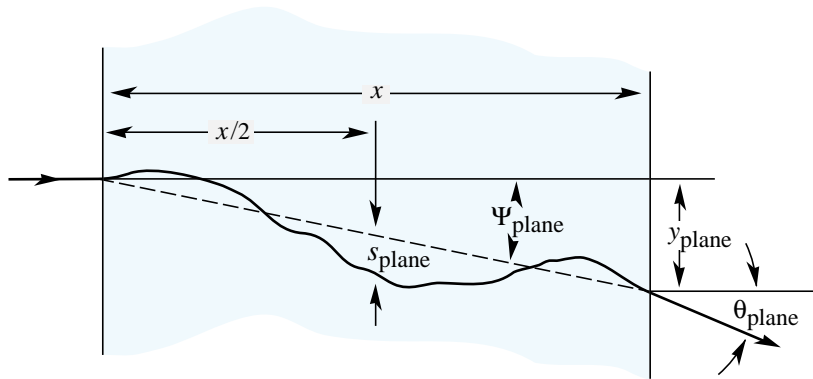


Fig. 3.4: Incident particle undergoing multiple Coulomb scattering in a material [7].

As a consequence, tracking detectors are required to have a low overall material budget using low X_0 materials to minimise adverse effects from photon interactions and multiple scattering and therefore to ensure the overall stability and efficiency of the whole detector.

3.2 Vertex and momentum measurement

The development of tracking detectors for applications in particle physics has been mainly motivated by two important requirements: the ability to study short lived particles decaying into secondary ones and the capability to cope with the increasing number of interaction rates and energies. For the first requirement particle tracks have to be measured and extrapolated to determine whether their common origin is a decay vertex which differs significantly from the interaction point (or *primary vertex*). The latter point requires the detector to be able to detect multiple tracks and select the hit patterns of interest. As a consequence, sufficiently high spatial resolution is needed, which is primarily achieved by segmenting detectors into parts separated by the *pitch* p .

The spatial resolution of a segmented tracker with pitch p can be calculated in the exemplary case of a segment with a single threshold binary readout centred around the position 0. In this case one assumes only one segment per track to be triggered in addition to a uniform density of incident particles. The resulting one-dimensional spatial resolution is

$$\sigma_x = \sqrt{\text{Var}(\Delta x)} = \sqrt{\frac{1}{p} \int_{-p/2}^{p/2} x^2 dx} = \frac{p}{\sqrt{12}} \quad . \quad (3.10)$$

That means that the actual impact position of an incident particle differs from the measured position by $p/\sqrt{12}$ on average [48]. However, this value can be further improved if a group of segments, a so called *cluster*, is triggered due to *charge-sharing* between neighbouring electrodes. Using the optimal configuration for segments in order to allow charge-sharing essentially halves the segment pitch.

The principles of vertex reconstruction can be derived in a simple detector model, shown in Fig. 3.5 consisting of two segmented layers located around the beam axis at radii r_1 and r_2 with $r_1 < r_2$, respectively, and a one-dimensional spatial resolution of σ_1 and σ_2 . The *impact parameter*, i.e. the distance to the interaction point, of the vertex position d_0 can be determined by measuring the hits $d_{1,2}$ in the individual layers and extrapolating the track to $r = 0$

$$d_0 = \frac{r_2 d_1 - r_1 d_2}{r_2 - r_1} \quad , \quad (3.11)$$

up to a resolution of [29]

$$\sigma_{d_0}^2 = \frac{r_2^2 \sigma_1^2 + r_1^2 \sigma_2^2}{(r_2 - r_1)^2} \quad . \quad (3.12)$$

Apart from the limited precision due to the segmentation, there are additional contributions from multiple scattering in the beam pipe material and detector layers themselves, resulting in a distribution and hence a smearing of the particle direction according to Eq. 3.9. The net uncertainty yields a constant term depending on the geometry and a term for multiple scattering depending on the material

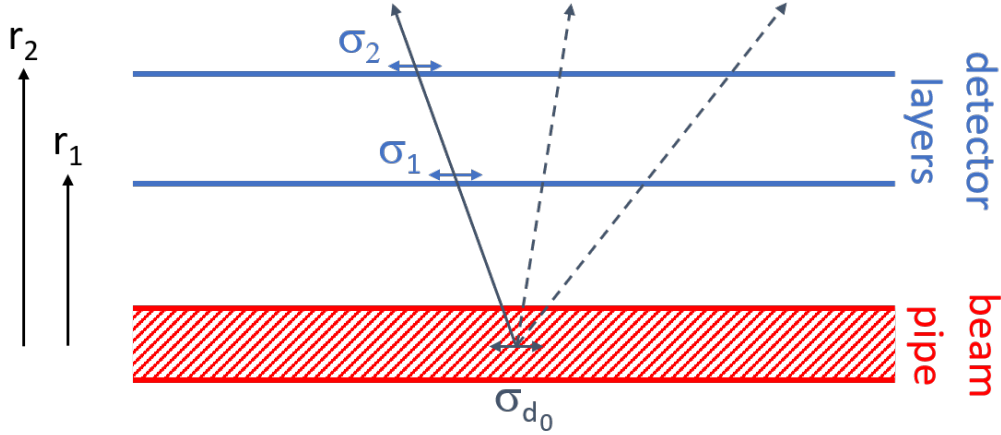


Fig. 3.5: Sketch of a simple vertex detector with important quantities for its vertexing capabilities marked (figure adapted from [29]).

and decreasing with momentum p of a particle track with polar angle θ [49, 50]

$$\begin{aligned}
 \sigma_{d_0} &\approx \sigma(d_0)_{\text{track}} \oplus \sigma(d_0)_{\text{MS}} \\
 &\approx \sqrt{\frac{r_2^2 \sigma_1^2 + r_1^2 \sigma_2^2}{(r_2 - r_1)^2}} \oplus \frac{13.6 \text{ MeV} r^2}{p \sin^{3/2} \theta} \sqrt{\frac{L}{X_0}} \\
 &\approx A \oplus \frac{B}{p_T \sin^{1/2} \theta} \quad ,
 \end{aligned} \tag{3.13}$$

where \oplus denotes addition in quadrature assuming non-correlated errors in both terms, L the traversed distance and X_0 the average radiation length of the material.

With respect to the vertex resolution, there are several ways to improve the tracker design. Eq. 3.12 suggests the inner radius to be as small as possible, moreover, the outer radius should be as large as possible. On the other hand, these suggestions are limited either by the beam pipe, the track density near the interaction point, and the radiation damage for the inner radius, or the costs for large tracking detectors, the enclosing magnets, as well as the other detector systems in the case of the outer radius. The contribution of multiple scattering is negligible for large particle momenta. However, for low-momentum tracks thin detectors and a large radiation length are important.

Vertex detectors are usually located inside a high magnetic field B , leading to a deflection of the trajectories of charged particles due to the Lorentz force. For tracking detectors in collider experiments such as ATLAS, the magnetic field is usually provided by a *solenoid* resulting in a homogeneous field parallel to the beam axis so that the transverse momentum p_T can be measured with high precision. The resulting curvature $R = p_T / eB$ of incident particle tracks can be used to determine the particle momentum, provided at least 3 layers of tracking devices are triggered. Taking the hits in the detector layers as measurement points of the sagitta s of the track curvature, the transverse momentum can

then be determined in the approximation for small deflection angles as

$$p_T \left[\frac{\text{GeV}}{c} \right] = 0.3 B[T] R[\text{m}] = 0.3 \frac{BL^2}{8s} \quad , \quad (3.14)$$

where L is the traversed distance in the tracker. The uncertainty of the *sagitta* (track curvature distance to arc centre) measurement decreases with \sqrt{N} , the number of measurement points, and increasing spatial resolution $\sigma_{r\phi}$ in cylindrical coordinates according to [50]

$$\left[\frac{\sigma(p_T)}{p_T} \right]_{\text{mom.}} = \frac{\sigma_{r\phi} p_T}{0.3BL^2} \sqrt{\frac{720}{N+4}} \quad . \quad (3.15)$$

In addition, similar to the vertex resolution there are contributions from multiple scattering

$$\left[\frac{\sigma(p_T)}{p_T} \right]_{\text{MS}} = \frac{0.05}{BL} \sqrt{\frac{1.43L}{X_0}} \quad . \quad (3.16)$$

Overall, the relative uncertainty increases with p_T .

From the transverse momentum the particle momentum can be reconstructed using the polar angle θ of the track relative to beam pipe and

$$p = \frac{p_T}{\sin \theta} \quad . \quad (3.17)$$

Taking into account the resolution of measurements in z along the beam axis, which depends on the number of measurement points along the trace, and the respective contributions from multiple scattering results in [50]

$$\begin{aligned} \sigma(\theta)_{\text{mom.}} &= \frac{\sigma_z}{L} \sqrt{\frac{12(N-1)}{N(N+1)}} \quad \text{and} \\ \sigma(\theta)_{\text{MS}} &= \frac{0.015}{\sqrt{3}p} \sqrt{\frac{L}{X_0}} \quad , \end{aligned} \quad (3.18)$$

which concludes the assessment of particle trajectory uncertainties in a tracking detector.

Apart from incident particles, charge carriers within the detector are deflected by the *Lorentz angle* θ_L [48]

$$\tan \theta_L = \mu_H B \approx \mu B_{\perp} \quad , \quad (3.19)$$

where B_{\perp} is the magnetic field component perpendicular to the electric field within the detector, μ_H the *Hall mobility* and μ the respective carrier mobility. A consequence of this dependence is that if radiation damage (see Section 3.5) changes the mobility of charge carriers in the sensor over time, the Lorentz angle will change with increasing radiation damage.

3.3 Silicon detectors

Tracking detectors are divided into two types: *hybrid detectors* and *active detectors*. While the different concepts of active pixel or strip detectors have in common that the sensor volume already includes charge amplification and signal discrimination electronics, the general idea of hybrid detectors, which will also be used in the ITk Strip Detector, is the separation of sensor and readout chips. The signal is generated in a sensor chip, which in the case of the strip detectors of the ATLAS experiment have a thickness of $\sim 300\ \mu\text{m}$, the amplification and signal processing is done in a dedicated front-end readout chip, which includes the necessary electronics and is connected to the sensor, e.g. via bump or wire-bonds. Thus there is a 1:1 correspondence between sensor cells and channels in the readout chip, as shown in Fig. 3.6 for a strip detector.

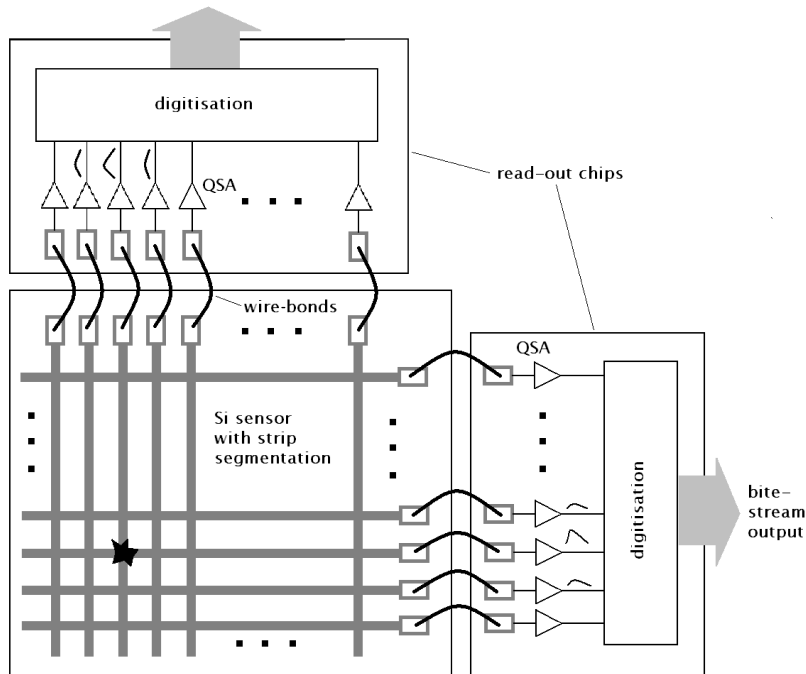


Fig. 3.6: Schematic view of a two-layer hybrid strip detector module. Each strip is directly connected to their respective readout channels via wire-bonds [29].

The advantages of such a detector setup are that the production process can be picked to match the specific application, and optimisation of sensor and readout chips are done in tandem. That way, even different underlying materials are possible. In general, hybrid detectors provide a very fast and parallel readout with subsequent processing, in conjunction with a good radiation hardness (see Section 3.5), by developing or selecting radiation-hard technologies. Furthermore, the overall mature technology of semiconductor p-n junctions leads to affordable cost with respect to the total detector area. However, the interconnection between sensor and electronic chip, often achieved via wire-bonds, is not only a specialised technology but also rather time and labour intensive. Moreover, the full

hybrid modules, including the two chips as well as the necessary power dissipation structures, have an increased material budget compared to monolithic detectors. Apart from these aspects, the strip size is limited due to the direct coupling to the size of the electronics cell. Also, compared to integrated detector concepts, a relatively large signal is required for a good signal to noise ratio due to the input capacitance of the readout chips resulting in an overall higher noise of hybrids.

In the following section, the principles of hybrid strip detectors are presented with respect to the most commonly used sensor material: silicon.

3.3.1 Silicon sensors

Silicon (Si) is a semiconductor, and the fundamental material modern chip technology is based upon. The band gap of Si is $E_g = 1.1$ eV, however, since Si is an indirect semiconductor and additional phonons need to be created in the case of energy deposition, the average energy required for the generation of electron-hole pairs is $W_{\text{Si}} = 3.6$ eV. Thus if particles deposit energy, as described in Sections 3.1.1 and 3.1.2, exceeding W_{Si} electron-hole pairs are generated in the semiconductor. A m.i.p. would deposit on average an energy of $\langle \Delta E \rangle = \langle dE/dx \rangle_{\text{m.i.p.}} \rho_{\text{Si}} d \simeq 0.1$ MeV in silicon of thickness $d = 300$ μm , resulting in $\langle \Delta E \rangle / W_{\text{Si}} \simeq 29 \times 10^3$ electron-hole pairs.

Particle detection in semiconductor devices is done through the usage of a p-n junction with applied reverse bias in the sensor material. Charge carriers generated in the depleted region of a semiconductor can be detected by being swept towards externally biased electrodes. In addition, as described by the Shockley-Ramo theorem ([51], see Section 3.4), already during the drift to the readout electrodes, a signal is induced which can be measured.

p-n junction

The number of free charge carriers in a semiconductor, as well as their temperature dependency can be altered significantly by implementing *acceptor* or *donor* atoms as dopant in the crystal. Acceptors or donors, which replace silicon in the lattice, create a *p*- or *n*-type material with localized energy levels close to the valence or conduction band edge, respectively. Hence for the transition to the conduction or valence band only energies comparable to $k_B T$ at room temperature are needed, providing more electrons (n-type) or holes (p-type) as free charge carriers. The remaining donor atoms become positive *space charges* and accordingly acceptors become negative ones. The following aspects and equations describing a p-n junction are presented in accordance to the explanations in [52].

A p-n junction, as illustrated in Fig. 3.7, is created between p-type, with holes as majority charge carriers, and n-type material, with electrons as majority carriers. The concentration difference of the majority carriers yields a diffusion of respective carriers at the junction. The electric field caused by these space charges subsequently compensates the diffusion leaving the vicinity of the p-n junction fully depleted of free charge carriers, resulting in a *space charge region* (SCR), also called *depletion*

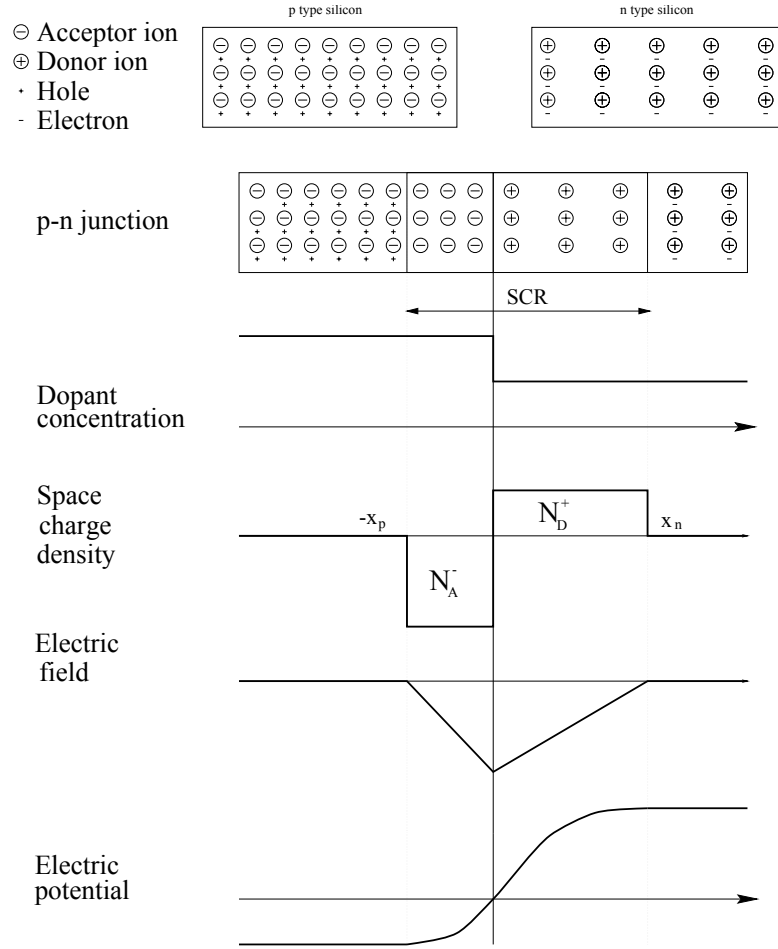


Fig. 3.7: p-n junction in position space: dopant concentration, space charge density, electric field strength and electric potential [52].

zone. The electrostatic potential ϕ can be derived from the Poisson equation

$$-\frac{d^2\phi}{dx^2} = \frac{\rho(x)}{\epsilon_{Si}\epsilon_0} \quad \text{with} \quad \rho(x) = \begin{cases} eN_D & \text{for } 0 < x < x_n \\ -eN_A & \text{for } -x_p < x < 0 \end{cases}, \quad (3.20)$$

which leads to the electric field described by

$$E(x) = \begin{cases} \frac{eN_D}{\epsilon_{Si}\epsilon_0} (x - x_n) & \text{for } 0 < x < x_n \\ -\frac{eN_A}{\epsilon_{Si}\epsilon_0} (x + x_p) & \text{for } -x_p < x < 0 \end{cases}, \quad (3.21)$$

with the extension of the depletion zone in the p- and n-doped material x_p and x_n respectively, as well as $\epsilon_{Si} = 11.75$ being the dielectric constant for silicon and ϵ_0 denoting the vacuum permittivity. The continuity of the electric field provides neutrality of the entire silicon detector with $N_D x_n = N_A x_p$. In detector application, the used p-n junctions usually contain one thin but highly doped implant and

a lightly doped bulk, so that $N_A \gg N_D$ and $x_n \gg x_p$ in the case of p-strips in n-type silicon or vice versa $N_A \ll N_D$ and $x_n \ll x_p$ for n-in-p. The depletion depth d is approximately equal to the extension in the lightly doped material. Considering that semiconductors usually contain both donors and acceptors due to fabrication impurities or radiation damage results in an *effective doping concentration* $N_{\text{eff}} = N_D - N_A$.

The electric field corresponds to a *built-in potential* V_{bi} within the material

$$V_{\text{bi}} = \int_{-x_p}^{x_n} E(x) dx = \frac{e}{2\epsilon_{\text{Si}}\epsilon_0} (N_D x_n^2 + N_A x_p^2) \approx \frac{e|N_{\text{eff}}|d^2}{2\epsilon_{\text{Si}}\epsilon_0} \quad (3.22)$$

An external *bias voltage* V_{bias} will either increase the depth of the depletion zone if applied in the same direction as V_{bi} (*reverse bias*) or reduce it (*forward bias*). The *depletion depth* d is calculated with respect to Eq. 3.22 as follows

$$d \approx \sqrt{\frac{2\epsilon_{\text{Si}}\epsilon_0 (V_{\text{bias}} - V_{\text{bi}})}{e|N_{\text{eff}}|}} \quad (3.23)$$

The permanent thermal generation of charge carriers and subsequent separation in the depletion zone leads to a *leakage current* I_{leakage} throughout the sensor volume

$$I_{\text{leakage}} = \frac{en_i A d}{2\tau} \propto T^{\frac{3}{2}} \cdot \exp\left(-\frac{E_g}{2k_B T}\right), \quad (3.24)$$

with n_i being the *intrinsic charge carrier density*, A the area of the junction, d the depletion depth, and τ the *minority carrier lifetime*. Other effects such as surface currents as well as charge carrier generation in defects and damaged parts of the crystal contribute to the overall leakage current of the sensor.

Capacitance of a p-n junction

The definition of capacitance at a given voltage V_0 is

$$C(V_0) = \left. \frac{dQ}{dV} \right|_{V=V_0} = \left. \frac{dQ}{dw} \frac{dw}{dV} \right|_{V=V_0}, \quad (3.25)$$

with w being the distance between the respective electrodes. In the case of a p-n junction w is the width of the depletion zone. Additionally, the space charge of the diode can be defined as $Q = eN_{\text{eff}}Aw$ where A is the area of the p-n junction and N_{eff} the effective space charge concentration (see section 3.3.1). Assuming a parallel plate capacitor model for the diode where the electrode distance is equal to the depletion depth, the capacitance changes with the applied external reverse bias voltage V_{bias} . With $V_{\text{FD}} > V_{\text{bias}} \gg V_{\text{bi}}$, the respective depletion depth is described by Eq. 3.23 and $\frac{dw}{dV} = \sqrt{\frac{e\epsilon_r\epsilon_0}{2eN_{\text{eff}}V}}$. For $V_{\text{bias}} \geq V_{\text{FD}}$ the depth of the depletion zone equals the thickness D of the diode.

Considering the case of an abrupt p-n junction and neglecting any edge effects, the capacitance of the diode is

$$C(V) = \begin{cases} \frac{\epsilon_r \epsilon_0 A}{w} = \sqrt{\frac{e \epsilon_r \epsilon_0 N_{\text{eff}}}{2V}} A & , \quad V < V_{\text{FD}} \\ \frac{\epsilon_r \epsilon_0 A}{D} & , \quad V \geq V_{\text{FD}} \end{cases} . \quad (3.26)$$

With respect to this dependence it is apparent, that in the case of reverse bias and constant N_{eff} over the detector thickness, the graph of $C^{-2}(V)$ versus V yields a straight line below the full depletion voltage V_{FD} and a constant value for higher voltages. The kink of the graph then yields V_{FD} and the effective doping concentration can be determined either by the slope

$$\frac{d(C^{-2}(V))}{dV} = \frac{2}{e \epsilon_0 \epsilon_r N_{\text{eff}} A^2} \quad (3.27)$$

for a voltage $V_{\text{bias}} < V_{\text{FD}}$ or from the depletion voltage via

$$N_{\text{eff}} = \frac{2 \epsilon_r \epsilon_0 V_{\text{FD}}}{e D^2} . \quad (3.28)$$

Contacting and biasing of sensors

Due to the difference of the Fermi and vacuum levels in metals and semiconductors, a metal-semiconductor contact usually results in a *Schottky contact* including a potential barrier that prevents efficient charge carrier transport into the semiconductor. The solution to this issue is the use of highly doped layers for the contact. Because of the doping the difference in Fermi levels becomes smaller, thus yielding a small junction between metal and semiconductor through which charge carriers can tunnel. Hence the junction behaves like an ohmic contact. For a strip sensor this is realised by using the already highly doped strip implants and providing an additional highly doped thin layer of the same type as the bulk, spanning the whole backplane of the sensor.

The biasing itself can be done by various techniques. The most straightforward, which is also used for SCT sensors, is a resistor network, which can be integrated in the sensor using poly-silicon structures.

Punch-through mechanism and guard rings

Another effect, which can also be used to bias a p-n junction without directly contacting it, is the lateral growth of a depletion zone. This *punch-through* mechanism happens if an external voltage is applied to another p-n junction in the vicinity of the readout contact such that the depletion zone of the biased contact reaches the intrinsic zone of the readout contact. The effect is shown in Fig. 3.8(a). The voltage at which the depletion zone extends to the readout electrode is the punch-through voltage V_{pt} , hence the depletion zone in the active sensor grows with increasing bias voltage V_{bias} together with the depletion zone of the biasing contact. The resulting reverse bias at the readout electrode is

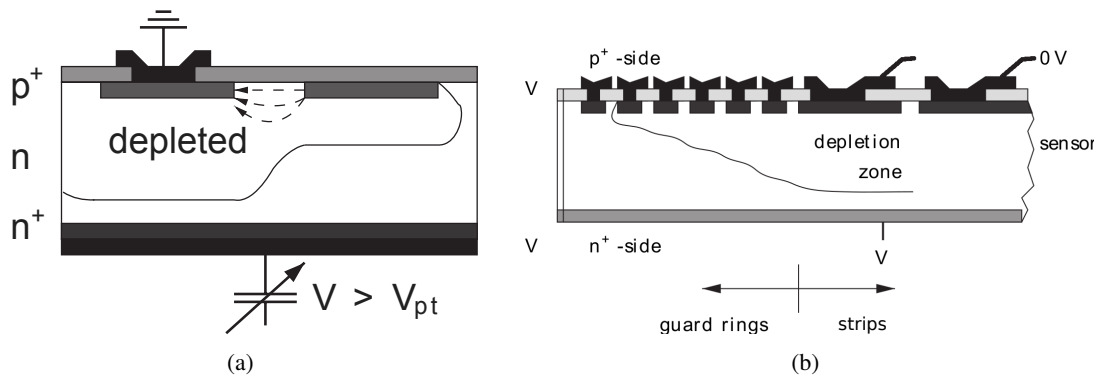


Fig. 3.8: (a) Punch-through effect illustrated with the depletion zone of the biasing contact reaching the intrinsic zone of the active sensor; (b) Depletion region below guard rings and potential of surfaces and edges [48].

therefore the difference $V_{\text{bias}} - V_{\text{pt}}$, with the exact quantity V_{pt} depending on the distance between the two junctions, the concentration of the dopant and the potential distribution in the sensor bulk.

The punch-through mechanism is also used to avoid leakage current at the sensor edge. The bias voltage is usually applied on the backplane, whereas the strip implants are grounded by the electronics. The main problem arising is that due to mechanical damage it cannot be completely avoided that the dicing edges of the silicon wafers are conductive. Due to this effect the potential of the surface between the cutting edge and the active area sits between the ground potential and the bias voltage, and in the extreme case is equal to either one. If the potential at the cutting edge is approximately equal to the ground potential, the depletion zone reaches the surface, hence the surface defects inject a large leakage current into the active area. If the surface is at the bias potential, accumulated charge carriers form a conductive layer close to the strip implant yielding a high local electric field and leading to the risk of a sensor breakdown. Implementing *guard ring* structures, floating highly doped rings of the same type as the strips as shown in Fig. 3.8(b), around the active area leads to a potential drop between each subsequent ring through the punch-through mechanism until the outermost ring reaches the bias potential, thus preventing the depletion zone from reaching the dicing edge.

3.3.2 Detector readout

Even though many different sensor geometries, readout techniques, and analogue circuits exist for hybrid detectors, many parts of the overall design are common among most of them. In general, the chips are divided into an *active area* for each corresponding strip, with sensitivity to incident particles or photons, respectively, and the *chip periphery* containing the controlling elements and data buffering. A typical front-end circuit is shown in Fig. 3.9.

The SCT and ITk strip sensors are AC-coupled to the readout circuit to remove the constant offset of leakage current. The generated charge of a signal is measured with an amplifier, the most common being a *charge-sensitive amplifier* (QSA), i.e. a device to directly measure the collected charge by

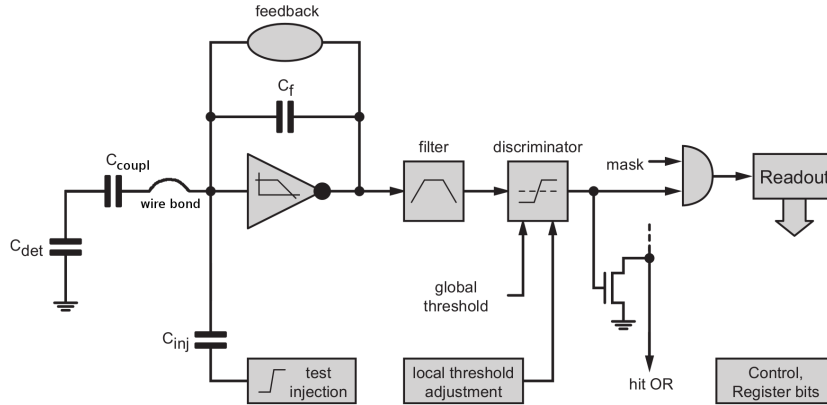


Fig. 3.9: Schematic circuit of a typical AC-coupled front end cell. The sensor is represented by the capacitor C_{det} [48].

integrating the current of a feedback capacitor C_f . A feedback circuit is required to define the DC operation point of the QSA as well as remove signal charges from C_f after the dynamic response of the amplifier. The choice of the applied feedback current is also critical for the measured signal, since either a too small feedback cannot discharge the capacitor in time with regard to the bunch crossing time, or a too large current reduces the signal even during the respective readout, leading to a *ballistic deficit*.

To modify the overall shape of the signal pulse and remove unwanted oscillations, a *CR-RC-shaper* is used, which is a differentiator and subsequent integrator acting as a high-pass and low-pass filter, respectively. After the shaping of the signal, the signal threshold is defined by a discriminator and it is decided whether the signal will be further processed. A common discrimination value is the *time over threshold* (ToT) of the signal.

3.4 Signal formation in silicon detectors

Charge carrier transport

The transport of charge carriers in a material can occur via *drift* or *diffusion*. Diffusion originates from Brownian motion further directed by differences in concentration and is a thermally driven statistical random-walk. As a result, a local δ -distributed charge carrier concentration spreads to a Gaussian. The width σ of the corresponding Gaussian distribution depends on time and is defined by the material-dependent *diffusion constant* \mathcal{D} with

$$\sigma = \sqrt{\mathcal{D}t} \quad . \quad (3.29)$$

Charge carrier drift requires the presence of an electric field. In contrast to the typically accelerated movement of charge carriers in an electric field, continuous energy transfer by scattering off atoms in

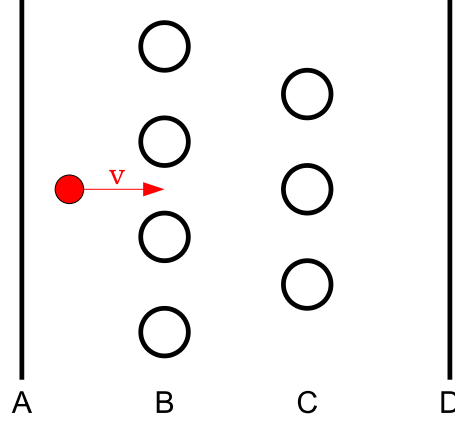


Fig. 3.10: Illustration of a number of electrodes A, B, C, D of a grid in the presence of a moving charge whose path $\vec{r}(t)$ and instantaneous velocity v are known (figure redrawn from [51]).

the crystal lattice yields an additional deceleration and results in a net constant *drift velocity* \vec{v}_D within the material. The drift velocity is usually described by the respective charge carrier mobility $\mu_{e,h}$ and depends on the electric field

$$\vec{v}_D = \mu \vec{E} \quad . \quad (3.30)$$

Drift and diffusion in thermal equilibrium are connected by the *Einstein relation* [53]

$$\mathcal{D}_{e,h} = \frac{k_B T}{e} \mu_{e,h} \quad . \quad (3.31)$$

Shockley-Ramo theorem

The general derivation of induced currents on electrodes originating from the drift of mobile charges in an electric field can be very difficult with increasing complexity of the underlying setup. Additionally, in the case of charge carriers with relatively long transit times, the low-frequency concept of instantaneous current, taken by the electrode once the charge reaches the electrode and hence proportional to the induced current from the amount of electrons received, has to be discarded. Moreover, electrodes may carry current even though they collect no charges at all and current can be noted during the time the charges are still approaching the electrodes. A simple method of computing the induced current for a specified electron motion has been shown in a work by Simon Ramo [51].

One considers a charge e in the presence of any number of grounded electrodes (as illustrated in Fig. 3.10), for one of which, say A , the induced current has to be derived. The general equation describing a current, induced on an electrode by a charge q moving in an electric field with velocity v_D , is the *Shockley-Ramo theorem*

$$I_{\text{ind}} = q \left[\vec{E}_w(\vec{r}(t)) \cdot \vec{v}_D(\vec{r}(t)) \right] , \quad (3.32)$$

Silicon tracking detectors

where \vec{E}_w is the *weighting field* with potential ϕ' . The weighting potential is obtained by solving the Laplace equation under the boundary conditions of its definition ($\phi' = 1$ at the surface of electrode A, $\phi' = 0$ for any other electrode).

Assuming the case of a silicon pad detector composed of two parallel electrodes with lateral dimensions much larger than the detector thickness D , a constant weighting field $E_w = -1/D$ is obtained [51]. An induced current due to the drift of electrons and holes can be described by

$$I_{e,h}(t) = -\frac{eN(t)}{D}v_D(t) \quad , \quad (3.33)$$

with N being the number of drifting charge carriers and v_D the drift velocity. The latter requires the knowledge of the electric field profile in the detector. In the case of an overdepleted detector ($V > V_{FD}$) the electric field usually exhibits a linear behaviour [52]

$$E(x) = \frac{1}{D} \left(V - z \left(1 - \frac{2x}{D} \right) V_{FD} \right) \quad , \quad (3.34)$$

where z denotes the sign of the space charge in the depletion zone. Using the approximation of constant mobility $\mu_{e,h}(E) \approx \mu_{0,e,h}$, which is valid for moderate field strengths, an analytical expression for the induced current can be found. Taking

$$\frac{d\vec{r}_e}{dt} = v_D(\vec{r}_e) = \mu \vec{E}(\vec{r}_e) \quad \implies \quad \frac{dx_{e,h}(t)}{dt} = \mp \mu_{0,e,h} E(x) \quad (3.35)$$

and inserting Eq. 3.34 yields a solution for the equation of motion as follows [52]

$$x_{e,h}(t) = \frac{zV - V_{FD}}{2V_{FD}} D \left[\exp\left(\frac{\mp zt}{\tau_{\text{eff},e,h}}\right) - 1 \right] + x_0 \exp\left(\frac{\mp zt}{\tau_{\text{eff},e,h}}\right) \quad (3.36)$$

$$\text{with } \tau_{\text{eff},e,h} = \frac{D^2}{2V_{FD}\mu_{0,e,h}} = \frac{\epsilon_{\text{Si}}\epsilon_0}{e\mu_{0,e,h}|N_{\text{eff}}|} \quad (3.37)$$

in which x_0 is the starting point of the drift and $\tau_{\text{eff},e,h}$ the *transient time* of electrons and holes, respectively. The resulting drift velocity is

$$v_{D,e,h}(t) = \mu_{0,e,h} \left[\frac{V - zV_{FD}}{D} + \frac{2zx_0V_{FD}}{D^2} \right] \exp\left(\frac{\mp zt}{\tau_{\text{eff}}}\right) = \mu_{0,e,h} E(x_0) \exp\left(\frac{\mp zt}{\tau_{\text{eff},e,h}}\right) \quad . \quad (3.38)$$

As conclusion, the current can be calculated with respect to Eqs. 3.40, 3.33 and 3.38 as

$$I_{e,h}(t) = \frac{eN(t=0)}{D} \mu_{0,e,h} E(x_0) \exp\left(\frac{\mp zt}{\tau_{\text{eff},e,h}} - \frac{t}{\tau_{e,h}}\right) \quad . \quad (3.39)$$

Charge trapping

Charges can be trapped during drift in a material. This effect becomes even more important in the case of semiconductor devices after operation in high-radiation environments. It is due to increased bulk impurities acting as trapping centres. The drift velocity of trapped charges becomes zero, hence they no longer contribute to the induced current according to Eq. 3.32.

The probability of a charge being trapped is proportional to the traversed length in the material represented by the *effective carrier trapping distance* $\lambda_{e,h}$. Since the thermal velocity $v_{th,e,h}$ of charge carriers is typically much larger than the drift velocity, this quantity can be expressed as the *effective carrier trapping time* $\tau_{e,h} = \lambda_{e,h}/v_{th,e,h}$. Consequently, the number of charge carriers exhibit an exponential behaviour over time [52]

$$dN = -N_0 \cdot \frac{1}{\lambda_{e,h}} dl = -N_0 \cdot \frac{1}{\tau_{e,h}} dt \implies N(t) = N_0 \cdot \exp\left(-\frac{t}{\tau_{e,h}}\right). \quad (3.40)$$

3.5 Radiation damage

In particle physics, silicon sensors, as well as the readout electronics, suffer from radiation damage during operation. This happens due to the interactions of detector material nuclei with high-energy particles produced in collisions within the collider. Such damage becomes increasingly important with particle accelerator experiments moving to higher luminosities and radiation doses in the inner detector layers. Radiation induced defects in detectors can be divided into two categories, *surface* and *bulk damage*. Surface defects are especially important for the oxide structures of readout electronics, manifesting themselves in charge accumulation and subsequent electrical breakdown. Bulk damage, i.e. damage in the crystal lattice, is the dominating effect leading to diminishing performance over time, and will be the main focus of this section.

Bulk damage originates from the interaction of incident particles which transfer sufficient energy to remove atoms from the lattice. The necessary energy is called *displacement energy* and accounts for ~ 25 eV/atom in silicon [54]. The underlying energy transfer is mediated by Coulomb interaction, as described by the Bethe-Bloch formula Eq. 3.1, for charged particles as well as nuclear forces in the case of neutrons. Lattice atoms removed from primary interactions can subsequently remove additional secondary atoms, provided the residual kinetic energies of the primary atoms still exceed the displacement energy.

The displacement of single atoms may lead to empty lattice sites, so called *vacancies*, with the displaced atoms being repositioned between actual lattice sites, referred to as *interstitials*. These defects can occur in a local concentration within the material, hence bulk damage is further classified into *point* and *cluster defects*. Moreover, since thermal energy at room temperature provides mobility of the defects within the crystal, defects are generally unstable, thus they may *anneal* over time or rearrange to form more stable defect combinations [48, 54, 55].

A general consequence of radiation damage to the sensor bulk is the creation of additional energy levels within the band gap. Defect levels which are located in the middle of the band gap usually act as recombination and generation centres because of the almost similar distance to the edges of the valence and conduction band. This leads to a reduced charge carrier lifetime and measured charge. As opposed to these, defect levels in the vicinity of the band edges act as *trapping* centres of free charge carriers from the respective bands. Trapped charges are subsequently released with a delay in the order of μs . The result is a modification of the effective doping concentration, i.e. space charges, because of the overall removal of free charge carriers from the material and a reduction of the net signal due to the delayed release of trapped charges [48, 54, 55].

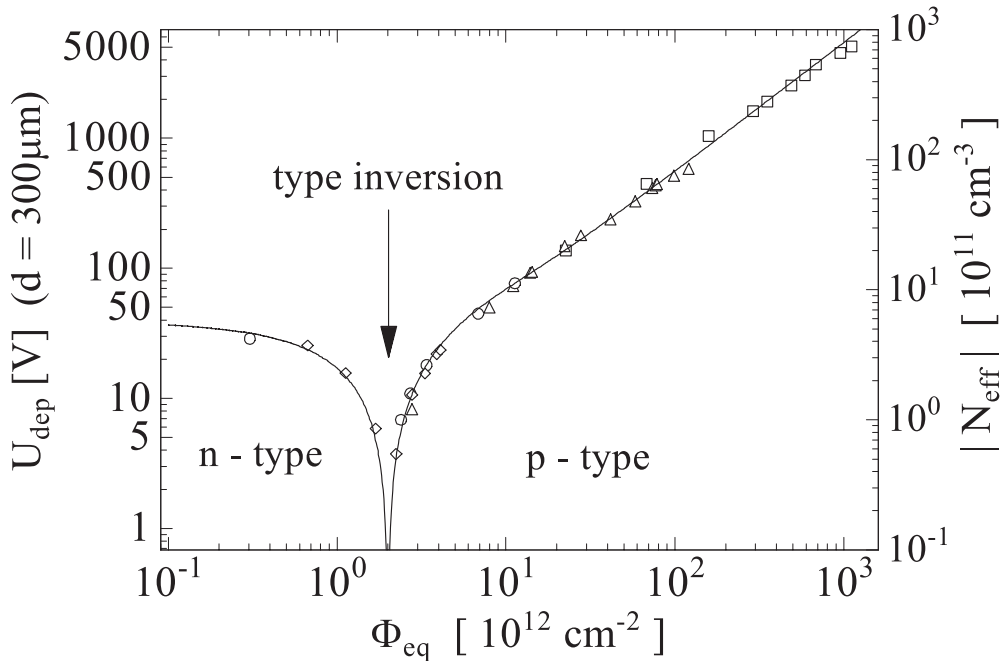


Fig. 3.11: Change of the absolute effective doping and hence the full depletion voltage of a $300\ \mu\text{m}$ thick silicon sensor versus the fluence normalized to 1 MeV neutrons [55].

Type inversion

The modification of the effective doping concentration has an even more severe consequence for the sensor material. As shown in Fig. 3.11, for an original n-type bulk material the modification of the effective doping, because of the generation of additional acceptor atoms due to radiative defects, leads to a change from n-type to an effective p-type material in the case of high radiation doses. This is easily achievable with hadron colliders such as the LHC. Hence, because of this *type inversion*, the depletion zone not only grows in the opposite direction but this effect may yield an electric breakdown of p-in-n detectors. Furthermore, since the depletion depth is dependent on the effective space charge concentration (see Eq. 3.23), an increasing N_{eff} after type inversion reduces the depletion depth and accordingly increases the necessary voltage for full depletion.

Radiation hard silicon sensor technologies

Due to a lack of commercially available high-quality p-type silicon wafers at the time of the initial ATLAS ID design, there was only a choice between two silicon sensor technologies.

The first were p⁺-in-n sensors, which can be manufactured in a single-sided process where only one side has to be processed using a mask, e.g. for strip segmentation or guard rings. Because of this and the readily available production capacities, p-in-n technology offers a simpler design and lower production cost. But due to the aforementioned type inversion, the use of this technology in high-radiation environment is limited. After type inversion the depletion zone grows from the backside towards the segments which in conjunction with the increasing depletion voltage requires the sensor to be operated in overdepletion. Despite this limitation it can still be used for detector components in tracker layers further removed from the interaction point like the ATLAS SCT.

The second technology uses highly-doped n⁺-implant segments in an n-type bulk (n⁺-in-n), which are operated as a p-n junction through p-type implants on the backside. As the doping of the bulk and that of the implants only differs in concentration and not in its type, they need to be isolated using small p-implants between segments, the most common techniques for which are *p-stop* and *p-spray* (see Section 4.1 for more details on strip isolation). The p-type implants on the backside also require a guard ring structure which makes the fabrication of n-in-n sensors a double-sided process. The double-sided processing makes production more expensive, however, the depletion zone of n-in-n sensors after type inversion grows from the n-implant side, which allows charges to drift to the segmented electrodes even in a partially depleted state after high fluences. Before type inversion, reaching full depletion is not an issue [29]. Therefore n⁺-in-n devices were used for the Phase-I pixel detectors in ATLAS and CMS, which are exposed to the highest fluences.

For forthcoming upgrades, as well as new accelerators, more radiation hard detector materials and concepts have been and are still being investigated. One result of those investigations, in addition to the availability of high-quality p-type wafers and the accompanying processing technology nowadays, is that p-bulk silicon has been shown to have radiation hardness which is similar to that of the n-in-n technology currently used [56]. But n-in-p devices also offer additional advantages compared to n-in-n sensors. Firstly, it always depletes from the implant side, allowing for partially depleted operation without screening the strip implants. Secondly, since it can be manufactured in a single-sided process, there is more production capacity already available worldwide, which can lower production cost. Lastly, the lack of patterned backside implants facilitates handling and testing. Hence n⁺-in-p sensors have been chosen for the ITk sensor upgrade.

A high interstitial oxygen concentration in the silicon bulk was also found to improve the radiation hardness, as demonstrated for example in [54]. For n-type silicon, the use of such *oxygenated* silicon bulk material shifts the type inversion to higher fluences, while for p-type material it suppresses the generation of additional negative space charge and thus bulk degradation. The introduction of interstitial oxygen into the material is a prominent case of *defect engineering* used to control defect formation from radiation damage to well-defined defect complexes.

Chapter 4

Evaluation of prototype ITk Strip Sensors

After the high-luminosity upgrade, the new microstrip detector for the ATLAS ITk requires stable operation for its intended lifetime of about 10 years. At the same time, due to the proximity to the interaction point, both solid state sensors, as well as electronics, will have to operate in extremely harsh environments with radiation doses of up to 50 MRad. Hence the sensor layout must be optimised for the instantaneous and integrated luminosity of the HL-LHC as well as tracking performance requirements stipulated by the ATLAS Collaboration. Apart from that, it provides one of the largest silicon surfaces of any microstrip detector in history, However, because of the number of individual modules required for this, their sensor and chip production, module assembly, and testing of all components have to be both cost and time-effective.

All these factors combined have led to an exceptional research and development effort which went on for more than a decade in preparation for the production and installation of the upgrade in LS3 after 2024. During that phase, formerly novel sensor technology in the form of n-in-p devices have been advanced to the state of production readiness. Furthermore, the necessary surface structures for good tracking performance and radiation hardness were established during the multiple iterations of prototypes.

In this chapter, firstly an overview of the main sensors for the ITk Strips Detector and the evaluation process to determine the compliance with mechanical and electrical specifications will be given. Secondly, a compilation of the results of a large variety of electrical tests conducted on more than a hundred sensors will be presented, summarising the data with respect to sensor evaluation of two generations of prototypes. Lastly, the Quality Control process during the production phase will be outlined and how the procedure design was determined by the previously reported findings.

4.1 Large area sensor design

Microstrip sensors for the ITk have to remain operational as a tracker with signal-to-noise ratio > 10 in an environment which requires unprecedented specifications in terms of radiation hardness while at the same time providing an active area more than 100 m^2 larger than the SCT. In order to allow for further operation after suffering radiation from $1 \times 10^{15} \text{ n}_{\text{eq}}/\text{cm}^2$ fluence, the detector is foreseen to work in partially depleted mode towards the end of its lifetime. To maintain strip isolation even under increased radiation damage, the sensor will need specially designed structures to mitigate these effects besides providing a low inter-strip capacitance.

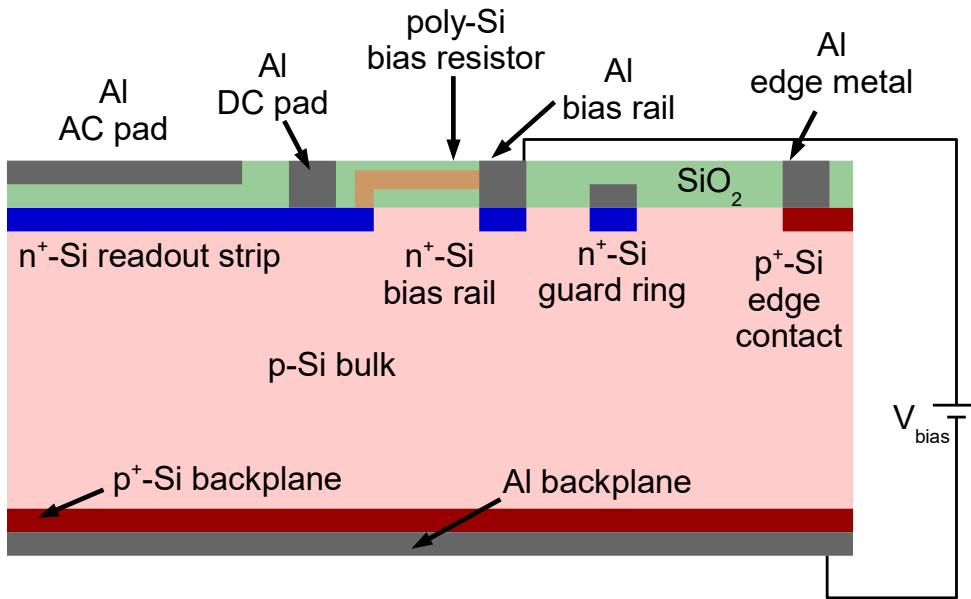


Fig. 4.1: Schematic cross-section of a sensor along the strip direction (not to scale).

The design of choice, a single-sided n^+ -in- p sensor, offers good trade-off of these requirements and cost. As pointed out in the overview given in Section 2.4.1, the sensor shape in the ITk barrel region is square whereas in the end-cap sensors are trapezoidal with two curved edges at constant radius relative to the centre of the disk. Unlike the current SCT sensors, ITk sensors are produced in a 6-inch wafer process, which allows for a larger sensor area size. The *large area sensors* (also referred to as *main sensors*) are being cut out from the central region of the processed wafer with the largest possible dimensions. Alongside them a number of *miniature sensors* (*minis*) and other test structures are produced on the same wafer. These many additional sensors allow for extensive irradiation and testing programs.

In order to determine the characteristics of silicon sensors intended to be used in the upgrade, a large number of prototype sensors, received in multiple batches from different manufacturers from 2005 to 2019, were thoroughly tested. The results presented in this chapter were all obtained on the

full-sized main sensors. A more detailed explanation about their mechanical properties, structural composition, and the different prototype batches will be given in the following.

Radiation hard bulk material

The investigation of silicon bulk material with increased radiation hardness led to the discovery of the advantages of defect engineering through oxygen enrichment (details in Section 3.5) and the space charge limited avalanche (SCLA) effect [57, 58]. Following the research efforts of the RD48 [59, 60] and RD50 [61, 58] collaborations with regards to performance and charge collection efficiency after irradiation, in particular, the material of choice is oxygenated p-type float-zone silicon. In addition, in order to ensure low depletion voltage, even with accumulated radiation damage, the resistivity of the silicon wafer should be at least in the region of $3\text{ k}\Omega\text{cm}$ to allow (unirradiated) operation voltage below 330 V.

Strip isolation structure

The surface structures of a microstrip sensor have a large impact on charge-sharing between neighbouring strips and therefore the magnitude of the collected charge per channel. As too much charge sharing can degrade position resolution, because of the necessity for voltage pulses to exceed a set threshold, it is an important factor in the sensor design. Like other parts of the sensor, strip isolation will suffer from radiation damage. The positive Si/SiO₂ interface charges due to built-in defects of thermal oxide will lead to an *inversion layer*, which is further exacerbated by long-term operation and the accumulation of surface damage from ionising radiation (see Chapter 6), which can result in short-circuiting of n-implants in n-in-p sensors similar to the operation of n-channel MOSFETs. To prevent this, a potential barrier is required to interrupt the formation of the inversion layer, which is usually done by implanting acceptor atoms in shallow structures at the surface, hence creating floating p-type implants resulting in depleted restricted areas between n-type strips to maintain strip-to-strip isolation even at the end of the detector life. In early prototyping, a large variety of isolation structures were tested, most of which include a combination of *p-stop* and *p-spray*, but also variations of strip pitch. The different structures were electrically tested in large and miniature sensors before and after irradiation and results compared to simulations for further optimisation [62]. The conclusion drawn from those investigations was to use narrow, common p-stop traces with doping dose concentrations of $4 \times 10^{12}\text{ cm}^{-2}$ for the final design.

Punch-through Protection

While AC-coupled sensors have the advantage of decoupling leakage current from the front-end preamplifier input, they are susceptible to large potential differences between the AC readout pads, which are grounded through the readout electronics, and the strip implants. Especially in the case of an uncontrolled beam loss, the voltage can exceed the specification for the hold-off voltage of the

Evaluation of prototype ITk Strip Sensors

SiO₂ acting as the coupling capacitor which is typically tested against (see Section 4.2) and that way damage the readout chips or even destroy the sensor. Therefore, in a beam splash the *Punch-through Protection* (PTP) structure aims to short circuit the bias resistor and drain the charge directly from the strip implant into the bias rail, protecting the coupling capacitor. The historical implementation of this is to introduce a small gap between the strip implant and the bias ring structure in the sensor edge, which generates avalanche breakdown towards the bias rail in the presence of a large voltage pulse. During the development of the ITk sensor layout, different PTP structures have been tested [63]. The finalised layout employs a *gated* PTP, which has the Aluminium layer of the bias rail overhanging onto the strip implant while also having the p-stop underneath [64]. The reason for that decision was the more uniform PTP breakdown voltage and predictable behaviour.

Edge structure and guard rings

One goal of the sensor design was to minimise dead area in order to take space limitation in the inner part of the detector into account, but also to decrease the probability of multiple scattering within the tracker, and improve the accuracy of the subsequent calorimeter. On the sensor surface a p⁺-implant extending from the cut edge to the aluminium edge-metal (see Fig. 4.1) is connected to the p⁺-backplane through the conductive sensor edge. Openings in the passivation on the edge-metal allow topside contacting to provide sensor bias during electrical evaluation. Moreover, as detailed in Section 3.3.1, a guard ring structure is important so as to prevent high voltage breakdown around the cut edge by weakening the electric through floating n⁺-implants. To achieve this, the performance of diode test sensors with different edge widths and number of guard rings has been evaluated by comparing the radiation tolerance and the onset of voltage breakdown [63, 65], ultimately deciding on the usage of a single guard ring in the final design.

Prototype sensor batches

Starting with the earliest prototypes of large p-type microstrip sensors as part of the SCT R&D [67, 68], multiple iterations of prototype sensors have been manufactured for mechanical and electrical evaluation. An overview of wafer layouts of all different ITk Strips prototype batches is shown in Fig. 4.2. The first two generations of sensors designed for the ITk upgrade, ATLAS05 and ATLAS06, were mostly used to develop the overall architecture and strip isolation structures necessary to cope with HL-LHC fluences. The ATLAS06 generation also marked the transition from 4 to 6-inch wafers. Following those early iterations, three generations of true ITk prototype barrel sensors have been fabricated by *Hamamatsu Photonics K.K.* (HPK): two generations of short-strip sensors, ATLAS07 and ATLAS12, and one generation of long-strip sensors, ATLAS17LS. Likewise, the first ever generation of full-sized end-cap sensors ATLAS12EC with similar characteristics as the ATLAS12 has been delivered, these are R0-type sensors, but are not investigated in detail within the scope of this chapter. In addition, as part of a market survey for the final manufacture during the production phase, one generation of long-strip sensors was produced by *Infineon* (IFX), IFX-ATLAS17LS.

4.1 Large area sensor design

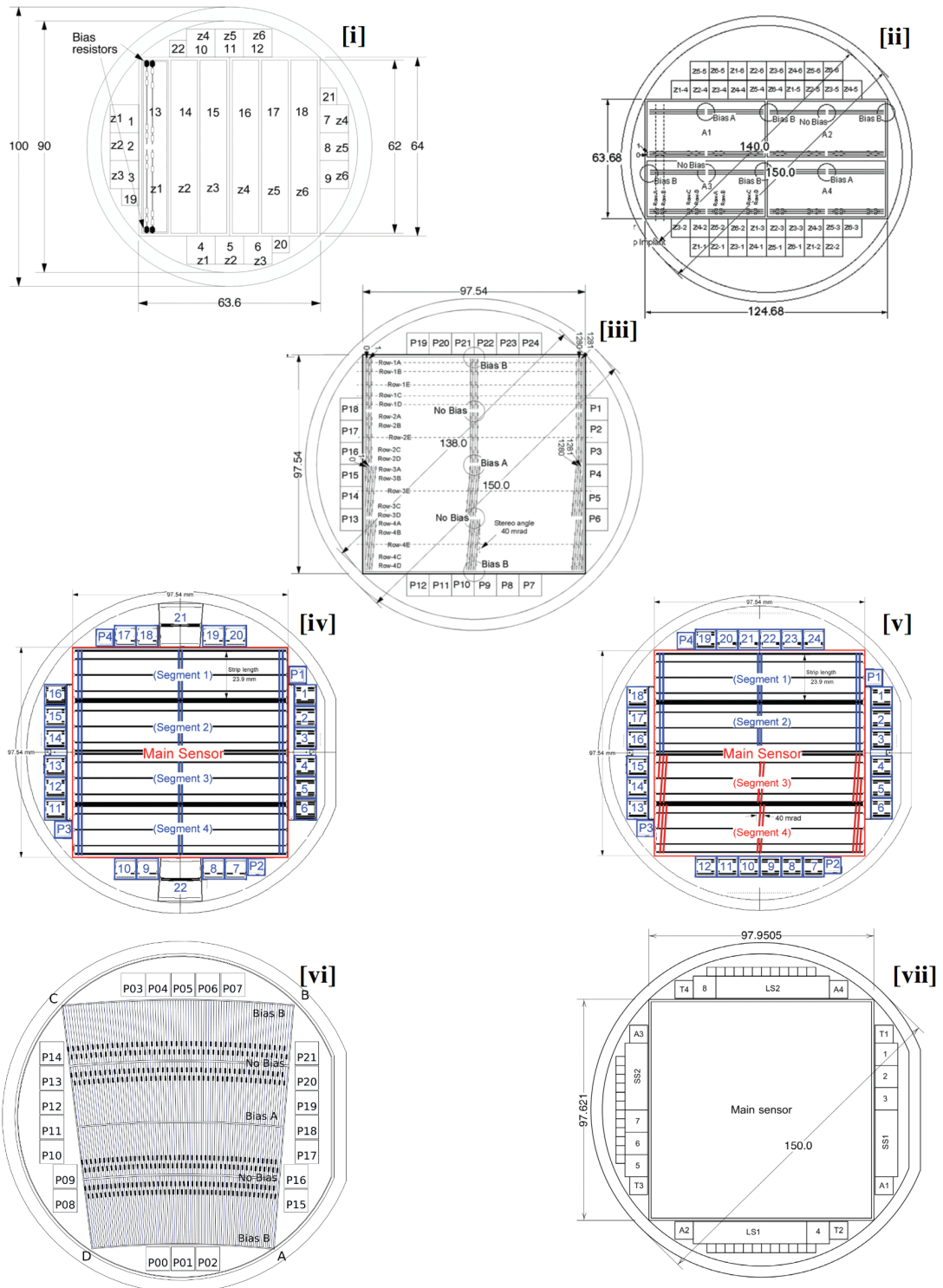


Fig. 4.2: ITk microstrip sensor prototype fabrication wafer layout: [i] ATLAS05, [ii] ATLAS06, [iii] ATLAS07, [iv] ATLAS12A (axial strips), [v] ATLAS12M (stereo/axial strips), [vi] ATLAS12EC (RO end-cap), [vii] ATLAS17LS. Between the ATLAS05 and ATLAS06 generation the transition was made from 4-inch to 6-inch wafer process (adapted from [66]).

Evaluation of prototype ITk Strip Sensors

As the first true ITk prototype, the production goal of the ATLAS07 (or A07) generation was a proof-of-principle of the baseline sensor technology with respect to the specifications and requirements of the finalised tracker. This included the investigation of different sensor layouts in terms of strip isolation and PTP as well as a review of silicon wafer characteristics. The strip layout was that of a short strip barrel sensor with 1280 active readout strips per segment and two additional *field-shaping strips* at either end of the rows (strip number 0 and 1281, respectively). As can be seen in Fig. 4.2, in two rows the strips were parallel to the sensor edge (*axial strips*), while in the other two rows they were inclined by the prospective stereo angle between the sensors of a double-sided module in the final tracker of 40 mrad (*stereo strips*). The different batches of ATLAS07 sensors included two different types of p-type float-zone silicon material, float-zone type 1 (FZ1) with higher quality and resistivity and type 2 (FZ2) with lower resistivity but significantly lower cost. The strip isolation varied between different batches, using either p-spray, p-stop or a combination of both. Furthermore, miniature sensors fabricated along main sensors allowed for a wider range of differences in sensor architecture by varying the width of implant and top-side aluminium or the number of p-stop traces. Results of measurements on ATLAS07 sensors are summarised in [38, 68, 69].

Tab. 4.1: Overview of prototype sensor batches of the ATLAS12 and ATLAS17 generation.

ATLAS12 short strip barrel sensors			
ATLAS12A		120 sensors	4 rows axial strips
ATLAS12M		45 sensors	2 rows axial + 2 rows stereo strips
	VPX12318	33 sensors	all tested in Cambridge
ATLAS12A	VPX12518	32 sensors	all tested in Cambridge
batches	VPX12519	35 sensors	all tested in Cambridge
	VPX14757	20 sensors	all tested in Santa Cruz, cross-checked in Cambridge
ATLA17LS and IFX-ATLAS17LS long strip barrel sensors			
	HPK sensors	51 sensors	2 rows axial strips
	IFX sensors	5 sensors	2 rows axial strips
	VPX26244	33 standard sensors +5 reduced active thickness	23 tested in Cambridge 2 tested in Cambridge
ATLAS17LS		5 standard sensors	5 tested in Cambridge
batches	VPX29549	+5 special passivation	3 tested in Cambridge
	VPX29548	3 defective sensors	many defects; QC verification
IFX2017	VC820647	5 sensors	4 tested in Cambridge

Sensors of the ATLAS12 (or A12) generation, which supersede the ATLAS07 types, were produced and delivered in 5 batches comprising a total of 165 sensors. Four of those batches with 120 sensors in total were produced with 4 segments of axial strips (ATLAS12A or A12A) for detailed studies of sensor properties and module prototyping, results of which will be presented in the following

4.2 Sensor technical specifications and evaluation

section. The final batch again had two rows of axial and two rows of stereo rotated strips (ATLAS12M or A12M). The ATLAS12A batches VPX12318, VPX12518, and VPX12519 – consisting of 33, 32, and 35 sensors respectively – were shipped to the University of Cambridge, United Kingdom, for full quality control reception testing. Batch VPX14757 with 20 sensors was delivered to the University of California, Santa Cruz, United States. In contrast to the A07 generation, A12 exclusively utilise p-stop traces for strip isolation. Moreover, the punch-through protection has been improved by using the gated structure and the bond pad layout has been modified to match the future ABCStar readout ASICs [17]. Like the ATLAS07 sensors, ATLAS12 sensors have a sensor pitch of $74.5\ \mu\text{m}$ and more AC pads for contacting and testing purposes than necessary for module production. In order to reduce the dead region at the sensor edge, the majority of sensors in the batches were of the “*Inner Cut*” (also referred to as “*slim edge*” or “*slim diced*”) design, which has edge metal around the sensor reduced by $450\ \mu\text{m}$ in longitudinal direction and $500\ \mu\text{m}$ in lateral direction, compared to the “*Outer Cut*” design similar to the previous generation of sensors.

The latest generation of sensors that has been manufactured, as of the writing of this thesis, ATLAS17LS (or A17), is the first prototype batch with a strip pitch of $75.5\ \mu\text{m}$ consistent with that of the finalised tracker. Currently there are a total of 48 sensors, divided into two batches, VPX26244 and VPX29549, with 38 and 10 sensors respectively. Along the standard sensors, 5 sensors belonging to batch VPX26244 are produced with reduced active thickness and 5 sensors of VPX29549 have special surface passivation. Three more sensor samples (VPX29548), which have been tested by Hamamatsu and found to have many defects, were provided to Cambridge in order to verify production Quality Control (QC) procedures and to subsequently be delivered to other institutes for the same purpose. Apart from the doubled strip length and a reduction of AC pad rows to only 2 per segment – one at each end of the strip – the sensor architecture is similar to those of the A12 generation. The sensors produced by Infineon have identical layout compared to the Hamamatsu sensors.

4.2 Sensor technical specifications and evaluation

Besides prospective operation conditions and requirements, the capabilities of mechanical structures, electrical connections, and cooling dictate a strict set of technical specifications which sensors have to comply with. Throughout the prototyping phase, these specifications have been revised and adjusted to the respective sensor generation, ultimately arriving at the finalised specifications which will be tested against during production (see Section 4.11 for details on this).

Apart from basic mechanical properties like the edge dimensions and thickness, all sensors have to undergo visual inspection of their surface structures. Checking for chipped edges, large scratches, or other unusual visual appearances a necessity as those visually apparent faults are often reflected in the electrical properties. Moreover, the feasibility of successful module assembly, and subsequent embedment onto local support, places a limit on the maximum bow of the sensor as a whole, which can be further exacerbated by the addition of glue and hybrids during the assembly process. For this reason metrology measurements have to be conducted.

Evaluation of prototype ITk Strip Sensors

The electrical specifications of sensors are equally strictly stipulated [17, 70], since those are not only defined by the limits of available electrical infrastructure, but also have a direct impact on the tracking performance and long-term reliability. Because both the maximum possible power of bias supplies and the provided CO₂ cooling of modules on staves and petals, in order to cope with the unavoidable power dissipation, has its limits, there can be neither an excessive sensor *leakage current* present during operation, nor should the *depletion voltage* exceed certain levels. The latter also has to be taken into consideration for the radiation hardness and the changes of depletion voltage over the course of HL-LHC runtime. For a similar reason, the development of the leakage current under constant bias has to be tested for extended periods of time. This can obviously not be done for a time period comparable to the planned total operation period of the detector, however, at least cases like runaway currents during the first days of the virgin detector being operated have to be guarded against and a general estimation of the long-term reliability can be given.

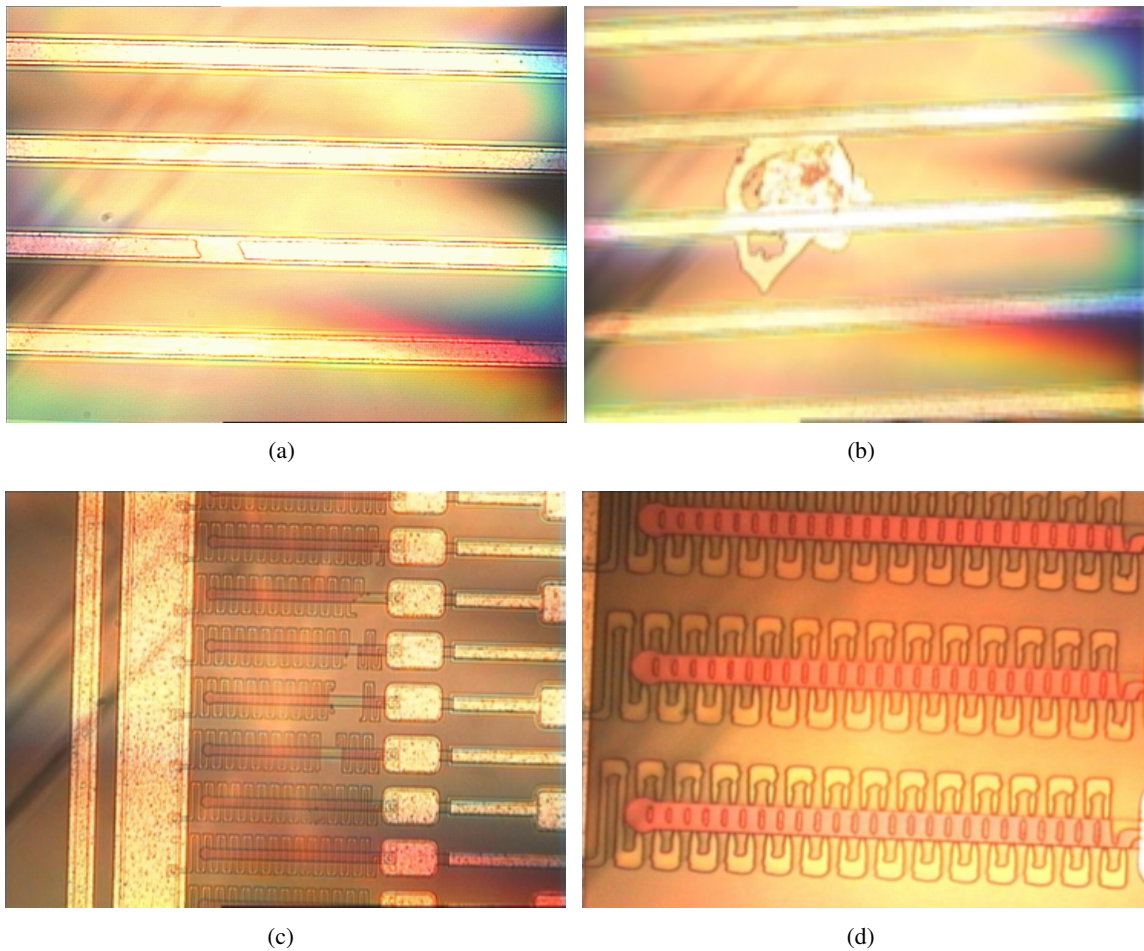


Fig. 4.3: Different types of electrical and their corresponding visual defects detectable with a full strip test: (a) implant break, (b) metal short, (c) broken/open resistor, (d) resistor process defect [71].

Many detector faults can already be spotted from the visual inspection of the sensor surface. But as the sensor area grew larger from the days of the SCT, spotting minuscule suspicious structures in all of the up to 5120 active channels and the surrounding guard and bias rings can be exceedingly difficult. Some of these faults can often not be directly spotted and rely on special lighting or different viewing angles. Thus, a measurement of the electrical properties, a full *strip test*, of each individual active strip is sensitive to any strip or general processing defect that may effect operation of the sensor. This test is conducted by probing the robustness of the dielectric, by applying a voltage across it, and the underlying R-C network of the AC readout pads, which yields the bias resistance and coupling capacitance for every strip. Upon closer subsequent inspection, many of the defect strips found in the strip test have a visual fault corresponding to the electrical defect, as shown in Fig. 4.3.

As mentioned in the previous section, the strip isolation structure is important for the position resolution and long-term reliability due to its effect on charge-sharing as well as radiation hardness. Therefore, the *inter-strip resistance* (R_{is} or $R_{inter-strip}$) has to be measured. In addition, it also influences the detector noise, since the capacitance between strips, the *inter-strip capacitance* (C_{is} or $C_{inter-strip}$), is the dominant contributor to the input capacitance of the readout ASICs, hence warranting the scrutiny of this characteristic. For that reason, an optimal detector would seek to employ a strip isolation structure that minimises C_{is} while at the same time maximising R_{is} . Likewise, the function of the PTP has to be tested and verified as part of detailed measurements of the prototype sensors in order to guarantee safe protection against potentially damaging voltage pulses in the case of beam loss.

4.3 Instrumentation

In the following, an overview of the various instruments and their different features used for the evaluation of prototype sensors will be given.

Instruments for electrical measurements

In order to bias the *device under test* (DUT) and measure occurring leakage current, *Source/Measure Units* (SMUs) are needed. The instruments used are the *Keithley 2410* (KE2410), *Keithley 487* (KE487), and *Keithley 6517* (KE6517). The KE2410 has its current meter directly connected to its potential source, whereas the KE487 and KE6517 are instruments with high input impedance and have current meters which are separate from the voltage source. Furthermore, all supplies have a selectable *compliance*, i.e. a limit to which the SMU can source voltage or current.

The capacitance C of a DUT cannot be measured directly, unlike e.g. current or voltage. In general, it is derived from the *complex impedance*

$$Z = R + i \left(2\pi fL - \frac{1}{2\pi fC} \right) \quad , \quad (4.1)$$

Evaluation of prototype ITk Strip Sensors

where R and L are the resistivity and inductance of the DUT respectively, and f the frequency of an applied AC test voltage. The measurement is usually conducted by determining the absolute value of the impedance, normally done by employing the *4-Terminal Sensing* technique for highest precision and negation of wire resistance, and subsequently combining it with the phase shift of the response to the AC signal in the DUT. Besides this, a DC voltage is applied in order to bias the device.

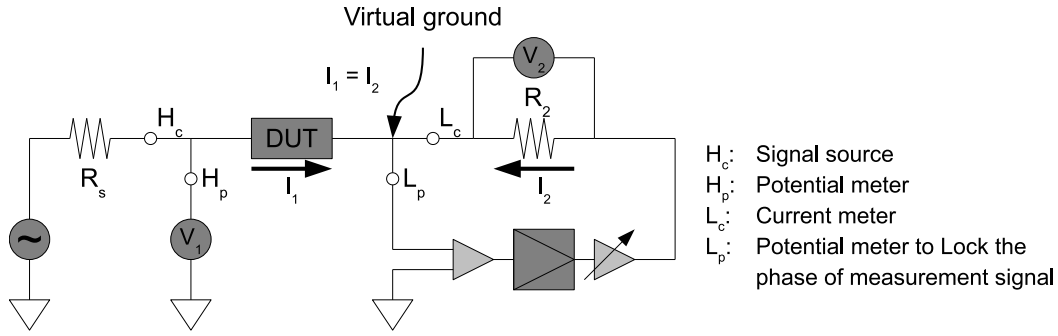


Fig. 4.4: Schematic circuit of the auto balancing bridge capacitance measurement method [72].

The utilised internal method of operations within LCR meters is the *auto balancing bridge*, as shown in Fig. 4.4. The bridge itself can be conceptualised as an operational amplifier circuit. The AC signal, which is used to stimulate the device, is monitored at the H (high) terminal along with the DC bias V_1 , whereas the L (low) terminal is driven to 0 V by the virtual ground of the operational amplifier. Thus, the current $-I_2$ through the resistor R_2 is equal to the current through the DUT I_1 . Therefore, the output voltage V_2 is proportional to the current through the DUT and voltages and currents are automatically balanced. Applying Ohm's law yields the impedance of the device as

$$|Z_{\text{DUT}}| = \left| \frac{V_1}{I_1} \right| = \left| \frac{V_1}{I_2} \right| = \frac{|V_1| R_2}{|V_2|} \quad , \quad (4.2)$$

The complex impedance of a device leads to a phase shift φ between voltage and current

$$\tan \varphi = \frac{\text{Im } Z}{\text{Re } Z} = \frac{\omega L - \frac{1}{\omega C}}{R} \quad , \quad (4.3)$$

with $\omega = 2\pi f$. The capacitance of the device can be calculated from Eq. 4.1 by using the measurement results in combination with Eqs. 4.2 and 4.3, provided the inductance L is negligible.

The LCR meter used for the sensor studies presented in the following is a *Wayne Kerr 6640B* (WK6460B). It can source AC test voltages with amplitude between 1 mV and 10 V, and frequencies in the range from 20 Hz to 3 MHz. The instrument can also provide DC bias up to 2 V (internal supply) or 60 V (external power supply needed). However, since the conducted measurements require high voltage biasing, this feature was not used and it is connected through a blocking capacitor. To have the instrument automatically compensate for the effects of residual impedances and stray admittances of the setup without DUT, automated trimming procedures are conducted before the actual scan.

Coordinate measurement machine

A *coordinate measurement machine* (CMM) allows the mapping of the sensor height and thus a measurement of its planarity. The *BATY Venture 3030* CMM used, shown in Fig. 4.5, can do this with a touch probe as well as in a contactless, optical scan, with a precision better than $2\ \mu\text{m}$ in $x - y$ and $4\ \mu\text{m}$ in z . The same device is also used in the visual inspection of sensors.

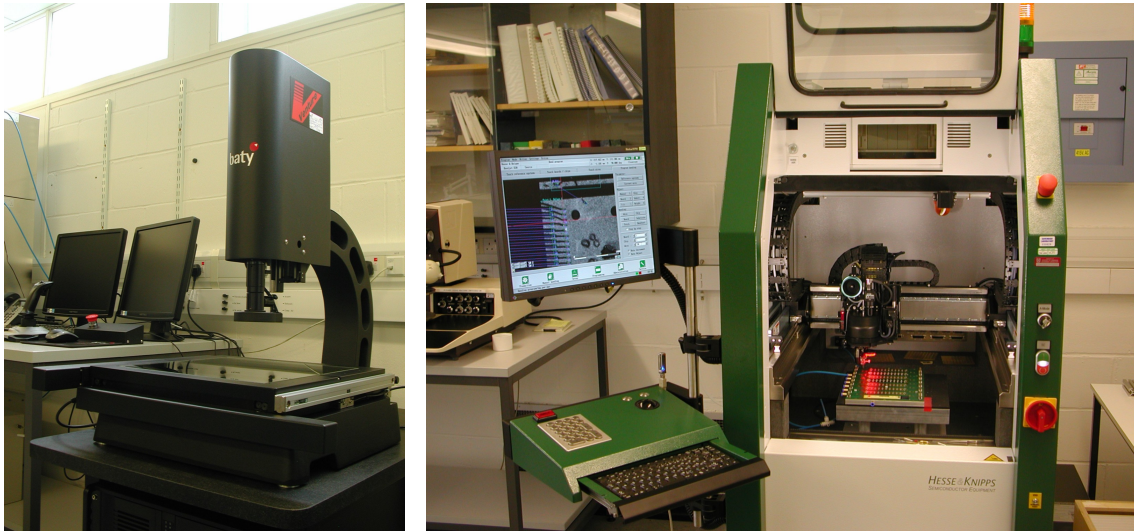


Fig. 4.5: Left: coordinate measurement machine used for visual inspection and sensor bow measurements. Right: automatic wire bonder used to make wire-bonds for electrical contacts.

Wire-bonder

Some electrical tests, such as the strip test, require fixed electrical contacts between the sensor and the jig. The *Hesse-Knipps BondJet BJ820* automatic bonding machine seen Fig. 4.5 (right) is used to place aluminium wire-bonds between passivation openings on the sensor surface and the pads on the jig. Similarly, for future module assembly purposes, the same wire-bonder will be used, e.g. for the electrical connections between the AC bond pads and the readout ASICs.

Probe station

The Alessi Rel-6100 semi-automatic probe station, shown in Fig. 4.6 (left), plays an essential role in most sensor tests and the strip test in particular. It consists of a movable chuck that can be controlled manually or remotely, a pneumatic support platen which holds probe needles, and a microscope. A vacuum system in the chuck allows for bare wafers, or jigs loaded with samples, to be fixed. The chuck can be moved in all three directions and also rotated for alignment purposes, all with micrometer precision. Tungsten probe needles, which are fixed to the platen with vacuum feed, are used for electrical contact with the sensor surface. The microscope with a maximum magnification

Evaluation of prototype ITk Strip Sensors

of $\times 50$ has an incorporated CCD camera connected to a computer and can be used for both manual visual observation and automatic pattern recognition in conjunction with the probe station software. Alternatively, the camera can be replaced by a near/short-wavelength infrared camera from Hamamatsu whose cooled, low-noise CCD can be used to pinpoint and capture sensor breakdown, as demonstrated later in Section 5.2.1.

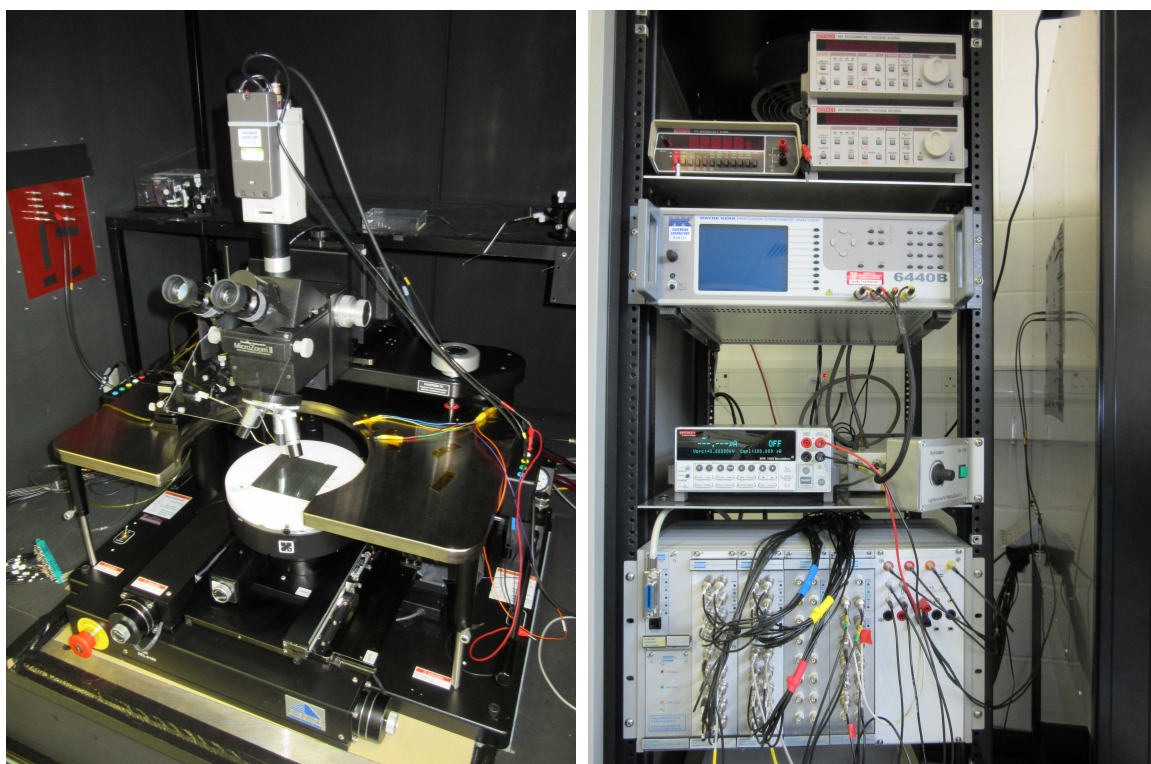


Fig. 4.6: Alessi probe station (left) and instruments (right) used for the studies of strip sensors at Cambridge.

Switching matrix and multiplexers

The different SMUs, the LCR meter, and the probe needles or probecard, respectively, are connected and switched through using a *switching matrix* and *multiplexers* (MUX). These devices are designed for high-speed switching hence allowing almost instantaneous switching between instruments or probecard channels. Since the expected leakage current is rather low with $\mathcal{O}(100 \text{ nA} \dots 1 \mu\text{A})$ and the applied voltages as high as 1 kV, excellent internal isolation between matrix/MUX channels is needed as well as high-precision current meters in the SMUs.

Peripheral monitoring: probe touchdown, temperature, humidity, and light sensor

An active touchdown feedback – commonly referred to as *edge-sense* – is highly recommended for a probecard-based test procedure in order to prevent damage of either the card itself or the sensor and ensure consistent contact quality. Furthermore, temperature and humidity monitoring capabilities are a prerequisite for Quality Control, and an interlock system as a safety measure to switch off sensor bias in case of a light source within the probe station is a sensible addition to the setup. These different functions are all provided by contacts or sensors connected to an Arduino board which is readout along the SMUs and LCR meter. In the following the functionalities provided by this peripheral monitoring are explained.

The probecard currently used in Cambridge provides two touchdown needles in addition to the 32 signal channels used for measurement. These needles can be used in a *make* or *break* contact configuration, i.e. one needle (*make*) touches down on the sensor surface in alignment with the measurement needles, whereas the second one (*break*) loses contact to the first needle upon touching a surface due to the make needle being lifted off. The implemented edge-sense circuit uses the break contact configuration in conjunction with a *Schmitt trigger* on a digital input pin of the Arduino to provide the necessary touchdown trigger.

The light sensor which in combination with the Arduino is used as an interlock for the voltage supplies consists of a *light dependent resistor* (LDR) in a voltage-divider circuit. With this setup, the potential on the digital input of the Arduino corresponds to the probe station enclosure being sufficiently dark to test the sensor without the influence of photo current generation. The value of the second resistor in the voltage-divider has been chosen after extensive testing in order to ensure prompt response, even from relatively weak or collimated light sources such as stray illumination by the microscope lamp, on the one hand, and stable conditions while in the dark on the other hand. The thermometer as well as a combined temperature and *relative humidity* (RH) sensor is used in particular for monitoring during long-term measurements, both of which are also readout by the Arduino board in the Cambridge setup.

LabVIEW implementation

All measurements, of which the results are presented in the following chapters, were performed using instrument control and data acquisition via *National Instruments LabVIEW*. For that purpose, more than 200 *virtual instrument* (VI) files were developed with emphasis on a modular structure for easy inclusion of additional instruments as well as use in the implementation of future measurement procedures. These VIs are now used widely by ITk Strip Sensor groups in other institutes as well.

4.4 Planarity of sensors

The planarity of every main sensor that was delivered to Cambridge has been measured using the CMM detailed in the previous section. This is done on a grid of at least 11×11 , which corresponds to 9.44 mm spacing between points distributed on the full sensor surface, with the contactless mode of the CMM. The coordinate system is defined with the origin $(0, 0, 0)$ at the centre of the sensor and a right-handed orientation of the axes so that the z -axis points upwards. To account for the slope of the suspended sensor on the microscope plate or a jig, if used, results are evaluated by performing a planar fit of the raw data points and subtracting them from the same, yielding a plot of the surface with its *net bow* as displayed in Fig. 4.7(a).

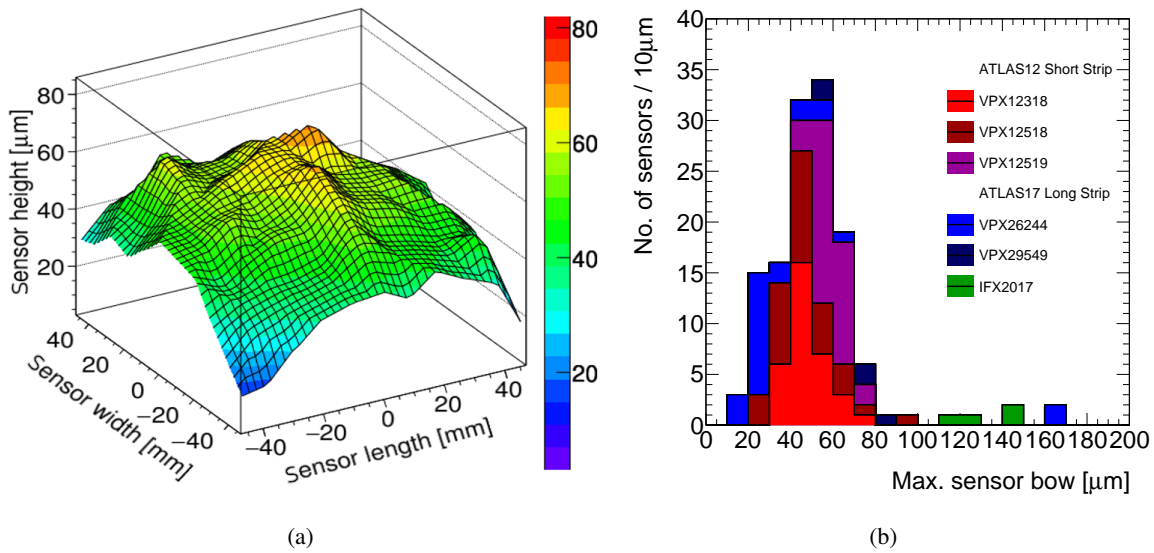


Fig. 4.7: (a) Example interpolated net bow measurement on a full-size barrel sensor performed with the CMM. (b) Histogram of the maximum bow of all sensors measured in Cambridge.

The *maximum sensor bow* is defined as the difference between the minimum and maximum z -height as measured. Results of all tested sensors show that almost all sensors have a maximum bow of less than 100 μm, thus easily complying with specifications. A comparison of the different batches of sensors is shown in Fig. 4.7(b). In that plot one can see that the first two batches of the A12 generation have a similar distribution of maximum bow, with the third batch being only slightly worse but with less spread. The first A17 prototypes from HPK have the least bow of all batches to date, as the two outliers in that batch are specifically produced with reduced active thickness and the rest of the manufacturing process was not optimised towards this. The IFX version of the ATLAS17 sensors has a relatively large bow when compared to those from HPK, but still within specifications.

4.5 Bias voltage dependence of sensor properties

For the reasons given in Section 4.2, the macroscopic sensor properties such as the *leakage current* (IV, Section 4.5.1) and the *bulk capacitance* (CV, Section 4.5.2) have been measured as a function of the applied bias voltage. To establish the validity of the measured quantity versus AC frequency used, the resulting *frequency dependence* has to be verified for the measurement setup, as shown in Section 4.5.2. Furthermore, using the results of CV scans in combination with the sensor geometry one can derive multiple important sensor characteristics, namely the *full depletion voltage*, *active thickness*, and *effective doping concentration*, which in turn yields the overall *bulk resistivity*. Lastly, a direct measurement of the coupling capacitance and implant resistance has been conducted, with the outcome being presented in Section 4.5.3.

4.5.1 Sensor leakage current

The measurement of the leakage current with increasing bias voltage has been conducted by ramping up the voltage in increments of 10 V in a range from $V_{\text{bias}} = 0 \text{ V}$ to -1000 V , applied to the sensor backplane through the edge metal contact. Current is measured with nA precision with 10 s intervals in between steps at ambient temperature of $T \simeq 21^\circ\text{C}$ in the air-conditioned cleanroom and should not exceed $2 \mu\text{A}/\text{cm}^2$.

The IV curves of all 120 ATLAS12A sensors grouped per batch are plotted in Fig. 4.8, with the leakage current normalised with respect to the active sensor area, taken as the area confined by the bias rail. The IV measurements of the 30 sensors of the initial batch VPX12318 was taken using a dry N_2 environment by placing the sensor in a nitrogen flushed metal box. For this the sensor had to be contacted with wire-bonds. Subsequent A12 sensors have been tested in ambient cleanroom humidity. As a result, initially only two sensors – VPX12318-W613 and VPX12518-W698 – failed the IV specifications with a leakage current exceeding $I_{\text{leakage}} = 2 \mu\text{A}/\text{cm}^2$ at bias voltage below $V_{\text{bias}} = -600 \text{ V}$, a third sensor – VPX12518-W657 – started exhibiting a very high current $\mathcal{O}(10 \mu\text{A})$ even at low voltages $\sim -40 \text{ V}$ after the subsequent CV measurement.

Fig. 4.8(a) also shows, that in batch VPX12318 a substantial number of sensors have shown an early but very soft micro-discharge resulting in a proportionally higher leakage current compared to other batches. It was suspected that this stems from those measurements being conducted in a dry N_2 environment, as the subsequent batches were only stored in dry atmosphere and afterwards tested in a standard cleanroom environment with $\text{RH} = (40 \pm 10)\%$ at room temperature. A possible explanation for the suppression of this micro-discharge in moderately humid conditions is the fact that a higher conductivity of the sensor surface due to the humidity of the ambient atmosphere yields a reduction of the electric field and therefore the charge multiplication process associated with the avalanche breakdown of p-n junctions [73, 74]. However, as is explained in Chapter 5, this mechanism only holds true for short timescales $\mathcal{O}(1 \text{ min})$ typical for IV/CV measurements, as it will be shown that protracted exposure to humidity is detrimental for IV performance. The overall best ATLAS12 sensors

Evaluation of prototype ITk Strip Sensors

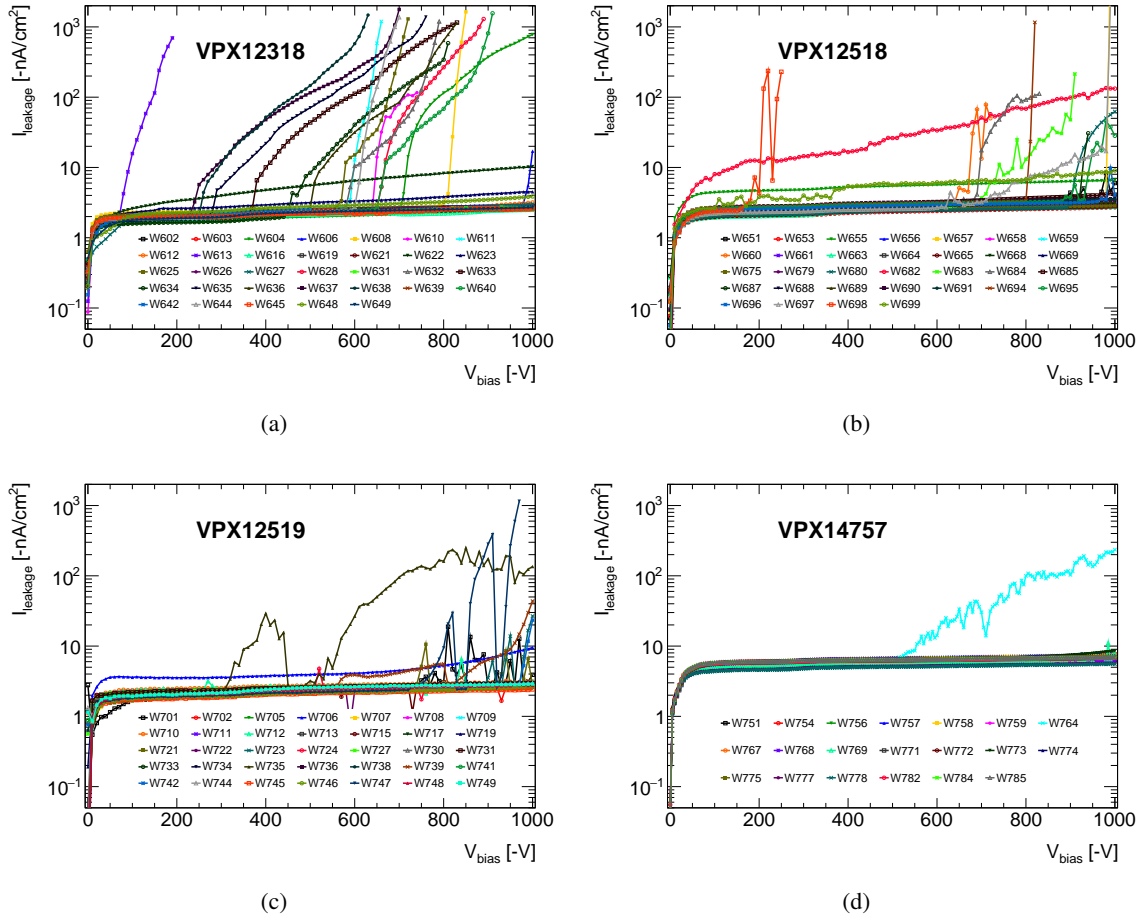


Fig. 4.8: IV curves of all tested large ATLAS12A sensors, grouped per batch. The leakage current is normalised with respect to the active sensor area. Measurements were taken at 21°C, most of the first batch (VPX12318) was tested under dry N₂ environment (a), all others under normal cleanroom conditions with RH = (40 ± 10)% (b-d).

in terms of uniformity of IV results are those from VPX14757, even though the current baseline is about twice as high as the majority of other A12 batches.

As a consequence of the humidity sensitivity observed in extensive studies of the ATLAS12 prototypes, the following generation of A17 long-strip sensors were all tested in dry conditions for their initial IV and CV tests after reception. Compared to their A12 predecessors, the majority Hamamatsu A17 sensors have a much lower baseline leakage current, with most of them well below 1 nA/cm². One sensor, VPX26244-W017, showed early hard breakdown and exceeded the current compliance set by the supply below $V_{\text{bias}} = -500$ V, but was still used in all subsequent tests as the breakdown voltage was not critically low. A second sensor, W007 of the same batch, broke down even earlier, but was later successfully reconditioned using a bake-out procedure (see Section 5.2.3 for further details).

4.5 Bias voltage dependence of sensor properties

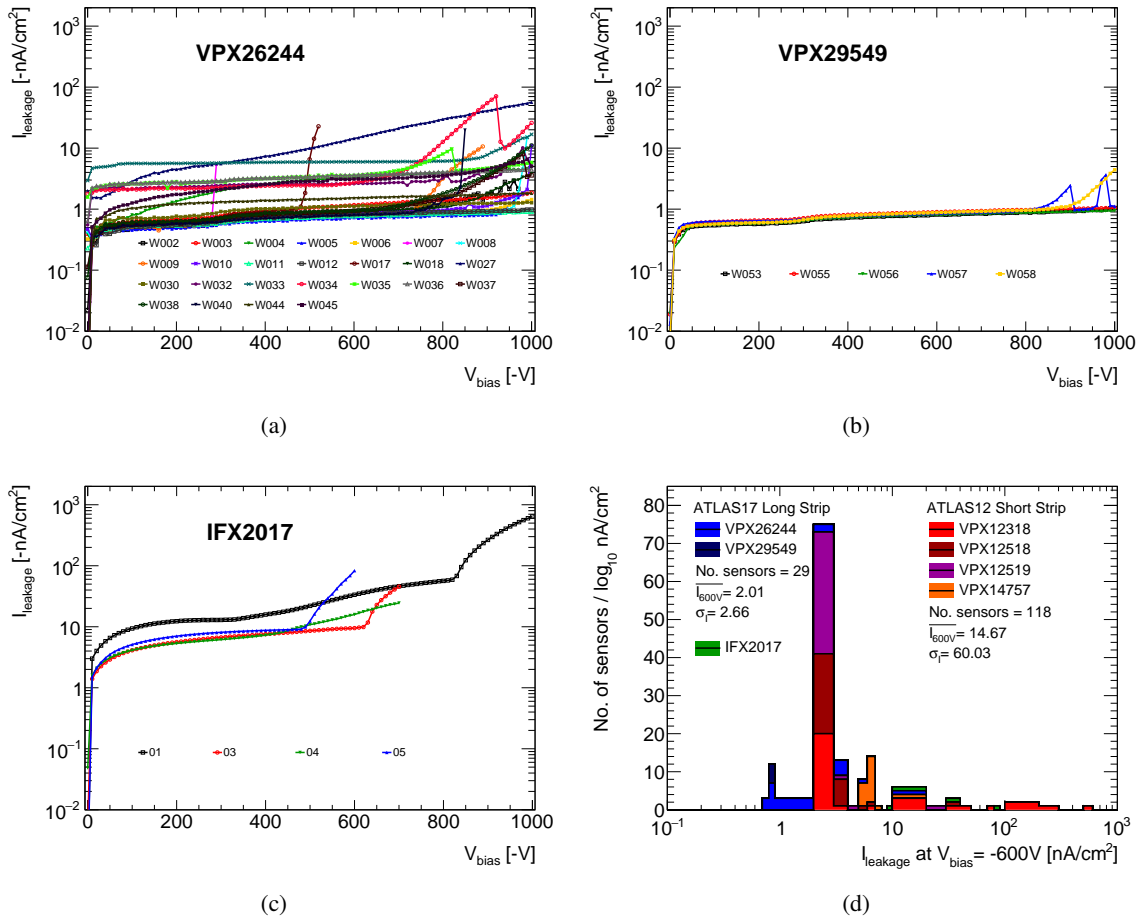


Fig. 4.9: IV curves of all large ATLAS17LS sensors tested in Cambridge, normalised with respect to the active sensor area, taken at 21°C under dry N₂ environment. Data plotted in (a-b) are the two A17 batches produced by Hamamatsu, (c) are the corresponding sensors from Infineon. (d): Histogram of normalised leakage current at $V_{bias} = -600V$.

All four ATLAS17 Infineon sensors show IV behaviour within the specifications, albeit with an overall higher current compared to average HPK sensors. Further verdicts on the constancy of those results and a more detailed comparison could not be made due to the lack of samples.

In conclusion, as summarised in the histogram in Fig. 4.9(d), in initial IV scans almost all of the last two generations of prototype sensors sit well below the required $I_{leakage} = 2 \mu A/cm^2$ at $V_{bias} = -600V$ and only four sensors failed, of which one has undergone a successful recovery treatment.

4.5.2 Bulk capacitance

In order to determine the full depletion of the silicon strip sensors the bulk capacitance C_{bulk} is measured as a function of the bias voltage V_{bias} . The measurements were taken using a Wayne-Kerr 6440B LCR meter and the Keithley 2410 SMU for biasing the DUT. Data points were taken in steps of 10 V with a delay of 5 s after raising the voltage before the actual measurement in order to allow the current to settle in the test circuit. The AC voltage had an amplitude of 100 mV with a frequency of 1 kHz to 2.5 kHz.

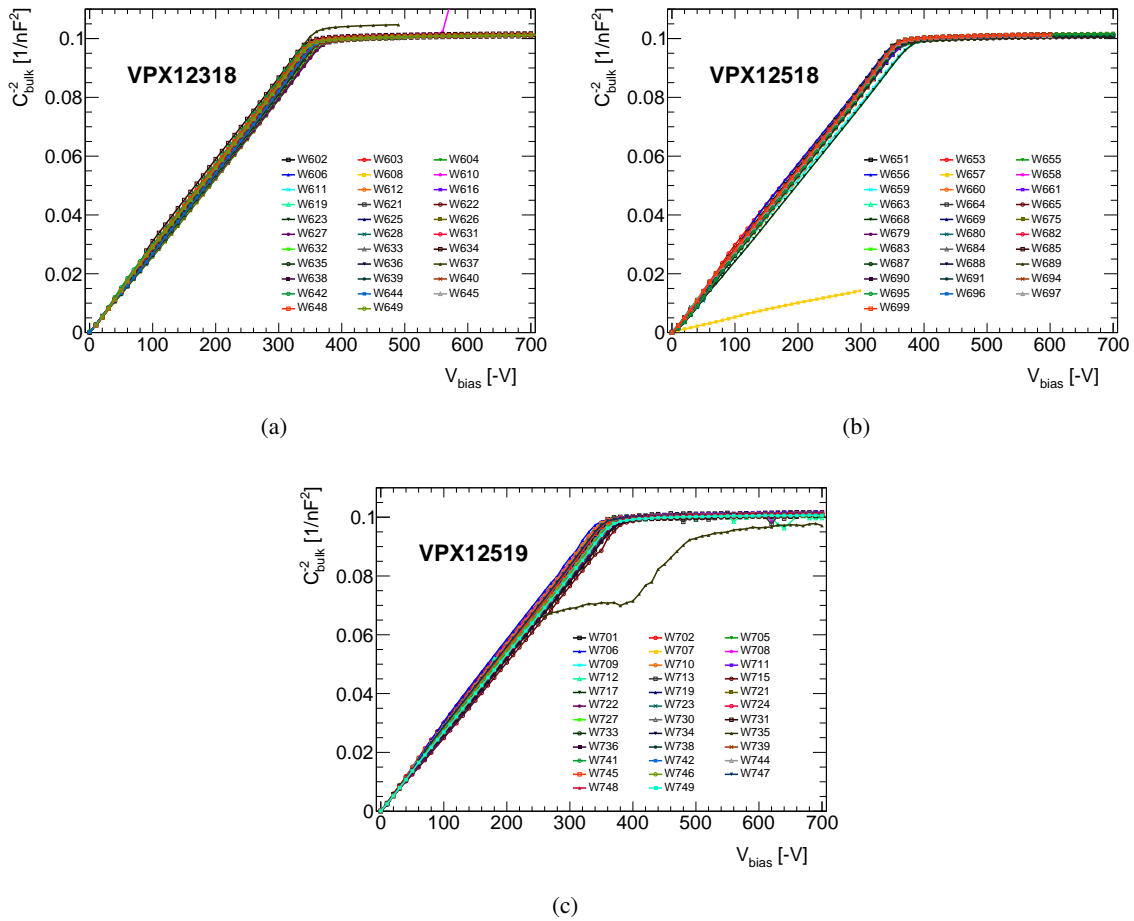


Fig. 4.10: CV curves for the bulk capacitance measurement of all tested ATLAS12 (a-c) sensors split into their respective batches.

The corresponding curves of all ATLAS12 sensors tested in Cambridge and plotted as $1/C_{bulk}^2$ vs. $-V_{bias}$ are shown in Fig. 4.10. In all plots a very consistent behaviour for all three batches can be observed. The two sensors which initially failed the IV specifications were excluded for these measurements, as their breakdown happened at values of V_{bias} which was too low to obtain their respective depletion voltages. In addition to those sensors, two more – VPX12518-W657 and VPX12519-W735 – failed the CV specifications, quite visibly so in view of the CV plots shown.

4.5 Bias voltage dependence of sensor properties

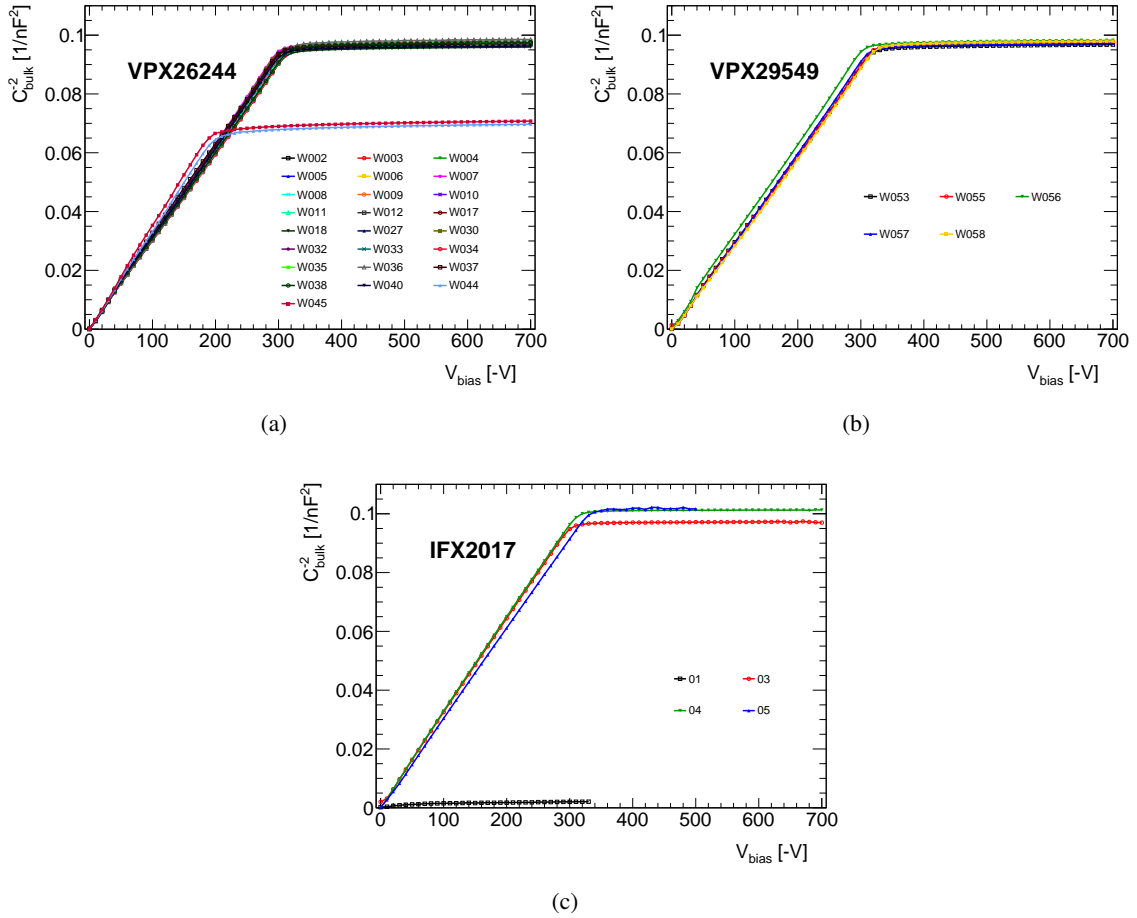


Fig. 4.11: CV curves for the bulk capacitance measurement of all tested ATLAS17LS sensors produced by HPK (a-b) and IFX (c) divided into their respective batches.

In Fig. 4.11 the results of the A17 sensors produced by both manufacturers are shown. All HPK sensors show equally consistent behaviour to their A12 predecessors, with none of them failing the CV scan. Sensor W017, which had previously exhibited an onset of micro-discharge at ~ -500 V, could even be complete – and pass – its CV test, as it could be biased to voltages beyond its full depletion. For batch VPX26244 in Fig. 4.11(a), the two sensors with reduced active thickness can be easily distinguished by their much earlier kink in the plot and the comparatively reduced capacitance thereafter. The few available IFX sensors are similar to their HPK counterparts, but have one sensor failing, which seems to be related to high currents disturbing the R-C network during the measurement.

Overall, only two ATLAS12 sensors and one IFX ATLAS17 sensor failed the CV specification. A more comprehensive analysis of the quantities derived from these measurements will be given below after the following paragraph.

Frequency dependence

According to Eq. 4.1, the impedance and thus the capacitance measured in an R-C network is dependent on the AC test frequency. In order to verify the validity of the measurements and the frequency used, the frequency dependence of C_{bulk} is determined for frequencies between 200 Hz and 100 kHz under various bias voltages. For sensors measured on the probe station utilising the switching matrix, the SMU used to bias the DUT in this and any following frequency dependence measurements was the Keithley 487 with its current meter disconnected in order to minimise resonances in the test circuit. Hence, this measurement could only be conducted for up to $V_{\text{bias}} = -500 \text{ V}$. The results for sensor VPX12519-W748 are plotted in Fig. 4.12.

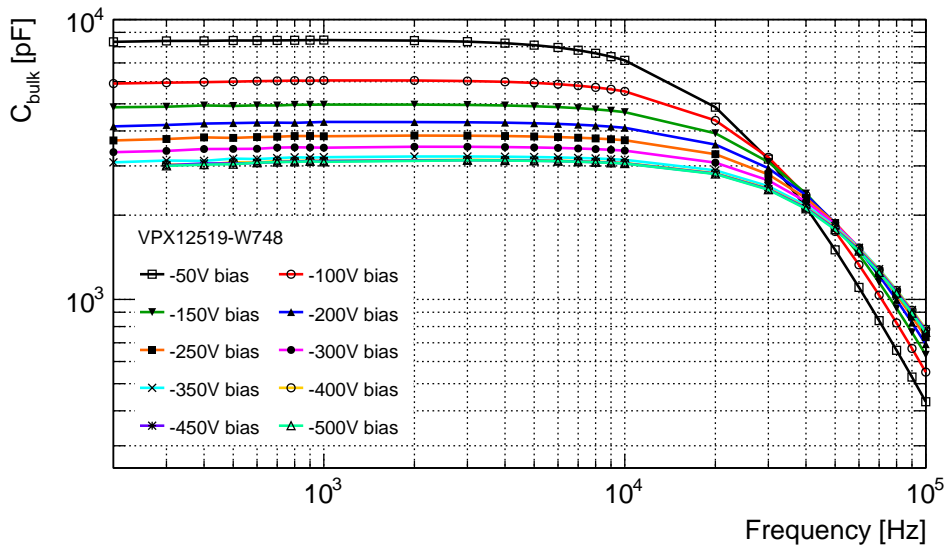


Fig. 4.12: Frequency dependence of the bulk capacitance of sensor VPX12519-W748 for bias voltages up to $V_{\text{bias}} = -500 \text{ V}$ in increments of $\Delta V_{\text{bias}} = 50 \text{ V}$.

As can be seen in the plots, C_{bulk} is largely constant within 500 Hz ... 5 kHz, thus the used AC test frequency of 1 to 2.5 kHz is viable. Similar results were obtained for multiple A12 and A17 samples, confirming the shown findings.

It can be seen that there is a significant drop in the capacitance measured by the LCR meter for higher frequencies. This effect originates in the method by which the capacitance is determined by the instrument, as detailed in Section 4.3. The meter settings for bulk capacitance measurement assume a series network of capacitance and resistance. However, the resistance present in the DUT due to the contribution of surface current and the bias resistors (more details in Section 4.10, Fig. 4.27) cannot be compensated for by the trimming procedure of the LCR meter. Thus, the measured phase shift according to Eq. 4.3 would be smaller for higher frequencies because of the reduced imaginary part of the complex impedance, resulting in lower perceived capacitances.

Full depletion voltage and doping concentration

For all measured sensors the full depletion voltage V_{FD} is determined as the position of the intersection of the linear rise and the saturated value in the respective $1/C_{bulk}^2$ vs. $-V_{bias}$ plots. This was done by fitting two linear functions to the curves according to Eq. 3.26, one to the rising slope of the partially depleted sensor, and the second to the plateau region of constant C_{bulk} . The respective fit intervals were chosen from visual examinations of the plot, and specifically adjusted for each of the two sensor generations and the sensors with reduced active thickness (“*thin*” sensors).

A histogram of V_{FD} for the all tested sensors which could be biased to sufficiently high voltages is shown in Fig. 4.13(a). The distribution has a mean value of $\overline{V_{FD}} = -366$ V with a standard deviation of 10 V for the ATLAS12 prototypes. This value is a lot higher than the initially desired ~ -300 V, but since the manufacturer was allowed to provide sensors with up to $V_{FD} = -400$ V in case of lacking availability of high resistivity ingots [70], the A12 sensors ultimately met the specifications. As can be seen in the histogram, all three tested batches were very similar in terms of their mean V_{FD} and spread, yielding a mean value of $\overline{V_{FD}} = -318$ V and a standard deviation of 8 V (excluding the thin sensors). For the A17 sensors the full depletion specification was changed to -330 V, which all of the HPK sensors fulfilled. Moreover, just as the CV plots have already indicated, the two thin sensors deplete more than 100 V earlier than any other A17 sensor. The corresponding Infineon sensors are comparable to the ones from Hamamatsu. Whether the spread also has the same magnitude could not be investigated from the small sample size.

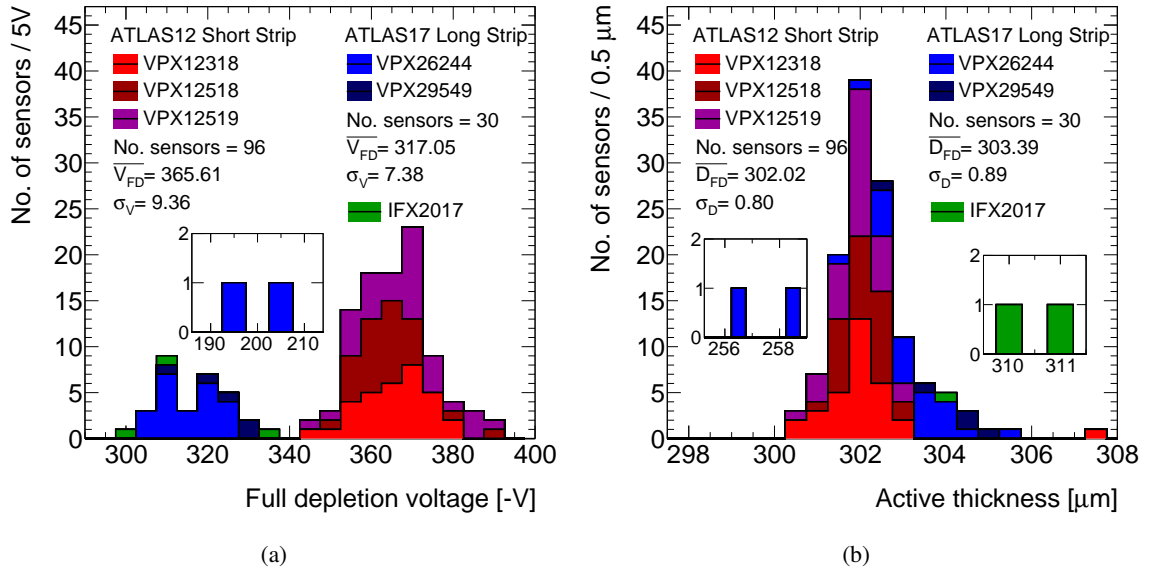


Fig. 4.13: Histograms of the distribution of the derived full depletion voltages (a) and active thickness (b) of all sensors tested in Cambridge, broken down into their respective batches.

From the capacitance at full depletion the active thickness D , i.e. the maximum extension of the space charge region throughout the depth of the sensor, can be calculated using Eq. 3.26 with the

Evaluation of prototype ITk Strip Sensors

active area defined by the bias rail as its boundary. On the one hand, this serves as a preliminary step to determine the effective doping concentration and, on the other hand, will be used to verify sensor models for simulations. The active thickness of a sensor is also an important factor for the amount of collected charge, and the fraction of dead material when comparing it with its physical thickness. In the histogram in Fig 4.13(b) it can be observed that the mean active thickness of the HPK ATLAS17 sensors is larger by $\sim 1 \mu\text{m}$ with a similar standard deviation, whereas the IFX sensors are spread out a lot compared to any HPK sensor batch or generation. Likewise, it can be seen that the thin sensors have their active thickness reduced by $\sim 45 \mu\text{m}$ in relation to the other sensors of the same batch.

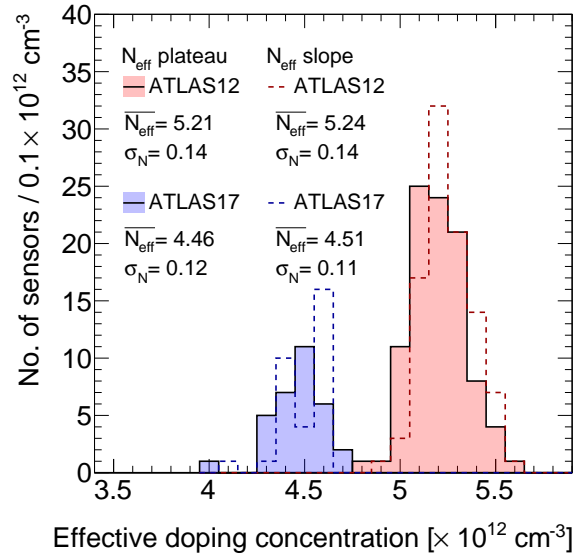


Fig. 4.14: Distribution of the effective doping concentration of all A12 and A17 sensors measured. The histograms drawn with dashed lines are obtained by determining N_{eff} from slope of the linear fit below V_{FD} and the filled histograms from the plateau region of the CV curves.

The effective doping concentration N_{eff} can be extracted in two ways, using Eqs. 3.27 or 3.28. This is increasingly important as irradiated sensors may not be fully depleted at the maximum voltage measured, leaving only the calculation from the rising slope. The active thickness is measured for each sensor individually as shown in Fig 4.13(b), while the area is taken from the surface layout as the area surrounded by the bias rail. Histograms for both results are shown in Fig. 4.14, with the values derived from the plateau as the filled histograms and those extracted from the slope plotted with dashed lines. The resulting effective doping concentrations of $N_{\text{eff,A12}} = (5.2 \pm 0.2) \times 10^{12} \text{ cm}^{-3}$ and $N_{\text{eff,A17}} = (4.5 \pm 0.2) \times 10^{12} \text{ cm}^{-3}$ reflect the improvement with regards to the depletion characteristics from the ATLAS12 to the ATLAS17 generation. Comparing the different ways to calculate N_{eff} shows good agreement and serves as a sanity check with respect to the previously shown results for V_{FD} and D . Utilising the obtained mean values of the effective doping concentration yield a bulk resistivity of $\rho_{\text{A12}} = 2.55 \pm 0.11 \text{ k}\Omega\text{cm}$ and $\rho_{\text{A17}} = 2.95 \pm 0.14 \text{ k}\Omega\text{cm}$, which is within specifications for prototypes and also agrees with the intended level of production quality $\rho_{\text{ITk}} > 3 \text{ k}\Omega\text{cm}$, albeit barely so.

4.5.3 Coupling capacitance and implant resistance

Aside from the full strip tests (see Section 4.8) the coupling capacitance C_{coupling} between the strip implant and the top metal readout strip was verified in direct measurements for a small subset of sensors along an assessment of the implant resistance R_{implant} . This measurement was conducted by contacting the strip implant through a DC pad and the AC-coupled top metal of the sensor while using the LCR meter in R-C series network mode. As can be seen in the plots shown in Fig. 4.15, C_{coupling} and R_{implant} are constant within 2 kHz... 100 kHz and drop for higher frequencies, which is to be expected by the transmission line formed between the strip implant and the top metal. With a value of 25.7 pF/cm, C_{coupling} is well within the specifications of > 20 pF/cm.

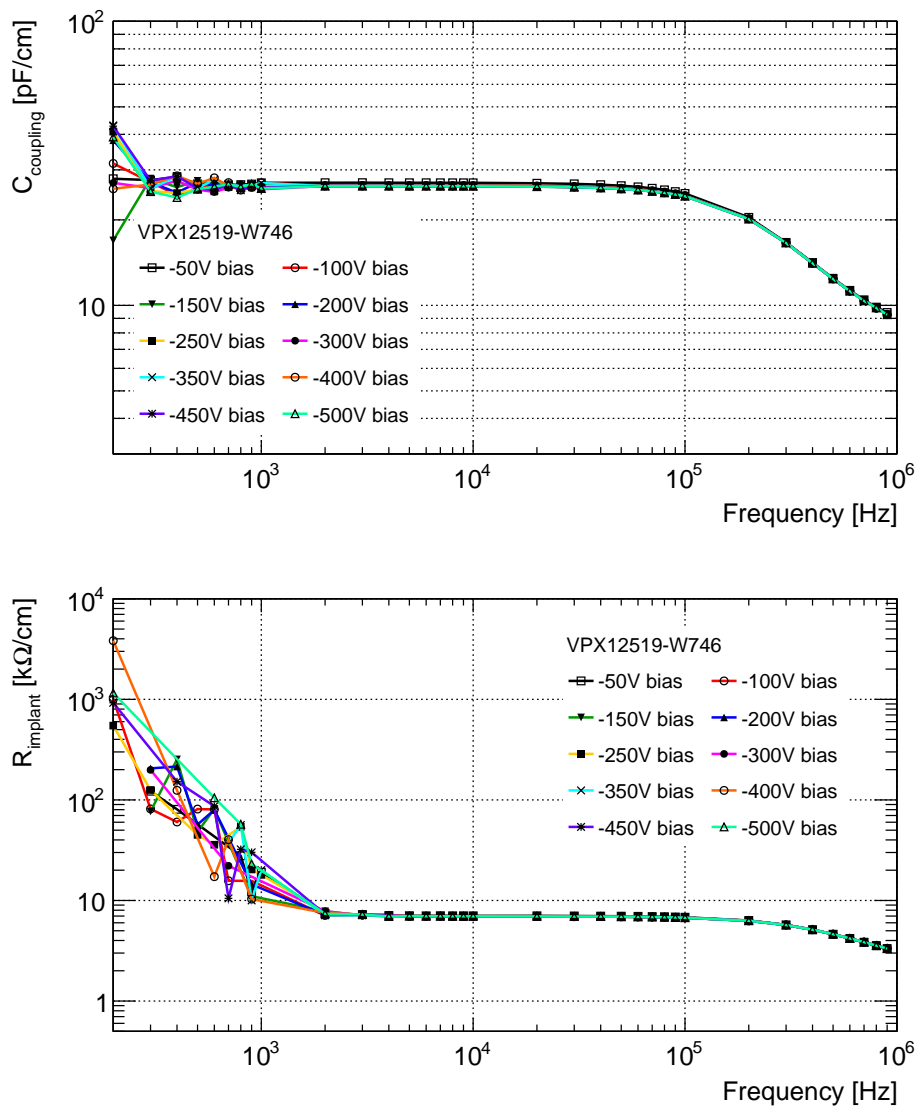


Fig. 4.15: Frequency dependence of the measured coupling capacitance (top) and implant resistance (bottom) of sensor VPX12519-W746 normalised with respect to the strip length.

4.6 Inter-strip measurements

Checks of inter-strip capacitance (C_{is}) or resistance (R_{is}) which would require contacting sample channels across each sensor, has been carried a small subset of prototype full-size sensors. A summary of the findings will be shown in the following.

4.6.1 Inter-strip capacitance

A low inter-strip capacitance C_{is} is crucial for effective detector operation since it is one of the dominant contributions to the input capacitance of the front-end readout electronics and thus to the overall noise level (see Section 3.3.2). Therefore, it should be as low as possible, with the specifications for C_{is} being given as $< 0.8 \text{ pF/cm}$ at $V_{bias} = -300 \text{ V}$. The method to determine C_{is} is to contact the AC pads of three adjacent strips with probe needles and connect them to the LCR meter with all other strips floating. Contributions from next-nearest neighbours are measurable but negligible for the overall assessment [38].

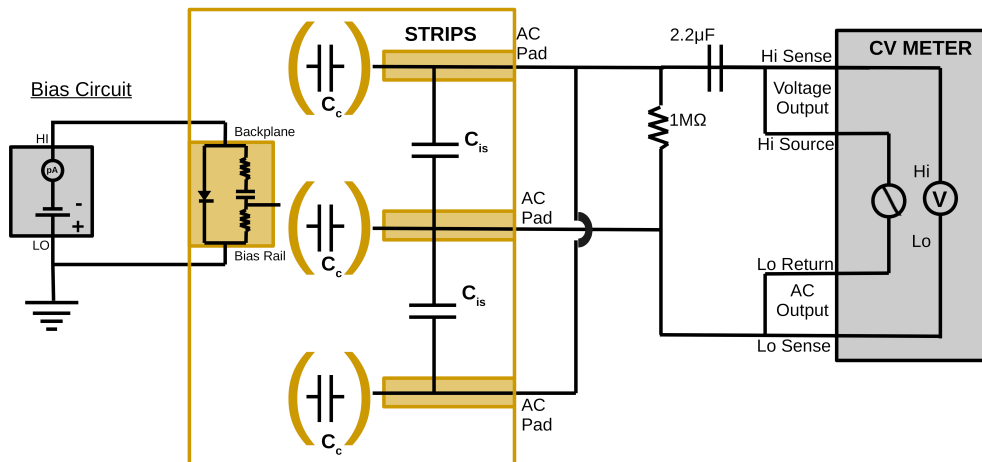


Fig. 4.16: Conceptual diagram of the inter-strip capacitance measurement setup [66].

The equivalent circuit of such a setup is shown in Fig. 4.16. As the expected capacitance is very small with $\mathcal{O}(1\text{pF})$ and, due to its nature as a surface characteristic, may be influenced by increasing surface currents during reverse biasing, the choice of the right leads and correct grounding has a deciding factor on the feasibility of a C_{is} measurement. Most notably, the use of shielded cables to contact the AC pads is advisable and special diligence has to be taken to connect the shields of the leads with each other and to the ground of the bias circuit as close to the DUT as possible.

Results of the inter-strip capacitance taken for sensor VPX12519-W746 are shown in Fig. 4.17. The capacitance between the central strip and the neighbouring strips were measured using an AC test frequency of 100 kHz as stated in the technical specifications. In order to verify the frequency setting, the frequency dependence of C_{is} is measured similarly to C_{bulk} earlier (see section 4.5.2). The results shown in Fig. 4.18 suggest a test frequency between 50 kHz and 1 MHz.

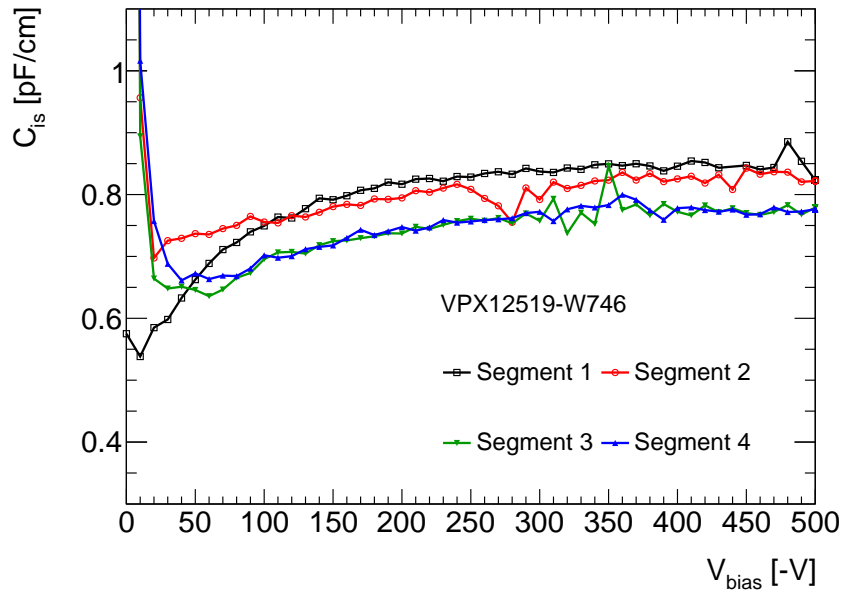


Fig. 4.17: Sample inter-strip capacitance measurement versus V_{bias} taken for sensor VPX12519-W746 on all four segments respectively. Measured values are normalised with respect to the strip length.

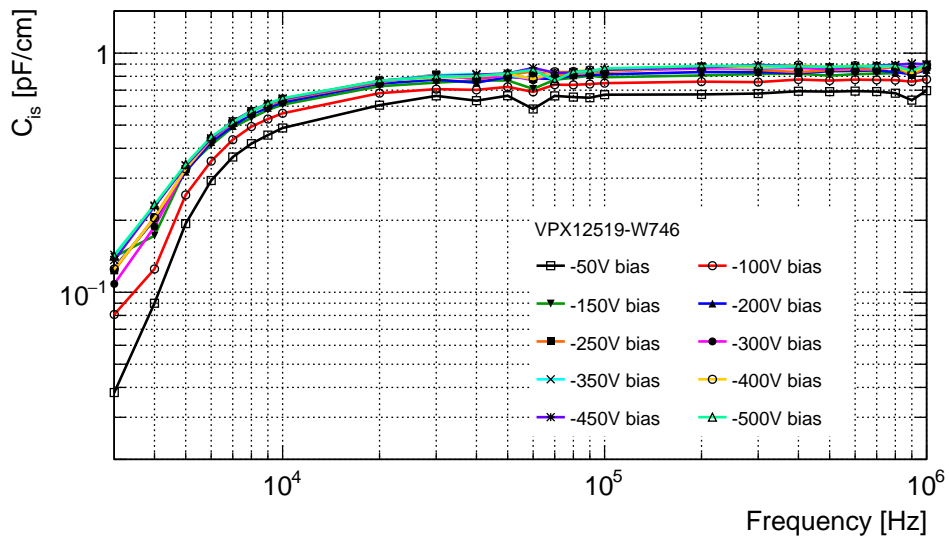


Fig. 4.18: Frequency dependence of the inter-strip capacitance of sensor VPX12519-W746 for bias voltages up to $V_{\text{bias}} = -500$ V.

4.6.2 Inter-strip resistance

On all tested sensors of the ATLAS12 and ATLAS17LS batches, neighbouring strips are isolated from each other via *p-stop*, localised high-dose p^+ -implant between strips. This strip isolation manifests itself in a high inter-strip resistance R_{is} , which is measured by contacting adjacent DC pads with probe needles and applying an external master voltage V_m to one strip. The circuit diagram in Fig. 4.19 shows such a test configuration, where only two strips are contacted, with one being driven by the test SMU and the induced voltage being extracted from the other. Similarly one can contact three neighbouring strips, for which the voltage is measured on the centre strip while the master voltage is applied to the other two.

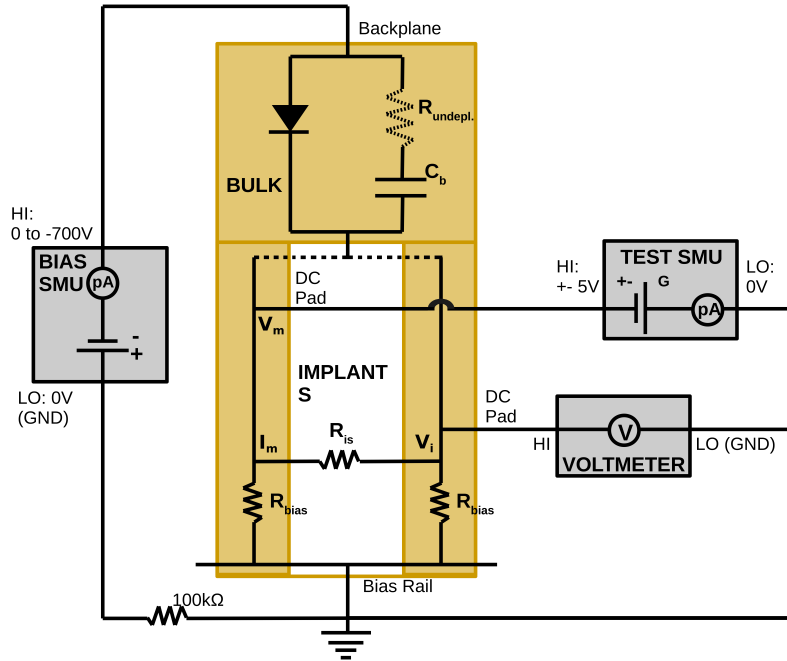


Fig. 4.19: Conceptual diagram of inter-strip resistance measurement with all major components marked (adapted from [66]). Note that strip implants are only connected through the sensor bulk.

The master voltage is ramped in the interval of $[-5\text{ V}; +5\text{ V}]$ with a step size of $\Delta V_m = 1\text{ V}$, while the induced voltage V_i towards common ground is measured on the neighbouring pad using a *Kethley 2000* (KE2000) voltmeter. Since the induced voltage in the case of large inter-strip resistance is naturally very small and the possibility of hysteresis has to be excluded, the testing procedure was implemented so that the voltage was first ramped down from 0 V to -5 V , then up to $+5\text{ V}$, and back to 0 V . In this process data acquisition was repeated 5 times for each master voltage step and the resulting mean values were used for the calculation of R_{is} . The inter-strip resistance was determined according to

$$R_{is} = \frac{dV_m}{dI_i} - R_{bias} = \left(1 - \left(\frac{dV_i}{dV_m}\right)^2\right) \left(\frac{dV_m}{dV_i} \frac{dV_m}{dI_m}\right) \xrightarrow{R_{is} \gg R_{bias}} \approx \frac{dV_m}{dV_i} \cdot R_{bias} = \frac{dV_m}{dV_i} \cdot \frac{dV_m}{dI_m} \quad (4.4)$$

4.6 Inter-strip measurements

Here I_i is the induced current in the floating strip, which can be calculated using the measured V_i and the bias resistance, which itself is derived from the slope of V_m and the respective supplied current I_m . Eq. 4.4 shown here allows estimation of R_{is} in a measurement setup with two needles. In the case of three needles, the induced voltage and supplied current are larger by a factor of 2 due to the additional R_{is} and R_{bias} in parallel. The approximation is usually valid for all unirradiated sensors, the full calculation is necessary for irradiated samples, sensors with small R_{is} relative to the bias resistance, or in the case of large bulk resistivity contributions. The slopes were obtained by fitting linear functions to the respective plots. For all steps the standard deviation of the mean data points, as well as the uncertainties of the fitted values, were taken into account via error propagation.

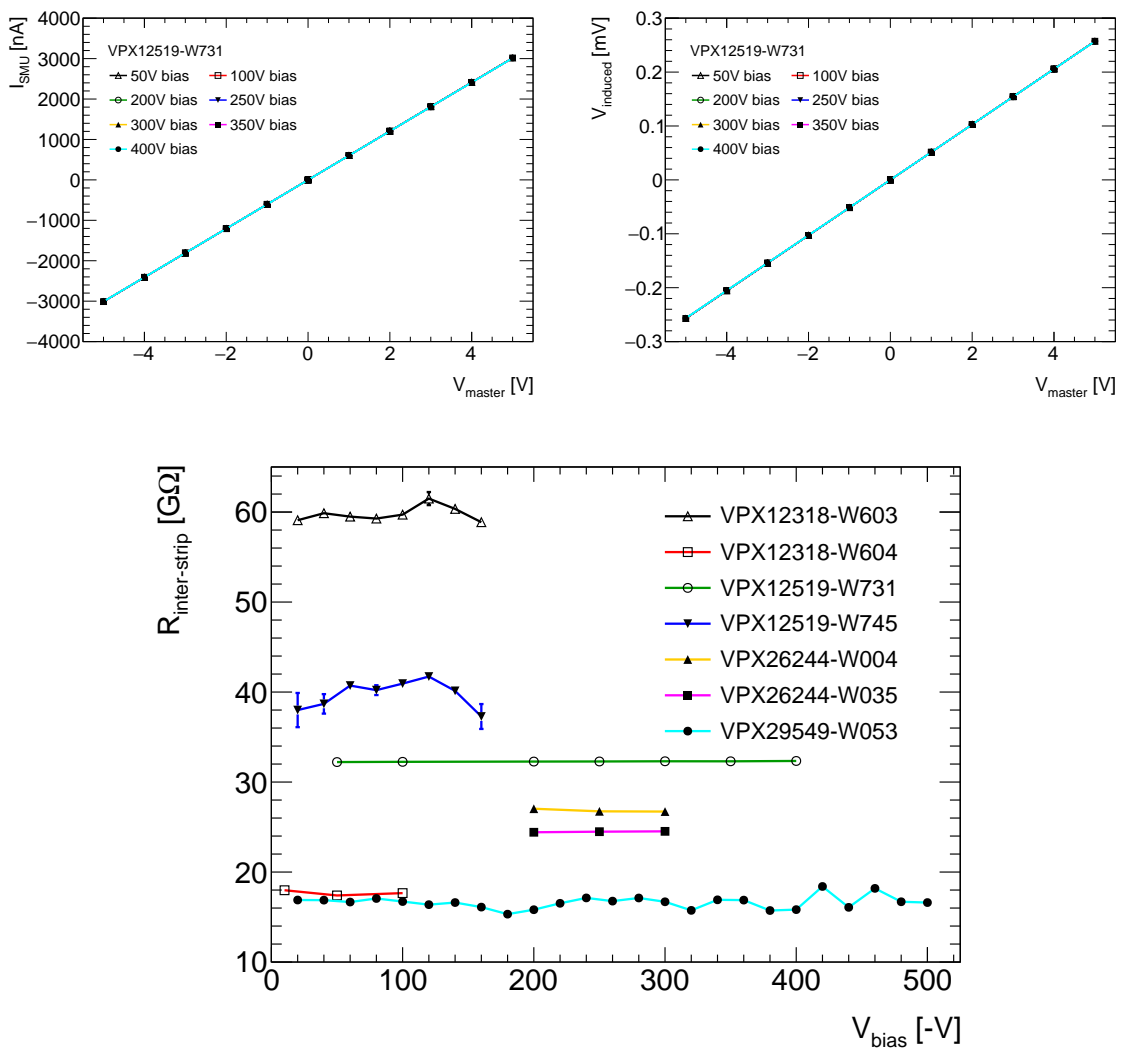


Fig. 4.20: Top plots: current sourced by the test SMU I_{SMU} (left) and induced voltage V_i (right) for an example sensor as function of the applied master voltage V_m , taken at different values of V_{bias} in increments of $\Delta V_{bias} = 50$ V. Bottom plot: inter-strip resistance R_{is} , derived using Eq. 4.4 and measured on various A12 and A17 sensors versus bias voltage.

Evaluation of prototype ITk Strip Sensors

The results of V_i versus V_m and R_{is} up to $V_{bias} = -400$ V for sensor VPX12519-W731 are shown in Fig. 4.20 (top). The linear dependence of V_i with respect to the master voltage is clearly visible in the plot. However, even though instruments with high input impedance were used in addition to the repeated data acquisition, the induced voltage was very low $\mathcal{O}(100\ \mu\text{V})$ due to the high inter-strip resistance and thus the accuracy is limited by setup systematics. The lower plot of Fig. 4.20 shows results obtained on a variety of sensors from all batches and prototype generations. The outcome of those measurements is a fairly large spread of R_{is} , but overall values of R_{is} with $> 15\ \text{G}\Omega$ are well above the specifications of $R_{is} > 10 \times R_{bias} = 15\ \text{M}\Omega$.

4.7 Punch-through Protection

The *Punch-through Protection* (PTP) is verified by measuring the sudden change in current when increasing the voltage over the bias resistor when contacting the DC pad of a channel and the bias rail. To compare the PTP behaviour the measurement is repeated with the needle placed on the far end of the implant with respect to the bias resistor. As can be seen in Fig. 4.21 from the sharply decreasing apparent resistance from the $\sim 1.5\ \text{M}\Omega$ bias resistance to $\mathcal{O}(10\ \text{k}\Omega)$ the PTP is put into effect at ~ 15 V. If measured from the far end of the strip, the drop in resistance is less sharp due to the non-negligible implant resistance in case of a bridged bias resistor.

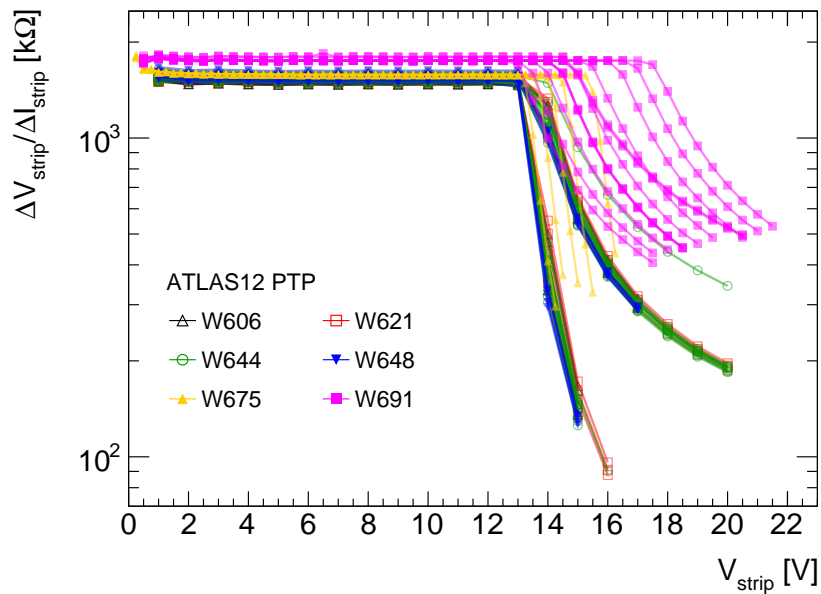


Fig. 4.21: PTP measurements on a select sample of sensors showing the apparent resistance between implant and bias rail against the the applied voltage on the DC pad. Multiple measurements on the same sensor at different positions are overlaid.

4.8 Strip tests

Full Strip Tests were conducted on most available prototype sensors which passed their initial IV and CV tests, or those which were at least able to hold the bias voltage necessary for carrying out this measurement. The strip test is a test sequence performed on each individual strip on a sensor biased to -150 V to achieve full strip isolation. Through this test one can identify metal shorts, broken implants, faulty or open bias resistors, and pinholes or punch-throughs in the dielectric. It is also used to measure the bias resistance and coupling capacitance between metal strips and implants for each individual channel, thus verifying the manufacturing process quality and identifying potential variations of these quantities throughout the wafer surface. The testing sequence for a single strip is specified as follows:

1. establish connection to the strip metal with a probe needle
2. connect an SMU set to 10 V to the needle through a $1\text{ M}\Omega$ current-limiting series resistor and measure the strip current
3. the SMU voltage is increased to 100 V and the current is recorded after a short delay
4. the strip is connected to the common GND and subsequently to the LCR meter
5. the R-C series network of C_{coupling} and R_{bias} are measured, using the LCR meter and an AC voltage of 100 mV with a frequency of $f_{\text{AC}} = 1\text{ kHz}$, the results are recorded
6. the strip metal is connected to GND and the sequence recommences with the next strip

During this sequence, if the current exceeds $1\text{ }\mu\text{A}$ when applying 10 V or 100 V across the dielectric, the strip is denoted as having a *pinhole* or *punchthrough*, respectively, and it is omitted from subsequent steps. Similarly, if the coupling capacitance or bias resistance do not comply with their specifications, the respective strip is denoted as faulty. Depending on the combination of measured C_{coupling} and R_{bias} in a faulty strip, a hint towards the nature of the fault can be perceived. A diagram of the equivalent circuit for a strip test can be seen in Fig. 4.22.

In the course of the evaluation of the ATLAS12 prototype barrel sensors, the transition was made from the single-needle probing to a multi-channel probecard. The main reason to use a probecard is the opportunity to measure multiple strips in quick succession without having to move the chuck to a new position for each new strip. Hence, the original strip test procedure was edited in order to minimise the time needed for the full strip test. According to the technical specifications, each strip has to be tested for electric continuity across the oxide (*pinholes*) before the actual resistance and capacitance measurement. For this purpose a voltage of 10 V and 100 V respectively are applied to each strip instantaneously. The easiest way to implement this using a probecard would be by setting the SMU to 10 V first, (hot) switching through all card channels while measuring the respective current for each channel, then increasing the voltage to 100 V and repeating the process. However, hot switching at 100 V has been proven to yield difficulties due to the R-C behaviour of the cables

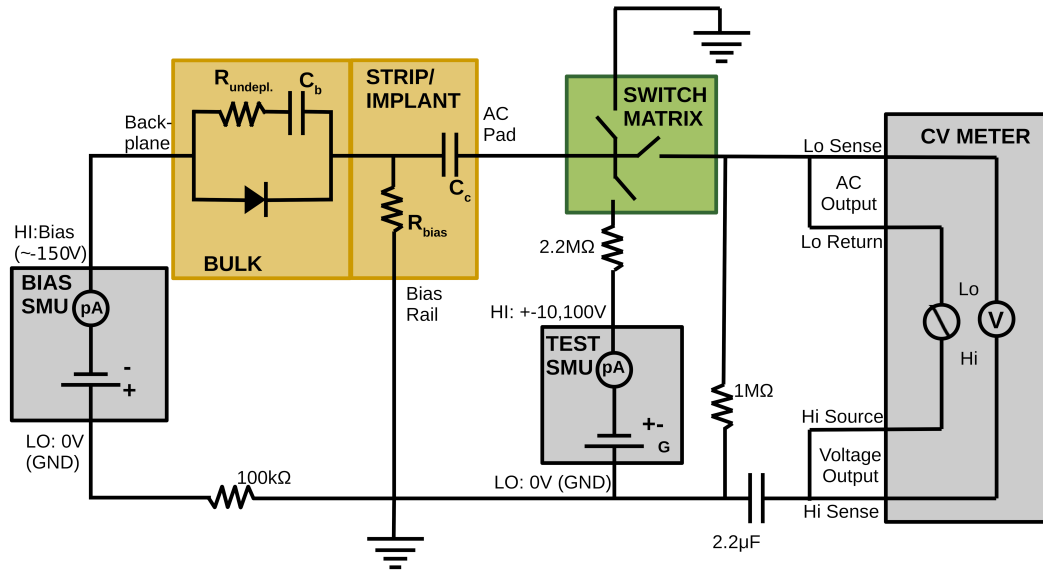


Fig. 4.22: Conceptual diagram of full strip test with all major components marked [66].

and the probecard itself. Thus current spikes originating from discharge processes can occur while switching the card channels, leading to potential problems if the current threshold or even compliance is exceeded in the process. Therefore, at least for 100 V, the voltage has to be ramped down first before switching the channels and capacitive effects have to be accounted for with a reasonable settling time, hence introducing an additional delay in the test and limiting the measurement speed.

A specific readout procedure (*rolling current readout*) has been devised in order to minimise the time necessary for the strip current measurement. This fully utilised the four probecard channels available from the two 8×2 multiplexers. Having each MUX output in a different state, corresponding to the stages of the switching process at any given time during the measurement, allows for the necessary delay to be reduced, since the switching and the SMU readout introduce a natural delay. During this the current of the channels, which have just been previously switched to high voltage/GND, are allowed to settle before being readout or disconnected, respectively. As the 4 MUX outputs are “rolling” through this procedure, the probecard channel connected to the output is swapped out after the current has settled at GND level.

In Fig. 4.23 results for a single-needle measurement (a) and a probecard-based strip test (b) are shown. For both strip test procedures overall fluctuations in C_{coupl} and R_{bias} within the segments can be seen in the plots. Furthermore, a notable periodic structure with fluctuations of δC_{coupl} and $\delta R_{\text{bias}} \approx 5\%$ can be observed in the probecard-based test. This occurrence is a result of the inner needles of the probecard being surrounded by a higher number of needles. As the crosstalk between channels is small, but nonetheless present in sensors, like seen in the inter-strip measurements, having floating strips in the vicinity with the probecard needles contacting them will change the electrical properties. The effect is then seen in a measurement of the R-C network due to the additional stray impedance introduced by the traces on the card and the leads connected to it. Unlike for single-needle

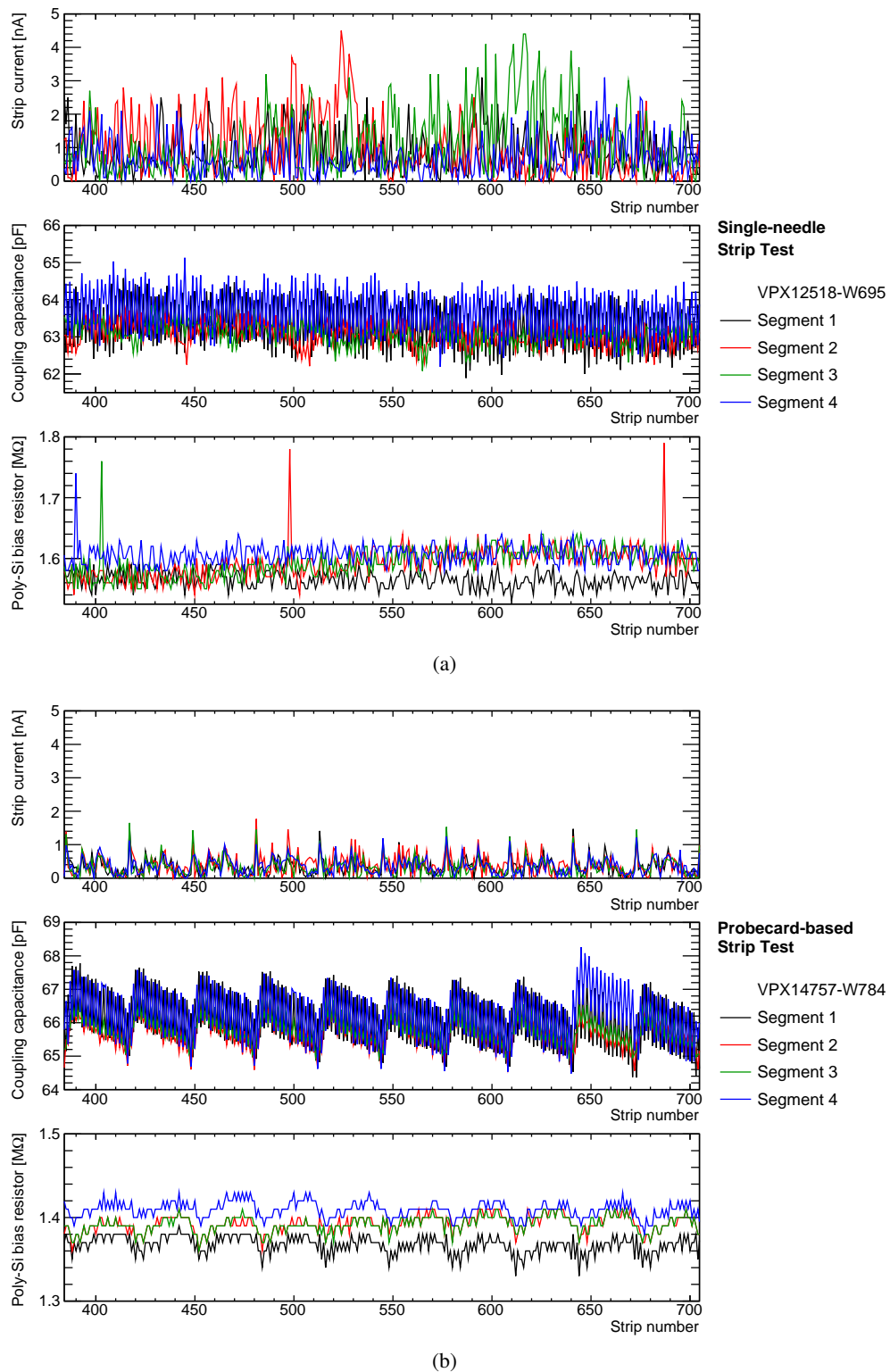


Fig. 4.23: Comparison between strip test results obtained with a single needle (a) and a probecard (b).

Evaluation of prototype ITk Strip Sensors

measurements, this cannot be compensated for by the hardware trimming function of the LCR meter. However, this feature has not been observed to falsify the overall outcome of a strip test.

If this *probecard imprint* proves to be a problem in the future, it could be corrected on a software basis by performing a reference measurement on a test-structure with well-known R-C characteristics in the beginning or at the end of the strip test. This would not add much time to the test duration and would easily tie in with the automatic inspection of the probecard with regards to continuity and potential hot channels, which is already conducted as part of the LabVIEW implementation of the strip test procedure.

In addition to the periodic structure due to the probecard needles, there is also a small fluctuation for alternating channels in segment 1 and 4 of A12 prototypes from the additional bond pad of odd-numbered strips in segment 1 and even-numbered strips in segment 4, respectively.

Another result which can be seen in this comparison is the consistent contact quality achieved for the probecard. Due to the edge-sense feature and the pre-defined overdrive, a uniform contact across all needles is ensured. As a consequence the R_{bias} measurement, in particular, became exceedingly reliable with the probecard, which is in stark contrast to the single-needle measurement, where the variable contact quality because of the non-planarity of the sensor on the jig, made (manual) re-testing of individual channels necessary. Furthermore and most notably, the time needed for a full strip test has been significantly reduced from ~ 14 h, in addition to the time necessary for retesting individual strips, to less than 2.5 h.

In total, strip test results from almost 500,000 channels for 97 sensors of the ATLAS12 generation and around 70,000 channels for 27 ATLAS17 sensors were accumulated. Histograms of all strip test data are shown in Fig. 4.24. The large spread observable for batch VPX12318 in the bias resistor histogram stems from the single-needle measurement used on those sensors and its less consistent contact quality.

Sensor W611 of the ATLAS12 prototypes was the only sample found not to meet the specifications, due to having 220 strips with faulty bias resistors. Said strips were within two groups of 110 channels situated symmetrically in the two centre segments. Upon closer scrutiny of that region, an unusual sheen could be seen, but only under an angled light source, which explains why it was not spotted during the initial inspection. All the other A12 sensors amount to only 136 faulty channels, which were recorded across all 97 sensors probed. Of those, 71 strips have either a pinhole or punchthrough. From the measured C_{coupl} and R_{bias} of the other defective strips, 3 display the characteristics of a broken implant, 9 are presumed to be from metal shorts, and the remaining 53 have either open or otherwise damaged poly-Si bias resistors (see Fig. 4.3 for visual examples of different failure modes). In conclusion, a total of 99.93% good strips has been observed, exceeding the 98% required in the specifications by a large margin. The tested ATLAS17 sensors all passed the strip test criteria. A total of 25 faulty strips were found, of which 10 were pinholes, 1 a suspected implant break, and the other 14 having some kind of defect bias resistor. Hence, the A17 have 99.96% good channels. The occurrence of faulty strips on all tested sensors did not show any regular pattern and appeared to be random.

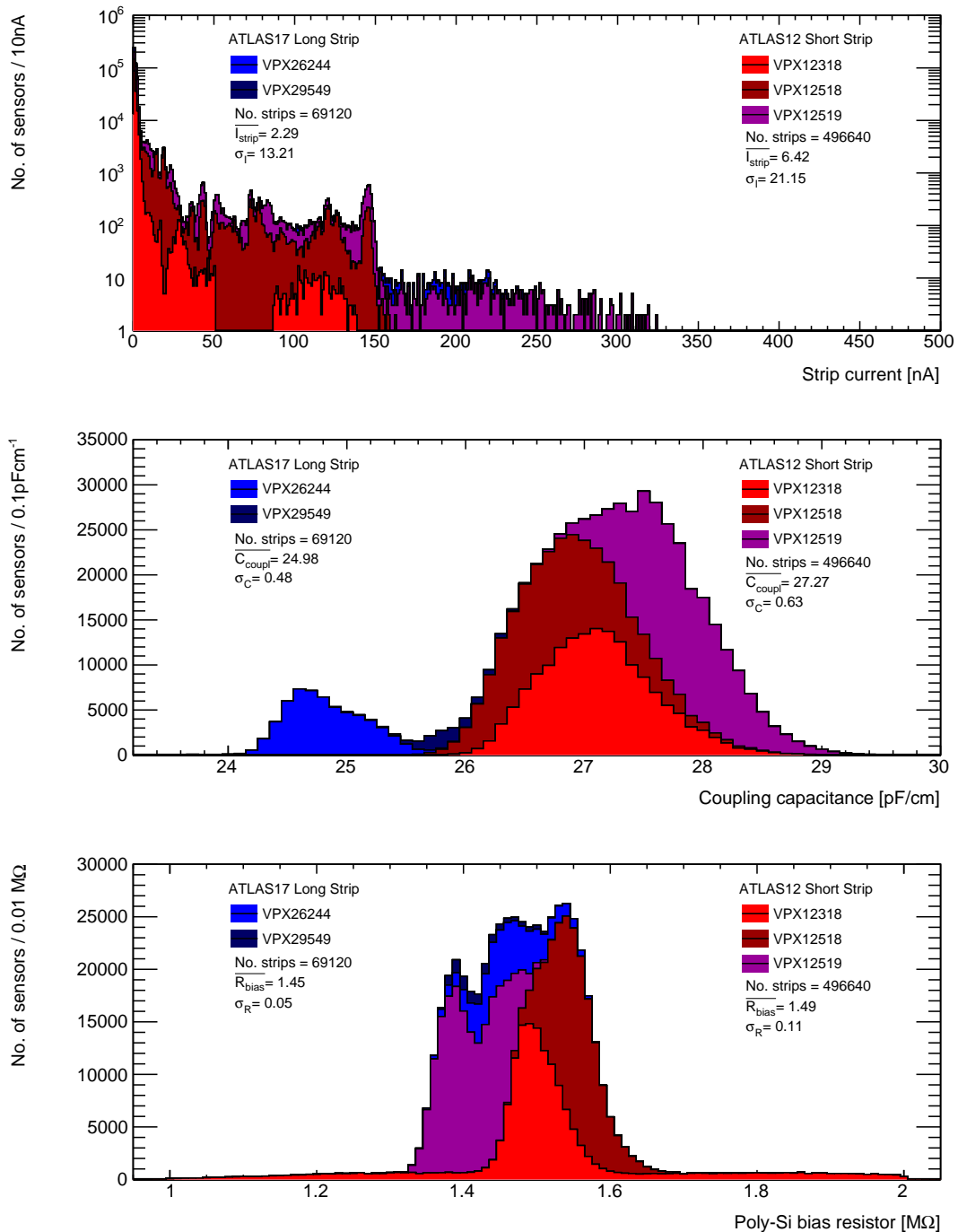


Fig. 4.24: Summarised striptest results for all 97 ATLAS12 and 27 ATLAS17 tested sensors broken down into their respective batches. C_{coupl} is normalised with respect to the strip length of the sensor.

4.9 Measurements of long-term leakage current stability

An important parameter for the long-term reliability of sensor operation is the stability of the leakage current. The technical specifications of the ATLAS12 sensors give a limit of no more than $\pm 3\%$ on the fluctuations during a 24 hour measurement, with bias voltage set to -600 V or to the onset of occurring soft breakdown, if lower. Measurements on these A12 sensors were usually performed with the same setup as standard IV measurements, i.e. the sensor on a plastic jig in the probe station, electric contact via probe needles or wire bonds, and in cleanroom ambient atmosphere.

Over the course of those measurements, a fairly large number of sensors failed the stability specifications in ways which were unique to individual sensors. However, three general categories could be determined, which coarsely describe the characteristics of sensors during leakage current stability measurements. It has to be noted that sensors do not necessarily fall into a single category and often a convolution of different effects can be observed.

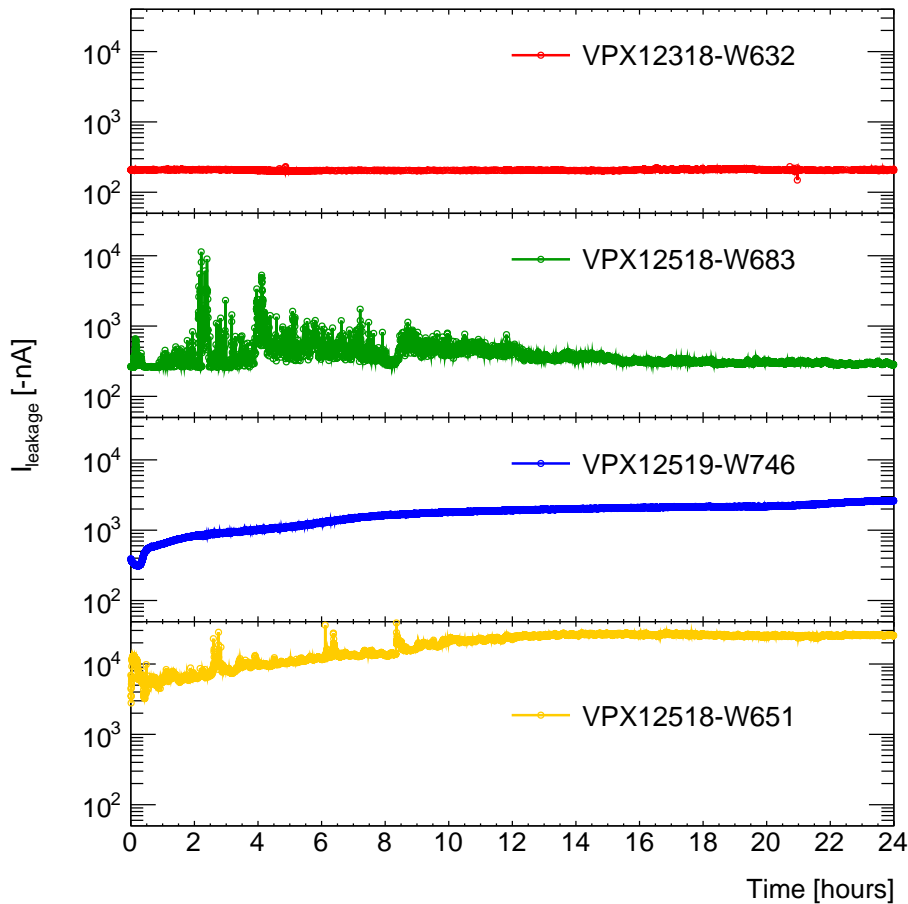


Fig. 4.25: Leakage stability measurements of various sensors with exemplary results (from top to bottom): stable (W632), erratic fluctuations (W683), perpetually increasing current (W746). These kinds of behaviour do not only occur as isolated cases but are often combined (W651). All measurements were taken at $V_{\text{bias}} = -600$ V for 24 h.

stable current: After settling, the current remains stable over the whole duration of the measurement (see Fig. 4.25, W632). However, only a fraction of sensors were stable from the first stability measurement on and remained that way for subsequent tests. Most notably, a comparatively larger number of sensors from the first batch VPX12318, many of which were outer cut sensors, have been stable under the specified conditions.

erratic fluctuations: One form of leakage instability manifests itself in erratically occurring current spikes during the measurement, as can be seen in Fig. 4.25 (W683). The overall duration of such spikes is usually rather short, ranging from a few seconds to several minutes. The defining characteristics of these spikes are the large fluctuations and erratic nature, which makes the time development highly unpredictable, as they have been observed to recur even after extended periods of stability. Most of the sensors with this behaviour had their breakdown from otherwise stable characteristics close to the test voltage used for biasing the sensor. This correlation, and their short duration, points towards micro-discharges occurring from fluctuations in the environmental conditions as possible causes for this form of leakage instability.

perpetually increasing current: Most of the unstable sensors have been found to yield a perpetual increase in leakage current throughout the duration of the measurement. While this increase can initially be rather moderate, as displayed in Fig. 4.25 (W746), often there would be a sharp kink at some point in the time development with the leakage current multiplying in a runaway effect. This resulted in those sensors exceeding compliance and not even finishing the full test duration. IV scans before and after the stability measurement indicate that the runaway characteristic usually occurs in combination with a clearly visible shift of the breakdown onset between the repeated IV measurements. This result suggests that this form of instability is caused by the onset of breakdown which continually decreases during the stability measurement until reaching the bias voltage used for the stability test.

In the end almost half of all ATLAS12 sensors tested for leakage stability showed some sort of instability in their first measurement. Due to the deterioration of breakdown, many of the sensors which exhibited that behaviour had to be tested at a much lower bias voltage than the proposed -600 V , or their initial display of the onset of micro-discharge, for subsequent tests, as they would otherwise exceed the hardware current compliance shortly after starting the measurement. Several more sensors have not been further investigated because the breakdown had shifted to a much lower value compared to the result of the initial IV scan not even while being tested, but while being stored in the desiccator. In conclusion, it can be said that there seems to be a general problem with leakage current stability and breakdown behaviour of ATLAS12 sensors. Furthermore, the deterioration of breakdown, not only through repeated measurements, but just from storing makes the long-term reliability questionable.

From these results and the findings shown in Chapter 5 related to the humidity dependence of sensor breakdown, the measurement routine was changed for ATLAS17LS sensors. The stability

Evaluation of prototype ITk Strip Sensors

measurement was now performed in a dry environment, e.g. in a desiccator or in an airtight enclosure while being flushed with dry air or nitrogen. Moreover, an effort was made to minimise the exposure to ambient humidity as much as possible. As a result, the observed leakage current was found to be stable for a much larger proportion of sensors from those batches. Most notably, no cases of erratic fluctuations were observed for A17 sensors. However, even with these actions being taken, some sensors still exhibited an increasing current leading to early breakdowns.

In conclusion, leakage current stability is one of the means of sensor evaluation which is able to spot problems with long-term operation of sensors and modules. Using the observations in the ATLAS12 batches as an incentive, further and more thorough investigations into the nature and cause for the seen instability has been carried out. As will be shown in the following chapter, this ultimately led to a better understanding of the sensor performance and an optimisation of sensor handling and testing procedures.

4.9.1 Changes in IV behaviour

During the ongoing sensor evaluation of the large ATLAS12 sensors there were multiple instances where the leakage current changed over the course of the interval between measurement steps in IV scans, similar to long-term observations during stability measurements. It could be observed that, depending on the sensor, this could manifest either, as a beneficial *training effect* where a high leakage current decreased over time, or as a detrimental effect where the current was further and sometimes even more rapidly increasing. A second effect can also be seen in the case of repeated measurements, regardless of general breakdown behaviour. With increasing number of measurements, the leakage current for low bias voltage is steadily decreasing. Moreover, the longer the delay between measurement steps, the more pronounced this effect becomes, which already indicates a certain time dependence of this effect. A more detailed investigation of the changes in the low voltage behaviour, and especially of the recovery time needed to revert the sensor back to its original behaviour, can be found in Chapter 6.

4.10 Evaluation of irradiated full-size sensors

After performing a detailed investigation of the ATLAS12 generation of prototype sensors, a select few of them were irradiated with 60 MeV protons at the *Cyclotron and Radioisotope Center (CYRIC)* of Tohoku University in Japan alongside many miniature sensors. The final assessment of the accumulated *neutron-equivalent fluence* (fluence of monoenergetic 1 MeV neutrons to produce equivalent damage [54]) yielded $\Phi_{\text{eq}} = 1 \times 10^{15} \text{ n}_{\text{eq}}/\text{cm}^2$, which corresponds to the estimated amassed fluence for inner-layer barrel strip sensors at the end of the HL-LHC lifetime with a safety factor of 2. With the accumulation of such high radiation damage, and to prevent uncontrolled annealing, the sensors have to be kept in a nitrogen-flushed freezer at $\sim -22^\circ\text{C}$ for storage and evaluation of their characteristics after irradiation. The results of these measurements will be presented below.

4.10 Evaluation of irradiated full-size sensors

The sensors were prepared for measurements by placing them in a module testframe (see Chapter 2, Fig. 2.13). In order to allow for bias voltage to be reliably applied to the sensor backplane bias contact, an HV-tab was directly wire-bonded to the aluminium layer of the sensor backside. This is done so as to avoid having the voltage drop along the conductive edge, which has been found to be affected by radiation damage in the oxide layer of the cut edge. All other electric contacts to the pads of the testframe are similarly provided by wire-bonds.

The first measurements performed with the irradiated full-size sensor were repeated standard leakage current versus bias voltage scans. Obtained IV curves are displayed in Fig. 4.26(a). For the data shown, the current has been normalised with respect to the active sensor area, which was assumed to not have changed after irradiation, and a correction factor according to Eq. 3.24, using the average freezer temperature, was used to calculate the respective leakage current at ambient cleanroom temperature of 21°C. Since the IV behaviour was previously observed to change over time in unirradiated sensors (Section 4.9.1), multiple iterations of bias voltage sweeps were conducted and the data recorded, the resulting curves are overlaid with the first obtained IV scan of the corresponding sensor. As expected, the overall current increased significantly, by approximately 6 orders of magnitude, after irradiation. This increase originates from both surface and bulk damage. Furthermore, no significant changes from repeated measurements could be seen apart from fluctuations stemming from the cooling cycle of the freezer.

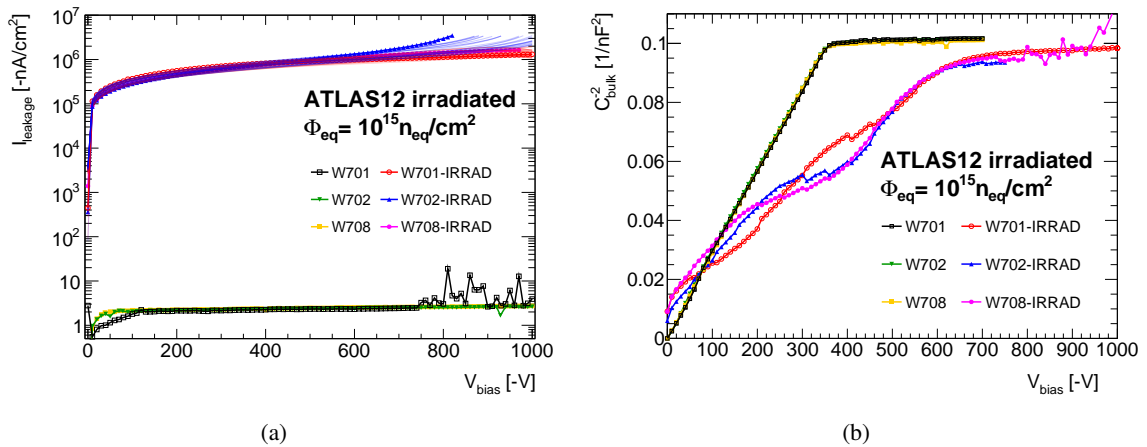


Fig. 4.26: (a): Leakage current, normalised with respect to the active sensor area and corrected to 21°C, measured for proton irradiated ATLAS12 main sensors against the applied bias voltage. Multiple iterations of IV scans on the same sample are overlaid. (b) CV curves for the bulk capacitance. Both IV and CV curves are shown in comparison to the scans performed on the same unirradiated sensors.

Subsequent CV measurements demonstrate the effect of radiation damage on the doping characteristics of the silicon bulk. As the bulk damage accumulated, the effective doping concentration increased and along with it the voltage necessary for full depletion of the device. The comparison of CV curves in Fig. 4.26 reveals the extent to which bias would have to be increased if it is desired

Evaluation of prototype ITk Strip Sensors

Tab. 4.2: Comparison of V_{FD} , D , and N_{eff} of tested sensors before and after proton irradiation to $1 \times 10^{15} \text{ n}_{eq}/\text{cm}^2$.

Sensor No.	V_{FD} [V]	D [μm]	N_{eff} [10^{12} cm^{-3}]	
			slope	plateau
VPX12519-W701	355	303	5.1	5.0
	irrad. 605	296.5	10.5	8.9
VPX12519-W702	350	302.5	5.1	5.0
	irrad. 645	290.5	12.0	9.9
VPX12519-W708	355	302	5.1	5.0
	irrad. 695	294.5	13.3	10.4

to still operate the ITk sensors fully depleted at the end of the prospected lifetime. An estimation of the quantities derived from these measurements is summarised in Tab. 4.2 and compared to the unirradiated samples. The depletion voltage increased to values beyond -600 V for all three samples, as was already apparent from the CV curves, while the active thickness decreased by about 3%. The effective doping concentration increased by approximately a factor of two after irradiation, the derived values for the plateau and slope region of the curve deviated now by a significant margin compared to unirradiated sensors. Because, unlike the curves for the samples before being irradiated, the kink in the transition from partially to fully depleted devices is not as sharp and the slope does not exhibit a constant gradient like before.

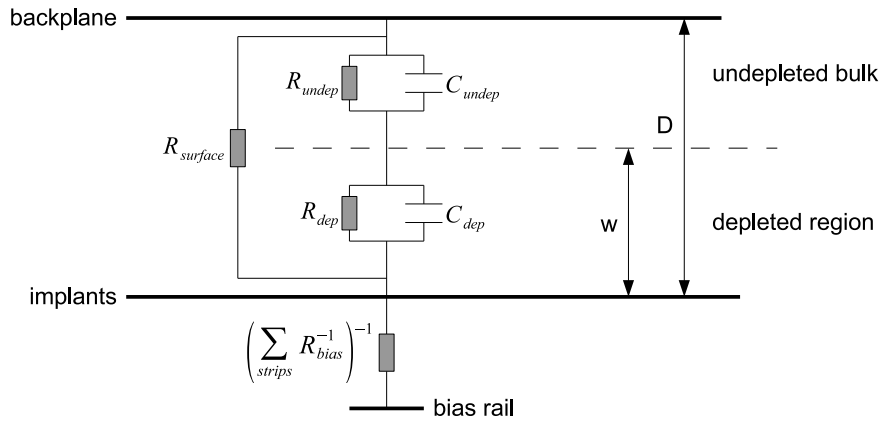


Fig. 4.27: Equivalent circuit of a simple R-C model representing a partially depleted sensor. Depletion region and undepleted bulk are connected in series and are modelled by a parallel capacitor and resistor each. An additional parallel resistor accounts for surface current and a series resistor between the implants and the bias rail is the equivalent resistance of all R_{bias} in parallel (sketch redrawn from [52]).

This result originates from a deviation of the simple model of a p-n junction as a growing capacitance of the space charge region, and the decreasing resistance of the depleted bulk, as assumed by the LCR meter settings. Fig. 4.27 shows the equivalent circuit of a more precise model for a

partially depleted sensor diode, with a parallel capacitor and resistor accounting for the resistance and capacitance of the depleted (*dep*) and undepleted bulk (*undep*) regions respectively, in addition to a resistor for surface currents. In the specific case of the ITk strip sensors, the contribution of the equivalent resistance of all polysilicon bias resistors in parallel also cannot be neglected, as it is part of the CV test circuit. In the depletion zone the capacitance usually dominates over resistance in that region, since the differential resistivity of a reversely biased diode is high $R_{\text{dep}} = dV_{\text{bias}}/dI_{\text{leakage}} \gg (\omega C_{\text{dep}})^{-1}$. Contrary to this, the undepleted bulk can be described by the resistor alone for low voltages and measurement frequencies as $R_{\text{undep}} \ll (\omega C_{\text{undep}})^{-1}$ for $f \lesssim 40$ kHz. At voltages close to the full depletion voltage, the sensor bulk can be described by a single capacitor parallel to the surface resistor. Between those two extreme cases, the resistance of an undepleted bulk decreases with $R_{\text{undep}} \propto (1 - \sqrt{V/V_{\text{FD}}})$ while its capacitance increases according to $C_{\text{undep}} \propto 1/(1 - \sqrt{V/V_{\text{FD}}})$ with applied bias [52].

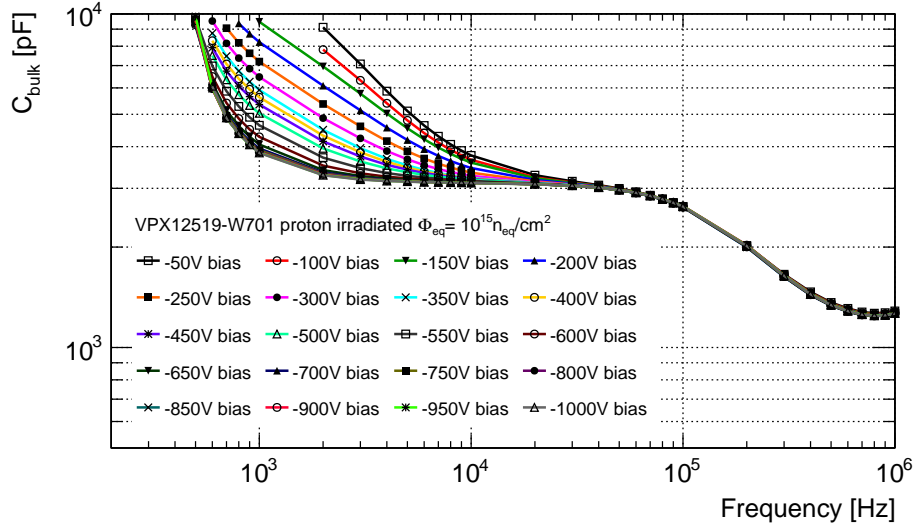


Fig. 4.28: Frequency dependence of the bulk capacitance of irradiated sensor VPX12519-W701 for bias voltages up to $V_{\text{bias}} = -1000$ V in increments of $\Delta V_{\text{bias}} = 50$ V.

Due to this additional complication of the diode R-C characteristic, the frequency dependence of C_{bulk} was again determined with results being shown in Fig. 4.28. Observable in the curves for different bias voltages is that at frequencies $f > 40$ kHz the measured capacitance seems to be independent of the applied voltage. This is expected from the model, as increasing the frequency will lead to a more dominant contribution of capacitance in the total impedance of an irradiated device, in both the depleted and undepleted region. As such the measured impedance would be equivalent to that of a circuit consisting of two capacitors and a resistor, for the contributions from the bias resistors, in series.

The final measurement on the irradiated sensors was a leakage current stability measurement similar to those described in Section 4.9. The measured current is plotted against the respective

Evaluation of prototype ITk Strip Sensors

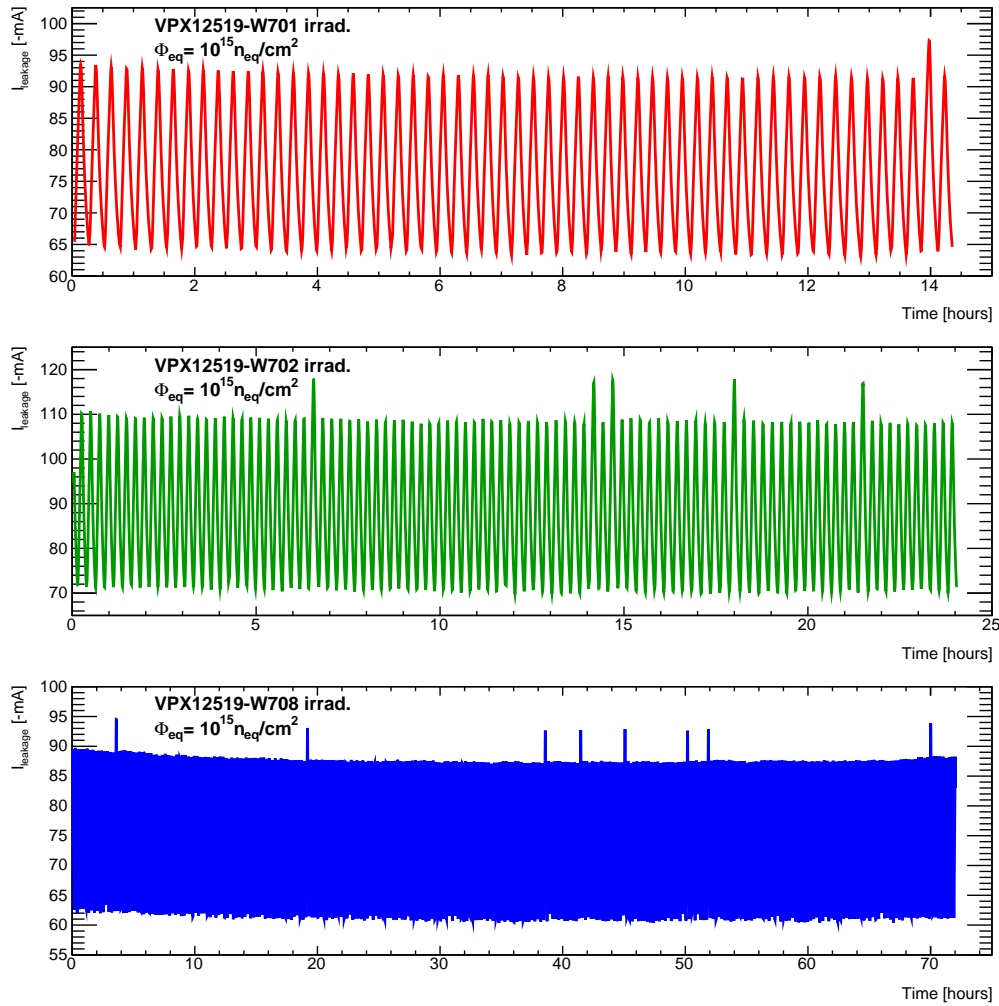


Fig. 4.29: Results of leakage current stability measurement performed on irradiated ATLAS12 main sensor samples. Values are corrected to 21°C and periodic fluctuation in the current stem from the cooling cycle of the freezer.

measurement duration in Fig. 4.29. A temperature and humidity sensor recorded the environment within the freezer during throughout the whole period of data taking. Precise correction of the cooling cycles of the freezer was not possible, and a temperature correction factor was only applied with respect to the average freezer temperature because the response time of the T/RH sensor was faster than the changes seen in the leakage current. As can be seen in the graphs, the current was very stable and only varied in conjunction with the periodic freezer cycles.

In conclusion, the tested irradiated sensors show good continuity in their IV characteristic and current stability. The measurement of their bulk capacitance complies with the expected behaviour of an irradiated diode, including the frequency dependence of the measurement, and despite the heavy irradiation equal to the total fluence throughout the ITk lifetime, the sensors could still be fully depleted, albeit at much higher bias.

4.11 Design of Quality Control procedure for production

Sensor pre-production is scheduled to start in late 2019. For this, sensors have to undergo Quality Control (QC) so as to make sure only sensors which adhere to the specifications listed in Tab. 4.3 are used in the module production process. Basic mechanical and electrical tests will be carried out for every sensor, while more detailed measurements will be done on a sample basis.

Tab. 4.3: List of ITk microstrip sensor specifications to be met during production [17]. Given values for voltage refer to reverse bias.

Substrate material	
Size	8-inch/200 mm or 6-inch/150 mm
Type	p-type FZ
Crystal orientation	$\langle 100 \rangle$
Thickness (physical)	300 – 320 μm
Thickness (active)	$\geq 90\%$ of physical thickness
Thickness tolerance	$\pm 5\%$
Resistivity	$> 3 \text{ k}\Omega\text{cm}$
Oxygen concentration	1×10^{16} to $7 \times 10^{17} \text{ cm}^{-3}$
Sensor specifications before irradiation	
Full depletion voltage	$< 330 \text{ V}$ (preference for $< 150 \text{ V}$)
Maximum operation voltage	700 V
Poly-silicon bias resistors	1 – 2 M Ω
Inter-strip resistance	$> 10 \times R_{\text{bias}}$ at 300 V for $T = 23^\circ\text{C}$
Inter-strip capacitance	$< 1 \text{ pF/cm}$ at 300 V, measured at 100 kHz
Coupling capacitance	$> 20 \text{ pF/cm}$ at 1 kHz
Resistance of readout Al strips	$< 15 \Omega/\text{cm}$
Resistance of n-implant strips	$< 20 \text{ k}\Omega/\text{cm}$
Onset of micro-discharge	$> 700 \text{ V}$
Total initial leakage current, including guard ring	$< 0.1 \mu\text{A}/\text{cm}^2$ at room temperature
Number of strip defects	$< 1\%$ per segment and $< 1\%$ per sensor
Sensor specifications after irradiation ($1.2 \times 10^{15} \text{ n}_{\text{eq}}/\text{cm}^2 - 50 \text{ MRad}$)	
Onset of micro-discharge	$> 700 \text{ V}$ or $V_{FD} + 50 \text{ V}$
Inter-strip resistance	$> 10 \times R_{\text{bias}}$ at 400 V for $T = -20^\circ\text{C}$
Collected charge	> 7500 electrons per MIP at 500 V
Mechanical specifications	
Dicing precision	$< \pm 20 \mu\text{m}$ or better
Sensor bow after process and dicing	$< 200 \mu\text{m}$

The focus of the QC procedure is on issues identified based on past experience. A large part of that experience comes from similar tests during the SCT production. At that time many sensors failed the basic visual inspection due surface scratches or faulty implementation of critical structural sensor

Evaluation of prototype ITk Strip Sensors

architecture such as bias resistors. Another large portion of failures occurred during the reverse bias leakage current measurement. As QC procedures are a trade-off between effort and time spent to check specifications to ensure sensors are good for use in the module assembly process, tests are divided into those conducted on every sensor and those on a select sample per production batch. QC tests on every sensor focus on integrity and condition of sensor through visual methods and basic electrical tests, while tests on sample sensors are used to check batch quality and verify uniformity within and across batches.

As a consequence of the results for Sensor Quality Control on prototype sensors, many of the scan parameters used originally have been revised, and a complete QC procedure for every sensor reception site during production has been developed. During production, results of all tests will be uploaded to a common database for logging purposes. The individual tests and how they were influenced by the previous experience is explained in the following paragraphs.

Tests performed for each individual sensor

After reception at the QC site, each individual sensor is checked for cracks, chips, or other irregularities, and an image of the entire sensor surface is captured at high-resolution. In addition to the aforementioned, sensor bow as the maximum difference in z is not to exceed $200\mu\text{m}$ when measured with a non-contact Coordinate Measurement Machine (CMM). Compared to manual or automated visual inspection, image capturing allows for quicker testing and the image can serve as a future reference to pinpoint potential mishandling during testing or module production.

Subsequently, reverse bias leakage current (IV) and sensor bulk capacitance (CV) measurements are carried out for each individual sensor in the range $V_{\text{bias}} = 0\text{ V}$ to -700 V in a dry, humidity-controlled atmosphere on either custom made jigs or a probe station. For the IV scan, current should not exceed $0.1\mu\text{A}/\text{cm}^2$ when measured with nA precision in steps of 10 V with 10 s intervals in between steps. In contrast to IV scans on prototype sensors, at the end of the standard voltage sweep the voltage has to be held at -700 V for an additional 30 s so as to spot potential onset of micro-discharge after short periods of time. This is done in response to the observed training effects and current instability in prototypes. For CV measurements, the bias voltage is increased by 10 V with 5 s pauses and measured with an LCR meter at a frequency from 500 Hz to 5 kHz . For all sensors the extracted full depletion voltage is not to exceed -330 V .

Tests performed on a subset per batch

On 10% to 20% of sensors per batch leakage current stability will be monitored over 24 hours at $V_{\text{bias}} = -700\text{ V}$ and current variations should not exceed 3% . Owing to the experience with prototype sensors, as given in further detail in Chapter 5, all of the aforementioned tests will be carried out in dry nitrogen atmosphere. This was decided in order to minimise the accumulated impact of humidity on sensor performance and disentangle true sensor faults from those induced by the presence of elevated humidity.

On 2% to 5% of sensors per batch, a Full Strip Test with the sensor on a probe station will be performed. Where applicable, e.g. on barrel sensors, this test is conducted using a multi-channel probecard.

Additional checks of inter-strip capacitance or resistance, and punch-through protection will be mostly carried out on test structures manufactured on the same wafers as the full-size sensors. If a significant number of test results on those in a particular batch do not meet specifications, the tests are to be verified on main sensors. For the inter-strip measurements, between adjacent strips C_{is} should not exceed 1 pF/cm and R_{is} be in the G Ω range. PTP is verified by measuring the sudden change in current when increasing the voltage over the bias resistor.

4.12 Summary and conclusions

A detailed evaluation of the ATLAS12 and ATLAS17LS generation of prototype sensors for the ITk Strip Detector was conducted and the findings were presented in this chapter. Of all 134 tested sensors, all satisfy the maximum bow requirement and 128 passed their subsequent initial IV and CV tests. In strip tests, less than 0.07% channels were characterised as defective with all other strips fulfilling the specifications for their individual C_{coupl} and R_{bias} . In more detailed measurements, the inter-strip capacitance and resistance, the implant resistance and the Punch-through Protection have been confirmed to comply with the expectations for the prototypes. However, many sensors did not exhibit the required leakage current stability and, furthermore, the onset of current breakdown has been observed to deteriorate over time. These results warrant further investigation, which will be presented in the following chapter.

Chapter 5

Anomalous sensor breakdown and the dependence on environmental conditions

From the evaluation of prototype sensors presented in the previous chapter, it could be concluded that while the large majority of sensors passed their initial assessment of maximum sensor bow, IV, and CV tests, as well as detailed testing of all readout strips, there has, however, been a clear discrepancy between those overall good results and the leakage current stability measurements. On top of that, re-testing stored sensors often yielded a significant shift of the onset of micro-discharge, mostly in the form of a deterioration of performance.

Many sensors which have initially been evaluated and found to pass their initial quality requirements have been sent out to other institutes in the collaboration in order to be turned into prototype modules. In that process, the hybrid chips with the front-end readout chips are glued on top of the sensor and connected to the respective AC-coupled strips via wirebonds. Leakage current measurements at different stages of the assembly process often featured early breakdowns once they were glued, even though the sensor passed the initial IV measurement without any such indications.

This chapter focusses on investigations to gain better understanding of sensor breakdown and ways to mitigate it, not least to facilitate the critical sensor quality control during the module production phase. The first part in Section 5.1 will show the results of a study regarding the influence of mechanical stress on leakage current and sensor breakdown. A detailed examination of the dependence of sensor breakdown on the humidity of the surrounding environment will be presented in the following sections. This also includes combining visual and short-wavelength infrared (SWIR) imaging to establish where breakdown typically occurs in the sensor geometry, and ways to potentially reverse sensor deterioration due to humidity in some cases. The last part of the chapter deals with sensor simulations in an attempt to model the observed breakdown behaviour in TCAD.

5.1 Influence of mechanical stress on leakage current

As detailed before in Section 2.4.1, strip modules will be built by connecting sensors, readout chips, and flex circuit boards using different kinds of adhesives. Moreover, the finalised module will be placed in a mechanical local support structure. Since the operational temperature of the detector is planned to be $\sim -30^{\circ}\text{C}$ to counter adverse increase of currents due to radiation damage, thus minimise the load on the power supplies, and prevent uncontrolled annealing, the modules will be exposed to a large temperature difference compared to their construction at room temperature. Taking into account the different thermal expansion coefficients of the various materials used, this will lead to the module being subject to mechanical stress with a potential impact on sensor properties. A simulation of the induced mechanical stress just due to the temperature difference is shown in Fig. 5.1.

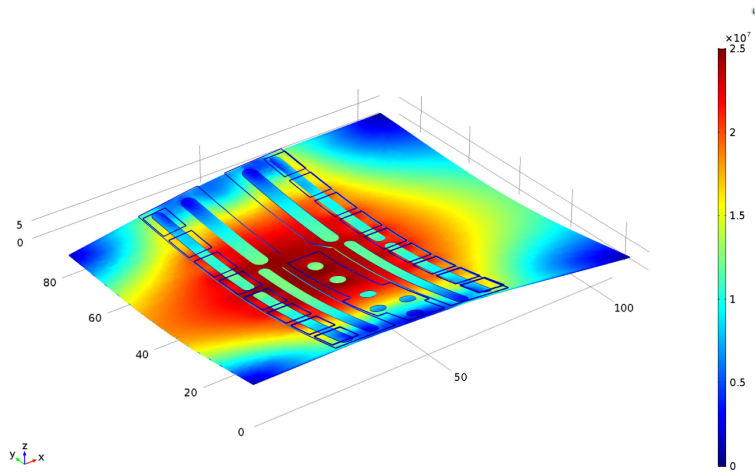


Fig. 5.1: Simulated mechanical stress in MPa on an end-cap R0 module (dimensions in mm) after being cooled down by 50°C to operational temperature [75].

Moreover, during the assembly of prototype modules, measurements of the sensor bow before and after gluing yielded an increase in the maximum bow of almost $200\ \mu\text{m}$ in the direction perpendicular to the strips. In view of the natural bow of ATLAS12 sensors, which is towards the sensor backplane, this might be even more problematic since all tested sensors were bent towards the side with strip implants after applying the glue. In this section, the results of an investigation into whether that induced mechanical stress could be a cause of the observed early breakdown will be presented.

5.1.1 Inducing controlled sensor bow

In order to determine the influence of mechanical stress on the leakage current behaviour of ATLAS12 strip sensors, one has to induce mechanical stress in a controlled way. The setup used for this is a flat jig made from stainless steel with attachable bars to press down the sensor. Those bars can be used in combination with strips of precision plastic shims placed underneath the sensor to induce a well-defined bow depending on the thickness of the shim. The setup was designed in a way that

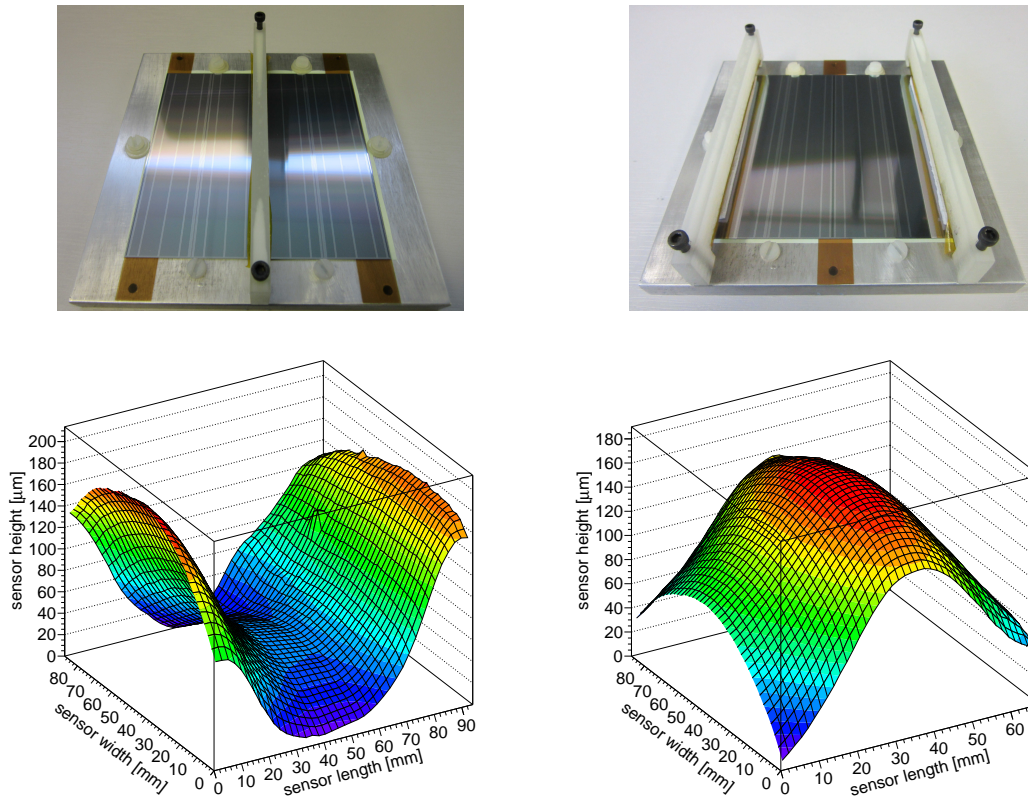


Fig. 5.2: Profile of a glass plate similar to the sensor in size and thickness on the metal jig. Plate flexed using 100 μm shim(s) with inner bar (left) and outer bar (right) placements.

allows two different placements of the bars and shims: the *inner bar* (IB) placement (see Fig. 5.2 (left)), which is used to achieve bowing perpendicular to strips towards the implants similar to the effect of glue, and the *outer bar* (OB) placement (Fig. 5.2 (right)) for the opposite sensor bow.

The devised testing procedure, which was used to yield the results presented in the following sections, is displayed in Fig. 5.3. For each step in the sequence, several IV curves were taken in order to check for consistent behaviour. Furthermore, as the result from the experience with the first sensor tested (see Fig. 5.5(a)), leakage current stability measurements were included starting with the second sensor tested. The stability measurements were usually taken at the onset of soft breakdown or $V_{\text{bias}} = -600 \text{ V}$, with a duration of 1 h, or for longer periods at the final step during relaxation. Additional measurements were conducted if anomalous behaviour was observed during any scans.

5.1.2 Breakdown characteristics

The onset of breakdown has proven to be an important indicator in these studies. In this section and the following, often the development of $V_{\text{breakdown}}$ is plotted in various instances. The different forms of breakdown and the rate of the leakage current increasing depends on a multitude of factors such

Anomalous sensor breakdown and the dependence on environmental conditions

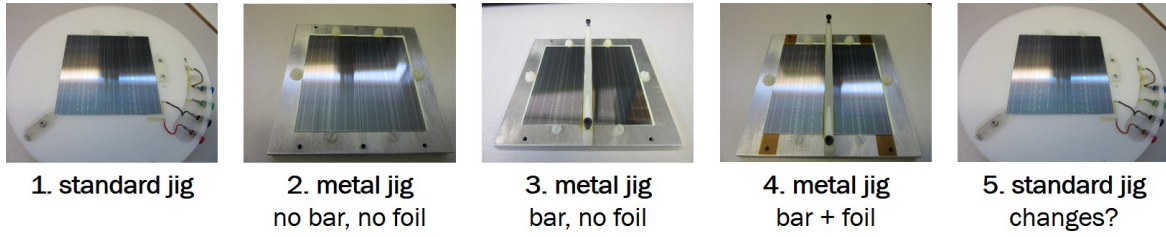


Fig. 5.3: Testing procedure with inner bar placement used to determine the influence of mechanical stress on the IV characteristic of sensors. For the 4th step strips of shims with a thickness of 100 μm and 188 μm , respectively, were used subsequently.

as the beneficial reconditioning (training effect) of the sensor or the testing environment. Taking the onset in the IV curve where I_{leakage} starts to increase rapidly, one can differentiate between *hard* or *soft breakdown* (often referred to as *micro-discharge*), depending on how sharply the rate increases. The two IV curves in Fig. 5.4 are presented here as examples for the sensor undergoing a fairly soft (red curve) and hard breakdown (green curve).

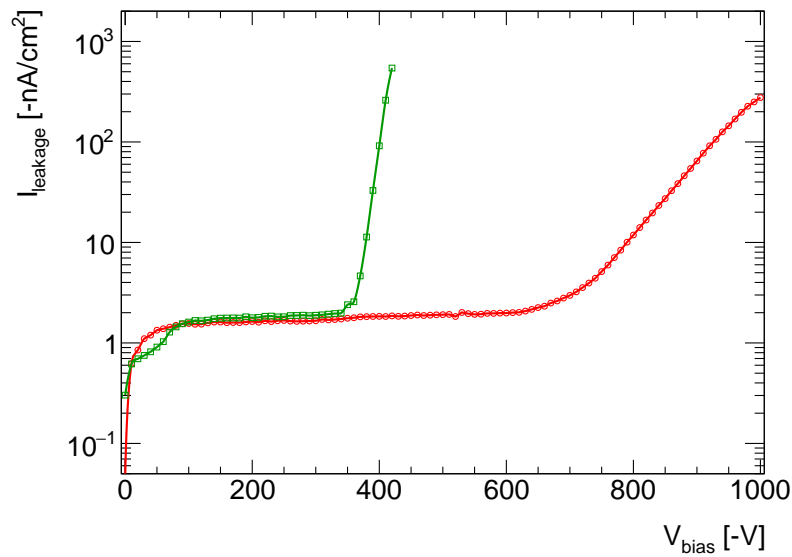


Fig. 5.4: IV measurements of sensor W747 taken during mechanical stress studies for illustrating different breakdown characteristics.

In general, there is a gradual transition between the two extreme cases of soft micro-discharge and (instantaneous) hard breakdown. Therefore, there is no clear demarcation and criteria as to how they can be objectively classified. In the following, the *breakdown voltage* $V_{\text{breakdown}}$ for any kind of micro-discharge or breakdown was defined by the condition

$$\frac{\Delta I}{\Delta V} / \frac{I}{V} > 10 \quad , \quad (5.1)$$

where ΔI und ΔV are calculated from the discrete data point at bias voltage V and the prior point taken. For that reason, the uncertainty on $V_{\text{breakdown}}$ is estimated to be equal to the step size of the respective IV scan.

5.1.3 IV characteristic of sensors under mechanical stress

ATLAS12 sensors

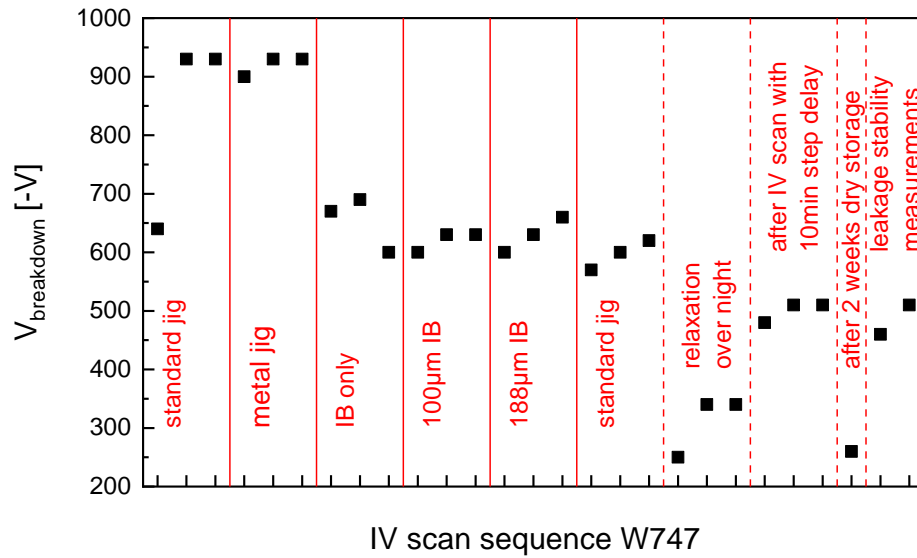
The first device tested for the influence of mechanical stress was sensor VPX12519-W747. It passed all initial IV, CV, and strip test specifications, however, it exhibited a soft breakdown at ~ -700 V in the initial IV scan and was therefore chosen for the stress studies to determine changes in the breakdown behaviour. The development of $V_{\text{breakdown}}$ during the different stages is displayed in Fig. 5.5(a). As can be seen in the data points, the onset of the soft breakdown shifted to higher voltages for repeated IV scans and initially remains there as a consequence of a beneficial training effect. In comparison to the IV characteristic without mechanical stress, the onset of the breakdown shifted to lower voltages under mechanical stress. The actual breakdown voltage did not appear to be dependent on the amount of pressure, at least in the case of this sensor and the strips of shims used here. Also, the observed initial shift for the inner-bar-only setting indicates that a certain amount of mechanical stress was already induced even without the shims due to the natural bow of the sensor.

After moving the sensor back to the standard jig, the onset of breakdown initially remained approximately at the same voltage as it was previously under mechanical stress. However, follow-up measurements on the next day showed that the sensor performance deteriorated over the extended period of relaxation and as a result breakdown shifted to a much lower voltage compared to data taken directly after flexing it (see Fig. 5.4). As consequence of the early breakdown after relaxation, efforts have been made to revert the device back to its original behaviour through training via repeated IV measurements, among others with a long delay between steps, as well as stability measurements. As shown in Fig. 5.5(a) this was partially successful, however, the recovery was not permanent.

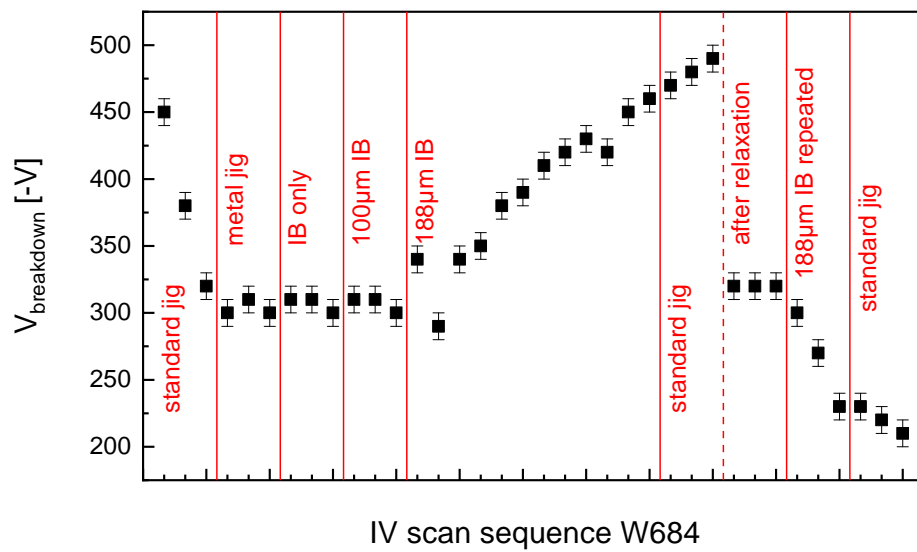
The second device tested was sensor VPX12518-W684. Like the W747 it exhibited a soft breakdown in the initial IV scan. However, re-testing the sensor in the first step of the measurement procedure showed that repeated IV and stability scans were detrimental to the performance of this sensor, which is in complete contrast to W747. As a result, the onset of breakdown shifted to lower bias until stabilising at $V_{\text{bias}} \simeq -320$ V.

Placing the sensor on the metal jig and using the bar either alone or in combination with $100\ \mu\text{m}$ shims did not influence the breakdown in any visible way. But the sensor characteristics changed significantly after using the $188\ \mu\text{m}$ shims to induce mechanical stress. As shown in Fig. 5.5(b), upon using that setup, the device began to exhibit a beneficial training effect from repeated IV scans as well as stability measurements.

Like the previous sensor, W684 first retained its characteristic when moved back to the standard jig (see Fig. 5.5(b)). Furthermore, also just like the other sensor, the onset of breakdown decreased after letting the previously flexed sensor relax on the standard jig. For this sensor, however, the



(a)



(b)

Fig. 5.5: Development of $V_{\text{breakdown}}$ for sensors W747 (a) and W684 (b) observed in subsequent IV measurements during different stages of mechanical stress test sequence. The different stages of the procedure are denoted as well as notable actions after moving back the sensor to the standard jig.

5.1 Influence of mechanical stress on leakage current

leakage current during the period of relaxation has been recorded, revealing a breakdown after ~ 36 h. As a consequence of these findings, the sensor was flexed a second time using the $188\ \mu\text{m}$ shims in order to test for the reproducibility of the beneficial training under mechanical stress seen before. But instead, the results show that additional measurements under mechanical stress deteriorate the performance of the sensor even further.

ATLAS07 sensors

To compare the observed behaviour of ATLAS12 sensors, most notably the early breakdown after sensor relaxation, to the characteristics of ATLAS07 sensors the same testing procedure was applied to two ATLAS07 devices. Both sensors had a highly stable performance without any noticeable change in behaviour during all stages of the measurement procedure. It has to be noted, though, that the A07 sensors used for these studies were from those manufactured using the high-quality float-zone silicon (FZ1) which differs significantly from the silicon used for A12 sensors.

5.1.4 Summary and referral to further studies

The two ATLAS12 sensors used to investigate the influence of mechanical stress on leakage current and breakdown behaviour differed in essential aspects. Sensor W747 had a known high soft breakdown voltage and the IV characteristic could be further improved by training via repeated IV measurements. Under mechanical stress, for any strength tested, the breakdown voltage decreased significantly. In contrast to this, the initial onset of breakdown seen for sensor W684 decreased even more under repeated tests before stabilising at a much lower value than seen in the first IV scan. However, under the mechanical stress induced by $188\ \mu\text{m}$ shims, the sensor became trainable, thus allowing an improvement in performance. Both sensors have in common that the sensor breakdown performance yielded significant alterations from the IV scans performed during the initial assessment of the A12 prototype batches. The tested ATLAS07 sensors, on the other hand, were seemingly not affected at all by mechanical stress. Instead they featured a highly stable performance at all stages of the testing procedure, just like they did for the leakage current stability.

The findings reported in this section triggered a more elaborate study on the influence of mechanical stress on a range of sensor quantities, including leakage current. That study, conducted by Martin Stegler and published in [75], shows a final outcome of all measured properties that is in good agreement with the theoretical predictions. While a notable decrease of inter-strip resistance could be observed with increasing stress, the changes are not critical and should not affect sensor performance. In the measured range, no sensor breakdown occurred and variations of the baseline leakage current was in the region of $\mathcal{O}(1\%)$.

In conclusion, from those results it can be assumed that mechanical stress itself is most likely is not the underlying cause of the observed breakdown shift. Rather, especially given the inconsistent breakdown behaviour of the two tested A12 sensors, the deciding factor seems to be the history of previous electrical tests and environmental conditions during those. For that reason, further

investigations were conducted with respect to the humidity dependence of sensor behaviour, which is explained in the following section. Moreover, preceding the results from that investigation, if one considers humidity as the principal cause of breakdown shifts, one could estimate that mechanical stress can exacerbate any such effect by creating microscopic cracks on the surface, which would allow for an easier adsorption of water molecules at the outer surface as well as facilitate subsequent diffusion into the passivation and oxide layer.

5.2 Humidity dependence of breakdown voltage

After the mechanical stress studies, it was suspected that while mechanical stress itself may not directly be the cause that leads to the deterioration of sensor breakdown, the presence of water vapour in the form of humidity during extended operation in an ambient atmosphere could be the underlying reason. Other observations that support this suspicion are the reports about the breakdown shift in assembled prototype modules and the shown discrepancy in the frequency of occurrence of soft micro-discharge when testing batches of sensors in a dry N₂ environment and in ambient conditions (see Fig. 4.8(a) in Section 4.5.1).

The explanation for the former is clearly the long-term exposure to humidity during the assembly process which would be comparable to the case of the leakage current instability observed and reported in Section 4.9. The latter is best explained in [48], where the case is being made that discrepancies between decent IV testing characteristics in ambient laboratory conditions and breakdown in dry nitrogen atmosphere stems from a change of the surface potential on the outer oxide surface (*gate boundary condition*, for more details see Section 6.2), which somewhat mitigates high electric fields. When tested in dry conditions this can also be mediated by humidity diffused into the passivation oxide during fabrication. However, that humidity would also evaporate slowly over weeks and months when stored in dry conditions and therefore the IV characteristic could change over time, which complies with the observations made (Section 4.9.1), where stable operation can sometimes only be resumed after a sensor training procedure, e.g. through long-step-delay IV scans or stability measurements close to breakdown, that (re-)establishes the surface boundary conditions.

Considering these explanations and the strong dependence on humidity on the sensor IV characteristic, a thorough investigation has been made into the breakdown behaviour of the prototype ITk Strip Sensors, the results of which will be shown below. One aspect which has been scrutinised was the location on the sensor where the breakdown occurs, using a short-wavelength infrared camera for hot-electron imaging. The second point was to quantify the shift of breakdown in relation to the relative humidity in the testing environment. The last part of the study concerns the possible reversal of any adverse effects introduced by the exposure to humidity.

5.2.1 Breakdown imaging

In order to pinpoint the exact location of breakdown occurring in the sensor, the radiative recombination of electrons created in the avalanche process yielding 1.1 eV photons ($\lambda \simeq 1130$ nm) was used in an image capture setup involving a short-wavelength infrared (SWIR) camera mounted on the probe station microscope. As the cooled, low-noise CCD in that camera is also sensitive to photons in the energy region of the silicon band gap, after applying some amplifying and filtering software, the excess photons created by the subsequent capture of hot electrons created in the avalanche breakdown become clearly visible in as bright spots on the sensor surface. By overlaying images captured under a visible light source and those in the dark under sensor breakdown, the exact location of the breakdown can be determined, and potential high field locations in the sensor layout in that regard can be detected.

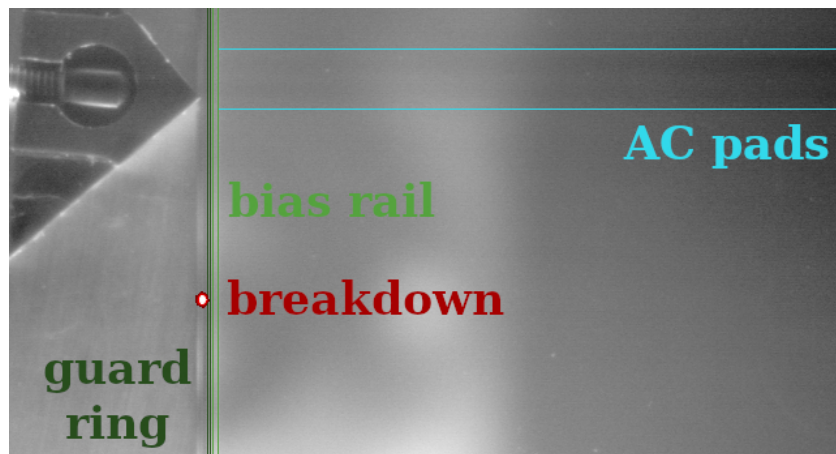


Fig. 5.6: Image of breakdown location in sensor VPX26244-W007 from overlaying a visual image with a SWIR photo of the same location. The captured region of breakdown (red spot) is at the outer edge of the guard ring. The drawn coloured lines and annotations only serve as guide to the eye.

Over the course of these investigations two major cases for the location of breakdown have been found. The first such case is depicted in Fig. 5.6 for sensor VPX26244-W007 as an example, and the area of breakdown is at the outer edge of the guard ring. This is the most commonly occurring location of breakdown seen in the tested sensor prototypes, where the exact position on the guard ring is not fixed but can move depending on the sensor. Since guard ring structures are implemented in the sensor for the express purpose of minimising the electric field at the sensor edge, they are naturally a point of high field strength in the sensor layout, making this result unsurprising.

The second observed breakdown location is shown in Fig. 5.7, where breakdown occurs in the strip region at the AC pads. As will be shown in sensor simulations in Section 5.3, the highest electric field in the strip region is located close to the metal overhang. At the AC pads the distance between strips is reduced, resulting in exceedingly high fields in that region, hence making them prone to breakdown in the strip region. However, having breakdown occur in the strip region before it happens at the guard ring indicates that some fault must have been introduced during the fabrication process which has not been detected in the strip test.

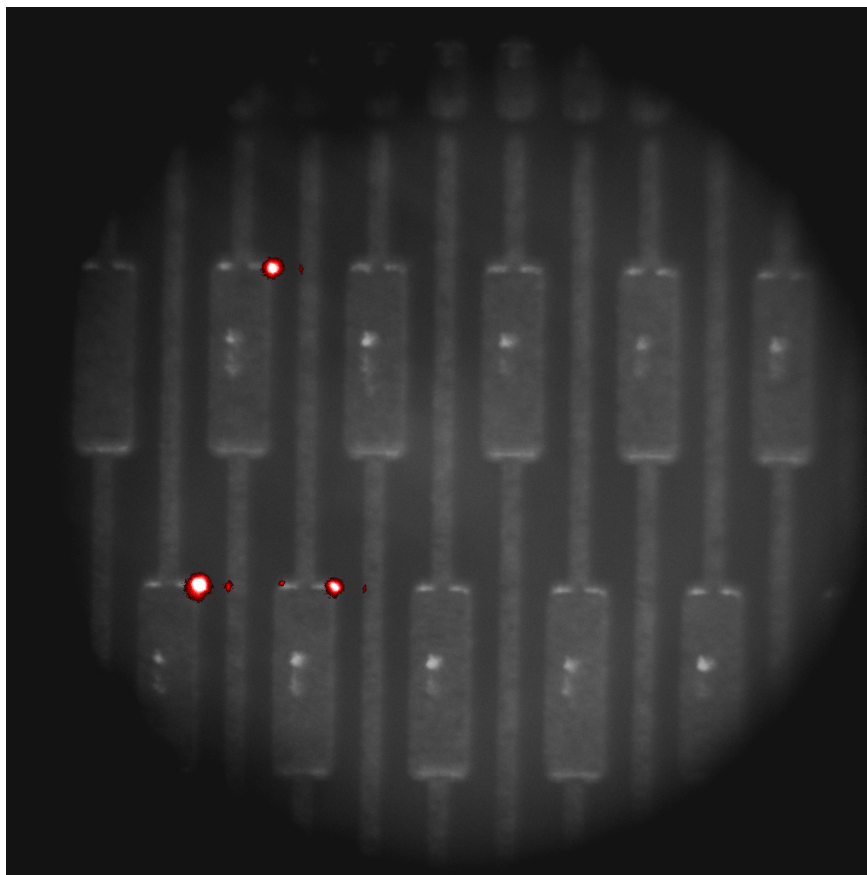


Fig. 5.7: Image of breakdown locations in sensor VPX12318-W608 produced by overlaying a visual image of the region with a SWIR photo of the same location. The visible region here are a group of neighbouring strips and their AC pads.

5.2.2 Humidity dependent breakdown characteristic

Since measurements with controlled humidity have to be performed in a closed environment, all subsequent measurements presented in this section were performed using an electrostatic discharge (ESD) safe and light-tight box which was subsequently modified to be airtight, but allow for N_2 inflow. By adjusting the nitrogen flow, RH levels below ambient can be easily achieved and disengaging the nitrogen inlet allows the humidity to slowly increase.

In Fig. 5.8 the results of IV scans performed on an A17 sensor with varying humidity are displayed. That particular sensor, W040, appeared to be within specifications during the initial IV and CV scans, but failed the current stability requirement due to breaking down after only a few minutes despite being tested in a dry atmosphere and with only minimal exposure to ambient humidity. All subsequent IV scans showed an early breakdown below -500 V. As can be seen in Fig. 5.8, breakdown occurs even earlier in damper conditions and some improvement can be achieved by testing in a dry atmosphere. But dry conditions alone are clearly not enough to revert the sensor back to its original behaviour, instead using them in conjunction with sensor training can lead to further improved performance. This

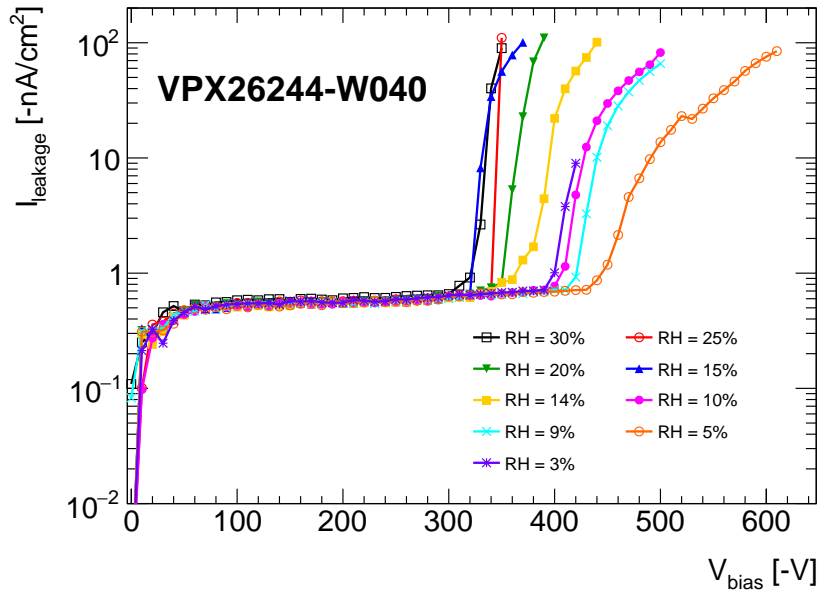


Fig. 5.8: IV curves of ATLAS17 sensors W040 during during a measurement sequence with decreasing humidity. The penultimate scan was performed with 10 min step interval to investigate whether sensor performance could be improved via sensor training, all others were conducted according to standard IV procedure with 10 s intervals.

effect goes so far that in subsequent tests even a full recovery was possible, however, the effect was not permanent as is already indicated in the regression between the IV scan with long and standard step intervals in Fig. 5.8.

To complement these observations, a leakage current stability test was performed on a different A17 sensor, W038, during which humidity was increased both steadily and abruptly to see whether there is a direct correlation between I_{leakage} and RH. According to the findings displayed in Fig. 5.9 this is clearly not the case at the voltage tested, which for that sensor is well below its $V_{\text{breakdown}}$. From this, it can be concluded that the previously reported cases of leakage current instability do not stem from a direct increase due to humidity, but rather are a consequence of a $V_{\text{breakdown}}$ shift. This would explain all observed cases:

- $V_{\text{breakdown}}$ of a stable sensor is still above the test voltage even after the shift in ambient environment, therefore they are unaffected
- fluctuating sensors have their breakdown shifted exceedingly close to the test voltage so that small fluctuations in the environment directly translates into a large increase in I_{leakage}
- sensors with increasing current have $V_{\text{breakdown}}$ shifted below the constant test voltage so that they are breaking down when tested, which can be exacerbated or mitigated depending on whether a particular sensor is prone to soft micro-discharge or hard avalanche breakdown

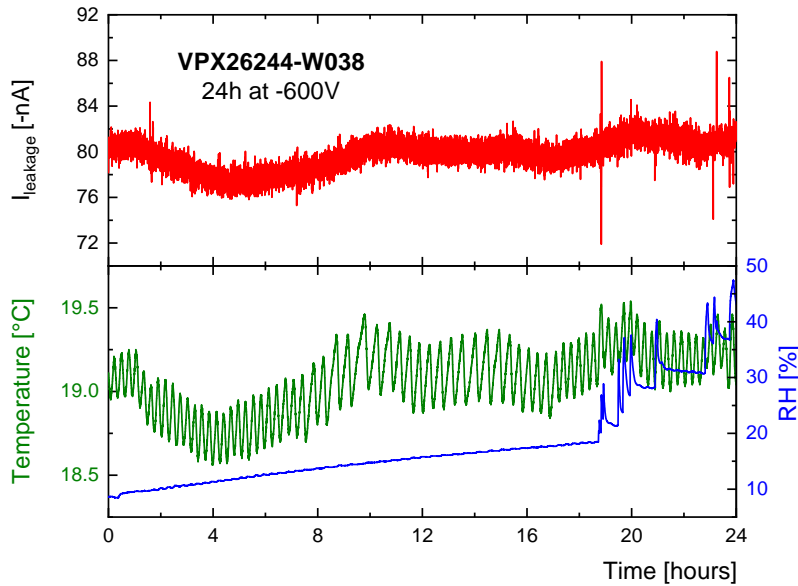


Fig. 5.9: Time development of I_{leakage} during a stability measurement with varying relative humidity (upper plot) and temperature-humidity monitoring over the course of that measurement (lower plot).

To perform a more systematic analysis of the dependence of humidity on sensor breakdown, a few hundred repeated IV scans over the course of multiple days were performed in the same airtight box. The chosen testing procedure required the sensor to be first stored and tested in dry conditions comparable to the usual storage in a desiccator with $\text{RH} < 5\%$. Afterwards, the nitrogen flush was reduced and subsequently completely stopped so that the relative humidity in the box slowly increased over time due to the innate existent, albeit small, gas exchange with the laboratory atmosphere. The IV scans themselves were performed automatically after a set time interval, thus depending on the rate at which humidity changes, this yielded redundant measurements for most RH values to check the consistency and stability of breakdown characteristics. Between individual scans the bias voltage was switched off to disentangle any potential biasing effects from the humidity dependence. The current limits of the supply was also purposely set fairly low, so that scans would be aborted shortly after the onset of breakdown, hence minimising the potential impact of hot electrons generated in the avalanche to affect the overall outcome.

Once the humidity inside the box reaches near-equilibrium values with the outside, a petri dish filled with a small amount of de-ionised water was placed inside the box. This measure allowed the investigation to also include RH values beyond ambient levels in order to complement the results. Depending on the observable breakdown shift, some sensors were also continued to be tested in a drying environment after removing the petri dish to see whether there were any discrepancies between IV curves obtained in a dampening or drying environment. This procedural cycle was also repeated multiple times for a few sensors to check the recovery ability of sensors and the consistency of results. $V_{\text{breakdown}}$ was again defined according to Eq. 5.1.

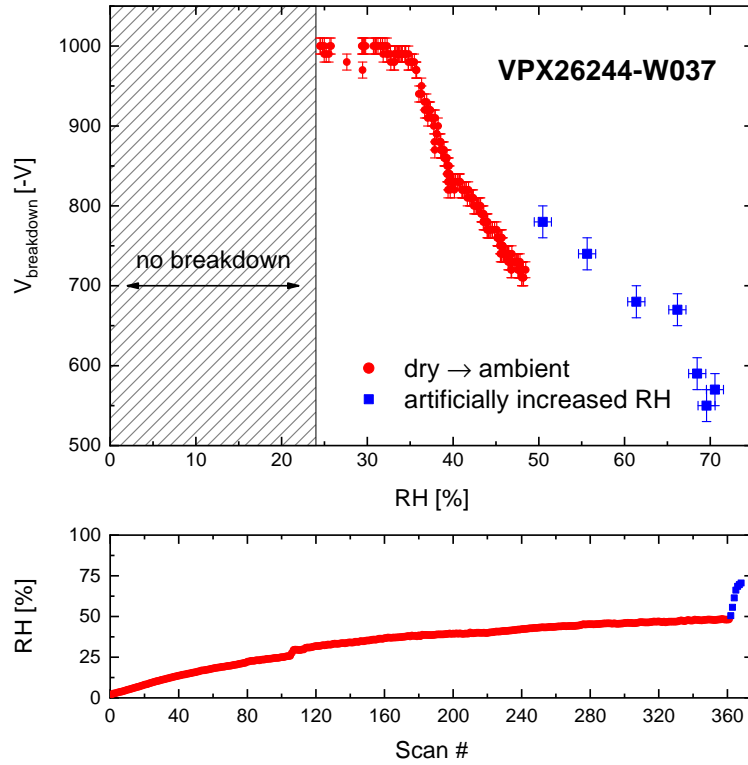


Fig. 5.10: Development of $V_{\text{breakdown}}$ for an ATLAS17LS sensor with varying relative humidity in the surrounding atmosphere obtained from repeated IV scans. The upper plot contains $V_{\text{breakdown}}$ versus RH while the lower plot shows the relative humidity during the respective IV scans. The colours in the legend apply to both.

Fig. 5.10 shows the results of a measurement sequence on an ATLAS17 sensor during which the humidity was gradually increased. As can be seen, $V_{\text{breakdown}}$ decreases consistently with increasing humidity. For $\text{RH} < 25\%$ no breakdown could be observed in the IV curves up to a maximum of -1000 V . However, similarly systematic results were difficult to produce on many sensors, in particular those which had already failed specifications due to low breakdown or leakage current instability. Instead, those sensors would mostly show a decreasing performance regardless of humidity level.

An exception to this is the A12 sensor W608 which was shown to have its breakdown occur in the strip region in the previous section (see Fig. 5.7). The outcome of the tests for that sensor in Fig. 5.11(a) shows a similar decrease of $V_{\text{breakdown}}$ at higher RH. But interestingly, performance improved after the first dampening cycle and remained that way for subsequent tests.

Because of the ongoing observations of deterioration of sensor performance as a consequence of the humidity sensitivity, despite all efforts to minimise exposure to ambient atmosphere, a few sensors of the last ATLAS17LS batch were fabricated with a Al_2O_3 *special passivation*. This passivation, albeit not possible to be used in the final ITk, served as an attempt to investigate possible ventures to

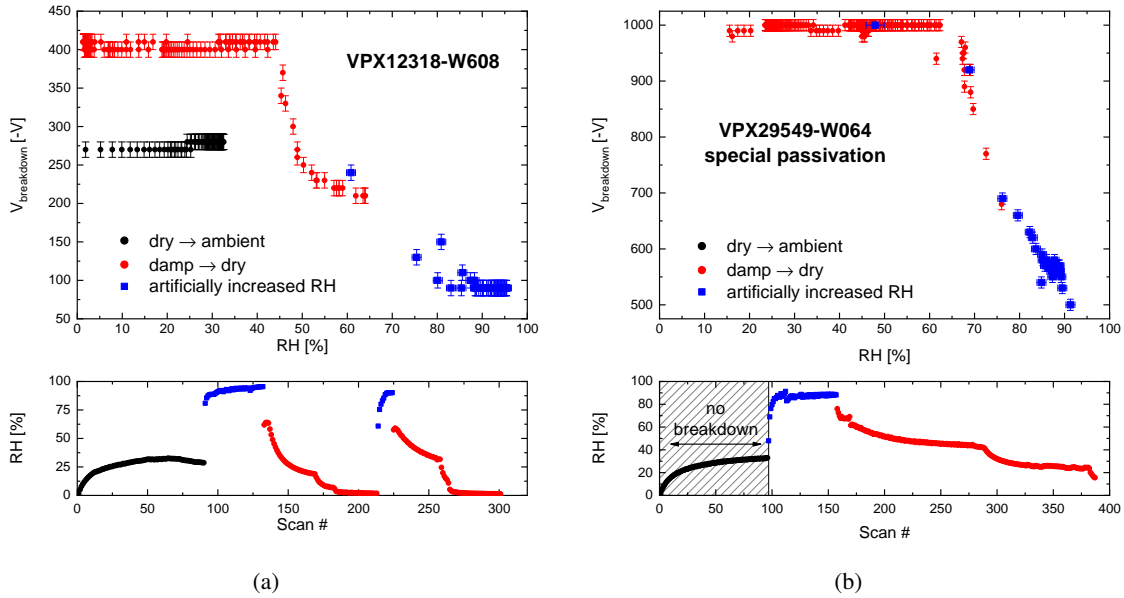


Fig. 5.11: $V_{\text{breakdown}}$ versus RH dependence for an A12 sensor with already low $V_{\text{breakdown}}$ (a) and an A17 sensor with special passivation layer (b).

mitigate humidity dependence for future applications. As demonstrated in Fig. 5.11(b), the tested sensor indeed performed much better compared to other sensors. Unlike those sensors which showed diminishing breakdown characteristic for relative humidity values at room temperature starting $\sim 30\% - 40\%$, that sensor did not show any significant decrease in breakdown before $\sim 60\% - 70\%$. At such high RH values, actual water condensation on the surface has already be taken into account considering the dew point.

Summary of findings

As shown in this section, there is a clear humidity sensitivity observable in ATLAS12 and ATLAS17LS sensors. The main conclusion is that a high relative humidity can lead to a significantly earlier breakdown when compared to tests in dry conditions. Therefore, $\text{RH} \gtrsim 20\%$ should be avoided during sensor tests, if possible, and the time in an ambient atmosphere should be minimised as far as practically manageable. While most of the sensors tested behaved in a systematic manner, where an increase in humidity resulted in a corresponding decrease in $V_{\text{breakdown}}$, others behaved more erratically. Also, for those more erratic sensors, depending on the history of prior measurements in a non-dry environment, solely low RH may not be enough to mitigate the early breakdown observed and it has to be accompanied by other treatments, e.g. sensor training.

Possible reasons for $V_{\text{breakdown}}$ degradation might be related to various convoluted effects in the oxide or at the interface. One effect might be oxide degradation due to humidity diffusion, as detailed in [76, 77]. As charge concentrations in SiO_2 may also change over time through the applied bias due

to high local electric fields, e.g. via hot-electron injection into the oxide [78], the basic physics of the observed behaviour is more complicated and further studies are needed to fully understand them.

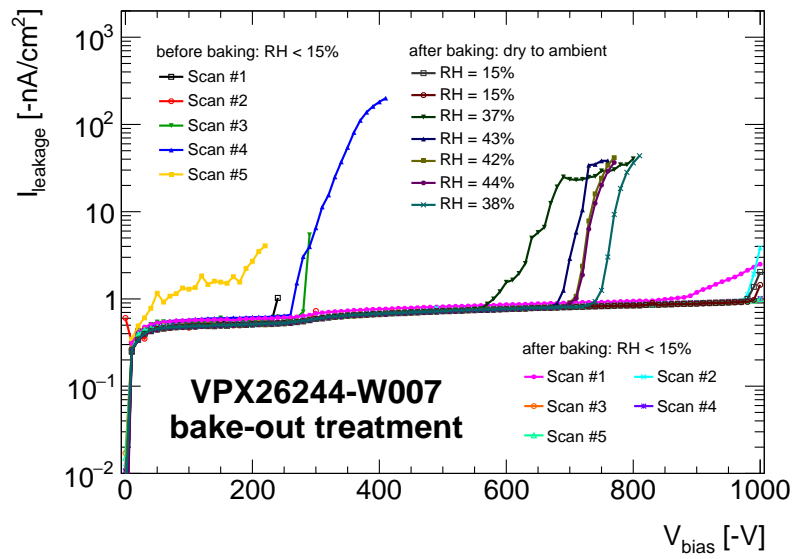
5.2.3 Sensor reconditioning treatments

From the results in the preceding section, it could be seen that not all sensors with a low breakdown voltage automatically recover in a dry environment or when stored in a desiccator over longer periods of time. In communication with the manufacturer three reconditioning treatments were proposed. The first two involved *cleaning* the sensor surface with either *isopropanol* or gas *plasma* to remove debris and organic dirt, which may be a cause of increased surface currents and even breakdown.

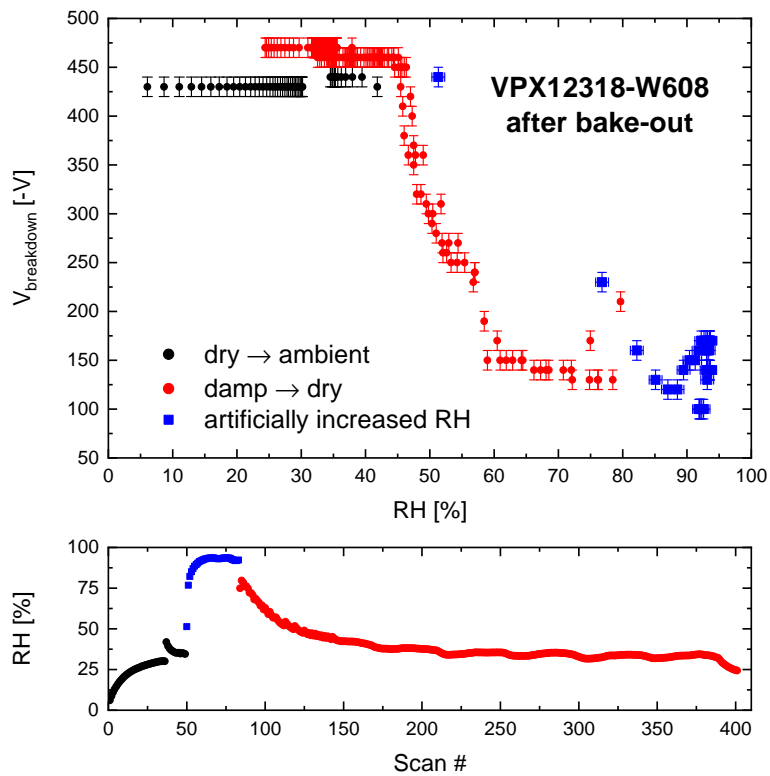
The final treatment, of which results will be reported below, requires baking out the sensor at 160°C for 24 h. This procedure was performed in Cambridge using a vacuum oven under a dry nitrogen environment of 0.5 atm pressure, which is a trade-off between lowering the water vapour partial pressure and accelerating the heat transport via convection. The underlying assumption for this procedure is that sensor stability is akin to a bistable state separated by a potential barrier. Transition between the two states is described by Boltzmann statistics, favouring the unstable state and being accelerated in the presence of humidity. Bake-out treatment is then expected to revert the sensor back to the stable state.

The results of the bake-out procedure used on two of the sensors which were previously seen to exhibit a low breakdown voltage are shown in Fig. 5.12. The sensors depicted here are exactly the ones for which an image of the breakdown location has been previously captured in Section 5.2.1. As can be seen for the first sensor shown in Fig. 5.12(a), which had its breakdown at the outer edge of the guard ring, the bake-out essentially (re)conditioned the sensor so that it now complied with the IV criteria. The sensor remained in that stable state for extended periods of time afterwards, provided that the humidity of the environment was low enough. Once the sensor was operated in ambient atmosphere, the IV characteristic deteriorated again, however, even then $V_{\text{breakdown}}$ was still much higher than before and did not show signs of further deterioration under those circumstances. The second sensor, with its breakdown in the strip region, benefited only marginally from the bake-out. The $V_{\text{breakdown}}$ versus RH plot in Fig. 5.12(b) shows that the overall behaviour with the $V_{\text{breakdown}}$ at high RH is still the same, the breakdown at low humidity now only occurs at higher voltages in general.

From these results it can be concluded that the bake-out procedure indeed provides a viable reconditioning treatment for sensors with low $V_{\text{breakdown}}$ after operation in environments with higher humidity. Its efficacy, however, seems to depend on the location of the breakdown, so that only those sensors which break down in the guard ring region truly benefit from bake-out. This could also indicate that breakdown in the strip region is not solely caused by humidity. As the number of thoroughly tested and subsequently treated sensors was very limited, this potential correlation has to be further investigated in future studies.



(a)



(b)

Fig. 5.12: Results of bake-out treatment for sensors where an image of the breakdown locations has been previously captured. (a) contains IV curves for A17 sensor W007 which had its breakdown at the guard ring edge, (b) is the $V_{breakdown}$ versus RH plot for A12 sensor W608 that broke down in the strips region.

5.3 Device simulations

The prevailing method used for modelling semiconductor devices is *Technology Computer-Aided Design* (TCAD). In TCAD one differentiates between several branches: the modelling of the fabrication process, the evaluation of the device electrical properties during discrete operation, and the simulation of the fully modelled device in an electric circuit configuration. The advantage of using sensor simulations to evaluate the results of measurements, or predict the characteristics in particular circumstances, lies in the versatility of TCAD and the models included within. These range from the simplest models to more complex ones which include convoluted effects from multiple sources. For that reason TCAD simulations are used, among others, to simulate the effects of radiation damage on devices. The software package used for obtaining the simulation results presented in the following section and the next chapter is the *Sentaurus TCAD* suite from Synopsys [79].

5.3.1 Synopsis Sentaurus TCAD suite

Fig. 5.13 shows the model of the strip region of an ITk microstrip sensor. Visible in the plots are the doping concentration of the n^+ -in-p device, the coupling and passivation SiO_2 , and the Aluminium electrode on top of the strip implant.

The modelling of such a device is done in *Process TCAD*, which can simulate standard manufacturing process steps like ion implantation, diffusion, oxidation, etching, and material deposition. The software suite allows 1D, 2D, and 3D process simulation and includes material tables which are calibrated to the latest experimental data. More simply, the device can also be modelled purely from geometric structural components depending on prior in-depth knowledge of the device or relying on information available from the manufacturer. In the Sentaurus package this kind of modelling is handled by the *Sentaurus Structure Editor* (SDE). SDE requires the geometric boundaries of the device to be defined first including the underlying material such as Si, SiO_2 , or others. Fixed doping concentrations like the native bulk doping are directly given and additional *doping profiles* are specified, which can include different mathematical operations, e.g. Gaussian or error functions. Those doping profiles are then applied to create surface implants or a highly doped backplane. In addition to the material properties, the electric contacts have to be implemented as part of the device editor or process model.

After modelling the device, either through its process flow or by giving its geometric outline and characterising the doping profiles, it has to be transformed into a number representative points on a grid for which the device operation is subsequently numerically simulated. This is done by creating a 2D or 3D *mesh* spanning the whole device. In Fig. 5.13 the generated mesh can be seen in the displayed region. Employing the meshing tool *Sentaurus Mesh* built in SDE, regions of interest in the device such as implants or interfaces between different materials are emphasised by creating a finer mesh with the smallest spacing between points in those regions.

After creating a model of the device and generating the mesh, the mesh file is then used in the device simulator *Sentaurus Device*. It models the device behaviour based on the solution of a set of

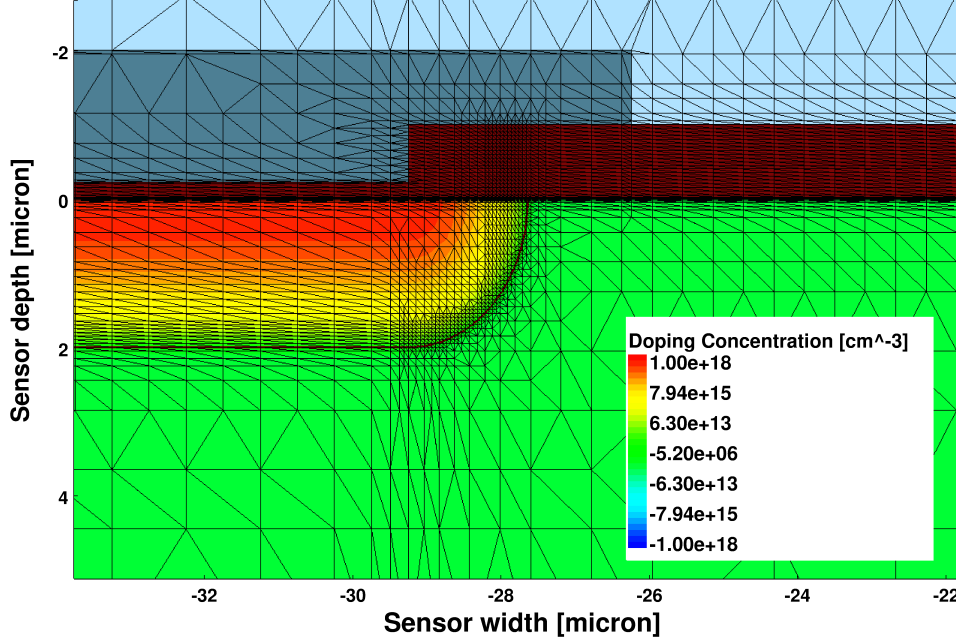


Fig. 5.13: Example of an AC-coupled readout strip of an n-in-p microstrip sensor modelled in SDE with its generated mesh.

partial differential equations on the discretised geometry provided by the mesh. For the simulation correct physics models which are applicable to the specific device have to be chosen. Options here include creating trap states or fixed charges in materials or interfaces, the application of specific recombination, mobility, and avalanche breakdown models, as well as the use of interaction with traversing charged particles or photons (see Section 3.1). The total number of models and their different parameters and options allow for adaptability many material properties and operational conditions. However, they also exponentially increase computing time if too complex, or unnecessarily many, physical models are incorporated.

The simulation itself is processed by using the boundary conditions given by doping concentrations in the device model and the boundary conditions at the electrodes and then solving the Poisson equation (see Eqs. 3.20, definition of symbols in Tab. 5.1)

$$\nabla \cdot (\epsilon \nabla \phi + \vec{P}) = -e(p - n + N_D - N_A) - \rho_{\text{trap}} \quad (5.2)$$

and the continuity equations which employs the drift-diffusion model for carrier transport

$$\begin{aligned} \nabla \cdot \vec{J}_n &= eR_n + e \frac{\partial n}{\partial t} & \text{with} & \quad \vec{J}_n = -ne\mu_n \nabla \phi_n \\ -\nabla \cdot \vec{J}_p &= eR_p + e \frac{\partial p}{\partial t} & \text{with} & \quad \vec{J}_p = -pe\mu_p \nabla \phi_p \end{aligned} \quad (5.3)$$

Tab. 5.1: List of symbols used in the device simulation formulas [80].

Symbol	Description
e	elementary electric charge
ϵ	electrical permittivity
ϕ	electrostatic potential
n, p	electron and hole density
N_D, N_A	concentration of donors and acceptors
ρ_{trap}	charge density of traps and fixed charges
\vec{P}	ferroelectric polarisation
\vec{J}_n, \vec{J}_p	electron and hole current density
R_n, R_p	recombination rate of electrons and holes
ϕ_n, ϕ_p	electron and hole quasi-Fermi potential

for every point in the mesh. The results of this computation are the electrostatic potential and the charge carrier current densities, as well as quantities derived from them, e.g. the electric field. In these equations, the electron and hole densities are calculated from either Boltzmann or Fermi statistics of the valence and conduction band.

5.3.2 Modelling ITk Strip Sensors

In order to properly model the ATLAS12 prototype sensors, the correct input parameters are needed to be utilised in Sentaurus Structure Editor. The ones used for the simulations presented in the following are summarised in Tab. 5.2.

The majority of the mechanical parameters which are easily verifiable by visual inspection, e.g. strip pitch and metal strip width, are taken directly from the sensor technical specifications [70] of the ATLAS12 generation. Most of the doping concentrations were assessed from the results of the sensor evaluation (see Chapter 4), mostly from the findings of capacitance measurements such as the active thickness. The thickness of the aluminium readout strip and the passivation layer were extracted from a scanning electron microscope image of a sensor. Other quantities which were not directly accessible, like the p-stop doping depth, were taken from previous sensor simulation efforts published in [62]. In preliminary simulations, these parameters were varied within reasonable margins and many were found to not influence the overall outcome of the simulation within those boundaries, e.g. the exact backplane concentration. The doping parameters of the bias rail, guard ring, and edge metal were assumed to resemble the strip doping for process conformity.

The physics models used in the device simulation were mostly those standard models used for silicon devices with a focus on breakdown investigations. As the simulations were performed with regards to unirradiated sensors, bulk traps were neglected and only a moderate positive oxide charge close to the interface was included.

Tab. 5.2: Input parameters for TCAD simulations of ATLAS12 prototype sensors.

Item	Value	Source
Si bulk	phys. thickness: 310 μm p-type: $5.2 \times 10^{12} \text{ cm}^{-3}$	Technical specification [70] C_{bulk} measurements
Strip implants	pitch: 74.5 μm width: 16 μm length: 23860 μm dop. depth: 2 μm n-type: $1 \times 10^{18} \text{ cm}^{-3}$	Technical specification [70] $C_{\text{bulk}} + R_{\text{implant}}$ measurements
p-stop	width: 6 μm p-type: $4 \times 10^{12} \text{ cm}^{-2}$ dop. depth: 1 μm	Technical specification [70] [62]
AC coupling Passivation	SiO ₂ : 250 nm SiO ₂ : 1 μm	C_{coupling} measurements SEM image and [62]
Al electrode	thickness: 1.75 μm strip overhang: 3 μm AC pad overhang: 20 μm	SEM image Technical specification [70]
Bias rail	doping: equals strips width: 63 μm inner overhang: 9 μm outer overhang: 27 μm gap to guard ring: 45 μm	estimate Tech. spec. [70] and visual inspection
Guard ring	doping: equals strips width: 18 μm inner overhang: 9 μm outer overhang: 32 μm gap to edge metal: 117 μm	estimate Tech. spec. [70] and visual inspection
Edge metal	dop. depth: 2 μm p-type: $1 \times 10^{18} \text{ cm}^{-3}$ width: 144 μm inner overhang: 54 μm gap to dice edge: 72 μm	estimate Tech. spec. [70] and visual inspection
Backplane	dop. depth: 5 μm p-type: $1 \times 10^{18} \text{ cm}^{-3}$	C_{bulk} measurements and [62] estimate

5.3.3 Sensor breakdown in device simulations

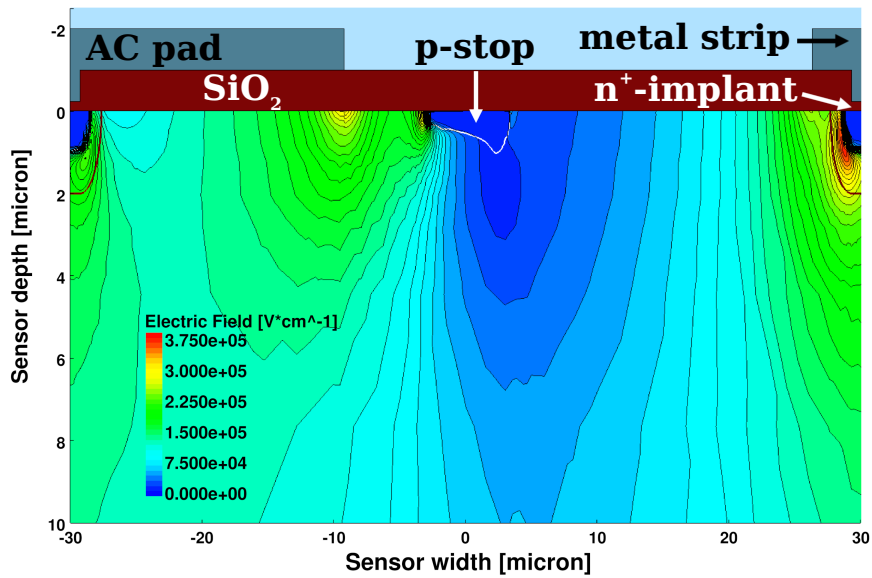
Using the parameters presented in the previous section, device simulations were performed for the case of ideal sensors, i.e. without assumptions as to how the effect of humidity influences the applied physics models or used device parameters. The goal of these simulations was to evaluate potential breakdown locations in the sensor layout and compare them to the results obtained from breakdown imaging (Section 4.9.1) for those sensors which clearly do not comply with ideal behaviour.

Fig. 5.14 shows the surface electric field of a simulated prototype sensor close to breakdown in the inter-strip region between an AC bond pad and the metal strip. As can be seen in the two-dimensional plot in Fig. 5.14(a), the electric field is highest directly at the Si/SiO₂ interface and at the depth of the strip implants. When looking at the electric field along a line directly at the interface and 1 μm below (Fig. 5.14(b)), the specific positions with the highest electric field become apparent. While the maximum in those plots is located $\sim 1 \mu\text{m}$ directly at the border of the implant on the side with the strip, on the AC pad side the highest E-field can be found at the interface due to the large metal overhang.

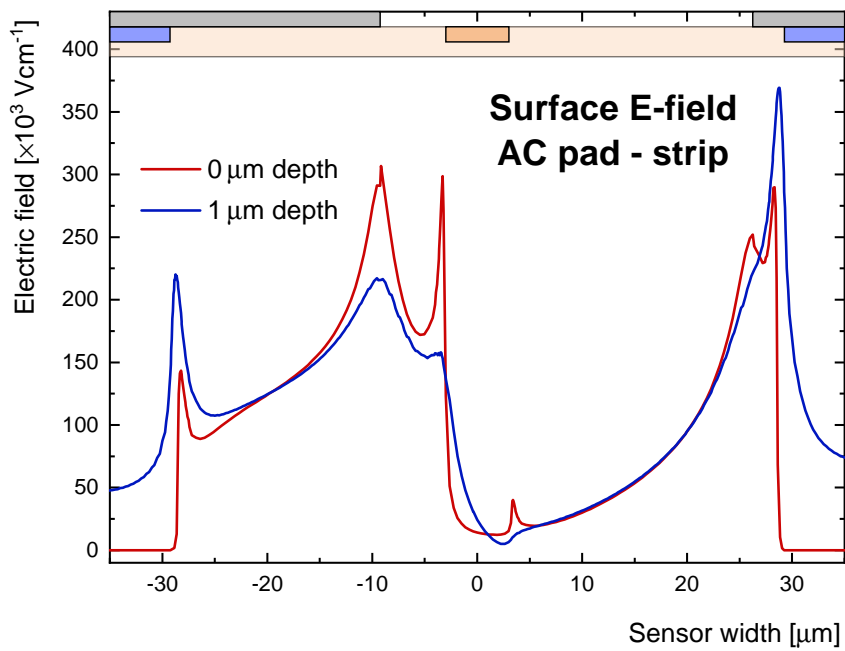
Recalling the breakdown locations in the SWIR image shown in Fig. 5.7, they were visible at the corner of multiple AC pads and the edge of the p-stops next to them. This corresponds to the two peaks shown in red curve of Fig. 5.14(b). Taking into account the true 3D structure of that region, this particular breakdown location can be explained by the higher concentration of field lines at the pad corner due to the transition between the configuration on the pad side towards the one on the strip side shown in the simulation.

Displayed in Fig. 5.15 is a similar selection of plots for surface electric field, but simulated for the edge structure of a sensor. As can be seen in both the 2D plot and the cross section at different depths, the peaks in the electric field are dominated by those at the edge of the respective metal overhangs.

However, in contrast to the SWIR breakdown image obtained for a sensor breaking down in the edge region (Fig. 5.6), the simulated ideal sensor shown here does not have its maximum electric field at the outer edge of the guard ring, but rather at the outer edge of the bias rail. The reason for this discrepancy could be that either the sensor model used for TCAD simulations is incomplete, or that for a non-ideal sensor with early breakdown its properties are changed in a way which leads to higher electric fields at the guard ring. The former could have been caused by the fact that the edge model for the sensor involves some assumptions with regards to the doping profile and concentrations for the bias rail, guard ring and edge implant. The latter would require a more precise understanding of the underlying physics which cause early breakdown in sensors and how to accurately model it in simulations. One way to gain a better understanding, e.g. as to whether the oxide and interface charge configuration changes as a consequence of the humidity sensitivity, would be through humidity-dependent measurements on test structures such as gated diodes.

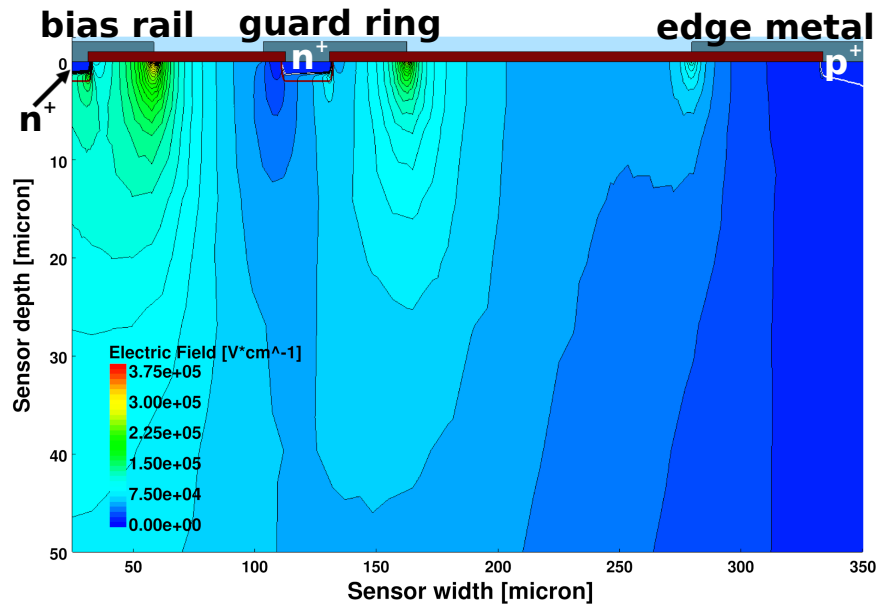


(a)

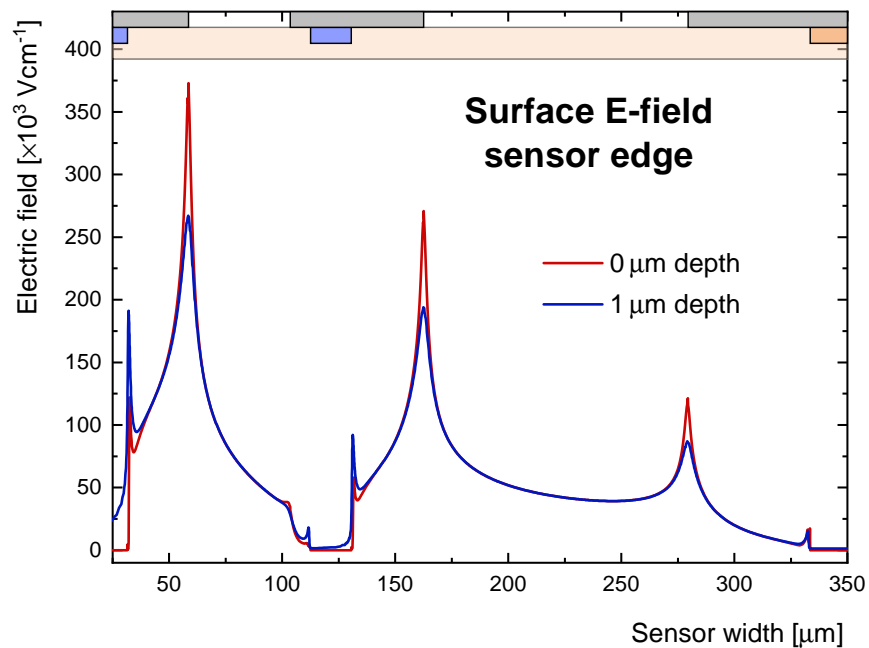


(b)

Fig. 5.14: Simulated electric field at the Si/SiO₂ interface and 1 μm below of an ideal sensor biased close to breakdown. The modelled sensor region reflect the breakdown previously imaged in the AC pad region.



(a)



(b)

Fig. 5.15: Simulated electric field at the Si/SiO₂ interface and 1 μm below of an ideal sensor biased close to breakdown. The modelled sensor region reflect the breakdown previously imaged at the sensor edge.

5.4 Summary and consequences for future sensor handling

As a consequence of the observed leakage current instability during prototype sensor evaluation, detailed investigations were conducted into the nature and causes, as well as the effects of electrical sensor breakdown. The focus was on mechanical stress and humidity as the potential origin, as well as TCAD simulation for in-depth studies of processes inside the sensor.

The results were that the breakdown voltage in IV measurements without constant bias voltage between individual scans is significantly reduced if the relative humidity of the testing environment increases to values $> 25\%$. If long-term biasing has a positive or detrimental effect on the development of the low $V_{\text{breakdown}}$ behaviour remains to be seen in future studies. Mechanical stress itself was not found to directly influence $V_{\text{breakdown}}$, but stress in the passivation layer could compromise its function through microscopic damage and hence exacerbate any humidity sensitivity. The importance of the passivation layer on the humidity dependence was ascertained by breakdown measurements conducted on sensors produced with a passivation specifically designed to mitigate or reduce those effects. Sensors, whose performance had presumably deteriorated by the extended exposure to a damp environment, were successfully reconditioned using a bake-out treatment in a vacuum oven. Whether this treatment procedure is viable for most sensors or specifically only for those which break down in the guard ring edge region, as indicated in the presented results, will have to be confirmed on a larger sample basis.

The conclusions of these findings are, firstly, that for Sensor QC during production (see Section 4.11) particular care has to be taken to only test sensors in a dry environment, if possible. For those tests which can only be conducted in ambient conditions, e.g. strip tests, the time exposed to ambient conditions should be as short as possible. Secondly, as sensor reconditioning is possible via bake-out, this could be used to counter the adverse effects accumulated during testing or handling in an ambient atmosphere. This could be done to ensure that those sensors are in pristine-like condition for module assembly, despite prior testing.

Chapter 6

Tracking reliability and the effects of long-term operation

Long-term reliability is one of the key issues in ITk sensor development. As has been shown in the previous two chapters, many prototype sensors, however, do not fulfil current stability criteria. Furthermore, the variability of test results, reported in Chapter 4 for example with regards to changes in IV curves, warrant an extensive scrutiny of both changes in sensor behaviour under long-term operation and the tracking reliability of prototype modules.

In this chapter, firstly, the observation of a significant and potentially consequential change in inter-capacitance is being reported and the characteristics of this change are outlined in Section 6.1. On the basis of specific properties of MOS capacitors a model of the underlying physics processes is then proposed for the observed effect, and a detailed explanation is given in Section 6.2. TCAD simulations to test and validate the developed model are presented in Section 6.3 and compared to the measurement results.

In the second part of this chapter, results on the long-term operation tracking reliability in testbeam campaigns at DESY and CERN are described. The findings are described in Section 6.5 after a brief introduction to the beam telescopes and testbeam sites in the preceding section.

To further investigate the findings, a novel application of Deep-Level Transient Spectroscopy (DLTS) is used to determine both temperature and humidity dependence of the observed effects. The third part of this chapter focuses on the particular DLTS application in Section 6.6 and the results obtained for the ITk prototype sensors at hand in Section 6.7.

6.1 Shift of C_{is} under long-term biasing

The input capacitance to front-end electronics, and hence the noise, is dominated by the inter-strip capacitance C_{is} . In order to study the effects of long-term biasing, repeated C_{is} measurements were performed with constant bias level V_{const} between individual C_{is} scans to emulate such long-term operation.

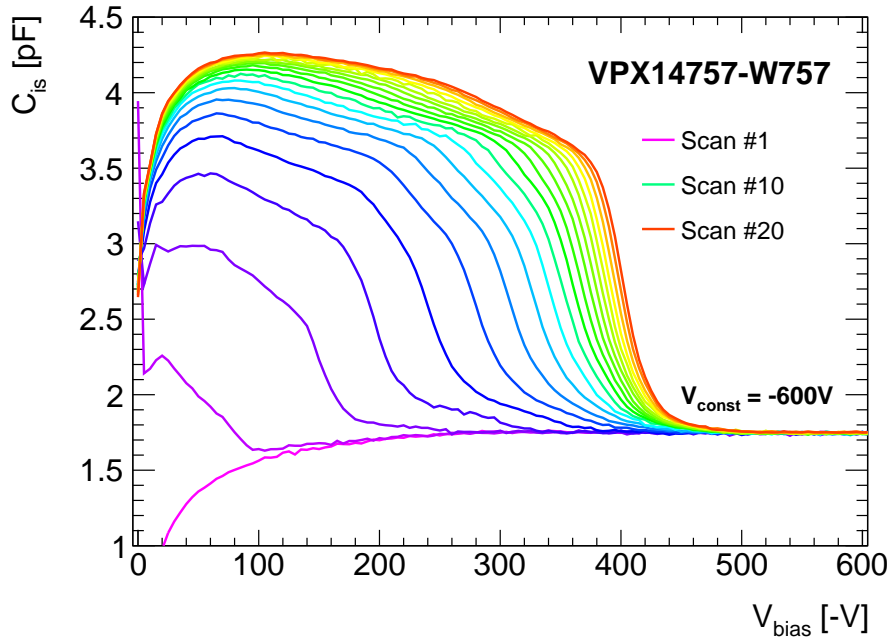


Fig. 6.1: Observed changes to inter-strip capacitance C_{is} versus bias voltage V_{bias} dependence under long-term biasing at a constant bias voltage V_{const} for 1 hour between individual scans.

The results on one ATLAS12 sensor displayed in Fig. 6.1 as an example show a continuous increase in C_{is} for bias voltage $V_{bias} < V_{const}$. In this plot and any of the following in this section showing C_{is} versus V_{bias} dependence, the colour gradient represents the progression in scan number under constant biasing. The C_{is} versus V_{bias} curves shown here are only for one of the many similarly tested sensors, but qualitatively identical results were obtained for sensors taken from all available prototype batches of the ATLAS12 sensor generation. Sensors tested under this procedure ultimately exhibit a plateau-like trend for low V_{bias} during the sweep for single C_{is} scans. Towards higher bias levels the plateau capacitance returns to its initial values in a steep flank, the tail of the flank, however, can vary in its form for individual sensors and even strips on each sensor. This signifies that even small variations present on each sensor can have an influence on the exact form of the curve, not the overall behaviour. The actual direction of the bias sweep does not affect the qualitative characteristic of the obtained curve, indicating a certain stability of the sensor state responsible for the C_{is} increase.

As becomes apparent from the curves shown, C_{is} increases continuously throughout the whole measurement sequence, however at the later stages this increase slows down and seems to *saturate*. For a clear picture of the time dependence seen here, the measured values at selected V_{bias} benchmarks have been plotted against the time at V_{const} in Fig. 6.2. From the curves shown in Fig. 6.2 the apparent saturation at different V_{bias} can be directly seen as well as the limit to which C_{is} is affected by long-term biasing. Capacitance values at low bias levels increase and saturate first, while at higher bias voltages they start doing so later and even from then on take longer to actually reach saturation. Close to V_{const} no change is observed.

6.1 Shift of C_{is} under long-term biasing

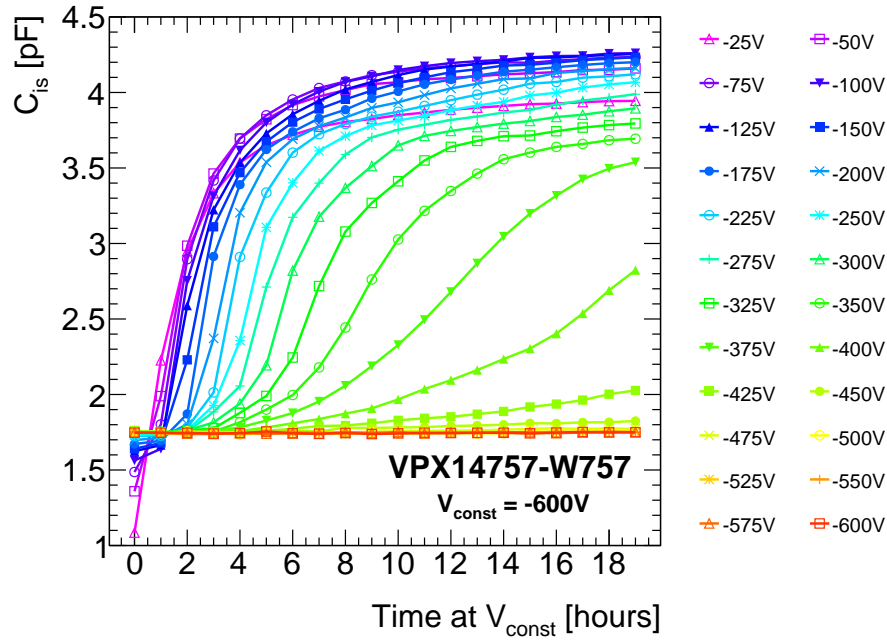


Fig. 6.2: Time dependence of measured C_{is} values when biasing the sensor at a constant voltage V_{const} for extended periods of time.

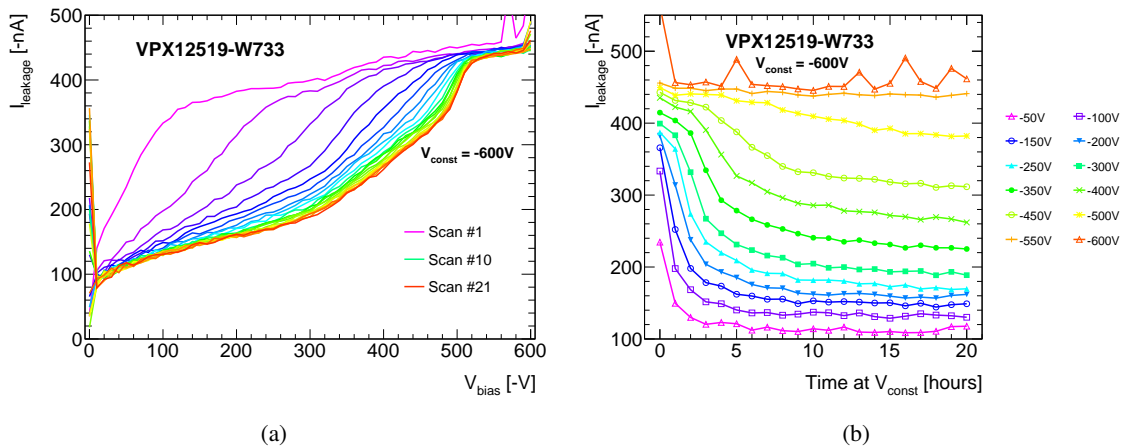


Fig. 6.3: Observed changes to IV characteristics under long-term biasing at a constant bias voltage V_{const} for 1 hour between individual scans (a) and time dependence of measured $I_{leakage}$ values (b).

Tracking reliability and the effects of long-term operation

This development is very similar to what has been noticed for IV curves of SCT sensors [81] and reported earlier in Section 4.9.1. When performing repeated measurements of the sensor leakage current where the sensor is biased at a constant level between the voltage sweep for individual scans, one can see a continuous decrease of leakage current until saturation, similar to the changes in capacitance for bias voltages $V_{\text{bias}} < V_{\text{const}}$. Fig. 6.3 contains plots of both the single IV curves and the time dependence of I_{leakage} for selected bias levels. The behaviour for IV curves appears to be in correlation with the corresponding C_{is} shift, as both only occur at $V_{\text{bias}} < V_{\text{const}}$, eventually saturate, but do so earlier and faster for values at lower bias.

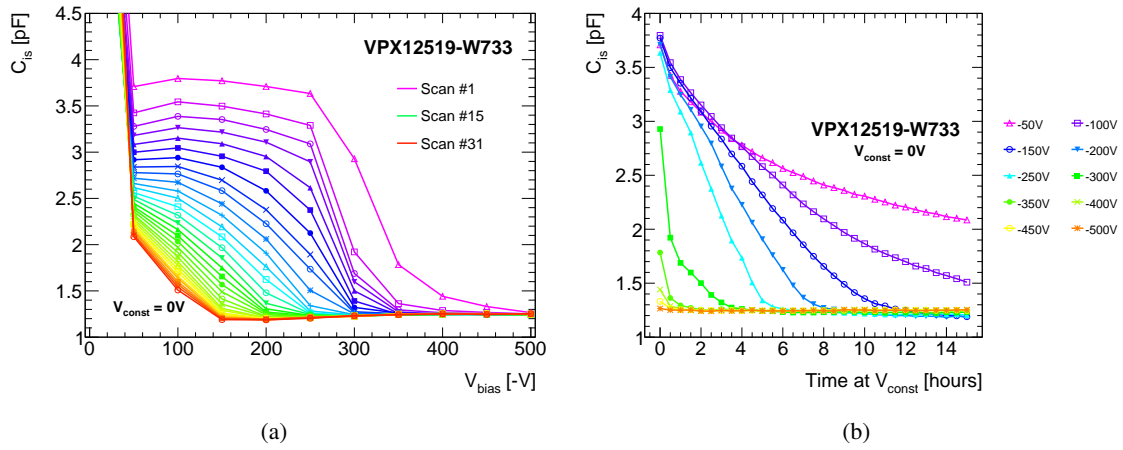


Fig. 6.4: Measured C_{is} values versus V_{bias} recorded during the recovery of hysteresis with an unbiased sensor (a) and their time dependence (b). The sensor has been biased for 4 h at -600 V prior to commencing the measurement.

With a shift of C_{is} to higher values simply by biasing a sensor for extended periods of time, one main concern has been the reversibility of it. To study the recovery of the C_{is} increase, a sensor which has been previously biased at $V_{\text{const}} = -600\text{ V}$ for 4 h has subsequently been kept unbiased while C_{is} scans were performed at regular intervals of 30 min. In order to keep the influence of the bias, which is necessarily applied during the scans, on the sensor at a minimum, only a few data points were taken every 50 V. The result is shown in Fig. 6.4 as both the accumulation of individual scans and the time dependence of C_{is} values. As becomes clear from the curves, the effect is fortunately fully reversible within $\mathcal{O}(10\text{ h})$ to a few days. This illustrates that the behaviour of observed C_{is} (and I_{leakage}) change constitutes a complete *hysteresis effect*.

The results indicate that only values $V_{\text{bias}} < V_{\text{const}}$ are causing the hysteresis. When increasing V_{const} during the measurement, as done in the measurement shown in Fig. 6.5(a), one can see that the visible *cut-off point* of affected measured capacitance is being shifted correspondingly to higher values. Moreover, the saturation value $C_{\text{is}}^{\text{sat}}$ also increases, demonstrating a dependence on V_{const} . This particular dependence has subsequently been obtained for a sensor in Fig. 6.5(b), the exact results of which will be important for assessing the dynamics of the underlying processes in Section 6.7.

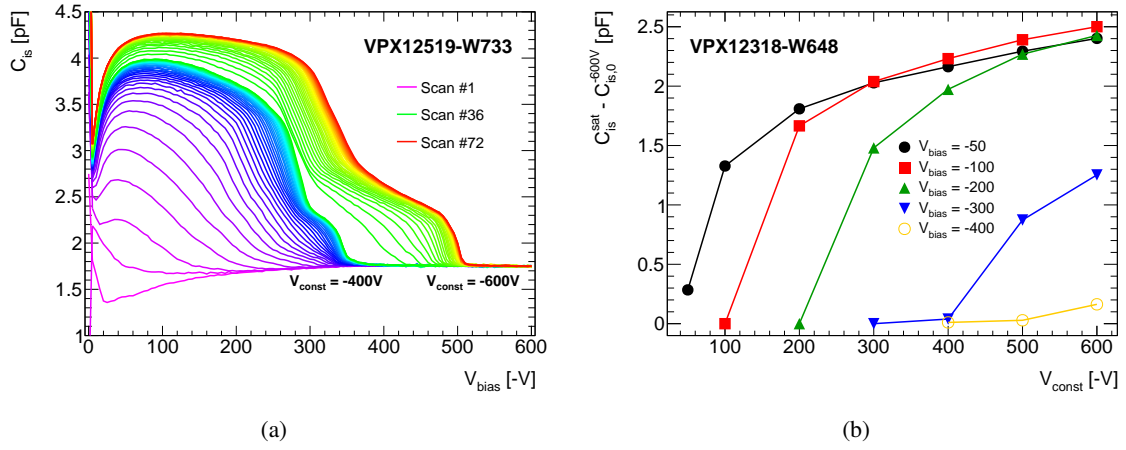


Fig. 6.5: (a): Increase of C_{is} observed in repeated measurements over more than 70 h with $V_{const} = -400V$ for the first and $V_{const} = -600V$ for the second half of the time. (b): Difference of saturation and baseline values $C_{is}^{sat} - C_{is,0}^{-600V}$ at different V_{bias} benchmarks versus applied V_{const} levels.

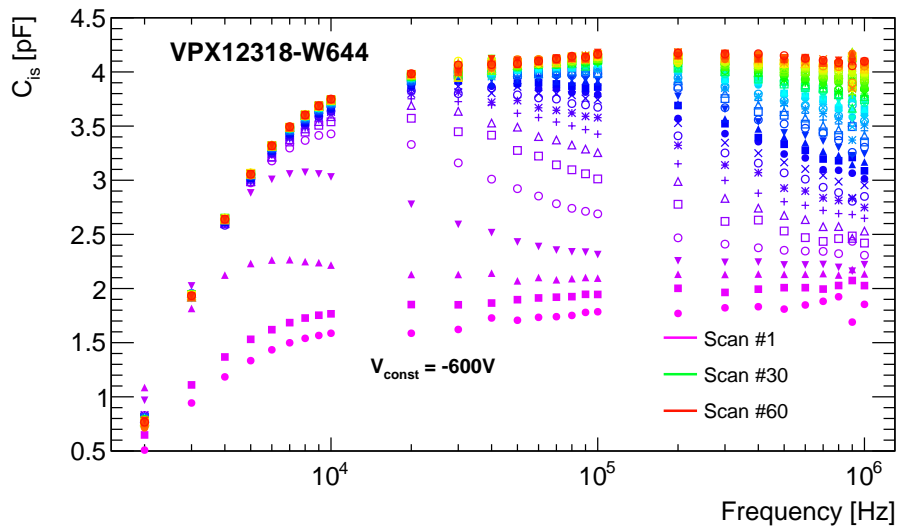


Fig. 6.6: Frequency dependence of C_{is} hysteresis for values measured at $V_{bias} = -250 V$.

Tracking reliability and the effects of long-term operation

In the previously shown results in Sections 4.5.2 and 4.6.1, there was a distinct frequency dependence of all capacitance measurements. To verify the observed hysteresis effect and investigate the frequency range in which it can be observed, frequency sweeps were performed during the measurement procedure in several instances and are plotted in Fig. 6.6 for C_{is} ($V_{bias} = -250$ V). The capacitance increase is present for all AC voltage frequencies $f \gtrsim 10$ kHz and therefore for all frequencies typically used for C_{is} measurements. At lower frequencies saturation occurs earlier than at higher frequencies, with comparable saturation values.

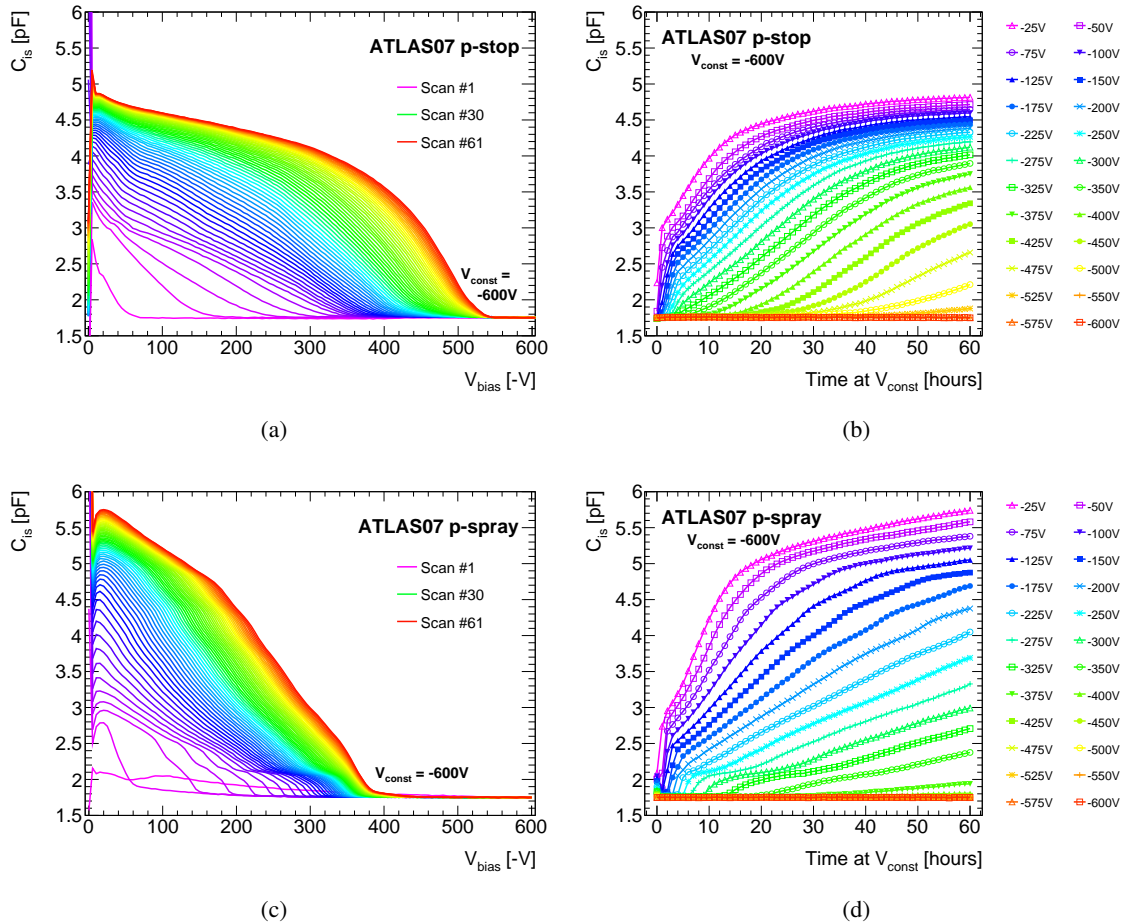


Fig. 6.7: Comparison of C_{is} versus V_{bias} hysteresis feature (a,c) and their time dependence (b,d) for two ATLAS07 sensors with p-stop and p-spray strip isolation structures, respectively.

One key aspect to the measured inter-strip capacitance is the layout of the sensor inter-strip region. While the latest generations of prototype sensors with the ATLAS12 and ATLAS17LS all have very similar inter-strip isolation involving narrow common p-stop structures between each strip implant, the previous generation of ATLAS07 sensors offer a broader variation, as the layout for the finalised version of the ITk Strip Sensors was still being evaluated (see Section 4.1). The characteristic features of C_{is} hysteresis on two ATLAS07 sensors with p-stop and p-spray isolation are displayed in Fig. 6.7.

6.2 Characterisation of long-term biasing effects on the sensor surface

The final trend of the p-stop sensor in saturation in Fig. 6.7(a) is more like that of the A12 sensors, exhibiting a plateau from which C_{is} falls off fairly steeply to the initial values beyond the cut-off point dictated by V_{const} . In contrast to this, the p-spray sensor in Fig. 6.7(c) does not show a plateau and instead only has an almost constant flank between its maximum at low V_{bias} and the cut-off point. The time development of C_{is} saturation of both A07 sensors shown in Fig. 6.7(b,d) looks similar to the A12 samples.

To gain a better understanding of the observed increase in C_{is} that could potentially increase noise, a model was developed to explain the sensor behaviour as well as study further consequences which could arise from it.

6.2 Characterisation of long-term biasing effects on the sensor surface

Due to the intricate inter-strip or inter-pixel structure, inter-strip (inter-pixel) capacitance is not trivial to determine as there is no suitable model providing an analytical solution for a microstrip or pixel sensor. When measuring C_{is} from the AC contacts one has to take into account the physical layout of the sensor and its inherent capacitances displayed in Fig. 6.8 as the cross section of an inter-strip region. There are four main components for the capacitance between strip i and its neighbour j [82], namely the capacitance between:

1. neighbouring n^+ strip implants ($C_{I_i-I_j}$)
2. adjacent metal strips $C_{M_i-M_j}$
3. the top metal of strip i and strip implant j and vice versa $C_{M_i-I_j}, C_{M_j-I_i}$
4. the metal and the implant on the same strip which is just the AC coupling capacitance $C_{M_i-I_i}, C_{M_j-I_j} = C_{coupl}$

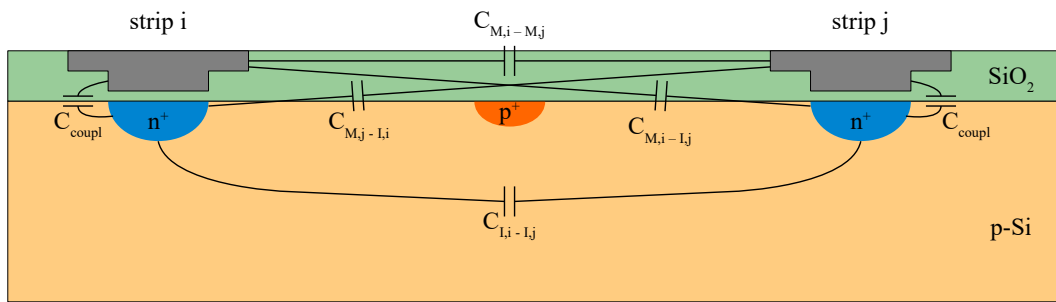


Fig. 6.8: Schematic cross section of an inter-strip region (not to scale) showing the different contributions towards C_{is} .

From this one can arrive at the expression

$$C_{is} = C_{M_i-M_j} + 2 \left(C_{M_j-I_i}^{-1} + C_{M_i-I_i}^{-1} \right)^{-1} + \left(C_{I_i-I_j}^{-1} + 2C_{M_i-I_i}^{-1} \right)^{-1} \quad (6.1)$$

for the measured inter-strip capacitance. The capacitance between the depleted region underneath the strip implant and the backplane acts as a stray capacitance to C_{is} with a frequency response akin to a low-pass filter, thus making C_{is} measurements impossible for AC voltage frequencies $f < 10$ kHz (see Section 4.6.1). Given that the coupling capacitance is more than an order of magnitude larger than the other components $C_{M_i-I_i} = C_{coupl} \gg C_{is}$, Eq. 6.1 is simplified to [82]

$$C_{is} = C_{M_i-M_j} + 2C_{M_j-I_i} + C_{I_i-I_j} \quad . \quad (6.2)$$

In Eqs. 6.1 and 6.2, $C_{M_j-I_i}$ and $C_{I_i-I_j}$ inherently depend on the charge distribution of the Si/SiO₂ interface. Therefore, an explanation of the observed C_{is} hysteresis lies in the changes of the oxide and interface.

6.2.1 Surface states at the oxide interface

Silicon oxide is used in ITk sensors as both an insulating layer to protect the underlying diode structure and as a coupling dielectric in a *metal-oxide-semiconductor* (MOS) structure for AC-coupled readout. As first postulated and analysed by Tamm [83] and Shockley [84], the transition from ordered crystal lattice in a semiconductor to a different material like an oxide layer is a discontinuity of the periodic structure and its resulting charge carrier bands and will lead to the formation of dangling or unsaturated bonds at the interface. Here, the interface region will result in *surface states*, as is the case for any discontinuity at a semiconductor surface. Such bonds and any incorporated defects or impurities will be localised states in the interface to act as charge traps.

Four states of the silicon surface depending on the type and amount of oxide charges close to the interface can be derived, all of whom are depicted in Fig. 6.9 for a p-type silicon substrate. This description can be similarly applied to a full MOS structure where an external bias is applied to the metal in order to influence the surface states. This is the working principle of the *Metal-Oxide-Semiconductor Field-Effect-Transistor* (MOSFET).

In the ideal situation of no charges present, the energy bands will remain flat, which is referred to as the *flat-band case* (Fig. 6.9(a)). Here, the Fermi level E_F is constant throughout the semiconductor as it is in thermal equilibrium and the oxide as an insulator does not conduct any current. If negative oxide charges are present or, in MOS structures, a negative external bias is applied, the electric field and potential difference will induce an upwards bending of the silicon energy bands. Thus, the valence band E_v edge is closer to the Fermi level at the Si/SiO₂ interface than compared to the bulk material, implying the *accumulation* of holes (Fig. 6.9(b)). In the case of thermal oxide grown on semiconductors the resulting interface produces donor states which yield a positive oxide charge close to the interface. The consequence is a downwards bend of the conduction and valence band edge similar to a p-n junction (compare with Fig. 3.7 in Section 3.3.1) and similarly this creates a *space charge region* of width x_d (see Fig. 6.9(c)). If an even larger amount of positive oxide charge is present, the bands will bend even further and the space charge region will grow to a point where the intrinsic Fermi level E_{Fi} at the surface is below the Fermi level, as shown in Fig. 6.9(d). The surface in

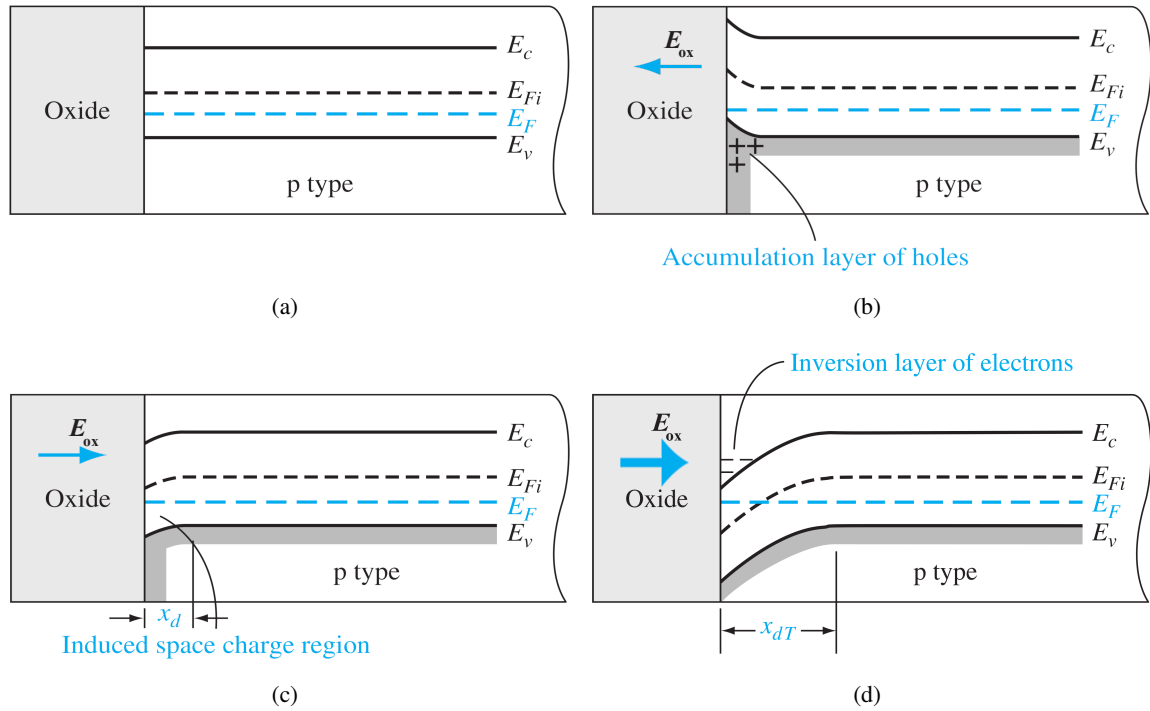


Fig. 6.9: Energy band diagram of an oxide/semiconductor interface with p-type substrate: (a) ideal flat-band case without oxide charges present, (b) negative oxide charges (or external bias voltage) induce a positive accumulation layer, (c) electric field \vec{E}_{ox} from positive oxide charges create depletion layer at the interface, (d) strong electric field from a large number of positive oxide charges invert the interface layer (adapted from [85]).

the semiconductor adjacent to the interface now has the conduction band E_c closer to the Fermi level than the valence band which implies an *inversion* of the p-type silicon to an n-type semiconductor. This electron *inversion layer* would short n-implant strips in a p-type silicon bulk, which is the reason for having p-stop between strips as an isolation structure (see Section 4.1).

Under normal circumstances, the outside oxide surface has no electric field component normal to the surface and therefore no charge present as the oxide has a high dielectric constant ($\epsilon_{ox} = 3.9$ [85]). However, measurements have shown that this is only true immediately after application of the bias voltage to an initially unbiased detector. If the detector is biased for long periods of time, the surface will assume the same potential as the neighbouring metal strips through the small *surface conductivity* on the outer oxide layer [86]. Therefore, the oxide dielectric and passivation layer of the ITk microstrip sensors can be viewed as being equivalent to an n-channel MOSFET with the charge distribution at the interface and the resulting inter-strip capacitance depending on the CV characteristic of such a device. In the following paragraphs the CV characteristic of a MOS structure are described and how its trend relates to the observed C_{is} hysteresis.

6.2.2 CV characteristic of an equivalent MOS structure

To get a complete picture of the capacitance of a MOS structure, one has to differentiate between the states of the interface described in the previous section. Depending on the interface conditions, different effects contribute towards the total MOS capacitance. A detailed explanation found in [85] is adapted to the given case.

Accumulation

One component is the oxide capacitance C_{ox} defined by the electric contact on the outside layer of the oxide and separated from the silicon by a dielectric of thickness W_{ox} . This corresponds to the AC coupling capacitance in strip sensors and is modelled by a simple parallel plate capacitor yielding

$$C'_{ox} = \frac{\epsilon_{ox}\epsilon_0}{W_{ox}} \quad . \quad (6.3)$$

For this quantity and any following capacitance or charge, the prime indicates the magnitude per unit area. If a MOS structure operates under accumulation conditions, a small differential change of the voltage across it will cause a differential change in the charge on both the metal contact and correspondingly in the accumulation layer mediated by the dielectric between them. As such, the capacitance in that case is just equal to the oxide capacitance $C'_{acc} = C'_{ox}$.

Depletion

A MOS structure in depletion is similar to a p-n junction that induces a space charge region (SCR) adjacent to the Si/SiO₂ interface. The corresponding energy band diagram is shown in Fig. 6.10(a). The *surface potential* ϕ_s is the potential difference between the energy levels of bands in the bulk material and at the surface and describes the band bending. The relation between the surface potential and the energy difference ϕ_{fp} between the Fermi level E_F of the doped and intrinsic semiconductor E_{Fi} define the transition from depletion to inversion with

$$\phi_{fp} = E_{Fi} - E_F = V_{th} \ln \left(\frac{N_A}{n_i} \right) \implies \phi_{fp}^{A12} \simeq 0.151 \pm 0.001 \text{ V} \quad , \quad (6.4)$$

where $n_i(T = 300 \text{ K}) = 1.5 \times 10^{10} \text{ cm}^{-3}$ [85] is the *intrinsic carrier concentration* in silicon and $V_{th} = k_B T / e$ the *thermal voltage*. Similar to Eq. 3.23 the *space charge width* x_d is calculated according to

$$x_d = \sqrt{\frac{2\epsilon_{Si}\epsilon_0\phi_s}{eN_A}} \quad . \quad (6.5)$$

For n-in-p microstrips, Si/SiO₂ interfaces at varying degrees of depletion is the usual initial state of sensors due to the presence of positive oxide charges.

6.2 Characterisation of long-term biasing effects on the sensor surface

The capacitance per unit area in a depleted surface state $C'_{SD} = \epsilon_{Si}\epsilon_0/x_d$ is solely dependent on the extension of the space charge region x_d and decreases with it. The total capacitance during depletion is a series combination of C'_{ox} and C'_{SD} and hence

$$C'_{depl} = \frac{C'_{ox}C'_{SD}}{C'_{ox} + C'_{SD}} = \frac{\epsilon_{ox}\epsilon_0}{W_{ox} + \left(\frac{\epsilon_{ox}}{\epsilon_{Si}}\right)x_d} \quad (6.6)$$

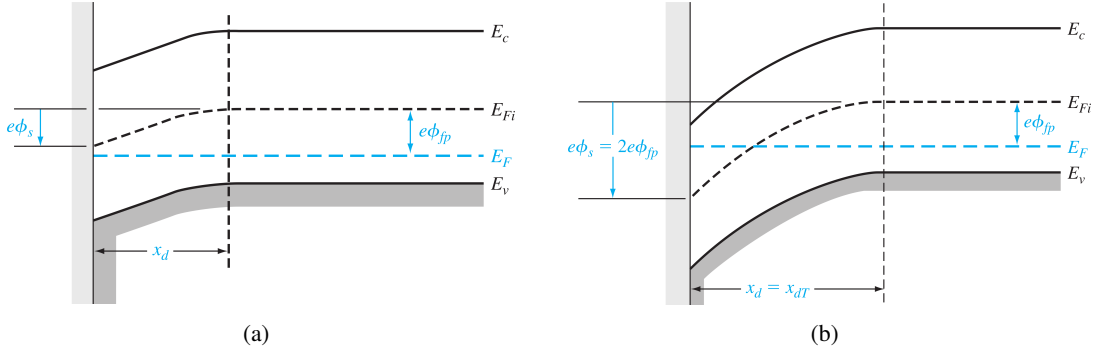


Fig. 6.10: Energy band diagram for a p-type Si/SiO₂ interface under depletion (a) and inversion (b) conditions indicating the surface potential and the space charge width [85].

Inversion

The inversion case of a surface is depicted in Fig. 6.10(b). For this the condition for the *threshold inversion point* is defined as $\phi_S = 2\phi_{fp}$, which results in an electron concentration at the surface equal to the hole concentration in the bulk. Further increasing the surface potential beyond the threshold, will cause the conduction band to bend only slightly closer to the Fermi level. However, the electron concentration at the surface is now an exponential function of the surface potential similar to the description for the majority carriers in the inverted type of the semiconductor. For p-type silicon, the density of the electron inversion layer n_s can thus be written as

$$\begin{aligned} n_s &= n_i \exp\left[\frac{e(\phi_{fp} + \Delta\phi_s)}{k_B T}\right] = n_i \exp\left[\frac{\phi_{fp} + \Delta\phi_s}{V_{th}}\right] \\ &= n_{st} \exp\left(\frac{\Delta\phi_s}{V_{th}}\right), \quad \text{with } n_{st} = n_i \exp\left(\frac{\phi_{fp}}{V_{th}}\right), \end{aligned} \quad (6.7)$$

where $\Delta\phi_s$ is the surface potential greater than $2\phi_{fp}$ and n_{st} the surface charge density at the point of inversion. As there is no current through the oxide, the electron inversion layer is created through the thermal generation of charge carriers. In thermal equilibrium an increase in the surface potential can increase the electron concentration by orders of magnitude, but the space charge width has essentially

Tracking reliability and the effects of long-term operation

reached a maximum width x_{dT} given by

$$x_{dT} = \sqrt{\frac{4\epsilon_{Si}\epsilon_0\phi_{fp}}{eN_A}} \implies x_{dT}^{A12} \simeq 8.7 \pm 0.2 \mu\text{m} \quad . \quad (6.8)$$

The threshold inversion point is defined to be the condition when the maximum depletion width is reached. But since there is essentially zero inversion charge density at the inversion point, this condition will yield a minimum capacitance of

$$C'_{\min} = \frac{\epsilon_{ox}\epsilon_0}{W_{ox} + \left(\frac{\epsilon_{ox}}{\epsilon_{Si}}\right)x_{dT}} \quad . \quad (6.9)$$

In the limit of an ideal strong inversion in thermal equilibrium, the space charge width is constant. An incremental change in voltage will result in a differential change in charge density of the inversion layer, if the inversion charge can respond to the frequency of the applied change in voltage. For MOS structures one has to differentiate between a low-frequency and a high-frequency case of the CV characteristic under inversion condition. In the low-frequency limit, the capacitance is again just the oxide capacitance, while at high frequencies the capacitance only depends on the space charges. From the typical frequency limits of these cases with $f_{HF} \gg 1 \text{ kHz}$ [87], it can be concluded that in C_{is} measurements the contribution of the inversion layer itself can be neglected, especially since very low frequencies cannot be used with the given setup and samples due to the capacitance to the backplane. Also, as observed in the frequency dependence of the hysteresis effect (see Fig. 6.6), the C_{is} increase happens throughout the whole applicable frequency spectrum ($f \geq 10 \text{ kHz}$) with a similar saturation value for all frequencies. The transition region between the initial inversion threshold and quiescent strong inversion, which is dominated by changes in the electron density of the inversion layer, is referred to as *moderate inversion* and denotes the combined contribution from the space charge region and inversion layer.

Flat-band and threshold voltage

In a normal MOS structure, the flat-band case is usually not achieved at zero gate voltage. The reason for that is the inherent difference between the *work function* ϕ_m in the metal and the *electron affinity* χ in silicon and χ_i in the oxide, which describe the potential difference to the vacuum level, as depicted in Fig. 6.11(a). As the Fermi level has to be a constant within the system when in contact, this difference causes a band bending even without any voltage applied to the metal or presence of oxide charge. Using the quantities displayed in Fig. 6.11(b) one can relate the surface potential ϕ_s , potential drop across the oxide V_{ox} , and *metal-semiconductor work function difference*

$$\begin{aligned} V_{ox0} + \phi_{s0} &= -\phi_{ms} \\ \phi_{ms} &\equiv \left[\phi'_m - \left(\chi' + \frac{E_g}{2e} \pm \phi_{fp,fn} \right) \right] \quad , \end{aligned} \quad (6.10)$$

where ϕ_{fp} and ϕ_{fn} are the respective quantities for p or n-type silicon.

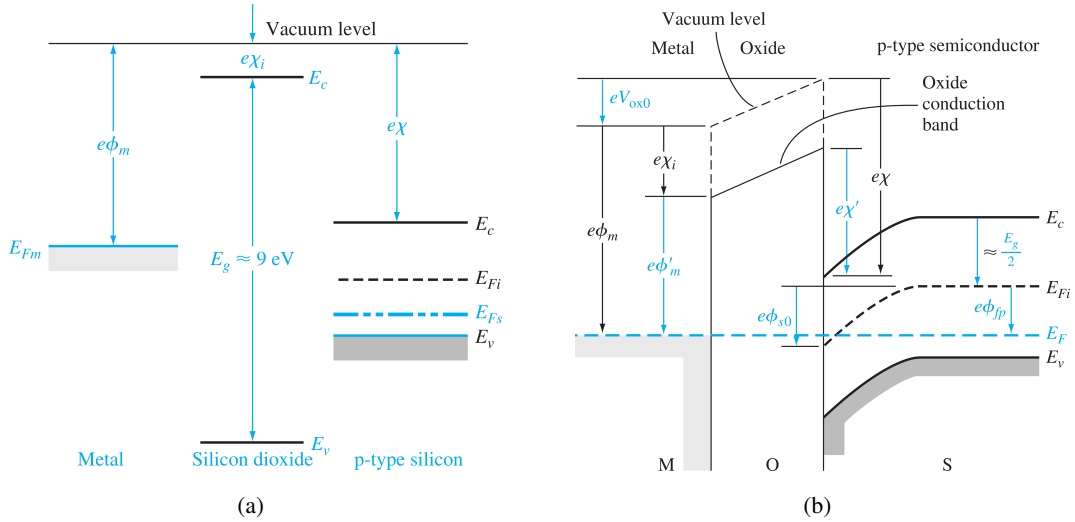


Fig. 6.11: Energy band diagram of a MOS system prior to (a) and in thermal equilibrium after contact (b) showing all relevant quantities [85].

Due to the work-function difference, in order to reach flat-band condition a non-zero voltage has to be applied to the metal, the so-called *flat-band voltage* $V_{FB} = \phi_{ms}$. The more realistic case with the presence of oxide charge, which is also the inherent situation of ITk sensors, and their effect on the flat-band voltage is discussed in Section 6.2.3.

In a similar way the voltage at which the inversion threshold is reached can be defined. At the threshold a maximum value of the space charge at the silicon surface is reached which has to be matched with an equal charge on the metal contact through the oxide capacitance, again, when ignoring oxide charge for now. Additionally, the surface potential has to be at the threshold of inversion with $\phi_s = 2\phi_{fp}$, all of which results in a *threshold voltage* for p-type bulk silicon according to

$$V_T = |Q'_{SD}(\max)| \left(\frac{W_{ox}}{\epsilon_{ox}\epsilon_0} \right) + \phi_{ms} + 2\phi_{fp} \quad (6.11)$$

CV curve of ideal MOS structures

Using the flat-band and threshold voltage as demarcation points, and the capacitance values at different surface states as boundaries, one can derive the ideal capacitance versus applied gate voltage curve of a MOS capacitor with p-type silicon substrate displayed in Fig. 6.12. The three components C'_{ox} , C'_{SD} , and C'_{min} are depicted by dashed lines. Apart from the moderate inversion which marks the transition between maximum depletion and strong inversion limits, the capacitance in flat-band condition lies in the transition between accumulation and depletion.

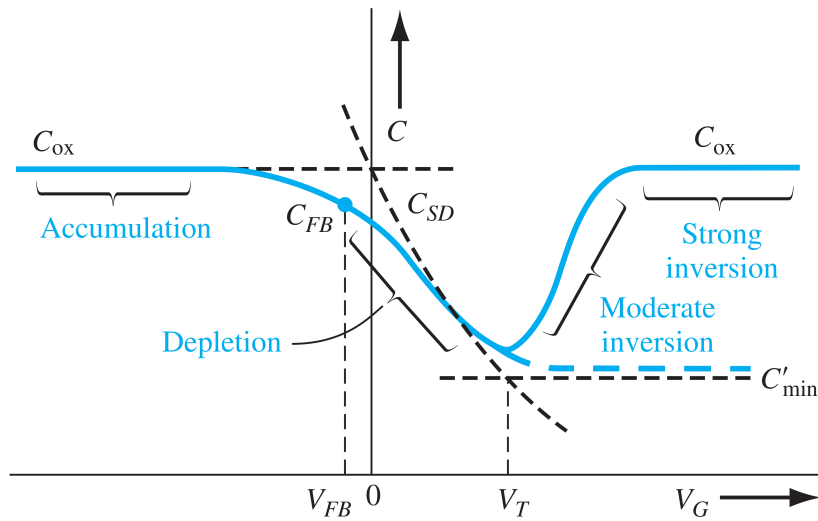


Fig. 6.12: Ideal capacitance versus gate voltage characteristic of a p-type MOS capacitor with individual capacitance contributions denoted (adapted from [85]). The dashed blue line indicates the limit for high frequency AC voltages.

6.2.3 Oxide and interface charge effects

The metal strips on ITk sensors are floating and have no defined potential. Right after applying a bias the outer oxide surface has yet to assume the same potential as the aluminium strips. Without a potential on the outer oxide surface, the properties that define the surface states in the interface region are solely the oxide and interface states. But even with a well-defined gate voltage, those charges have a significant impact on the CV characteristic of a MOS device. One can further classify oxide charges into 3 categories, all of which and including interface charges are sketched in Fig. 6.13.

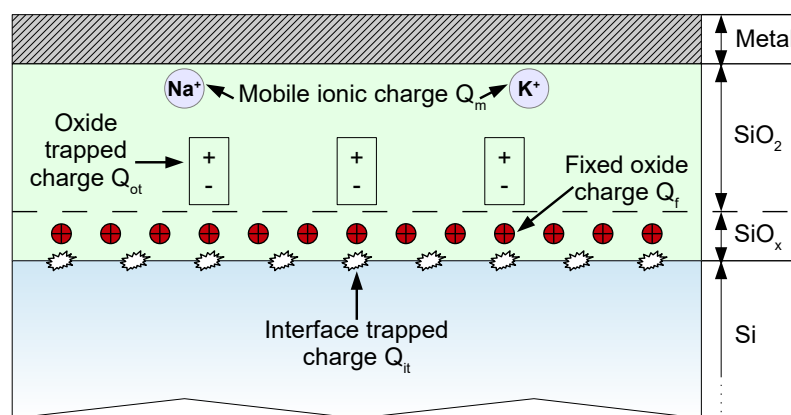


Fig. 6.13: Charges associated with thermally oxidized silicon (adapted from [87]).

6.2 Characterisation of long-term biasing effects on the sensor surface

The most relevant oxide charge influencing MOS characteristics are *fixed oxide charges* Q_f . They are usually located very close to the interface and, in the case of thermally grown oxide on silicon, positively charged, which can stem from trivalent silicon or excess oxygen centres in the transition region towards the interface [87]. They are immobile even under an applied electric field and are not affected by the oxide thickness. In simulations and calculation it can be considered a two-dimensional charge sheet. *Oxide trapped charges* Q_{ot} can be created either positive or negative by hot-electron injection or ionising radiation, making these traps the prevalent result of radiation damage in oxide. Initially, trapped charges are evenly distributed throughout the oxide bulk, given enough thermal energy or suitable potential difference, they can become separated. As the mobility of electrons ($\mu_{e,\text{SiO}_2} \approx 20 \text{ cm}^2/\text{Vs}$ [85]) is many orders of magnitude higher than that of holes ($\mu_{h,\text{SiO}_2} \approx 10^{-4} \dots 10^{-11} \text{ cm}^2/\text{Vs}$ [85]), electrons can drift to the metal electrode while holes are virtually rendered immobile. Over time, holes usually progress via hopping mechanism through shallow levels towards the Si/SiO₂ interface where a fraction is captured in localised traps and thus forming additional fixed oxide charges close to the interface. Hole traps in oxide are metastable states with release times ranging from hours to days and even years, especially in a low-temperature environment.

Complementary to those (semi-)localised charges are truly *mobile ionic charges* Q_m such as sodium, potassium, or hydrogen atoms. Mobile ionic charges can move through the oxide layer, e.g. between interstitials in the amorphous oxide, depending on biasing conditions. Those movement processes are usually enhanced at elevated temperatures.

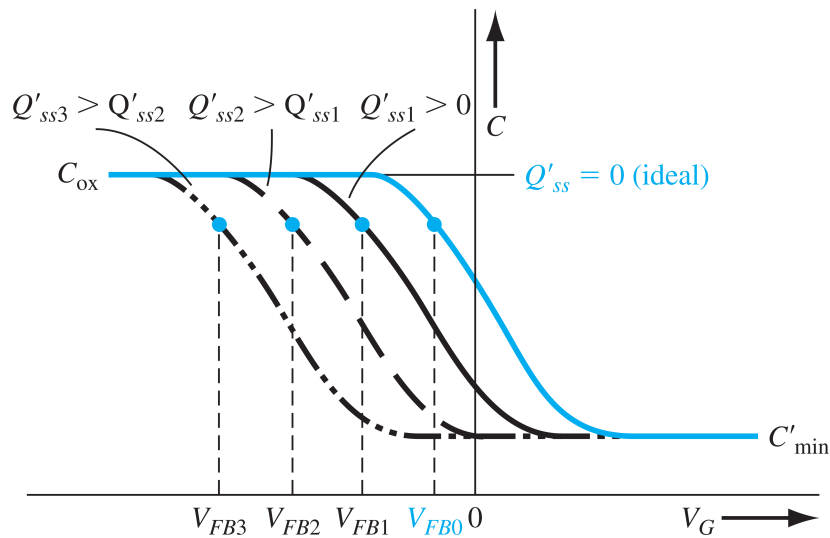


Fig. 6.14: Capacitance versus gate voltage characteristic of a p-type MOS capacitor for increasing values of effective fixed oxide charge [85].

In an unbiased sensor, a vertical electric field from positive oxide charges close to the interface induces a depletion or inversion layer depending on the amount of charge present in the oxide. When looking at the ideal CV curve of a MOS structure, the net oxide charge Q'_{ss} will affect the flat-band

Tracking reliability and the effects of long-term operation

and threshold voltage, as the additional charge concentration has the same effect as a positive gate voltage [85, 87]

$$V_{FB} = \phi_{ms} - \frac{Q'_f + Q'_m + Q'_{ot}}{C'_{ox}} = \phi_{ms} - \frac{Q'_{ss}}{C'_{ox}} \quad , \quad (6.12)$$

$$V_T = (|Q'_{SD}(\max)| - Q'_{ss}) \left(\frac{W_{ox}}{\epsilon_{ox} \epsilon_0} \right) + \phi_{ms} + 2\phi_{fp} \quad .$$

The resulting parallel shift of the CV curve towards more negative voltages (for p-type silicon) with increasing oxide charge concentration is shown in Fig. 6.14. One consequence of this shift is that the threshold voltage in a high-resistivity substrate, where $N_A x_d \ll Q'_{ss}$, is negative, thus allowing an inversion layer to develop even with a floating outer oxide surface at zero voltage.

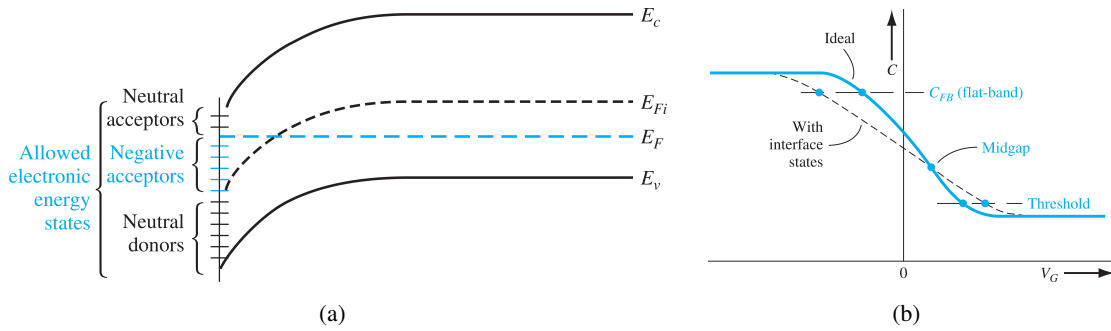


Fig. 6.15: Energy band diagram of a p-type MOS structure with interface states at inversion (a) and the change of the CV characteristic resulting from those states (b) [85].

Interface states that act as charge traps are introduced on the semiconductor surface by the abrupt termination of the periodic semiconductor lattice. These states are located in the band gap and, depending on the position of the Fermi level, charges can flow between bulk and interface states, unlike the fixed oxide charges. States in the upper half of the band gap act as acceptors which become negatively charged if the Fermi level is above them, states in the lower half are donor states which become positively charged if the Fermi level is below them. A band diagram with occupied interface charges at inversion is displayed in Fig. 6.15(a) as an example. Due to this change in the net charge of interface states, the flat-band voltage is shifted towards more negative values while the threshold voltage is shifted towards more positive values, leading to a smearing out of the CV characteristic, as shown in Fig. 6.15(b).

6.2.4 Substrate bias effects

In the previously detailed explanation the silicon substrate has always been in an unbiased condition and considered to be at ground potential, the same as the n-implant strips. However, one of the main observations regarding the C_{is} hysteresis was, that the increase is *not* constant regardless of bias, but rather a function of it.

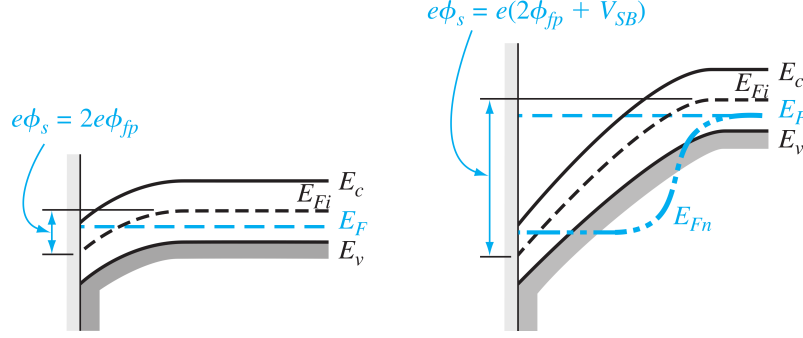


Fig. 6.16: Comparison of energy band diagrams for a p-type Si/SiO₂ interface at inversion point with $V_{\text{bias}} = 0 \text{ V}$ (left) and under reverse V_{bias} (right). E_{Fn} is the Fermi level at the surface from the n-implants through the reversely-biased p-n junction [85].

For standard MOS devices, applying a substrate (reverse) bias has an influence on the threshold voltage for inversion. Due to electrons in the p-type substrate being at a higher potential than in the n-implants, as shown in Fig. 6.16, free electrons created at the inversion threshold will instead move laterally along that potential gradient. It is only once the surface potential compensates for the applied bias at $\phi_s = 2\phi_{fp} + V_{\text{bias}}$, that the surface reaches an equilibrium inversion condition again (note that for an easier description the reverse bias is denoted as positive since it acts upon the energy levels in the same direction as the surface potential in depletion/inversion).

As a reverse bias increases the space charge region x_d under the oxide (see Eqs. 3.23 and 6.5), the voltage on the metal gate has to be increased to compensate for the increased negative space charge to reach the inversion point. The consequence is an increase of the threshold voltage

$$\Delta V_T = -\frac{\Delta Q'_{SD}}{C'_{\text{ox}}} = \frac{\sqrt{2e\epsilon_{\text{Si}}\epsilon_0 N_A}}{C'_{\text{ox}}} \left[\sqrt{2\phi_{fp} + V_{\text{bias}}} - \sqrt{2\phi_{fp}} \right]. \quad (6.13)$$

6.2.5 Summary and explanation of observed behaviour

The C_{is} hysteresis behaviour can be summarised in five main observations:

1. In all cases an *increase* in C_{is} was measured when biased at V_{const} over long periods of time.
2. A *saturation* value for C_{is} is reached where $\Delta C_{\text{is}}^{\text{max}}$ is depending on the applied V_{const} .
3. $\Delta C_{\text{is}} > 0$ only if applied bias $V_{\text{bias}} \lesssim V_{\text{const}} - (70 \dots 100) \text{ V}$.
4. The shape of the saturated C_{is} curve is depending on the type of inter-strip isolation.
5. The effect fully reversible.

As it is the case for a MOS structure, the measured inter-strip capacitance is highly dependent on the charge concentration in the surface region of the Si/SiO₂ interface and, in fact, the capacitance between implants is a function of the network created by the mutual capacitance between the surface

Tracking reliability and the effects of long-term operation

region and each implant [86]. The surface charge concentration in turn is defined by the voltage applied to the metal contact and the fixed positive oxide charges. This is not trivial in this case since there is no metal gate above the inter-strip region, and the AC-coupled metal strips are floating. Tab. 6.1 gives an overview of the relevant MOS quantities for a previously unbiased sensor. For those, V_T and V_{ox} are estimates for a sensor with a fairly low amount of fixed oxide charges. Generally, devices have a higher oxide charge concentration, resulting in a shift of both voltages towards more negative values.

Tab. 6.1: Characteristic quantities of the insulator-semiconductor and MOS structure in ATLAS12 prototype sensors calculated for an unbiased sensor and floating metal strip. Material constants for ϕ_{ms} were taken from [85], all other parameters from sensor evaluation (see Chapter 4).

Inter-strip region		AC-coupled readout strips	
ϕ_{fp}	+0.151 V	ϕ_{fn}	+0.47 V
C'_{ox}	3.5 nF/cm ²	C'_{ox}	17 nF/cm ²
$Q'_{SD}(\text{max})$	$4.5 \times 10^9 e \text{ cm}^{-2}$	ϕ_{ms}	-0.14 V
$V_T(N_{ox} \approx 10^{10} \text{ cm}^{-2})$	$\approx 0.05 \text{ V}$	$V_{ox}(N_{ox} \approx 10^{10} \text{ cm}^{-2})$	$\approx -0.1 \text{ V}$

Charge imprint and surface potential model

On the basis of physics of MOS capacitors detailed in the previous paragraphs, the listed observations can be fully explained under the assumption of the following: The overall C_{is} increase mainly arises from the component concerning the capacitance between implants with the cause of it being a significant gain in *negative interface traps*. The initially floating outer surface takes on a positive *surface potential* akin to a positive gate voltage over time due to the slow movement of charges from the strip metal along the oxide surface. Moreover, the high negative potential p-stop implants increasingly attracts mobile ionic charges in the oxide, leading to a *charge imprint* with a non-uniform distribution in the lateral (inter-strip) coordinate.

Under the initial conditions of the MOS structure a virgin sensor operates under interface depletion, if not (weak) inversion conditions. This is already the case even if the electrostatic potential on the outside of the oxide, i.e. the “gate voltage” in the equivalent MOS picture, is zero. As shown in several investigations of p-in-n devices before [86, 88, 89], the classical assumption of *Neuman boundary conditions* ($E_n = 0$) is in fact not the equilibrium condition for sensor operation. Instead, over a period of time charges can move on the outer oxide surface and therefore change the electrostatic potential. This *gate boundary condition* can actively influence the electric field through the oxide into the semiconductor surface and hence the charge distribution in the interface layer in the same way gate voltage does in a MOS capacitor. For the investigated n-in-p sensors, the charges accumulating on the outer oxide surface would be equivalent to a positive applied gate voltage, and therefore a shift of the interface towards inversion. However, as shown in Section 6.2.3, if a MOS structure is operated in inversion, more interface states will become negatively charged acceptor states and in this way

6.2 Characterisation of long-term biasing effects on the sensor surface

effectively act as *minority carrier traps* in the p-type bulk – an aspect which will become important for the further characterisation with DLTS (see 6.6). The capacitance between the strip implants and the surface region is similar to that of a depleted p-n junction and therefore is directly proportional to the amount of space charge present at any given voltage.

Consequently, the capacitance of C_{is} increases, in line with the first observation (1.). When the sensor surface approaches the limit of the gate boundary condition, and mobile ionic charges have been attracted to the interface, the effective (positive) “gate voltage” of the outer oxide layer and hence the populated interface states is a function of V_{const} . C_{is} saturates correspondingly, explaining the second observation. With the outer surface at a given fixed state during a bias sweep, the threshold voltage is shifted towards more positive values (see previous Section 6.2.4) as the bias voltage increases, which results in a neutralisation of interface states and the falling flank for higher bias in the hysteresis C_{is} curve. Calculated values of ΔV_T at selected V_{bias} are listed in Tab. 6.2. This depopulation of interface traps with increasing bias agrees with observation (3.).

Tab. 6.2: Calculated shift of V_T at selected V_{bias} for ATLAS12 prototype sensors.

V_{bias} [–V]	50	100	200	300	400	500	600
ΔV_T [V]	2.5 ± 0.1	3.6 ± 0.2	5.1 ± 0.2	6.3 ± 0.2	7.3 ± 0.2	8.2 ± 0.2	9.0 ± 0.2

With the outer oxide surface at a defined positive electrostatic potential through the gate boundary conditions, and a negative potential at the bulk surface, the resulting electric field will increasingly attract positive mobile ionic charges (see Section 6.2.3) towards the Si/SiO₂ region. This also further exacerbates the negative shift of V_T from already present oxide charges. However, the potential in the silicon bulk is not uniform due to the p-stop acting as an inter-strip isolation structure. At the p-stop the potential drops to values of $\mathcal{O}(-10 \dots -100 \text{ V})$ depending on the applied bias and increases laterally towards the n-implants [62]. As such, the amount of ionic charges attracted to the interface is not uniform along the inter-strip region, but rather a gradient with a maximum concentration at the p-stop, forming a characteristic charge imprint. Hence, V_T also becomes a function of the lateral coordinate. This is reflected in the shape of the hysteresis curve, with the interface levels in different parts of the inter-strip region becoming neutral at different bias voltages through the threshold shift, thus defining observation (4.).

Both the gate boundary conditions, as well as the charge imprint caused by the mobile ionic charges, are fully reversible given enough time and thermal activation. Therefore, one can repeatedly observe the formation and recovery of the hysteresis without adverse impact on the sensor itself, which concludes the observations listed.

Another indication for the change in interface state occupation and the formation of an inversion layer being the cause, is the analogous hysteresis observed in the $I_{leakage}$ versus bias voltage behaviour. Since there is an increase in occupied electron traps and an electron inversion layer, the electrons which are thermally generated in the space charge region and are attracted towards the charge collecting strip electrodes will experience a reduced electric field yielding an overall reduced leakage current.

In summary, the hysteresis effect is caused by a shift of the boundary conditions on the outer oxide layer and through a lateral charge imprint in the oxide that is induced by the potential differences in the sensor under long-term biasing, leading to the filling of localised interface trap states with electrons. In order to confirm the inference presented in this section, additional TCAD simulations were performed. To determine the time constants of the change in boundary conditions and the interface trap concentration involved in the presented processes, a novel application of capacitance DLTS was used. The results of the simulations and DLTS measurements will be presented in successive sections.

6.3 TCAD simulation of the ITk Strip Sensor surface

For the TCAD simulations, the model of the strip region that has already been presented in Section 5.3 was used as a basis. In addition to the previously discussed structures, a highly resistive, 10 nm thin conductive layer was added on the outer SiO₂ layer. This thin conductive layer was used in an attempt to emulate the surface conductivity which is established in an ambient atmosphere over time, motivated by simulation studies akin to the ones presented here, but for p-in-n devices in [88, 89].

The plot sequence in Fig. 6.17 shows the time development of the electrostatic potential at the sensor surface and the corresponding streamlines for a charge moving along the electric field lines. The first plot Fig. 6.17(a) displays the potential of a sensor without the conductive layer, signifying a virgin sensor with its ideal behaviour, the second one (b) depicts the quiescent sensor state in full equilibrium. For the simulation, a sensor bias configuration similar to the performed measurements was implemented with a voltage ramp of -10 V/s up to a maximum of $V = -600\text{ V}$, which is then held constant. To achieve the shown time dependence which is in the same order of magnitude as the observed behaviour, the resistivity of the conductive surface layer was chosen as $\rho_{\text{surf}} \approx 3 \times 10^{12}\ \Omega\text{cm}$.

From the time development, it can be seen that while for a virgin sensor the streamlines end directly at the readout strip, indicating a segmentation which allows for an easy discrimination between the main charge collecting electrode and minimal charge sharing, over time an increasing number of streamlines end at the interface. This happens because the potential of the outer oxide surface reaches the same potential as the metal strips when progressively nearing the gate boundary condition. A consequence of this is increased charge sharing between neighbouring strips as the weighting potential close to the Si/SiO₂ interface smooths out.

Using this implementation of the gate boundary condition, the full charge imprint and surface potential model for the observed C_{is} hysteresis has been implemented. The voltage settings for the simulation were the same as before with 1 h at $V_{\text{const}} = -600\text{ V}$. Additional oxide charges were introduced in the simulation as the assumed charge imprint of the mobile ionic charges in the oxide. Unfortunately, the simulation software does not allow the implementation of insulator charges with a distribution more complex than a Gaussian profile, therefore the oxide charges were included as a uniform distribution. The capacitance was simulated for the voltage ramps at the beginning and at the end of 1 h interval at constant bias.

6.3 TCAD simulation of the ITk Strip Sensor surface

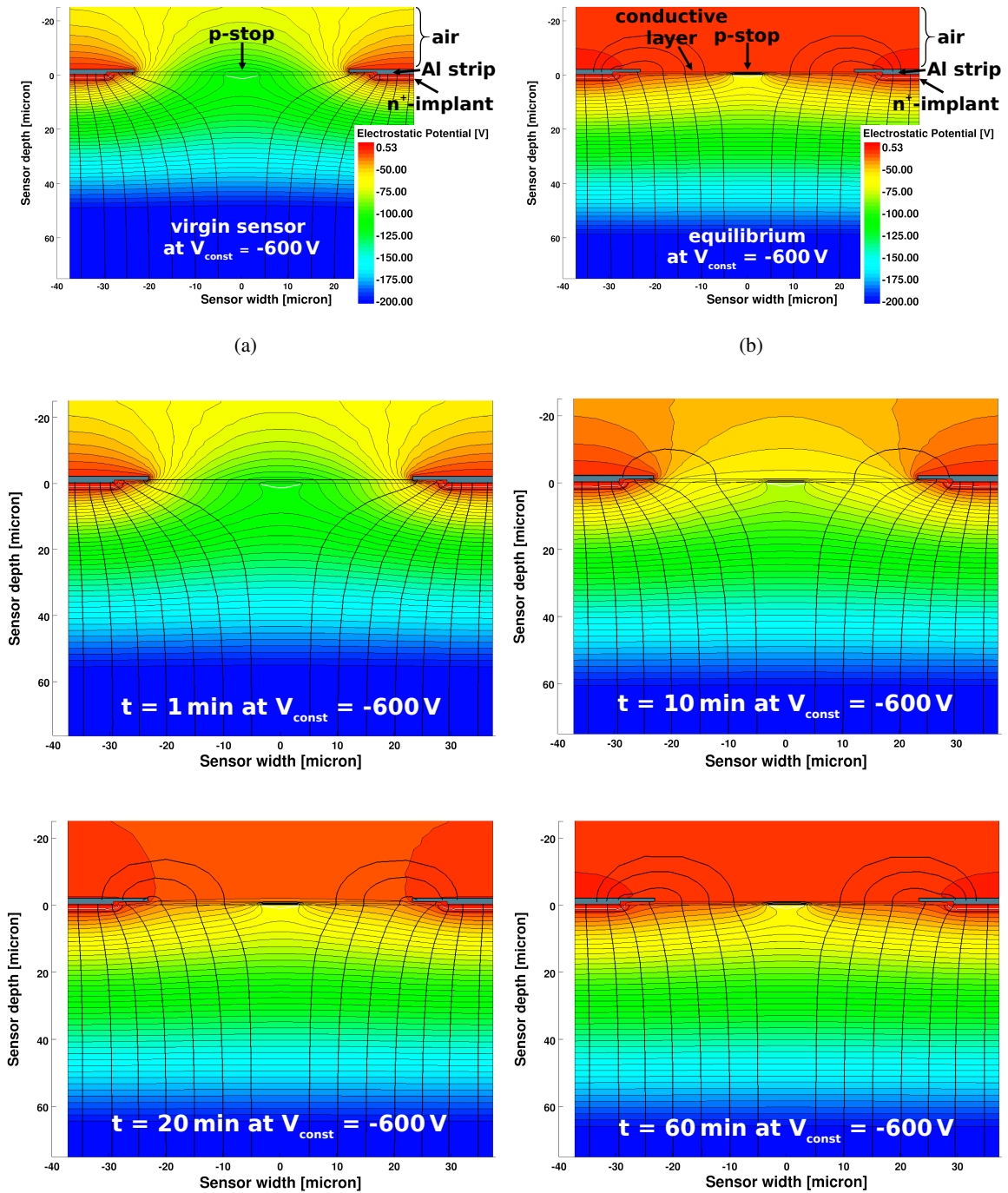


Fig. 6.17: Simulated changes in the electrostatic potential of the inter-strip region over time under constant bias. The modelled sensor regions consists of two half strips at both ends of the structures in x-direction with the p-stop between at the coordinate origin. The streamlines along the electric field lines are displayed to demonstrate the movement of charges generated from incident particles. The plot sequence here shows the potential for a virgin sensor (a), and one in equilibrium (b), as well as the time development between at $t = 1 \text{ min}$, $t = 10 \text{ min}$, $t = 20 \text{ min}$, and $t = 60 \text{ min}$.

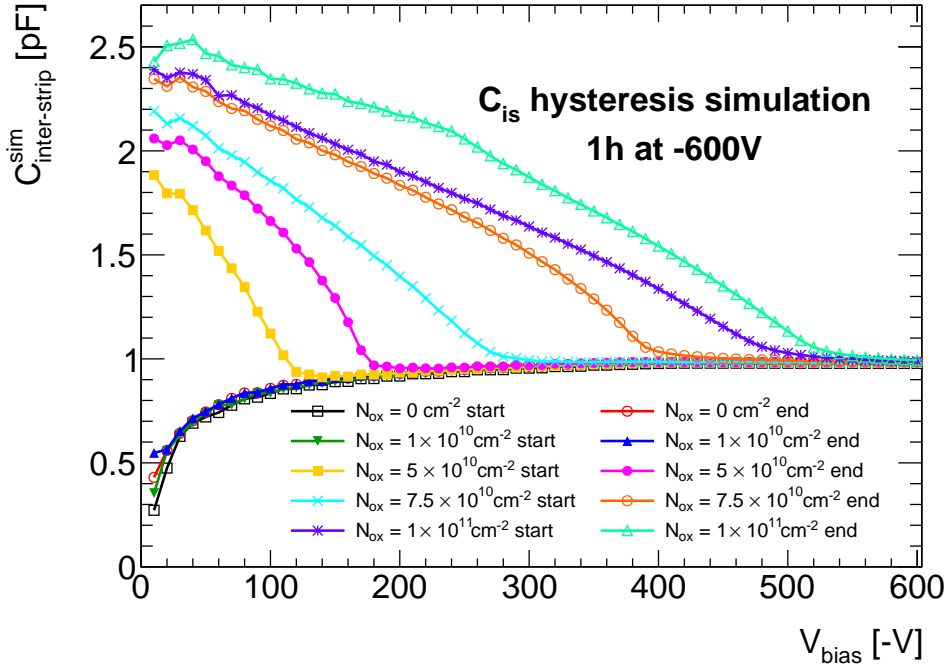


Fig. 6.18: Simulation of hysteresis in C_{is} measurements using the charge imprint and surface potential model. C_{is} curves for various oxide charge concentrations were simulated during the voltage ramp up at the start and the ramp down at the end after 1 h at $V_{const} = -600$ V.

The simulation results are plotted in Fig. 6.18. The first conclusion that can be drawn from this is that both effects have a similar influence on the simulated capacitance, supplementing and reinforcing each other. This is to be expected, as was pointed out in the detailed explanation of MOS structures in the previous Section 6.2. Positive oxide charges and a surface potential with the same function as a gate voltage which, as can be seen in Fig. 6.17, is also positive for the ITk Strip Sensors have the same effect with regards to the state of the Si/SiO₂ interface. Secondly, from the simulated curves it can be seen that for oxide charge concentration as high as $N_{ox} = 1 \times 10^{10} \text{ cm}^{-2}$ the capacitance does not significantly change, not even after the gate boundary condition is established. Thirdly, the positive surface potential alone is not enough to explain the magnitude of the observed hysteresis as it is limited by the materials properties of the sensor. This is additional evidence that the electric field in the sensor induces a charge imprint in the oxide, yielding in an increased oxide charge concentration contributing to the interface sensitivity. Lastly, from the shape of the obtained simulated curves and its similarity to the measurement results of sensors with p-spray (Fig. 6.7(c)), it can be inferred that this is most likely due to the lack of lateral profile in the oxide charge distribution. In future simulations attempts could be made to achieve a closer resemblance with the charge imprint assumed in the model and whether this would result in the observed plateau and sharp flank.

All in all, the simulations are strong evidence that the charge imprint and surface potential model for the observed C_{is} hysteresis is valid for the tested sensors.

6.4 The ITk Strips testbeam setup

The investigation of tracking performance is one of the most important techniques used to study prototype modules under realistic conditions. One way to do this is by using a well-defined beam of high-energy particles produced in an accelerator facility, a so called *testbeam*, in conjunction with well-known high resolution sensors that are used to reconstruct particle tracks, the *testbeam telescope*. The tracking efficiency of prototype modules and other properties can then be determined from hits registered in the *device under test* (DUT) and the discrepancy with the reconstructed tracks.

The beam telescopes used for testbeam campaigns of the ITk Strips Community were of the EUDET type, which will be further detailed in the following Section 6.4.1. The measurement campaigns producing the results presented in this thesis were performed at two different facilities located at DESY in Hamburg, Germany, and at the CERN site in Prévessin-Moëns, France, for previously irradiated devices. A description of the testbeam facilities will be given in Section 6.4.2. Lastly, having acquired the data from testbeam runs, one has to match the hit information on the telescope and test module planes in the raw data files and reconstruct the corresponding incident particle tracks. This was done with the EU Telescope package. The reconstruction procedure using this software will be explained in Section 6.4.3.

The execution of the testbeam campaigns, for which results will be presented in the following, were performed as part of the larger ITk Strips testbeam team. Testbeam setup and data acquisition were done in shifts with alternating groups.

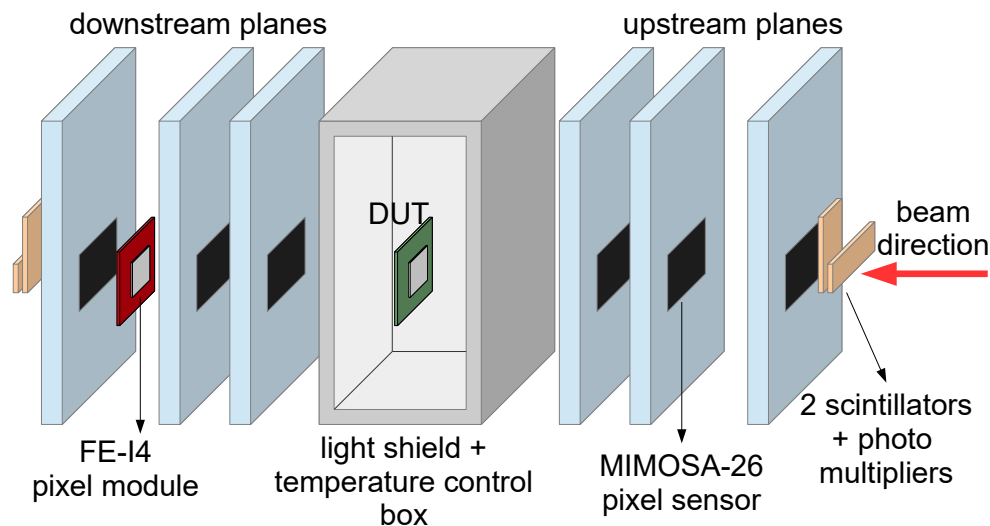


Fig. 6.19: Schematic setup of the EUDET beam telescopes used for ITk Strip Detector testbeam campaigns. An incident particle beam triggers readout by passing both sets of scintillators in front and behind the telescope planes. The telescope layers equipped with MIMOSA pixel sensors are arranged in groups of three upstream and downstream from the DUT. The DUT itself is placed inside a test box which provides light shielding and temperature/humidity control.

6.4.1 The EUDET telescope

The *European Union funded DETector R&D towards the International Linear Collider* (EUDET) within the *Advanced European Infrastructures for Detectors and Accelerator* (AIDA) project resulted in the development of a type of beam telescope with 7 copies at 5 different testbeam facilities around the world [90, 91]. A sketch of the EUDET-type telescope used for ITk Strip Modules can be seen in Fig. 6.19. It is composed of a mechanical and electrical support structure with two telescope arms which leave space between them for the installation of the DUT. The telescope arms can be rotated by a few degrees to allow precise alignment parallel to the beam axis. Each arm consists of three layers equipped with MIMOSA-26 (M26) pixel sensors which are denoted *upstream* or *downstream* depending on their relative position with respect to the DUT and the beam direction. The MIMOSA planes are complemented by a 3D pixel sensor employing FE-I4 (or FEI4) readout technology as a timing plane.

Mimosa Sensors

The *Minimum Ionizing MOS Active* (MIMOSA) pixel sensors [92] used in the EUDET-type telescopes are *Monolithic Active Pixel Sensors* (MAPS). They are used for their precise pointing resolution in determining particle trajectories and their low material budget with a specified thickness of $50\mu\text{m}$. This is especially important for facilities employing beams of only a few GeV resulting in non-negligible multiple scattering contribution in testbeam measurements.

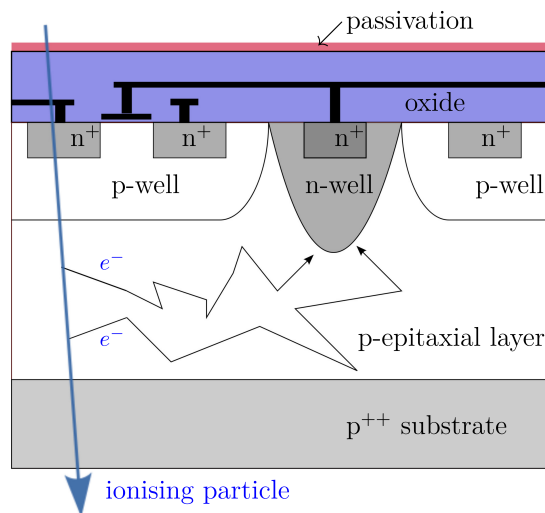


Fig. 6.20: Schematic cross section of a monolithic active pixel sensor. Charges generated by the incident particle diffuse towards the n-well where they are collected and read out through the integrated circuitry [90].

A cross section of a MAPS is displayed in Fig. 6.20. As active pixel sensors they have an integrated readout consisting of two transistors for charge integration and signal transfer as well as

a self-biased diode in forward bias to compensate for the leakage current in the device [91]. The pointing resolution for the region in the middle of six M26 telescope layers has been determined to be $\sigma_{\text{tel}} \sim 2 \mu\text{m}$. The disadvantages of MAPS sensor technology are the long readout and integration times as well as the slow charge collection through diffusion in the absence of strong electric fields. Hit information is read one by one using a rolling shutter mode at a 80 MHz clock frequency resulting in the whole pixel matrix being read out in 112 μs [90].

Devices Under Test and cooling box

The DUTs for which results will be presented in the following sections came from different batches and generation of sensors which have been assembled into prototype modules. While different other components of modules have been tested separately before, an assessment of the performance of full modules is critical to scrutinise their interplay and to validate the assembly process in realistic conditions before the production phase.



Fig. 6.21: Pictures of prototype modules evaluated in the 2018 testbeam campaigns at DESY (a) [93] and CERN SPS (b).

The shown results stem from the 2017 and 2018 testbeam campaigns at DESY as well as the 2018 CERN SPS testbeam. The DUT from the 2017 DESY measurements shown in this thesis is a single-sided end-cap R0 module. As the number of readout channels in R0 sensors varies between the lower (1024) and upper half (1152) of the sensor, 8 ABC130 ASICs mounted on a hybrid (R0H0) were used to retrieve hit information in the lower two strip segments and 9 more on a second hybrid (R0H1) in the upper half. In addition, each hybrid was equipped with one HCC130, but the module did not have a power board. The ABC130 and HCC130 ASICs used here are the prototype versions of the readout ASICs that will be used during module production (ABCStar and HCCStar) [17].

In the 2018 DESY campaign three unirradiated DUTs have been tested, shown in Fig. 6.21(a). Two modules under investigation were built with ATLAS17 barrel long-strip sensors at the University of Liverpool (LIV LS) and at the Rutherford Appleton Laboratory (RAL LS), respectively. Both modules

Tracking reliability and the effects of long-term operation

Tab. 6.3: Summary of investigated prototype modules for which results will be presented in this work.

Module	Description	Testbeam	Comment
R0	end-cap module with 8 + 9 ABC130 and 2 HCC130 ASICs	May-17 DESY	First-ever full end-cap module in testbeam
LIV LS	long-strip module with power board, 10 ABC130 and 1 HCC130 ASICs	Jun-18 DESY	
2×R0	double-sided end-cap module with partial power board, 8 + 9 ABC130 and 2 HCC130 ASICs for each; single modules: FR_2 and FR_5	Jun-18 DESY	First-ever double-sided full module in testbeam
R0 Irrad	end-cap module with power board, 8 + 9 ABC130 and 2 HCC130 ASICs	Nov-18 CERN	Irradiated at PS with protons to $1.63 \times 10^{15} \text{ n}_{\text{eq}}/\text{cm}^2$ (75 MRad)

were equipped with 10 ABC130 and 1 HCC130 ASICs, as well as one power board fully-equipped with an *Autonomous Monitoring and Control* (AMAC) ASIC and a shielded DC-DC converter [17]. The other DUT was a double-sided R0 module (DSR0 or 2×R0), built at the University of Freiburg. The sensors in that module were glued back-to-back into a petal-like support structure which contained an internal cooling circuit. The power boards on them contained the shielded DC-DC converter, but not the AMAC.

During the 2018 CERN SPS testbeam a single-sided R0 module was tested, which was irradiated beyond its expected lifetime dose with $1.63 \times 10^{15} \text{ n}_{\text{eq}}/\text{cm}^2$ (75 MRad) at the CERN PS over a period of three weeks. The power board of that module was fully-equipped, including the newer second version of the AMAC (AMACv2). A picture of the irradiated module is shown in Fig. 6.21(b).

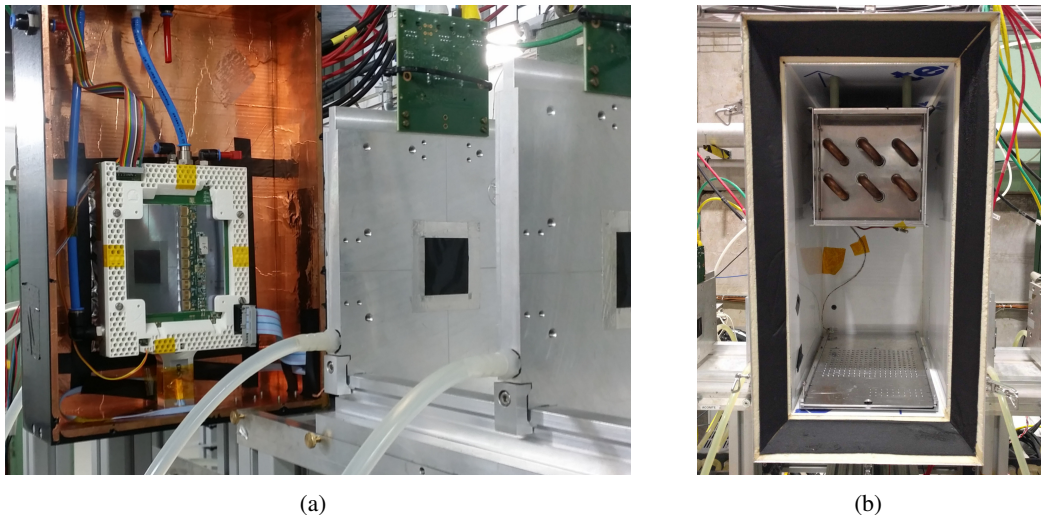


Fig. 6.22: Acetal (a) box used at DESY and MPI cooling box (b) for low-temperature testbeam measurements of irradiated devices at the CERN SPS testbeam.

The DUT in a testbeam is mounted on a testframe and supported inside a light and airtight box. Openings on the front and backside of the frames, and reduced material thickness of the box, are introduced for use in the DESY beamline to not overly increase the material budget in the beam. The box itself is placed between the two telescope arms on a precision $xy\phi$ -table to move the device through the beam spot area and aim at different spots on the module. During measurements the box is continually flushed with nitrogen to guarantee dry conditions and prevent condensation if a chiller is used to cool the DUT. The module boxes used for unirradiated DUTs at DESY can be connected to water-glycol or silicon-oil chillers, thus allowing the module temperature to be reduced down to just below 0°C through cooling jigs the modules can be mounted on. They are not specifically insulated and have a relatively large inner volume, therefore they are not ideal to be used for the low temperatures necessary to operate irradiated devices. For those samples, a special cooling box fabricated by the Max-Planck-Institute (MPI) Munich is employed, which can reduce the temperature at the module to $\sim -30^{\circ}\text{C}$ through indirect cooling of the air inside the inner volume to -50°C . As this box is used at the SPS testbeam with its high beam energy, the additional material introduced by the thicker walls of the MPI box does significantly impact the resolution. Photos of a standard DUT box and the MPI box, respectively, can be seen in Fig. 6.22.

Data Acquisition

In order to connect the hit information from the telescope planes and the DUT, the data streams of the different readout systems have to be connected and synchronised with respect to the same incident particle event. The integral hardware to do this is the *Trigger Logic Unit* (TLU) [94]. The TLU is used to send trigger signals to all connected devices at the same time thus creating a common trigger ID in each event recorded by the DUT or the MIMOSAs.

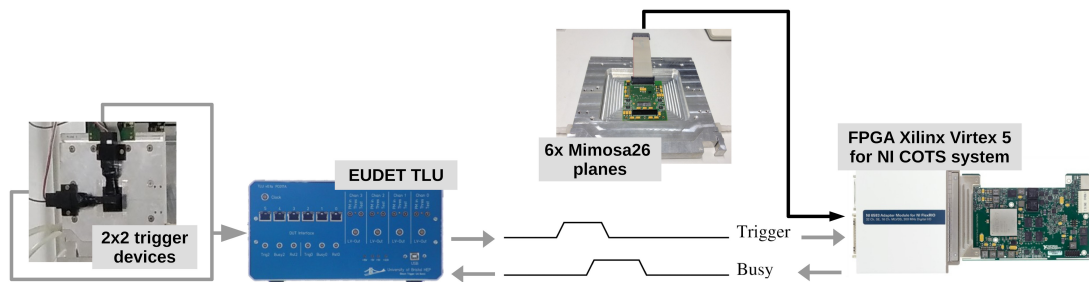


Fig. 6.23: Principle of TLU operation for EUDET-type beam telescopes showing the trigger handshake between TLU and connected devices [95].

The data acquisition (DAQ) procedure for a single MIMOSA plane is shown as an example in Fig. 6.23, but it can similarly be replaced by the DUT or the FE-I4. A trigger signal is sent if all scintillators at both ends of the telescope register an incident particle in coincidence. The TLU and DAQ systems of the connected devices operate in a handshake configuration, by which once the TLU asserts a trigger a busy signal is raised during the full readout of every device.

Tracking reliability and the effects of long-term operation

As the readout time of the M26 sensors with $112\ \mu\text{s}$ is much slower than the expected bunch crossing time in the LHC with $25\ \text{ns}$, which is therefore the required readout rate of a tracking detector in the ATLAS detector, the slow readout can cause ambiguities when matching tracks and triggers during reconstruction. For that reason, a FE-I4 pixel sensor with FE-I4 readout technology, and hence $25\ \text{ns}$ timing resolution, is used as an additional timing plane. Moreover, the well-known high tracking efficiency of the employed FE-I4 is used to calculate the efficiency of the DUT.

6.4.2 Testbeam facilities

The testbeam campaigns for the ITk Strip Detector are usually performed at DESY II for unirradiated devices and at CERN SPS for devices previously irradiated at the IRRAD facility of the CERN PS. The two testbeam facilities will be briefly introduced below.

DESY II

Located in Hamburg and founded in 1959, the German accelerator and particle physics research centre *Deutsches Elektronen Synchrotron* (DESY) hosted many famous accelerators and experiments in the past, in particular with the proton-electron collider HERA (*Hadron-Elektron-Ring-Anlage*) [96] and its experiments ZEUS [97] and H1 [98] which were in operation until 2007. Presently, the most famous experiment located at DESY is the European *X-Ray Free-Electron Laser* (XFEL) [99].

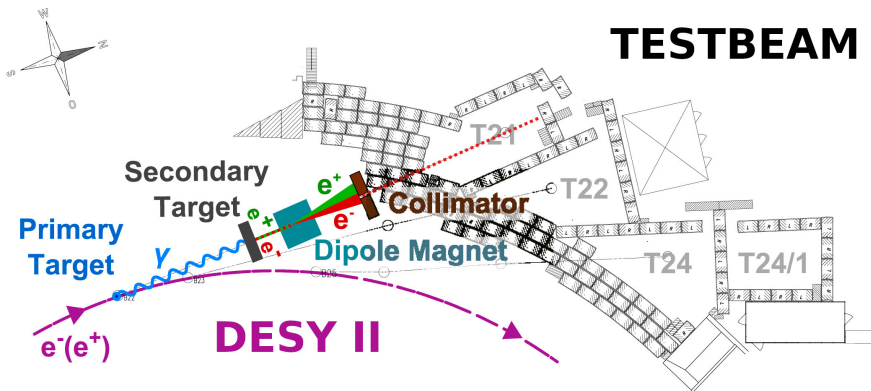


Fig. 6.24: Schematic view of the testbeam generation at the DESY II testbeam facility, here for beam line TB21, but equally applicable for all other beam lines. Electrons or positrons from the DESY II accelerator generate bremsstrahlung photons in the primary target which subsequently hit one of several secondary targets creating electron/positron pairs. Testbeam users can select particles according to their momentum and charge with a dipole magnet [100].

The DESY testbeams, as shown in Fig. 6.24, are generated from electrons or positrons accelerated in the DESY II ring which are firstly being guided onto a primary target of carbon fibres to produce bremsstrahlung photons. Further along the beam direction, the photons hit a secondary target which converts the photons to electron/positron pairs. A dipole magnet spreads out the produced charged particles into a horizontal fan to separate them by charge and energy. By adjusting the dipole magnet,

either electrons or positrons can be selected and the particle momentum can be varied between 1 GeV/c and 6 GeV/c.

As the maximum possible energy is relatively low, the material budget of the module box and the DUT support structure has to be kept as low as possible to minimise the impact of multiple scattering. For that reason the cooling boxes with thick isolation cannot be used and module temperatures $\ll 0^\circ\text{C}$ are an ongoing challenge. More details on the DESY testbeam facility can be found in [100].

Fig. 6.25 displays the available EUDET-type telescopes at DESY. For the ITk Strips testbeam the DURANTA telescope in beam line TB22 was used. In the 2017 campaign 4.4 GeV electrons were used, while in 2018 the selected energy was 4 GeV for a higher event rate.



Fig. 6.25: EUDET-type beam telescopes DATURA (a) and DURANTA (b) at the DESY II testbeam [100].

CERN SPS

Formerly the accelerator with the highest energy of its time, the CERN Super Proton Synchrotron [101] is currently mainly used as a pre-accelerator in the LHC accelerator chain, as was already detailed in Section 2.2. Besides that role, the SPS also provides high energy particles for testbeam operations and several fixed targets experiments, e.g. COMPASS [102] and NA62 [103], all of which are located in the North Area Experiment Hall of the CERN Prévessin site.

In order to generate a large range of different particles for use in the North Hall as a Secondary Beam Area, the primary 450 GeV proton beam is split up into three main branches and hits one of the primary targets, and similar to cosmic radiation, the SPS beam initiates hadronic cascades. As the production of hadrons in a fixed target is followed by an electro-magnetic cascade through the decay of hadrons with short lifetimes, the secondary beam after each primary target contains a mixture of hadrons and electrons/positrons in a large momentum range. However, testbeam campaigns and fixed target experiments require particle beams with a high purity of particle types and small momentum

Tracking reliability and the effects of long-term operation

spread. Therefore, a combination of absorbers, converters, radiators, and filters for the particle type selection in conjunction with the wobbling stations to feed particles at different momenta into separate beam lines are employed to achieve this. An overview over all CERN testbeam facilities was given during the annual “Beam Telescope and Testbeam Workshops” in recent years, e.g. [104].

A photo of the ACONITE telescope in beam area H6A is shown in Fig. 6.26. For the ITk Strips testbeams 120 GeV/c pions are used.

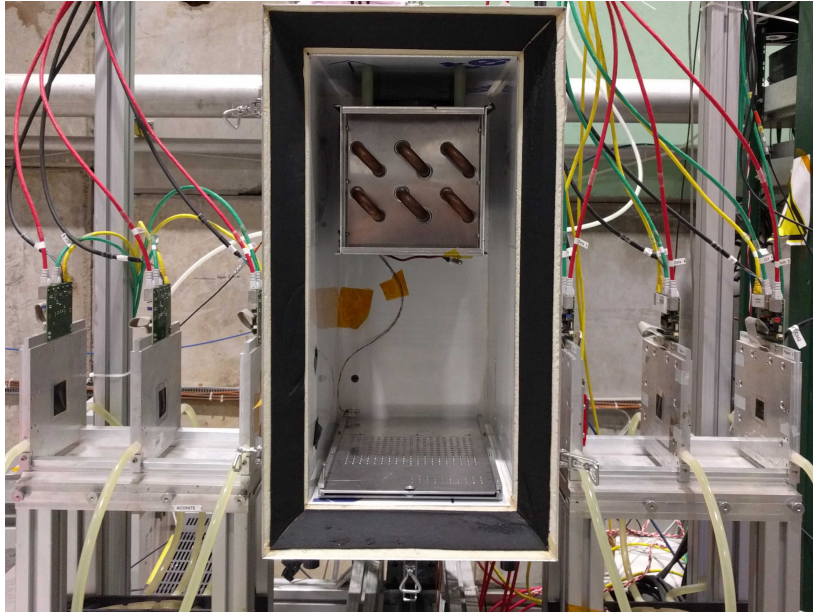


Fig. 6.26: ACONITE telescope with MPI cooling box at the SPS testbeam located in the North Area Experiment Hall, CERN Prévessin site.

6.4.3 Track reconstruction and data analysis

Track reconstruction for ITk Strips testbeam data is done with the EUTelescope software package [105]. EUTelescope has a fundamentally modular structure (Fig 6.27) and is based on a succession of Marlin (*Modular Analysis and Reconstruction for the LINear collider*) processors [106]. Every task done by EUTelescope during the track reconstruction is implemented as an independent step that is called by Marlin, thus allowing step-by-step analysis chains with separate processors running independently in parallel for different testbeam runs to be performed. For each processor the parameters can be adjusted by the user in a configuration file. The tracks obtained by the reconstruction can be used to characterize a DUT, such as the strip modules in the following, or allows measurements of radiation length of passive materials by measuring the scattering of tracks in the target.

A more detailed introduction of EUTelescope including details of the different reconstruction steps and step-by-step examples can be found in the “EUTelescope Guide for ATLAS ITk Strip” [107].

The post-reconstruction analysis consists of two main parts. Firstly, single runs are analysed and hits in the DUT and FE-I4 are associated with the reconstructed track. In doing so, several cuts can be

6.5 Tracking reliability of sensors under long-term operation

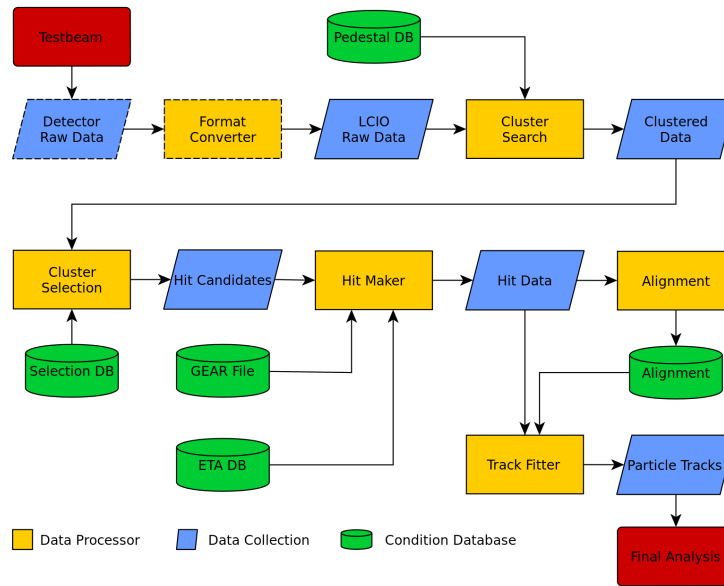


Fig. 6.27: Overview of the modular EUTelescope software framework [107]

applied, such as limiting the scope of the analysis to only a select area on the sensor or to a given timing window, furthermore noisy strips can be masked. In the second part of the analysis, all the runs of a certain measurement sequence are evaluated together based on the results from the previous step. As the ITk Strip Modules only have a binary readout and therefore cannot directly measure the collected charge, the standard type of testbeam measurement for module evaluation is a *threshold scan*, for which a sweep of threshold values in the readout is performed, yielding an efficiency versus threshold curve. This *s-curve* can be used to determine the mean deposited charge and the operational window when built into the detector in the future.

6.5 Tracking reliability of sensors under long-term operation

As detailed in the previous sections, long-term biasing of sensors leads to a significant change in their electric behaviour of the surface close to the Si/SiO₂ interface. The observed consequences are a large increase in the inter-strip capacitance, the main contribution to the input capacitance of readout electronics and therefore an important factor for amplifier noise. Moreover, sensor simulations imply alterations of the layout electric field near the electron-collecting strip-implants as well as an influence on the weighting field and drift field, which would lead to enhanced charge sharing.

In an ideal sensor with analog readout, the latter effect would not have a big impact as the total sum of collected charges would not change, given sufficiently long readout times, yielding a constant charge collection efficiency. The potential problem for ITk Strip Modules stems from the digital readout with fixed signal thresholds imposed on every strip. If the signal decreases below a certain level due to charge sharing with neighbouring strips, one would thereby have lower tracking efficiency.

Tracking reliability and the effects of long-term operation

To investigate whether this is the case in ITk prototype modules, during the last few testbeam campaigns efforts were made to perform threshold scans under conditions similar to the C_{is} measurements in which the hysteresis effects were first observed. At the beginning of the testing sequence for a particular module, the voltage is ramped up and threshold scans are performed at specific bias voltage levels below the intended operation bias for the remainder of the measurements, e.g. the individual ASIC scans. At the end, the same procedure is performed at the same beam position with reverse bias voltage order.

Of the many possible analyses of sensor performance which can be done with testbeam measurements this focus on the performance before and after extended operation is only one small aspect. It is, however, of utmost importance to get an understanding of the implication the hysteresis can have on the finished ITk and other future detectors using similar sensor technologies.

6.5.1 Testbeam results of un-irradiated modules

The first time the procedure to search for the impact of surface effects on the tracking performance was conducted was during the 2017 DESY testbeam campaign with the R0 module as DUT. Particular care has been taken to not operate the module for an extended period time before the start of the testbeam runs and enough time was given for the module to recover from any previous tests in lab. The temperature and humidity inside the box and on the module has been monitored with NTC sensors (*negative temperature coefficient* resistors) and a Sensirion SHT (see Section 4.3) on the hybrids and the module testframe. Throughout the approximately five days of data taking, the temperature on the module frame ranged between -5°C and -2°C , the humidity was controlled with nitrogen inflow to keep the dew point below the module temperature, but was not particularly low and varied during the days of measurements.

The efficiency is defined as the fraction of hit clusters

$$\varepsilon_{\text{DUT}} = \frac{N_{\text{tracks}}^{\text{DUT+FEI4}}}{N_{\text{tracks}}^{\text{FEI4}}} \quad (6.14)$$

in the DUT and FEI4 for which a reconstructed track within $200\ \mu\text{m}$ (barrel module) or $500\ \mu\text{rad}$ (end-cap module) exists. The threshold scans can be used to extract the distribution of collected charge by inferring that the difference of the signal between two threshold values is produced by deposited charge equal to the threshold difference between those two points [17]. By fitting the data points with a skewed error function the most probable value for the collected charge can be determined, which is why this kind of plot is normally referred to as s-curves.

The s-curves resulting from the bias ramps of the R0 module is shown in Fig. 6.28. Each of the data points shown represents one measurement run with $\sim 100k$ recorded events which were subsequently reconstructed and analysed as described in Section 6.4.3. The small embedded plot is the result of a pedestal scan, which is taken without beam and with auto-triggering the telescope instead, yielding the noise occupancy seen at small thresholds. During the voltage ramp up, one can

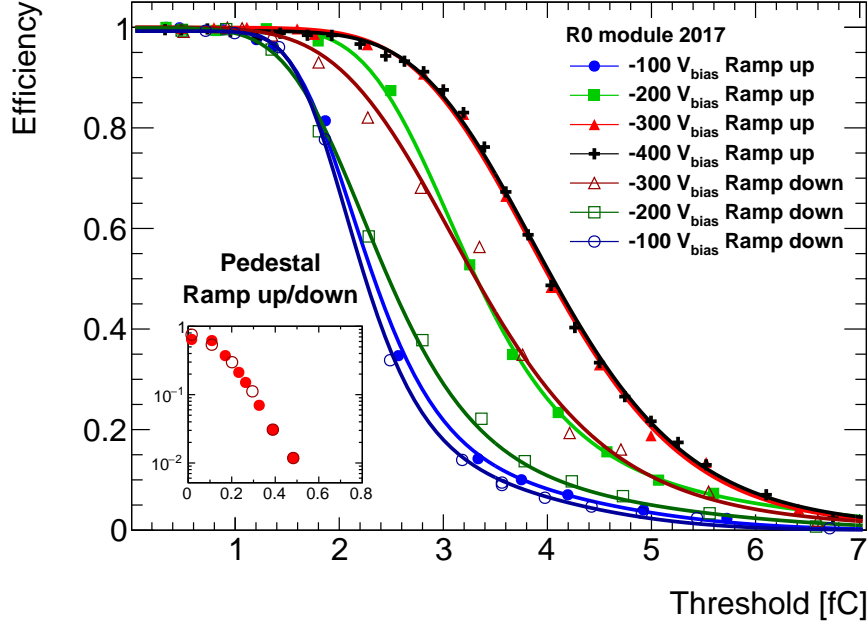


Fig. 6.28: Efficiency versus threshold data points and fitted s-curve of the R0 module at the DESY testbeam campaign from 2017. Filled markers represent runs during the ramp-up procedure, open markers indicate data points taken during the ramp-down scans. The embedded small plot shows the noise occupancy of the investigated ASIC measured with pedestal scans during the voltage ramps.

see a shift of the s-curve flank towards higher thresholds which signifies an equivalent increase in collected charge. The curves for -300 V and -400 V are on top of each other, expressing a saturation of collected charge, which confirms the findings of a depletion voltage $V_{\text{FD}} \simeq -300\text{ V}$ during the R0 sensor evaluation [40].

When comparing the s-curves obtained for the voltage ramp up and the respective ramp down, there is a significant discrepancy between the two. The collected charge in the -200 V and -300 V threshold scans is lower by $\sim 0.5\text{ fC}$. However, as can be seen in the results from the pedestal scans displayed, that loss of collected charge does not come from an increase in noise occupancy, which stayed constant. Instead, when investigating the average cluster size in Fig. 6.29, one can see that while the efficiency decreases on the ramp down scans, the cluster size increases in comparison to the ramp up threshold scans. Again, from the noise occupancy curves it can be concluded that this difference cannot be attributed to noise, as the noise occupancy for thresholds $> 0.5\text{ fC}$ is negligible.

Such a result is exactly what would be expected according to the charge imprint and surface potential model of long-term biasing consequences and its corresponding changes within the sensor. The cluster size increases due to more charge sharing between neighbouring strips which stems from the changes in the weighting field. At low thresholds $thr \lesssim 1\text{ fC}$ such a hit will still be registered as the signal exceeds the threshold of all strips in the whole, larger hit cluster and hence no change in the efficiency. At intermediate thresholds $1\text{ fC} \lesssim thr \lesssim 1.4\text{ fC}$ the cluster size decreases to similar values

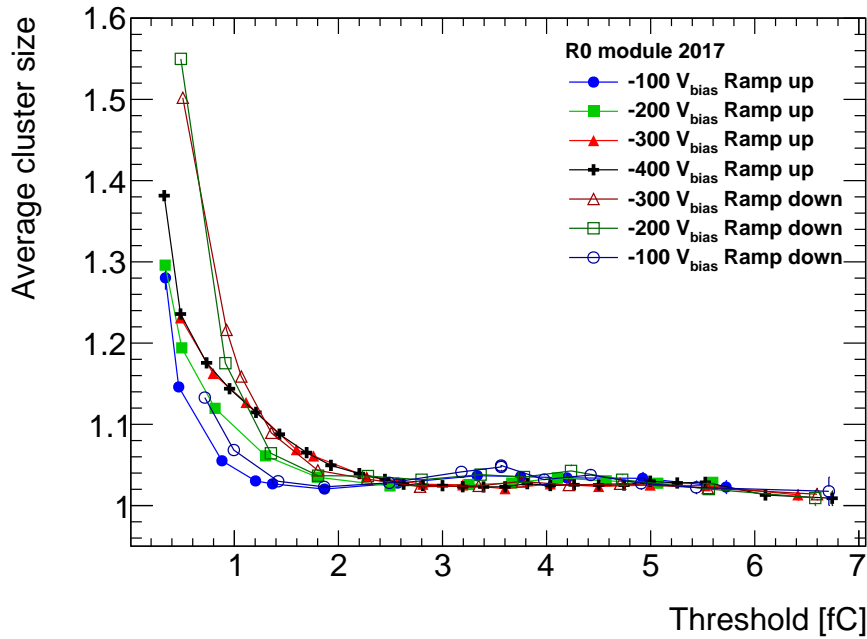


Fig. 6.29: Average cluster size versus threshold for the R0 module at the DESY testbeam campaign from 2017. Filled markers represent runs during the ramp-up procedure, open markers indicate data points taken during the ramp-down scans.

as those for the ramp down scans because the collected charge in strips adjacent to the central hit strip is not sufficient anymore to exceed the threshold. At even higher thresholds, the charge in the central hit strip becomes increasingly insufficient due to the charge fraction shared with its neighbouring strips, ultimately resulting in a significantly lower efficiency compared to the initial ramp up.

The success of seeing the effect of the charge imprint and surface potential affect tracking reliability resulted in this procedure now being one of the staple tests to perform during ITk Strips testbeam campaigns. Unfortunately, in the subsequent DESY testbeam this result could not be reproduced, as can be seen in Fig. 6.30. The three modules for which results are shown in this work show neither a reduction in tracking efficiency nor a significant increase in cluster size. One explanation for this is most likely the extensive workbench testing performed on those modules under full bias prior to them being tested in the testbeam. Unlike in the previous testbeam campaign, the modules were not given enough time or appropriate conditions to recover from the prior testing. Another factor was that during the 2018 DESY testbeam the humidity inside the box was kept much lower due to increased nitrogen flush. As will be shown in Section 6.7.2, having extremely dry conditions can lead to what can be considered a freeze-out of essential charge movement processes and therefore a very slow development or regression of the features. It has to be noted that absolute values of the different collected charges cannot directly be compared between different DUTs, as it largely depends on the ASICs used and usually even varies by a fair margin between chips on the same module.

6.5 Tracking reliability of sensors under long-term operation

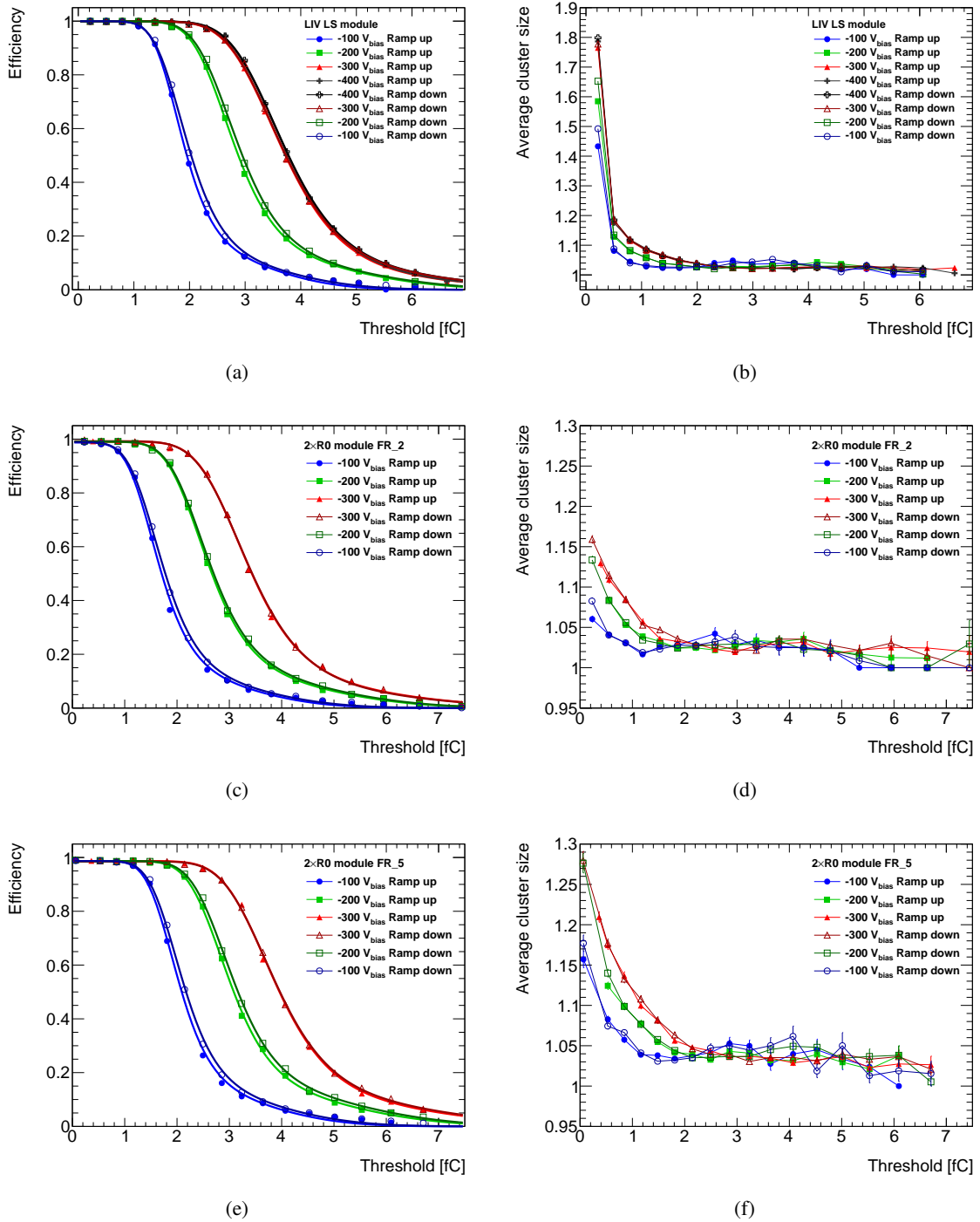


Fig. 6.30: Efficiency (a,c,e) and average cluster size (b,d,f) versus threshold for the long-strip module produced in Liverpool and the modules which constituted the double-sided R0 module, measured during the DESY testbeam campaign from 2018. Filled and open markers indicate data taken during the ramp up/down respectively.

6.5.2 Testbeam results of an irradiated module

The testbeam investigations of an irradiated R0 has been intended to be a benchmark to compare the performance of a module irradiated as a whole with prior results for those built from individually irradiated components. As such the module performance at, or even beyond the prospected lifetime can be evaluated. Also, those measurements would allow an examination of whether long-term biasing still has an impact on irradiated modules. The testing of the irradiated full end-cap module with an R0 sensor has been conducted at the CERN SPS due to the availability of the essential cooling box and its vicinity to the irradiation site.

The R0 module in question has been proton-irradiated at CERN PS to a level of $1.63 \times 10^{15} \text{ n}_{\text{eq}}/\text{cm}^2$, more than 50% above the expected lifetime dose which already includes a safety factor of 2. This heavy irradiation resulted in thermal runaway issues, despite the module being operated in cooled air at -50°C , so that, firstly, only one hybrid at a time has been used to minimise the heat load and, secondly, the module had to be operated below full depletion by a large margin, but despite that, the bias had to be reduced over the course of the testbeam runs. Due to the irradiation not only the sensor but also the electronics suffered, with two of the 17 ABC130 chips already dead and the AMACv2 control chip in an unstable state, which ultimately lead to it becoming unresponsive midway through the testbeam campaign.

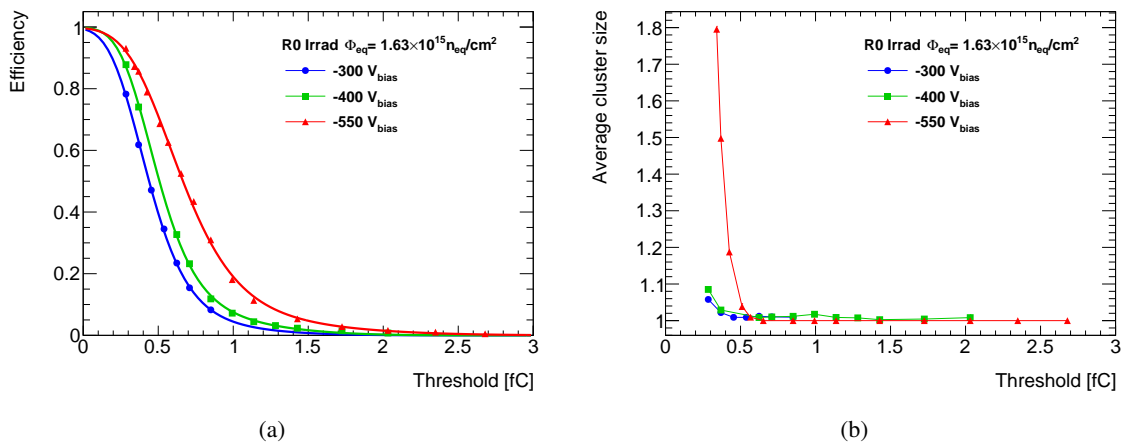


Fig. 6.31: Efficiency (a) and average cluster size (b) versus threshold of the irradiated R0 module measured during the CERN SPS testbeam campaign 2018.

The s-curves and the average cluster size of the irradiated R0 module measured during threshold scans at different V_{bias} during a bias ramp-up in the beginning of the testing sequence are shown in Fig. 6.31. The quoted voltages here were the supply settings, however, the effective voltage drop over the sensor p-n junction was much lower due to losses in the HV delivery as a consequence of the reduced bulk resistivity. From the apparent extremely low collected charge and already high cluster size, any additional effect from long-term biasing would most likely be overshadowed, even more so since the underlying processes of charge accumulation are fundamentally similar.

6.6 Deep-level transient spectroscopy

Deep-level transient spectroscopy (DLTS) is a spectroscopic method normally used to identify and characterise energy levels of defect states in semiconductor devices. This measurement technique uses transient signals in current, voltage, or capacitance generated from relaxation transitions to determine trap concentrations, thermal activation energies, and capture cross sections. The relaxation processes from or into trap states is initiated by either abrupt changes of the bias voltage or illumination from a light source. The method developed for the characterisation of the ITk Strip Sensor prototypes is a variant of the original capacitance DLTS (C-DLTS), originally proposed by D. V. Lang [108], that has been adapted to the specific task of investigating the charge trapping dynamic in the Si/SiO₂ interface.

6.6.1 Principle of capacitance DLTS

The goal of conventional (C-)DLTS is to obtain information about defect levels in the depletion region of a p-n junction or Schottky barrier by analysing capacitance transients resulting from a return of trap occupation to a thermal equilibrium state at different temperatures. The following explanation will be given on the basis of an n-in-p DUT which corresponds to the ITk sensors investigated. As the physics principles of DLTS measurements are completely general, an equivalent explanation for p⁺n-devices could be given by just changing some of the notations.

Assuming a defect with concentration N_t and an energy level E_t and provided the Fermi level is known, its occupation by either electrons or holes can be calculated using Fermi statistics according to [54]

$$\begin{aligned} n_t &= N_t \frac{1}{1 + \exp\left(+\frac{E_t - E_F}{k_B T}\right)} = N_t F(E_t) , \\ p_t &= N_t \frac{1}{1 + \exp\left(-\frac{E_t - E_F}{k_B T}\right)} = N_t (1 - F(E_t)) . \end{aligned} \quad (6.15)$$

In this definition, any defect level not being occupied by an electron is considered to be occupied by a hole and vice versa. Hence, the electron and hole occupation of trap levels fulfil

$$N_t = n_t + p_t . \quad (6.16)$$

Similar to the shallow level of dopants used in fabricating n and p-type silicon and interface states, one can differentiate between donors and acceptors in trap levels. An acceptor occupied by an electron is negatively charged while it is neutral when occupied by a hole. In contrast to this, a donor is either neutral or positively charged if occupied by an electron or hole, respectively (see Fig. 6.15). In this way the occupation of defect levels has an impact on the space charges in the depletion region of a p-n junction.

During steady-state operation, trap states of an n-in-p diode are in an equilibrium described by *Shockley-Read-Hall (SRH) statistics* [109, 110]

$$\left. \frac{\partial n_t}{\partial t} \right|_{\text{capture}} = \begin{cases} c_n p_t n & e^- \text{ capture} \\ -c_p n_t p & h^+ \text{ capture} \end{cases} \quad \text{and} \quad \left. \frac{\partial n_t}{\partial t} \right|_{\text{emission}} = \begin{cases} -e_n n_t & e^- \text{ emission} \\ e_p n_t & h^+ \text{ emission} \end{cases} . \quad (6.17)$$

Minority carriers, electrons in this case, have *thermal capture and emission coefficients* c_n and e_n , respectively, while holes as majority carriers are being captured and emitted depending on the coefficients c_p and e_p . This results in the net change of trap occupation [54]

$$\frac{dn_t}{dt} = (c_n p_t n - e_n n_t) - (c_p n_t p - e_p n_t) . \quad (6.18)$$

Moreover, from the *principle of detailed balance* in equilibrium, the emission and capture rates are equal, so that a relation between the corresponding coefficients can be derived

$$e_{n,p} = c_{n,p}(n, p) \left(\frac{p_t}{n_t} \right)^{\pm 1} = c_{n,p} n_i \exp \left(\pm \frac{E_t - E_{Fi}}{k_B T} \right) = c_{n,p} N_{C,V} \exp \left(\pm \frac{E_t - E_{C,V}}{k_B T} \right) . \quad (6.19)$$

Here the formulas for n_i , the intrinsic charge carrier density, as well as n, p , the density of states in the conduction and valence bands, has been used, all of which which can be found in most standard textbooks, e.g. [87].

1. Quiescent reverse bias The DLTS procedure, as displayed in Fig. 6.32 for both types of charge carrier traps, starts with the device in a quiescent state under reverse bias V_R (top row, 1.). All traps are in the depletion region which spans most of the bulk thickness. Due to the negligibly small concentration of free charge carriers in the space charge region, the capture rates into traps are assumed to be zero and dn_t/dt is reduced to being defined by the emission rates which then give a net occupation of the trap level as [54, 108]

$$n_t = \frac{e_p}{e_n + e_p} N_t \quad \text{and} \quad p_t = \frac{e_n}{e_n + e_p} N_t . \quad (6.20)$$

Electron traps in n^+ -p-diodes are ones which tend to be empty of electrons ($n_t = 0$), and thus capable of capturing them. Likewise, a *hole trap* is one which tends to be full of electrons ($n_t = N_t$), and thus capable of having a trapped electron recombine with a hole, i.e. capture a hole. For that reason and according to Eq. 6.20, $e_n \gg e_p$ has to be satisfied by electron traps and $e_p \gg e_n$ by hole traps. Taking also into account the Boltzmann – for the occupation of states with low carrier density – or Fermi statistics (Eqs. 6.15 and 6.17), the respective emission rates depend exponentially on the difference between trap energy and either conduction (electron emission) or valence band (hole emission) and the temperature of the device. As a consequence of this factor, electron traps are usually closer to the conduction band while hole traps are in the lower half of the band gap.

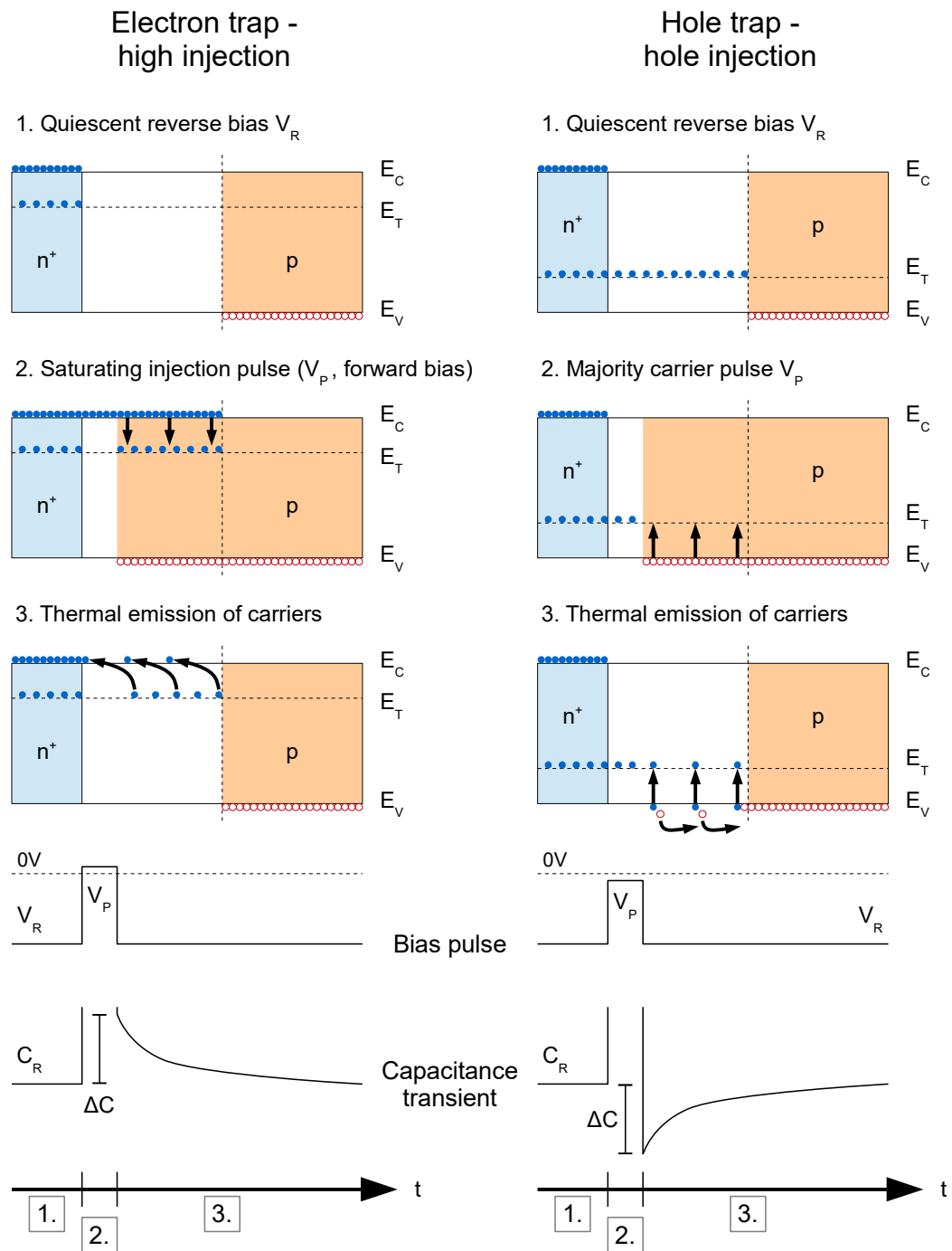


Fig. 6.32: Schematic procedure of C-DLTS measurements to evaluate trap level characteristics in an n-in-p silicon device. Depending on the nature of the traps being for minority (left) or majority (right) carriers, different bias pulses are required to fill the trap states and the resulting capacitance transient changes sign. The occupancy of trap states with electrons (blue) or holes (red) as well as the time dependence of the bias settings and capacitance transient are shown (adapted from [54, 108]).

2. Carrier injection In order to inject charge carriers into a quiescent p-n junction (see Fig. 6.32, second row, 2.), there are two main types of bias pulses. One can either use a *saturating injection pulse* which momentarily drives the diode into forward bias for the injection of both majority and minority carriers into the space charge region, or lower (or even switch off) the reverse bias for a *majority carrier pulse*. During the bias pulse V_p the occupation of trap states changes at a steady-state to

$$n_t = \frac{c_n}{c_n + c_p} N_t \quad \text{and} \quad p_t = \frac{c_p}{c_n + c_p} N_t \quad , \quad (6.21)$$

with the respective capture rates being proportional to their charge carrier concentration. As the defect states are below the Fermi level in the former space charge region during the pulse, they will end up being filled with electrons due to the capture rates there being much larger than the emission rates in this situation. The majority carrier pulse only introduces majority carrier, hence exclusively filling majority carrier (hole) traps. The forward injection pulse is used to introduce both a large enough number of electrons and holes so as to exceed any emptying process in all types of defects. This makes minority carrier capture possible but sensitivity to those levels is only possible for states with $c_n \gg c_p$. Other minority traps can be made accessible through other filling methods such as optical filling with short-wavelength lasers through the backplane [54].

3. Thermal carrier emission After the pulse the reverse bias V_R is re-established at $t = 0$ and the thermal emission of carriers yields a capacitance transient (see Fig. 6.32, third row, 3.). Due to the restored extension of the depletion region including the still occupied trap states, the electron occupation is again dominated by the emission rates. In the case of electron traps this leads to an emission of the electrons into the conduction band given sufficient thermal energy being present, and will ultimately result in the charge being swept away by the applied potential in the p-n junction. As capacitance is directly proportional to the effective space charge present at a given voltage V_R , and the amount of N_A^- charge in the p-side of the junction is larger directly after the bias pulse compared to the quiescent state with capacitance C_R , the measured capacitance transient starts off larger by ΔC and subsequently relaxes with the ongoing thermal emission of minority carriers from the defect states. For majority carriers the defect states have recombined with holes during the majority carrier pulse, thus reducing the amount of space charge in the junction right afterwards. Therefore, contrary to the case for minority carrier traps, the capacitance transient at $t = 0$ is reduced by ΔC and increases over time until equilibrium is reached again.

6.6.2 DLTS transient analysis for ITk Strip Sensors

The property of interest in unirradiated ITk Strip Sensors is not directly the concentration of defects in the bulk and their corresponding energy levels. This would be of concern for sensors after irradiation and studies have been performed which characterise radiation damage in silicon and try to improve on the radiation hardness of the bulk material, e.g. [54]. Instead, as can be seen from the increase of the

inter-strip capacitance and cluster size during testbeams, a study of the dynamics of electron traps in the Si/SiO₂ interface and the accompanying charge accumulation in oxide has become necessary. A measurement of interface trap levels directly on the tested prototype strip sensors is not possible due to the lack of metal contacts in the inter-strip region, but can be accomplished with test structures such as gate diodes which will be fabricated alongside future sensor batches for this purpose, among others. Nonetheless, the DLTS principle can be applied to the characterisation of mobile ionic charge accumulation in the oxide and the development of the gate boundary condition under long-term biasing of ITk sensors and details about the specific procedure used will be given below.

As shown in Section 6.1 and explained in Section 6.2, the shift of the boundary conditions on the outer oxide layer and the lateral charge imprint in the oxide lead to a filling of localised interface trap states with electrons and consequently an increase in C_{is} . This situation is equivalent to the filling of minority carrier trap states as described previously in Section 6.6.

The long-term biasing and associated change in the interface state towards stronger inversion upon lowering the bias serves as a variant of the injection pulse, whereupon lowering the bias from V_{const} more interface states have become available to act as electron traps and thereby become filled. The recovery time of the C_{is} hysteresis is in the order of days, which is much longer than any typical capture and emission time constants in semiconductors. Therefore, the observable C_{is} transient can be used to determine the characteristics, such as time constants and activation energies, of the processes responsible for the hysteresis as well as evaluate the trap concentration in the interface region induced by long-term biasing.

Interface trap concentration

The interface region can be regarded the same as an “electron trap” in the form of an acceptor level of concentration N_t that is negatively charged if occupied by an electron and neutral if not. The sensors bulk is of p-type with a measured effective doping concentration of $N_{eff,A12} \simeq N_A = 5.2 \times 10^{12} \text{ cm}^{-3}$. The traps are highly concentrated in a two-dimensional charge sheet at the interface and the inter-strip capacitance is measured versus reverse bias voltage which causes the space charge region to grow laterally and vertically from the strip-implants. When describing the inter-strip capacitance as a diode junction capacitance, albeit a more complicated one where (lateral) depletion depth does not necessarily grow linearly with $\sqrt{V_{bias}}$ as a result of the non-trivial inter-strip layout, it can again be seen as a function [111]

$$C_{is} \propto \sqrt{N_{SCR}} \quad \text{with} \quad N_{SCR}(t) = N_A + n_t(t) \quad , \quad (6.22)$$

where N_{SCR} is the concentration of ionised acceptors in the space charge region, which is composed of shallow-level dopants in the p-type bulk and the electron-occupied interface traps. In the lateral inter-strip region and its developing space charge region between neighbouring strips, these interface traps will be seen in the capacitance measurement as additional space charge, ultimately yielding an increase of the inter-strip capacitance by ΔC_{is} .

Tracking reliability and the effects of long-term operation

When conducting DLTS measurements, n_t and therefore ΔC_{is} becomes a time-dependent quantity. Moreover, under the assumption that only the depletion depth in the lateral junction is affected by the interface charges, one can forego the precise analytical description of C_{is} by focussing on the ratio of the capacitance transient and its initial value which at the same time is the limit for $t \rightarrow \infty$

$$\frac{C_{is}(t)}{C_{is,0}} \simeq \sqrt{1 + \frac{n_t(t)}{N_A}} \implies n_t(t) \simeq \left[\left(\frac{C_{is,0} + \Delta C_{is}(t)}{C_{is,0}} \right)^2 - 1 \right] N_A \quad . \quad (6.23)$$

With this relation one can derive the *saturation trap concentration* at the interface from $C_{is}(t = 0)$. This is the maximum increase of the inter-strip capacitance right after returning to the initial V_R after being biased at V_{const} until saturation. In literature, for example the original DLTS introduction [108], the approximation for small fractional increase $\Delta C(t)/C_0 \ll 1$ is often used. However, as seen in Section 6.1, ΔC_{is} is of the same order of magnitude as the initial value, therefore the full Eq. 6.23 has to be applied to characterise the DLTS measurements at hand.

Time constant and activation energy

The interface trap states in saturation are assumed to be filled with electrons only at a concentration of N_t . For that reason, during the initial emission period after returning to the steady-state bias $e_n \gg e_p$, and the time dependence of the trap emission is given by the integration of the corresponding SRH statistics differential equation. When only considering a single trap level, this yields [54, 111]

$$\left(\frac{C_{is}(t)}{C_{is,0}} \right)^2 \propto n_t(t) = n(t=0) \exp(-e_n t) \simeq N_t \exp\left(-\frac{t}{\tau_e}\right) \quad . \quad (6.24)$$

$\tau_e = e_n^{-1}$ is the *characteristic time constant* of electron emission from a particular trap level given by the reciprocal emission coefficient.

In terms of thermodynamics, the thermal transitions between trap states and band edge constitutes a change in (*Gibbs free*) energy, which can be written as a change in *enthalpy* and *entropy* $\Delta E = \Delta G = \Delta H - T\Delta S$. The change of entropy accompanying electron or hole emission is usually taken into account by introducing the *entropy factors* $X_{n,p} = \exp(\Delta S_{n,p}/k_B T)$, so that

$$\begin{aligned} E_C - E_t &= \Delta H_n - k_B T \ln(X_n) \\ E_t - E_V &= \Delta H_p - k_B T \ln(X_p) \quad . \end{aligned} \quad (6.25)$$

Moreover, the capture coefficient may be expressed in terms of the *capture cross section* $\sigma_{n,p}$ and the *thermal velocity* $v_{th,n,p}$

$$c_{n,p} = \sigma_{n,p} v_{th,n,p} = \sigma_{n,p} \sqrt{3k_B T / m_{dC,V}^*} \quad , \quad (6.26)$$

with $m_{dC,V}^*$ being the *effective carrier mass*. Using the relation between the capture and emission coefficients described in Eq. 6.19 and the introduced entropy factors one can write the emission coefficients as

$$\begin{aligned} e_{n,p} &= c_{n,p} X_{n,p} N_{C,V} \exp\left(-\frac{\Delta H_{n,p}}{k_B T}\right) \\ &= \sigma_{n,p} X_{n,p} v_{th,n,p} N_{C,V} \exp\left(-\frac{\Delta H_{n,p}}{k_B T}\right) \\ &= \sigma_{n,p} X_{n,p} \Gamma_{n,p} T^2 \exp\left(-\frac{\Delta H_{n,p}}{k_B T}\right), \end{aligned} \quad (6.27)$$

with the inherently temperature-independent constant [54]

$$\Gamma_{n,p} = \frac{v_{th}}{T^{1/2}} \cdot \frac{N_{C,V}}{T^{3/2}} = 2\sqrt{3} k_B^2 m_0 (2\pi/h^2)^{3/2} = 3.256 \times 10^{21} \text{ K}^{-2} \text{ cm}^{-2} \text{ s}^{-1} \quad . \quad (6.28)$$

As the entropy factor and the temperature dependence of the capture cross section are unknown, a temperature independent *effective cross section* $\sigma_{n,p}^{\text{eff}} = \sigma_{n,p} X_{n,p}$ is usually assumed, which finally yields the main equation by which the recorded transients are evaluated [54]

$$\ln(\tau_e T^2) = -\ln(\sigma_{n,p}^{\text{eff}} \Gamma_{n,p}) + \frac{E_A}{k_B T} \quad . \quad (6.29)$$

A plot of $\ln(\tau T^2)$ versus $1/T$ is known as an *Arrhenius plot*. From linear regression of the data points in an Arrhenius plot, the *activation energy* E_A , which is the enthalpy difference of the transition process under the assumption of temperature-independent cross section and constant entropy, can be determined from the slope, while the effective cross section can be extracted from the intercept.

Time constant extraction for continuous energy distribution

A single transition process can be described with a simple exponential decay with time constant τ in the general form

$$f(t) = A e^{-t/\tau} + B \quad , \quad (6.30)$$

where $\lambda = 1/\tau$ is the decay rate, A is the amplitude, and B the baseline offset. This simple relation, however, does not hold in the general case of traps with multiple energy levels, or superposition of more than one transition process each with its characteristic time constant. In such a case, the decay consists of a sum of n exponentials of the same general form (neglecting the baseline offset)

$$f(t) = \sum_{i=1}^n A_i e^{-t/\tau_i} \quad . \quad (6.31)$$

In the limit case where one has to expect a continuous distribution of energy levels, e.g. for interface traps, the decay is given by a spectral function $g(\lambda)$

$$f(t) = \int_0^{\infty} g(\tau) e^{-t/\tau} d\tau \quad . \quad (6.32)$$

A transient $f(t)$ of this form is the *Laplace transform* of the spectral function $g(\tau)$. In order to find the spectrum of emission rates one has to employ an algorithm that performs the inverse Laplace transform. Such an algorithm can discriminate between small variations of decay rates if given good enough signal to noise ratio and does not need any prior assumptions about the functional shape of the spectrum. DLTS measurements analysed this way are also referred to as *Laplace DLTS*.

Clearly, for the DLTS application for the ITk sensors at hand such a multi-exponential analysis is needed, considering that the dynamics of the transition processes as well as their exact number are unknown. Moreover, due to the extremely long decay times, the full transient curve can be obtained, however, the number of temperatures for which DLTS transients can be acquired is limited and therefore other analysis methods such as “double-boxcar” [108] cannot be effectively used.

For the following characterisation of the charge trapping dynamic, both fitting of discrete multi-exponential functions as well as Inverse Laplace Transform have been used and the respective results will be compared. The algorithm used to obtain the Inverse Laplace Transform is a MATLAB implementation of CONTIN [112].

6.6.3 DLTS setup and procedure

The instruments used in DLTS measurements are the same that have been used during sensor evaluation, the WayneKerr 6440B LCR meter and a Keithley 2410 SMU. In order to provide a controlled environment, the measurements were performed in the airtight box used for sensor breakdown investigations (see Section 5.2.2). The only difference to the aforementioned setups is the necessary control of sensor temperature. For that purpose the sensor was mounted in a modified module testframe, on which an additional piece of PCB with connector pins was attached to place the wirebonds on individual strips for the inter-strip capacitance measurement. The frame itself was attached onto a temperature-controlled jig which can be heated or cooled by connecting it to an external water chiller.

The procedure for DLTS measurements on ITk Strip Sensor prototypes is as follows: the sensor is biased at $V_{\text{bias}} = -600 \text{ V}$ for an extended period of time during which voltage sweeps are performed in regular intervals, similar to the hysteresis measurements in Section 6.1, in order to check the saturation of the sensor with regards to the C_{is} increase. When saturation has been reached, the bias is lowered to -50 V and the C_{is} transient is recorded immediately after the endpoint of the bias ramp. $V_{\text{bias}} = -50 \text{ V}$ has been chosen for the DLTS scans as C_{is} at this voltage has been observed to be quite sensitive with respect to long-term biasing and in saturation it is placed on the featured hysteresis plateau.

6.7 Charge trapping dynamics at the ITk Strip Sensor surface

The C_{is} hysteresis has been observed to recover over the period of a few days. In order to get a better understanding of the underlying processes, which have been explained in Section 6.2, and their dynamics, the resulting capacitance transient during the recovery period is scrutinised with help of the DLTS technique. DLTS is usually used to examine and quantify trap states in semiconductors, but using the features and dependencies of the hysteresis effect one can apply the same analysis to the ITk Strip Sensors to determine activation energies and effective cross sections. While the derived quantities may be referred to with similar terms, the processes under investigations are in their nature more akin to *thermal annealing* rather than trapping dynamics.

6.7.1 Temperature dependence of charge trapping

In order to determine the maximum trap concentration and extract the time constants through fitting exponential functions to the data, one has to employ the squared ratio of the time-dependent $C_{is}(t)$ over its limit for $t \rightarrow \infty$ which is $C_{is,0} = C_{is}^{sat}(V_{bias})$. When using a virgin sensor, one can determine $C_{is,0}$ during the voltage ramp at the start of the saturation biasing. However, considering the finite full recovery time of sensors, it is difficult to assure the sensor is in a virgin-like state prior to each new DLTS scan. As $\Delta C_{is}^{sat}(V_{bias} = -50\text{ V}) \simeq 0.25\text{ pF}$ has been determined before (see Section 6.1), the difference between that value and the unaffected C_{is} saturation value for the maximum applied bias $V_{bias} = -600\text{ V}$ can be used to calculate $C_{is,0}$ from the respective values prior to every DLTS saturation biasing.

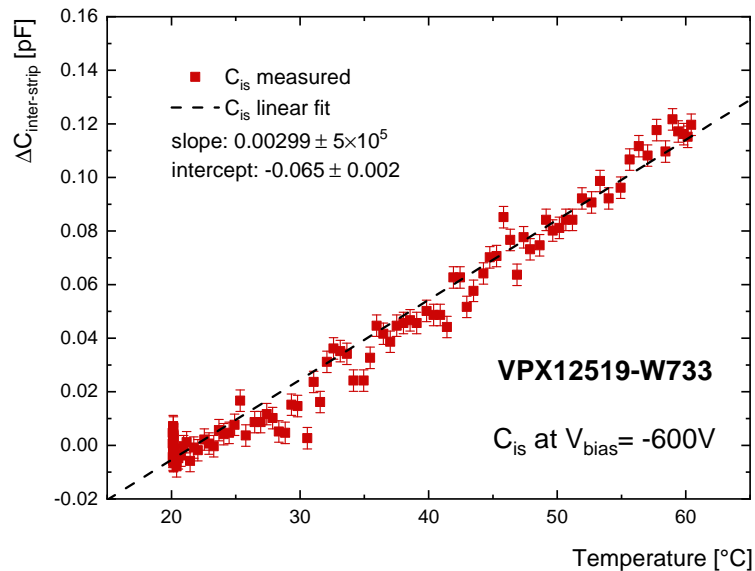


Fig. 6.33: Temperature dependence of C_{is} at a constant $V_{bias} = -600\text{ V}$. The temperature at the sensor has been increased with the water chiller from 20°C to 60°C .

Tracking reliability and the effects of long-term operation

Another complication arises from temperature-dependent surface effects. For example, additional band bending introduced at the Si/SiO₂ interface due to different thermal expansion coefficients of the materials, can make the saturation inter-strip capacitance also inherently temperature-dependent. For that reason, a measurement was performed during which C_{is} was recorded at constant $V_{bias} = -600$ V while the temperature was ramped up from 20°C to 60°C using the water chiller. The result of the scan is shown in Fig. 6.33 with a linear fit having been applied to the data points. Using the slope of the linear fit, $C_{is,0}$ can always be determined, even if the sensor was not in a virgin-like state prior to a DLTS scan.

DLTS measurements were initially conducted in dry conditions under constant nitrogen flush resulting in $RH \leq 1\%$ at all temperatures. This was done to eliminate the humidity dependency that is being expected from the model, and the underlying surface effects that are being investigated. The capacitance transients recorded at a constant bias of $V_{bias} = -50$ V for sensor temperatures of 40°C, 50°C, 60°C, and 70°C are plotted in Fig. 6.34. Lower temperatures were attempted but not completed, as the measurement time to record the transients to a sufficient decrease would have been too long because of the extremely slow observed transients. Higher temperatures would have been difficult to maintain, as the employed water chiller is not a closed system and even 70°C already warranted regular refilling of deionised water to compensate for evaporation losses.

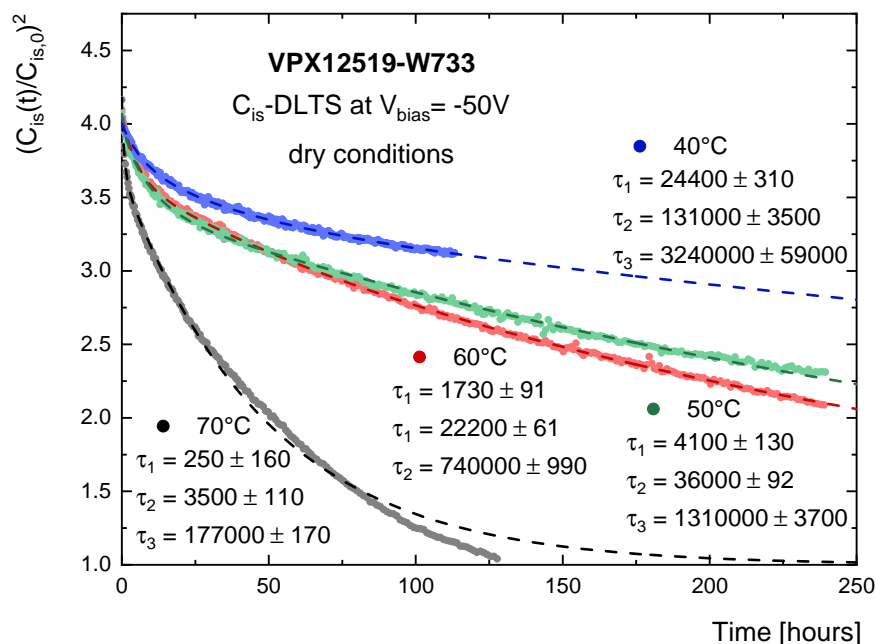


Fig. 6.34: DLTS transients taken in dry conditions $RH \leq 1\%$ for various temperatures plotted as $(C_{is}(t)/C_{is,0})^2$ versus time. The dashed lines are triple-exponential fits to the data points used for time constant extraction. The characteristic time constants from the exponential fits are listed with their fit uncertainties. Only 1% of collected data points are shown.

Time constants and trap concentration

In order to extract the time constants, two different methods were tested and compared. Firstly, a multi-exponential fit was performed with varying numbers of discrete exponential decay functions. In the fitting procedure the constant offset was fixed to $(C_{is}(t \rightarrow \infty)/C_{is,0})^2 = 1$ in correspondence to the underlying physics. It was found that a triple-exponential decay yields the least deviation seen in fitting residuals. A single-exponential function does not accurately reflect the overall shape of the measured transients while a double-exponential comes close, but does not quite capture the fast decay at the beginning of the transient. The fitted functions are plotted as dashed lines on top of the collected data points in Fig. 6.34 and the resulting time constants are given in the different plot legends.

The uncertainties quoted in the figure are solely those resulting from the fitting algorithm. For a final assessment of the time constant uncertainties, it has to be taken into account that the assumed (temperature-dependent) value of $C_{is,0}(T)$ can also be the source of additional errors. This additional uncertainty of τ was estimated by performing the same fitting procedure for DLTS curves with an assumed $C_{is,0}$ that differs from the initial value by $\pm 10\%$. Also, while the triple-exponential fit results in a function with the least deviation from the data points, the numerical stability of the obtained time constants relies on factors such as the boundaries of parameters during the fitting process. That is further exacerbated by the long tails of the transients, which could not be fully recorded due to the extremely slow processes. Therefore, during the assessment of the systematic uncertainties due to the asymptotic $C_{is,0}$ value, the fitting process was altered within sensible boundaries to estimate upper and lower limits on the time constants. It was found that those systematics clearly dominate over fitting uncertainty. The results for all time constants and the effective interface trap concentration (in cm^{-3}) calculated from Eq. 6.23 are summarised in Tab. 6.4.

Again, it has to be emphasised that the time constants derived here are not defined by the trapping dynamics of the interface levels directly, but rather by the development of the charge concentration in the oxide and the potential on the outer surface layer. The fact that the decay is defined by (at least) three time constants indicates three different access mechanisms in the underlying processes. As can be seen, the values for the times constants range from tens of minutes to several days and

Tab. 6.4: Summary of characteristic time constants and interface trap concentration of recorded DLTS transients in dry conditions. Systematic uncertainty estimates of the time constants are from variations in the fitting parameters and the asymptotic value $C_{is,0}$ and are shown together with uncertainties from the fitting algorithm. Uncertainties of N_t depend on the error of $C_{is,0}$ and the measured $N_{\text{eff}} \simeq N_A$.

	40°C $\begin{smallmatrix} \pm(\text{syst.}) \\ \pm(\text{fit.}) \end{smallmatrix}$	50°C $\begin{smallmatrix} \pm(\text{syst.}) \\ \pm(\text{fit.}) \end{smallmatrix}$	60°C $\begin{smallmatrix} \pm(\text{syst.}) \\ \pm(\text{fit.}) \end{smallmatrix}$	70°C $\begin{smallmatrix} \pm(\text{syst.}) \\ \pm(\text{fit.}) \end{smallmatrix}$
τ_1 [s]	24400 $\begin{smallmatrix} \pm 7400 \\ \pm 310 \end{smallmatrix}$	4100 $\begin{smallmatrix} \pm 1300 \\ \pm 130 \end{smallmatrix}$	1730 $\begin{smallmatrix} \pm 520 \\ \pm 91 \end{smallmatrix}$	250 $\begin{smallmatrix} \pm 150 \\ \pm 160 \end{smallmatrix}$
τ_2 [s]	131000 $\begin{smallmatrix} \pm 40000 \\ \pm 3500 \end{smallmatrix}$	36000 $\begin{smallmatrix} \pm 11000 \\ \pm 92 \end{smallmatrix}$	22200 $\begin{smallmatrix} \pm 6700 \\ \pm 61 \end{smallmatrix}$	3500 $\begin{smallmatrix} \pm 1800 \\ \pm 110 \end{smallmatrix}$
τ_3 [s]	3240000 $\begin{smallmatrix} \pm 650000 \\ \pm 59000 \end{smallmatrix}$	1310000 $\begin{smallmatrix} \pm 270000 \\ \pm 3700 \end{smallmatrix}$	740000 $\begin{smallmatrix} \pm 150000 \\ \pm 990 \end{smallmatrix}$	177000 $\begin{smallmatrix} \pm 36000 \\ \pm 170 \end{smallmatrix}$
N_t [$\times 10^{13} \text{cm}^{-3}$]	1.59 ± 0.40	1.60 ± 0.41	1.62 ± 0.41	1.65 ± 0.42

Tracking reliability and the effects of long-term operation

weeks, being smaller at higher device temperatures, just as expected. The effective saturation trap concentration extracted from the maximum increase of the inter-strip capacitance at $t = 0$ is constant within the relatively large uncertainties due to the potential error on the asymptotic value that the transient approaches.

Inverse Laplace Transform

One possible way to reduce the large uncertainties from the unknown offset of the exponential decay and the fitting boundaries would be to determine the Inverse Laplace Transform of the capacitance transient using the CONTIN algorithm. The main advantage of that algorithm is that no prior input about the transients such as the offset or the expected time constants is needed. Moreover, the output will be the full spectrum of time constants which can be found in the decay, which is not limited by the over-parametrisation of a least-squares fitting method when using too many exponentials.

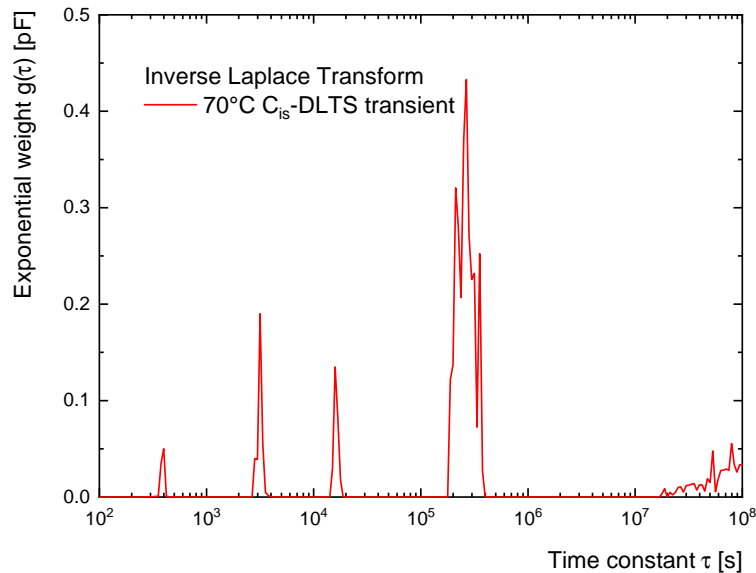


Fig. 6.35: Example of the Inverse Laplace Transform for the capacitance transient measured at 70°C numerically determined with the CONTIN algorithm.

An example output of an Inverse Laplace Transform for one of the transients is plotted in Fig. 6.35. The striking features of the plot shown are the three well-isolated peaks for $\tau < 10^5$ s, multiple peaks close together 10^5 s $< \tau < 10^6$ s, and the almost continuous spectrum thereafter. In the multiple close peaks and continuous spectrum one can see the disadvantage of the Laplace-DLTS method, as it aggressively discriminates between time constants of small variations. This trait was observed for the spectra of most other transients even for the low- τ peaks which are isolated in the plot shown, which would lead to even larger uncertainties when extracting the time constants compared to fitting discrete exponential functions. Therefore the results from the Inverse Laplace Transforms were ultimately not used in constructing the Arrhenius plots, but gave valuable hints for the exponential fits.

6.7 Charge trapping dynamics at the ITk Strip Sensor surface

In order to make full usage of the Laplace-DLTS method in this case, one would not only have to refine the CONTIN algorithm to discriminate less in the case of close, but otherwise isolated, peaks, e.g. by iterating the algorithm with different coarseness of the Laplace space. This would, however, make the algorithm even more computationally demanding than it already is, and developing and optimising such an algorithm goes beyond the scope of this work. Besides the improvements to the algorithm itself, the transients would have to be recorded for even longer periods of time, especially at lower temperatures, to yield clear peaks for large time constants.

Arrhenius plots

Using these time constants, Arrhenius plots according to Eq. 6.29 with $\ln(\tau T^2)$ versus $1/T$ were constructed to extract the quantities defining the dynamics of the underlying processes and are displayed in Fig. 6.36. A weighted linear regression is included to obtain the activation energy from the slope and the effective cross section from the intercept. The derived activation energies are given in the plot and summarised together with the effective cross section in Tab. 6.5.

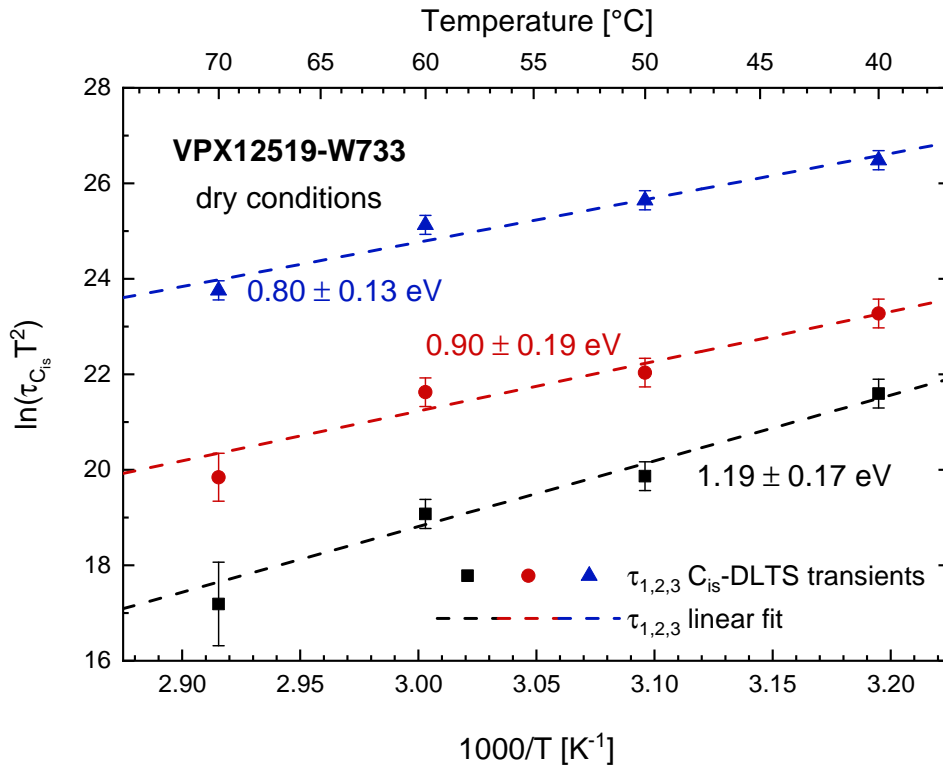


Fig. 6.36: Arrhenius plots $\ln(\tau T^2)$ versus $1/T$ obtained from C_{is} transients in dry conditions and linear fit to the data points. The activation energy derived from the slope is denoted for each time constant.

From the summarised quantities, it can be seen that not only is a fairly high activation energy necessary, but also that the effective cross sections are extremely small. The combination of these two

Tracking reliability and the effects of long-term operation

results explain the slow observed transients and the overall long recovery time. Considering that these quantities have been procured for the oxide layer, such long time constants are within expectation, albeit usually seen for example for annealing processes of radiation induced defects [85, 54, 87].

Tab. 6.5: Summary of activation energy and effective cross section extracted from the Arrhenius plots constructed from the results of exponential fits to recorded DLTS transients in dry conditions.

	τ_1	τ_2	τ_3
E_A [eV]	1.19 ± 0.17	0.90 ± 0.19	0.80 ± 0.13
σ_{eff} [cm ²]	$6 \times 10^{-15} - 6 \times 10^{-10}$	$1 \times 10^{-20} - 5 \times 10^{-15}$	$9 \times 10^{-23} - 5 \times 10^{-19}$

6.7.2 Humidity dependence of charge trapping

The recovery time for the hysteresis reported in Section 6.1 is in the order of a few days at room temperature ($\sim 20^\circ\text{C}$), which is significantly shorter compared to the transients obtained for the lowest temperature of the DLTS measurements (40°C). While part of that discrepancy can be attributed to the non-zero voltage being used as quiescent reverse bias during the recording of the capacitance transient, which has an influence on both mobile ionic charges and the outer surface layer boundary conditions in the hysteresis model, it would not affect the recovery time to such an extent.

Therefore, additional DLTS measurements have been conducted during which the humidity inside the test box was not lowered through an N_2 inflow. Instead a gas exchange with the ambient environment was enabled, thus keeping the relative humidity at the ambient level for each respective temperature. With these measurements and the comparison to the previous results in dry conditions, the influence of humidity on the recovery time of the system can be characterised and quantified.

As can be seen in the DLTS curves for ambient conditions shown in Fig. 6.37 and the time constants summarised in Tab. 6.6, the overall time needed is much shorter compared to the same transients recorded in a dry environment (Fig. 6.34). In particular, τ_3 is much smaller by about a factor of four, whereas the difference for the other time constants becomes larger the lower the temperature.

Tab. 6.6: Summary of characteristic time constants and interface trap concentration of recorded DLTS transients in ambient conditions.

	20°C $\begin{smallmatrix} \pm(\text{syst.}) \\ \pm(\text{fit.}) \end{smallmatrix}$	30°C $\begin{smallmatrix} \pm(\text{syst.}) \\ \pm(\text{fit.}) \end{smallmatrix}$	40°C $\begin{smallmatrix} \pm(\text{syst.}) \\ \pm(\text{fit.}) \end{smallmatrix}$	60°C $\begin{smallmatrix} \pm(\text{syst.}) \\ \pm(\text{fit.}) \end{smallmatrix}$
τ_1 [s]	$780 \begin{smallmatrix} \pm 240 \\ \pm 19 \end{smallmatrix}$	$3700 \begin{smallmatrix} \pm 1200 \\ \pm 84 \end{smallmatrix}$	$9000 \begin{smallmatrix} \pm 2800 \\ \pm 330 \end{smallmatrix}$	$2460 \begin{smallmatrix} \pm 740 \\ \pm 48 \end{smallmatrix}$
τ_2 [s]	$29100 \begin{smallmatrix} \pm 8800 \\ \pm 160 \end{smallmatrix}$	$25400 \begin{smallmatrix} \pm 7700 \\ \pm 1100 \end{smallmatrix}$	$61000 \begin{smallmatrix} \pm 19000 \\ \pm 3400 \end{smallmatrix}$	$18200 \begin{smallmatrix} \pm 5500 \\ \pm 1100 \end{smallmatrix}$
τ_3 [s]	$129000 \begin{smallmatrix} \pm 26000 \\ \pm 830 \end{smallmatrix}$	$298000 \begin{smallmatrix} \pm 60000 \\ \pm 850 \end{smallmatrix}$	$740000 \begin{smallmatrix} \pm 150000 \\ \pm 11000 \end{smallmatrix}$	$188000 \begin{smallmatrix} \pm 38000 \\ \pm 1300 \end{smallmatrix}$
N_t [$\times 10^{13}\text{cm}^{-3}$]	1.86 ± 0.47	1.73 ± 0.44	1.59 ± 0.40	1.77 ± 0.45

6.7 Charge trapping dynamics at the ITk Strip Sensor surface

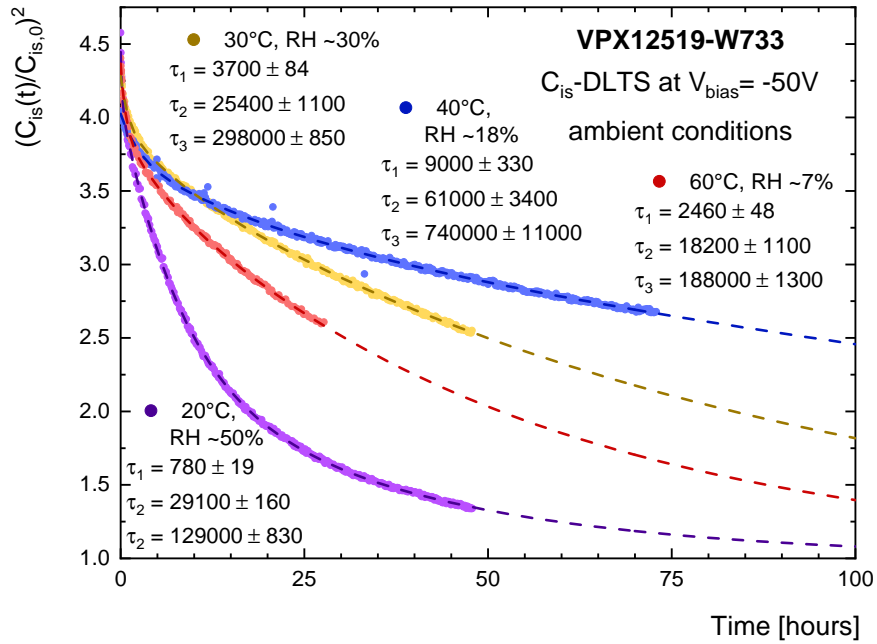


Fig. 6.37: DLTS transients taken in ambient conditions $RH(T = 20^\circ\text{C}) = 45 - 55\%$ for various temperatures plotted as $(C_{is}(t)/C_{is,0})^2$ versus time. The dashed lines are triple-exponential fits to the data points used for time constant extraction. The characteristic time constants from the exponential fits are listed with their fit uncertainties. Only 10% of recorded data points are shown.

Furthermore, unlike the previous DLTS measurements, the concentration of trapped charges contributing to ΔC_{is} now varies depending on the temperature, despite the effort to reach equal saturation before initiating the transient. While the slight deviations seen in dry DLTS can be attributed to minute differences in the saturation before reducing applied bias due to overall higher charge carrier mobility at higher temperatures, there seems to be a larger discrepancy between individual temperatures, albeit still within the margin of error.

Another change from dry to ambient DLTS can be seen in the shift of relative amplitudes obtained from the exponential decay fit. The values listed in Tab. 6.7 indicate that at ambient humidity not only is there an overall acceleration of all processes, but also a shift in the relative weight towards the fastest process described by τ_1 with $\mathcal{O}(1000\text{ s})$.

Tab. 6.7: Comparison of relative fitted decay curve amplitudes obtained for dry and ambient DLTS.

	40°C		60°C	
	dry	ambient	dry	ambient
A_1/A_3	0.101 ± 0.002	0.159 ± 0.004	0.031 ± 0.002	0.162 ± 0.003
A_2/A_3	0.159 ± 0.002	0.116 ± 0.004	0.197 ± 0.001	0.090 ± 0.003

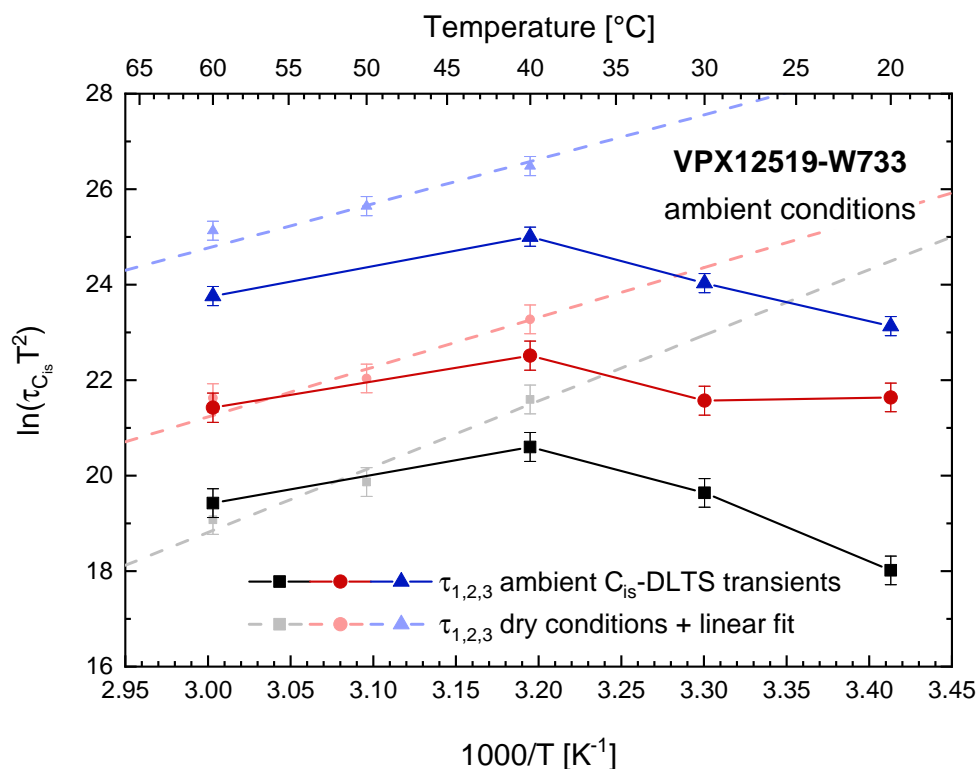


Fig. 6.38: Arrhenius plots $\ln(\tau T^2)$ versus $1/T$ obtained from C_{is} transients in ambient conditions (lines are a guide to the eye). Data for dry DLTS and respective linear fits are shown for comparison.

Similar to the dry DLTS results, Arrhenius plots have been constructed for the time constants extracted from ambient DLTS curves. The results are shown in Fig. 6.38 together with the previously obtained data points and linear fits for dry conditions.

When comparing the data points and the expected linear behaviour, there is an increasingly large deviation at lower temperatures, where the observed transient time constants are much smaller by orders of magnitude than expected from previous results. This indicates that the underlying processes on the oxide surface and within the bulk, which would normally require large activation energies, can be significantly accelerated in the presence of sufficient amounts water vapour.

For τ_1 and τ_2 , the temperature range between $30^{\circ}C$ and $40^{\circ}C$ seems to be the demarcation where those processes transition between dry-like behaviour and being accelerated by humidity. This is most likely due to a trade-off between temperature and humidity-assistance within the same process. As accumulated water on the sensor surface evaporates at higher temperatures, the fact that the time constants at high temperature are close to their values in dry conditions proves that the process that manifests itself in τ_1 and τ_2 relies on either moisture on the surface or high temperature. The final speed depends on the dominating contribution of the two.

τ_3 shows a similar transition between $30^{\circ}C$ and $40^{\circ}C$, but even at higher temperatures the respective values are smaller by approximately a factor of three compared to the same result from dry

6.7 Charge trapping dynamics at the ITk Strip Sensor surface

DLTS scans. This relation indicates that while the underlying process is also assisted by the dominant contribution of either sufficient thermal energy or water vapour present, it is at the same time always accelerated by the absolute amount of water vapour on the sensor surface, regardless of subsequent evaporation.

In conclusion, in the proposed model for the hysteresis $\tau_{1,2}$ is quite likely to stem from the regression of the gate boundary condition. Its development is dependent on the charge movement at the outer oxide surface which is determined by both temperature, through the Einstein relation of diffusion (Eq. 3.31), and humidity directly on the surface, which defines the surface conductivity. Therefore, as the temperature increases, the moisture on the surface increasingly evaporates which marks the reverting of the time constant to dry-like values. From its dependence on the absolute amount of water vapour present, τ_3 should be a manifestation of the mobile ionic charges in the oxide. Similar to what has been shown in the breakdown studies with respect to the humidity dependence, SiO_2 can degrade from H_2O diffusion [76, 77] given enough thermal energy, time, and being exacerbated by strong electric fields. All of which has been fulfilled in that situation as the sensor was also biased in equally damp conditions prior to recording the transient. The complexes in the oxide as a result from the reaction with diffused water can act in a similar way to mobile ionic charges, which would not only result in the observed higher trap concentration, but also in faster transients from the reformation of complexes in the oxide as an additional contribution to changes in the oxide charge distribution.

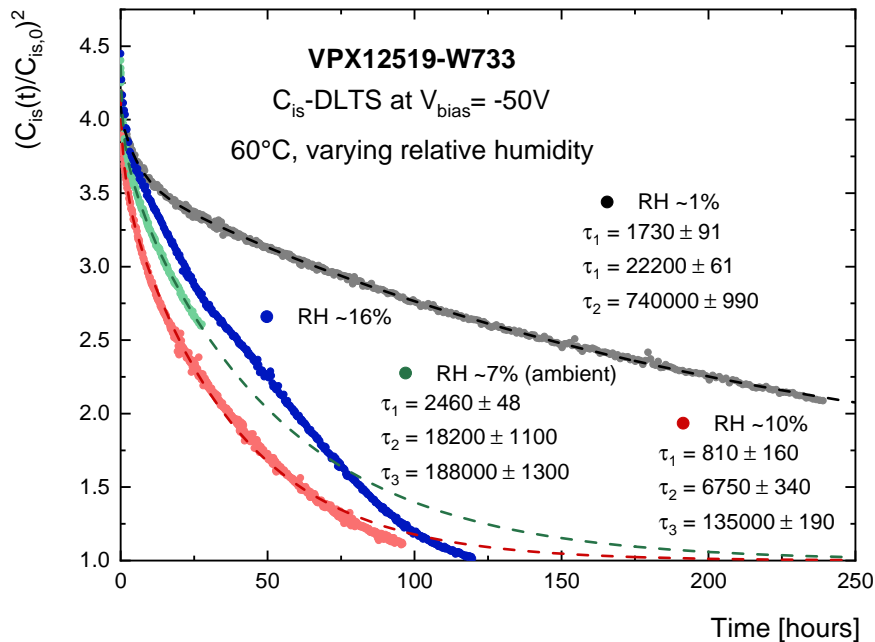


Fig. 6.39: Humidity dependence of DLTS transients at 60°C for varying relative humidity plotted as $(C_{is}(t)/C_{is,0})^2$ versus time. The dashed lines are triple-exponential fits to the data points.

Tracking reliability and the effects of long-term operation

In order to confirm these conclusions and further investigate the apparent humidity dependence, additional DLTS curves were recorded for the sensor at a temperature of 60°C but with artificially elevated humidity inside the sensor test box. The two additional curves recorded were taken for $RH \sim 10\%$ and $RH \sim 16\%$. Higher RH values were not possible due to the danger of condensation on the lid of the box. As can be seen from the DLTS curves in Fig. 6.39, when increasing the relative humidity beyond the ambient level, the transient is initially overall further accelerated. All three time constants with $\tau_{1,2}$, in particular, are reduced by a large margin most likely due to the higher surface conductivity. At even higher relative humidity, the transient does not follow the expected exponential decay anymore, but rather appears to be constructed of two separate exponentials. This further indicates that there seem to be two fundamental processes convoluted in each transient which react differently in the presence of humidity.

6.8 Summary and conclusions

Over the course of the investigation of the reliability of sensor quantities under long-term operation a significant change in inter-strip capacitance with the characteristics of hysteresis has been found. Upon fully investigating the observed effect and correlating the changes with known processes in MOS capacitors, a model was proposed explaining the behaviour as the consequence of a mobile ionic charge imprint in the oxide and establishing a positive surface potential on the outer oxide surface.

Further evidence regarding the viability of this model has been obtained through TCAD simulations which were able to reproduce the observed effects. The consecutive change in the electric field over time is reflected in the reduced tracking efficiency and increased cluster size during testbeam measurements of a module built from one of the prototype sensors. The impact of the effects described by the proposed model on SiO_2 properties is akin to radiation damage, as described in [113] among others. Hence this non-invasive, fully reversible, feature allows an insight into the behaviour of sensors with radiation damage in the oxide layer, and notably the recovery process is very similar to annealing processes. This is a unique opportunity, as under normal circumstances the characterisation of radiation induced defects is only possible at very low temperatures while standard pre-irradiation assessment is done at room temperature, and therefore the temperature dependent dynamic has to be extrapolated and is afflicted with errors and uncertainties.

Using a novel application of the C-DLTS technique, the different time constants of the underlying charge movement processes, as well as the concentration of interface trap states, have been determined. By constructing Arrhenius plots from the time constants extracted at different temperatures, the activation energies of the processes have been obtained. Moreover, using the same technique with measurements in different humidity conditions, the impact of humidity on reaching equilibrium conditions with regards to oxide surface charges was quantified for the first time. In contrast to what was concluded in [86], the outside oxide surface charges will still change in very dry conditions both during accumulation and recovery, given enough time or higher thermal energy. But, as previously described, the recovery process is accelerated by orders of magnitude at room temperature in the

presence of elevated humidity, which results in deviation from the standard linear behaviour of Arrhenius plots for a dry environment.

Future investigations into the process dynamics and further quantification of the impact of humidity would require DLTS measurements in a very precise environmental chamber. With this, one could also clearly distinguish whether a certain process relies on relative or absolute humidity. One additional effect, of which indications have been observed, but could not have been followed up on with the present setup, was the humidity conditions during the saturation process prior to the capacitance transient. By pairing different dry or damp conditions during the saturation process and transient, respectively, it could be investigated whether the observed humidity dependence for individual processes is already established during the saturation step or is only connected to the environment during the transient. Additional measurements regarding the effective trapping times of the interface states themselves, rather than a convolution with the surface recovery time, could be done on gated diode test structures or using Transient Current Technique [52, 114], among others.

6.8.1 Consequences for ITk operation

The findings reported and the conclusions drawn in this chapter demonstrate that during long-term operation of the ITk Strip Detector deviations of performance have to be taken into account. In particular, changes in tracking efficiency and charge sharing, as they have been observed in testbeam measurements, could be problematic if occurring unexpectedly.

As the underlying processes are induced by charges in the oxide bulk and on its outer surface, and hence akin to radiation damage in oxide, the contribution of long-term biasing towards changes in sensor performance should become negligible with increasing exposure to ionising radiation from particle collisions. Since it has yet to be determined at which level of fluence radiation damage becomes the dominant factor for surface properties, the effects of long-term operation should not be neglected in the early stages of detector lifetime. Fortunately, from the detailed characterisation of the hysteresis effect it can be concluded that the detector properties are only affected if the sensor bias is lowered from a previously higher value. Therefore, as long as the bias is only increased during the early stages of the detector lifetime, for example to counter bulk degradation from radiation damage, the impact on the tracking performance would be minimal. Furthermore, the cold and dry environment, in which the detector will be operated, effectively leads to a freeze-out of the underlying processes, as seen in the results of DLTS measurements. However, the finalised ITk will be continuously operated for weeks, while over the course of this work sensors have only been tested on a time scale of days, thus even very slow processes may gradually become of importance.

In summary, the properties and dynamics of the processes characterised in this investigation of long-term operational effects indicate that there will most likely not be a significant impact on the performance of the ITk Strip Detector given its proposed operational schedule and environment. However, the effects should be monitored as part of both quality assurance of sensors, and in coming testbeam campaigns with full modules, to prevent unexpected changes from going unnoticed.

Chapter 7

Summary, conclusion, and outlook

With the preparation for the Inner Tracker (ITk) Upgrade and the implementation of any new technology in future detector systems, rigorous testing of all characteristics is necessary to assess the quality of components and the longevity of any hardware. In the work that constitutes this thesis, the focus was on measuring prototype sensors in detailed investigations of their performance and the influence of environmental conditions seen in multiple instances throughout that investigation.

Prototype sensor evaluation

A detailed evaluation of the ATLAS12 and ATLAS17LS generation of prototype sensors for the ITk Strip Detector has been conducted and the findings were presented in Chapter 4. This included the testing of a wide range of mechanical and electrical properties. The testing procedure used for prototype sensors will also be the basis of Sensor Quality Control (QC) during the production phase of the ITk.

The vast majority of sensors were found to adhere to the technical specifications required for reliable operation under the prospected environment of the HL-LHC. However, while short-term tests yielded generally satisfactory results, many sensors did not exhibit the required leakage current stability during operation for longer periods of time and, furthermore, the onset of current breakdown has been observed to deteriorate over time. A large variability in test results was seen with a dependence on the history of operation for the individual devices. These results triggered further investigation into the breakdown characteristics and the overall long-term reliability.

Sensor breakdown

As a consequence of the observed leakage current instability, the nature and causes, as well as the effects, of electrical sensor breakdown were scrutinised. The focus was on mechanical stress and humidity as the potential origin, as well as TCAD simulations for in-depth studies e.g. of the electric field configuration inside the sensor.

Summary, conclusion, and outlook

The results were that the breakdown voltage in IV measurements without constant bias voltage between individual scans is significantly reduced when the relative humidity of the testing environment increases to values $> 20\%$. Mechanical stress itself was not found to directly influence $V_{\text{breakdown}}$, but stress in the passivation layer could compromise its function through microscopic damage and hence exacerbate any humidity sensitivity. Sensors, whose performance was presumably deteriorated by the extended exposure to an ambient humidity environment, were successfully reconditioned using a bake-out treatment in a vacuum oven.

The conclusions of these findings are, firstly, that for Sensor QC during production particular care has to be taken to only test sensors in a dry environment, if possible, or to minimise exposure time to ambient conditions. Secondly, as sensor reconditioning has been shown to be possible via bake-out, it could be used to counter the adverse effects accumulated during testing or handling in ambient humidity.

Long-term operation

Over the course of investigation regarding the reliability of sensor quantities under long-term operation a significant change in inter-strip capacitance with the characteristics of hysteresis has been found. Upon fully investigating the observed effect and correlating the changes with known processes in MOS capacitors, a model was proposed explaining the behaviour as the consequence of a mobile ionic charge imprint in the oxide and establishing a positive surface potential on the outer oxide surface.

Further evidence regarding the viability of this model has been obtained through TCAD simulations which were able to reproduce the observed effects. The consecutive change in the electric field over time is reflected in the reduced tracking efficiency and increased cluster size during testbeam measurements of a module built from prototype sensors. The impact of the effects described by the proposed model on SiO_2 properties is akin to radiation damage. Hence this non-invasive, fully reversible, feature allows an insight into the behaviour of sensors with radiation damage in the oxide layer, and notably the recovery process is very similar to annealing processes.

Using a novel application of the C-DLTS technique, the different time constants of the underlying charge movement processes, as well as the concentration of interface trap states, have been determined. By constructing Arrhenius plots from the time constants extracted at different temperatures, the activation energies of the processes have been obtained. Moreover, using the same technique with measurements in different humidity conditions, the impact of humidity on reaching equilibrium conditions with regards to oxide surface charges was quantified for the first time. It was found that while the recovery processes will still happen in very dry conditions, given enough time or higher thermal energy, it can be accelerated by orders of magnitude even at room temperature in the presence of elevated humidity, which results in deviation from the simple behaviour governed by Boltzmann statistics for a dry environment.

The reported findings of changes in tracking efficiency and charge sharing, in particular, could also have consequences during long-term operation of the finalised ITk Strip Detector. With increasing

radiation damage this should become negligible, as the underlying processes are induced by charges in the oxide bulk and on its outer surface, like radiation damage itself. Also, from the dynamics of the observed processes it can be concluded that the cold and dry environment for detector operation will also effectively freeze out the development of both the charge imprint on the oxide as well as the positive potential at the outer oxide surface. Nonetheless, given the continuous operation of the ITk for weeks, even very slow processes may play an important role. Hence caution should be taken in the early stages of the tracker lifetime as well as necessary monitoring should be part of both quality assurance of sensors and modules testing to prevent unexpected changes from going unnoticed.

Outlook

The work for this thesis and the obtained results are connected to a variety of topics impacting both current sensor testing as well as future tracker performance and development.

The implications on sensor testing and module assembly during production have been explained in great detail throughout this thesis. Nonetheless, the final outlook towards successfully building the strip detector for the new ATLAS Inner Tracker is overall positive as the influence of environmental conditions has now been acknowledged and precautions are being taken.

The observed changes in the charge configuration at sensor surfaces and Si/SiO₂ interfaces may not play a huge role in the performance of the ITk, in particular, considering the expected radiation damage. However, it could become an unwanted effect in future tracker development in the case of sensors with higher sensitivity to surface charge states. Further studies on the characteristics and dynamics of those processes will depend on the availability of specific test structures and more specialised testing environment.

References

- [1] ATLAS Collaboration: G. Aad, et al., *The ATLAS Experiment at the CERN Large Hadron Collider*, J. Inst. **3(08)**, S08003 (2008)
- [2] CMS Collaboration: S. Chatrchyan, et al., *The CMS Experiment at the CERN LHC*, J. Inst. **3**, S08004 (2008)
- [3] L. Evans, P. Bryant, *LHC Machine*, J. Inst. **3(08)**, S08001 (2008)
- [4] ATLAS Collaboration: G. Aad, et al., *Measurements of Higgs boson production and couplings in diboson final states with the ATLAS detector at the LHC*, Phys. Lett. **B726**, 88 (2013), [Erratum: Phys. Lett. B734,406(2014)], 1307.1427
- [5] CMS Collaboration: S. Chatrchyan, et al., *Observation of a new boson at a mass of 125 GeV with the CMS experiment at the LHC*, Phys. Lett. B **716(1)**, 30 (2012)
- [6] B. Lemmer, *Measurement of spin correlations in $t\bar{t}$ events from pp collisions at $\sqrt{s} = 7$ TeV in the lepton + jets final state with the ATLAS detector*, Ph.D. thesis, University Göttingen, II. Phys. Inst., Göttingen (2014), II.Physik-UniGö-Diss-2014/02, CERN-THESIS-2014-129, 1410.1791
- [7] Particle Data Group: M. Tanabashi, et al., *Review of Particle Physics*, Phys. Rev. D **98**, 030001 (2018)
- [8] S. L. Glashow, *Partial-symmetries of weak interactions*, Nuclear Physics **22(4)**, 579 (1961)
- [9] S. Weinberg, *A Model of Leptons*, Phys. Rev. Lett. **19**, 1264 (1967)
- [10] A. Salam, *Weak and Electromagnetic Interactions*, Conf. Proc. **C680519**, 367 (1968)
- [11] UA1 Collaboration: G. Arnison, et al., *Experimental observation of isolated large transverse energy electrons with associated missing energy at $s = 540$ GeV*, Phys. Lett. B **122(1)**, 103 (1983)
- [12] UA1 Collaboration: G. Arnison, et al., *Experimental observation of lepton pairs of invariant mass around $95 \text{ GeV}/c^2$ at the CERN SPS collider*, Phys. Lett. B **126(5)**, 398 (1983)
- [13] UA2 Collaboration: M. Banner, et al., *Observation of single isolated electrons of high transverse momentum in events with missing transverse energy at the CERN $p\bar{p}$ collider*, Phys. Lett. B **122(5)**, 476 (1983)
- [14] UA2 Collaboration: P. Bagnaia, et al., *Evidence for $Z^0 \rightarrow e^+e^-$ at the CERN $p\bar{p}$ collider*, Phys. Lett. B **129(1)**, 130 (1983)

References

- [15] P. W. Higgs, *Broken Symmetries and the Masses of Gauge Bosons*, Phys. Rev. Lett. **13**, 508 (1964)
- [16] F. Englert, R. Brout, *Broken Symmetry and the Mass of Gauge Vector Mesons*, Phys. Rev. Lett. **13**, 321 (1964)
- [17] ATLAS Collaboration, *Technical Design Report for the ATLAS Inner Tracker Strip Detector*, Technical Report CERN-LHCC-2017-005. ATLAS-TDR-025, CERN, Geneva (2017)
- [18] ATLAS Collaboration, *Expected Tracking Performance of the ATLAS Inner Tracker at the HL-LHC*, Technical Report ATL-PHYS-PUB-2019-014, CERN, Geneva (2019)
- [19] LHCb Collaboration: A. Augusto Alves, et al., *The LHCb Detector at the LHC*, J. Inst. **3**, S08005 (2008)
- [20] ALICE Collaboration: K. Aamodt, et al., *The ALICE experiment at the CERN LHC*, J. Inst. **3(08)**, S08002 (2008)
- [21] E. Mobs, *The CERN accelerator complex. Complexe des accélérateurs du CERN* (2016), general Photo, URL <https://cds.cern.ch/record/2197559>
- [22] HL-LHC Industry: Industry Relations and Procurement Website for the HL-LHC project, *Project schedule*, URL <https://project-hl-lhc-industry.web.cern.ch/>
- [23] ATLAS Collaboration, *ATLAS inner detector: Technical Design Report vol. 1*, Technical report, CERN, Geneva (1997)
- [24] ATLAS Collaboration, *ATLAS inner detector: Technical Design Report vol. 2*, Technical report, CERN, Geneva (1997)
- [25] ATLAS Collaboration, *ATLAS liquid-argon calorimeter: Technical Design Report*, Technical report, CERN, Geneva (1996)
- [26] ATLAS Collaboration, *ATLAS tile calorimeter: Technical Design Report*, Technical report, CERN, Geneva (1996)
- [27] ATLAS Collaboration, *ATLAS muon spectrometer: Technical Design Report*, Technical report, CERN, Geneva (1997)
- [28] ATLAS Collaboration, *ATLAS magnet system: Technical Design Report*, Technical report, CERN, Geneva (1997)
- [29] J. Große-Knetter, *Vertex Measurement at a Hadron Collider – The ATLAS Pixel Detector*, Habilitation, University Bonn, Bonn (2007), *BONN-IR–2008-04*
- [30] G. Aad, et al., *ATLAS pixel detector electronics and sensors*, J. Inst. **3(07)**, P07007 (2008)
- [31] ATLAS Collaboration: M. Capeans, et al., *ATLAS Insertable B-Layer Technical Design Report*, Technical Report CERN-LHCC-2010-013. ATLAS-TDR-19, CERN (2010)
- [32] A. Ahmad, et al., *The silicon microstrip sensors of the ATLAS semiconductor tracker*, Nucl. Instrum. Methods Phys. Res. A **578(1)**, 98 (2007)

-
- [33] ATLAS TRT Collaboration: E. Abat, et al., *The ATLAS TRT Barrel Detector*, J. Inst. **3(02)**, P02014 (2008)
- [34] ATLAS TRT Collaboration: E. Abat, et al., *The ATLAS TRT end-cap detectors*, J. Inst. **3(10)**, P10003 (2008)
- [35] J. R. Pater, *The ATLAS SemiConductor Tracker operation and performance*, J. Inst. **7(04)**, C04001 (2012)
- [36] CERN Finance Committee, *The High-Luminosity LHC Project: 298th Meeting of Scientific Policy Committee*, Technical Report CERN/SPC/1068. CERN/FC/6014. CERN/3255, CERN (2016)
- [37] A.-L. Poley, *Studies of adhesives and metal contacts on silicon strip sensors for the ATLAS Inner Tracker*, Dissertation, Humboldt-Universität zu Berlin, Hamburg (2018)
- [38] J. Bohm, et al., *Evaluation of the bulk and strip characteristics of large area n-in-p silicon sensors intended for a very high radiation environment*, Nucl. Instrum. Methods Phys. Res. A **636(1, Supplement)**, S104 (2011), proceedings of the 7th International "Hiroshima" Symposium on the Development and Application of Semiconductor Tracking Detectors
- [39] L. B. A. Hommels, et al., *Detailed studies of full-size ATLAS12 sensors*, Nucl. Instrum. Methods Phys. Res. A **831**, 167 (2016), proceedings of the 10th International "Hiroshima" Symposium on the Development and Application of Semiconductor Tracking Detectors
- [40] R. F. H. Hunter, et al., *First bulk and surface results for the ATLAS ITk Strip stereo annulus sensors*, Nucl. Instrum. Methods Phys. Res. A (2018), proceedings of the 11th International "Hiroshima" Symposium on the Development and Application of Semiconductor Tracking Detectors
- [41] Particle Data Group: J. Beringer, et al., *Review of Particle Physics*, Phys. Rev. D **86**, 010001 (2012)
- [42] H. Bethe, *Zur Theorie des Durchgangs schneller Korpuskarteilchen durch Materie* (in German), Ann. Phys. **5**, 325 (1930)
- [43] F. Bloch, *Bremsvermögen von Atomen mit mehreren Elektronen* (in German), Zeits. f. Phys. **76**, 363 (1933)
- [44] L. Landau, *On the energy loss of fast particles by ionization*, J. Phys. (USSR) **8**, 201 (1944)
- [45] P. V. Vavilov, *Ionization losses of high-energy heavy particles*, Sov. Phys. JETP **5**, 749 (1957)
- [46] H. Bichsel, *Straggling in Thin Silicon Detectors*, Rev. Mod. Phys. **60**, 663 (1988)
- [47] Y.-S. Tsai, *Pair Production and Bremsstrahlung of Charged Leptons*, Rev. Mod. Phys. **46**, 815 (1974)
- [48] L. Rossi, et al., *Pixel Detectors*, Springer Berlin Heidelberg (2006)
- [49] S. Haywood, *Impact Parameter Resolution in the Presence of Multiple-Scattering*, Technical Report ATL-INDET-94-091. ATL-I-PN-91, CERN, Geneva (1994)

References

- [50] K. Kleinknecht, *Detektoren für Teilchenstrahlung* (in German), Teubner Studienbücher Physik, Vieweg+Teubner Verlag, 4th edition (2005)
- [51] S. Ramo, *Currents induced by electron motion*, Proc. Ire. **27**, 584 (1939)
- [52] G. Kramberger, *Signal development in irradiated silicon detectors*, Ph.D. thesis, University Ljubljana, Ljubljana (2001), *CERN-THESIS-2001-038*
- [53] F. Thuselt, *Physik der Halbleiterbauelemente* (in German), Springer Berlin Heidelberg, 2nd edition (2011)
- [54] M. Moll, *Radiation damage in silicon particle detectors: Microscopic defects and macroscopic properties*, Ph.D. thesis, Hamburg University, Hamburg (1999), *DESY-THESIS-1999-040*
- [55] R. Wunstorf, *Systematische Untersuchungen zur Strahlenresistenz von Silizium-Detektoren für die Verwendung in Hochenergiephysik-Experimenten* (in German), Ph.D. thesis, Hamburg University, Hamburg (1992), *DESY-FH1K-92-01*
- [56] A. Affolder, et al., *Charge collection efficiencies of planar silicon detectors after reactor neutron and proton doses up to $1.6 \times 10^{16} \text{ n}_{\text{eq}}\text{cm}^{-2}$* , Nucl. Instrum. Methods Phys. Res. A **612(3)**, 470 (2010)
- [57] M. Mikuž and others, *Study of anomalous charge collection efficiency in heavily irradiated silicon strip detectors*, Nucl. Instrum. Methods Phys. Res. A **636(1, Supplement)**, S50 (2011), proceedings of the 7th International “Hiroshima” Symposium on the Development and Application of Semiconductor Tracking Detectors
- [58] M. Moll, *RD50 Status Report 2009/2010 - Radiation hard semiconductor devices for very high luminosity colliders*, Technical Report CERN-LHCC-2012-010. LHCC-SR-004, CERN, Geneva (2012)
- [59] RD48 Collaboration: G. Casse, et al., *Introduction of high oxygen concentrations into silicon wafers by high-temperature diffusion*, Nucl. Instrum. Methods Phys. Res. A **438(2)**, 429 (1999)
- [60] RD48 Collaboration: G. Casse, P. P. Allport, M. Hanlon, *Improving the radiation hardness properties of silicon detectors using oxygenated n-type and p-type silicon*, in *1999 Fifth European Conference on Radiation and Its Effects on Components and Systems. RADECS 99 (Cat. No.99TH8471)*, pages 114–119 (1999)
- [61] RD50 Collaboration: G. Casse, et al., *First results on charge collection efficiency of heavily irradiated microstrip sensors fabricated on oxygenated p-type silicon*, Nucl. Instrum. Methods Phys. Res. A **518(1)**, 340 (2004), frontier Detectors for Frontier Physics: Proceedin
- [62] Y. Unno, et al., *Optimization of surface structures in n-in-p silicon sensors using TCAD simulation*, Nucl. Instrum. Methods Phys. Res. A **636(1, Supplement)**, S118 (2011), proceedings of the 7th International “Hiroshima” Symposium on the Development and Application of Semiconductor Tracking Detectors
- [63] S. Mitsui, et al., *Evaluation of slim-edge, multi-guard, and punch-through-protection structures before and after proton irradiation*, Nucl. Instrum. Methods Phys. Res. A **699**, 36 (2013), proceedings of the 8th International “Hiroshima” Symposium on the Development and Application of Semiconductor Tracking Detectors

- [64] Y. Unno, et al., *Evaluation of test structures for the novel n^+ -in-p pixel and strip sensors for very high radiation environments*, Nucl. Instrum. Methods Phys. Res. A **731**, 183 (2013), pIXEL 2012
- [65] Y. Unno, et al., *Development of n-in-p silicon planar pixel sensors and flip-chip modules for very high radiation environments*, Nucl. Instrum. Methods Phys. Res. A **650(1)**, 129 (2011), international Workshop on Semiconductor Pixel Detectors for Particles and Imaging 2010
- [66] R. F. H. Hunter, *Development and Evaluation of Novel, Large Area, Radiation Hard Silicon Microstrip Sensors for the ATLAS ITk Experiment at the HL-LHC*, Master's thesis, Carleton University, Ottawa (2017)
- [67] S. Terada, et al., *Proton irradiation on p-bulk silicon strip detectors using 12 GeV PS at KEK*, Nucl. Instrum. Methods Phys. Res. A **383(1)**, 159 (1996), development and Application of Semiconductor Tracking Detectors
- [68] K. Hara, et al., *Performance of irradiated n^+ -on-p silicon microstrip sensors*, Nucl. Instrum. Methods Phys. Res. A **565(2)**, 538 (2006)
- [69] S. Lindgren, et al., *Testing of surface properties pre-rad and post-rad of n-in-p silicon sensors for very high radiation environment*, Nucl. Instrum. Methods Phys. Res. A **636(1, Supplement)**, S111 (2011), proceedings of the 7th International "Hiroshima" Symposium on the Development and Application of Semiconductor Tracking Detectors
- [70] ATLAS ITk Strip Sensor community, *Supply of Silicon Microstrip Sensors of ATLAS12 specification* (2012)
- [71] D. Robinson, *ATLAS QA Procedures for Silicon Microstrip Detectors*, 1st Workshop on QA Issues in Silicon Detectors (2001)
- [72] Agilent Technologies: A. Wadsworth, *The Parametric Measurement Handbook*, 1st edition (2010)
- [73] K. G. McKay, *Avalanche Breakdown in Silicon*, Phys. Rev. **94**, 877 (1954)
- [74] T. Kuwano, et al., *Systematic study of micro-discharge characteristics of ATLAS barrel silicon microstrip modules*, Nucl. Instrum. Methods Phys. Res. A **579(2)**, 782 (2007)
- [75] M. Stegler, et al., *Investigation of the impact of mechanical stress on the properties of silicon strip sensors*, Nucl. Instrum. Methods Phys. Res. A **924**, 133 (2019), proceedings of the 11th International "Hiroshima" Symposium on the Development and Application of Semiconductor Tracking Detectors
- [76] T. Bakos, S. N. Rashkeev, S. T. Pantelides, *Reactions and Diffusion of Water and Oxygen Molecules in Amorphous SiO₂*, Phys. Rev. Lett. **88**, 055508 (2002)
- [77] A. Thomson, et al., *Damp and dry heat degradation of thermal oxide passivation of p+ silicon*, Journal of Applied Physics **115(11)**, 114505 (2014), <https://doi.org/10.1063/1.4869057>
- [78] D. J. DiMaria, E. Cartier, D. Arnold, *Impact ionization, trap creation, degradation, and breakdown in silicon dioxide films on silicon*, J. Appl. Phys. **73(7)**, 3367 (1993), <https://doi.org/10.1063/1.352936>

References

- [79] Synopsis Inc., *Technology Computer Aided Design (TCAD)*, URL <https://www.synopsys.com/silicon/tcad.html>
- [80] Synopsis Inc., *Sentaurus™ Device User Guide* (2016)
- [81] Y. Nakamura, et al., *Anomalous IV behavior of ATLAS SCT microstrip sensors*, Nucl. Instrum. Methods Phys. Res. A **579(2)**, 812 (2007)
- [82] S. Chatterji, et al., *Analysis of interstrip capacitance of Si microstrip detector using simulation approach*, Solid-State Electronics **47(9)**, 1491 (2003)
- [83] I. E. Tamm, *Über eine mögliche Art der Elektronenbindung an Kristalloberflächen* (in German), Phys. Zeits. Sowjet. **1**, 733 (1932)
- [84] W. Shockley, *On the Surface States Associated with a Periodic Potential*, Phys. Rev. **56**, 317 (1939)
- [85] D. A. Neamen, *Semiconductor Physics and Devices : Basic Principles*, Irwin/McGraw-Hill, 4th edition (2012)
- [86] A. Longoni, M. Sampietro, L. Strüder, *Instability of the behaviour of high resistivity silicon detectors due to the presence of oxide charges*, Nucl. Instrum. Methods Phys. Res. A **288(1)**, 35 (1990), proceedings of the Fifth European Symposium on Semiconductors Detectors
- [87] S. M. Sze, Kwok K. Ng, *Physics of Semiconductor Devices*, John Wiley & Sons, Inc. (2006)
- [88] T. Pöhlsen, *Charge Losses in Silicon Sensors and Electric-Field Studies at the Si-SiO₂ Interface*, Dissertation, University of Hamburg (2013)
- [89] J. Schwandt, et al., *Surface effects in segmented silicon sensors*, Nucl. Instrum. Methods Phys. Res. A **845**, 159 (2017), proceedings of the Vienna Conference on Instrumentation 2016
- [90] J. Behr, *Test Beam Measurements with the EUDET Pixel Telescope*, EUDET-Report-2010-01 (2010)
- [91] I. Rubinskiy, *An EUDET/AIDA Pixel Beam Telescope for Detector Development*, Physics Procedia **37**, 923 (2012), proceedings of the 2nd International Conference on Technology and Instrumentation in Particle Physics (TIPP 2011)
- [92] J. Baudot, et al., *First test results of MIMOSA-26, a fast CMOS sensor with integrated zero suppression and digitized output*, 2009 IEEE Nuclear Science Symposium Conference Record (NSS/MIC) pages 1169 – 1173 (2009)
- [93] J. Kroll, *Strip Test Beam/Irradiations - Introduction*, Oxford ITk Week (2018)
- [94] D. Cussans, *Description of the JRA1 Trigger Logic Unit (TLU), v0.2c*, EUDET-Memo-2010-4 (2009)
- [95] J. Dreyling-Eschweiler, *Status of the EUDET-type beam telescope infrastructure*, 7th Beam Telescope and Test Beams Workshop (2019)
- [96] G. A. Voss, B. H. Wiik, *The Electron-Proton Collider Hera*, Annu. Rev. Nucl. Part. Sci. **44(1)**, 413 (1994)

-
- [97] ZEUS Collaboration: B. Foster, et al., *The design and construction of the ZEUS central tracking detector*, Nucl. Instrum. Methods Phys. Res. A **338(2)**, 254 (1994)
- [98] H1 Collaboration: I. Abt, et al., *The H1 detector at HERA*, Nucl. Instrum. Methods Phys. Res. A **386(2)**, 310 (1997)
- [99] R. Abela, et al., *XFEL: The European X-Ray Free-Electron Laser - Technical Design Report*, Technical report, DESY, Hamburg (2006)
- [100] R. Diener, et al., *The DESY II test beam facility*, Nucl. Instrum. Methods Phys. Res. A **922**, 265 (2019)
- [101] V. Hatton, *Operational history of the SPS collider 1981-1990*, in *Conference Record of the 1991 IEEE Particle Accelerator Conference*, pages 2952–2954 vol.5 (1991)
- [102] COMPASS Collaboration: P. Abbon, et al., *The COMPASS experiment at CERN*, Nucl. Instrum. Methods Phys. Res. A **577(3)**, 455 (2007)
- [103] NA62 Collaboration: E. Cortina Gil, et al., *The beam and detector of the NA62 experiment at CERN*, J. Inst. **12(05)**, P05025 (2017)
- [104] A. Gerbershagen, *Beam Generation for Test Beams*, 7th Beam Telescope and Test Beams Workshop (2019)
- [105] T. Bisanz, A. Morton, I. Rubinskiy, *EUTelescope 1.0: Reconstruction Software for the AIDA Testbeam Telescope*, AIDA-NOTE-2015-009 (2015)
- [106] DESY - ILC Soft, *Marlin: Modular Analysis and Reconstruction for the LINear Collider*, URL https://ilcsoft.desy.de/portal/software_packages/marlin/index_eng.html
- [107] D. Rodriguez Rodriguez, E. Rossi, *EUTelescope Guide for ATLAS ITk Strip: Reconstruction and Analysis* (2017), 1707.04535
- [108] D. V. Lang, *Deep-level transient spectroscopy: A new method to characterize traps in semiconductors*, J. Appl. Phys. **45(7)**, 3023 (1974), <https://doi.org/10.1063/1.1663719>
- [109] W. Shockley, W. T. Read, *Statistics of the Recombinations of Holes and Electrons*, Phys. Rev. **87**, 835 (1952)
- [110] R. N. Hall, *Electron-Hole Recombination in Germanium*, Phys. Rev. **87**, 387 (1952)
- [111] D. K. Schroder, *Semiconductor Material and Device Characterization*, Wiley-Interscience, New York, NY, USA, 3rd edition (2006)
- [112] S. W. Provencher, *CONTIN: a general purpose constrained regularization program for inverting noisy linear algebraic and integral equations*, Computer Physics Communications **27(3)**, 229 (1982)
- [113] R. Wunstorff, et al., *Damage-induced surface effects in silicon detectors*, Nucl. Instrum. Methods Phys. Res. A **377(2)**, 290 (1996), proceedings of the Seventh European Symposium on Semiconductor Detectors

References

- [114] G. Kramberger, et al., *Determination of effective trapping times for electrons and holes in irradiated silicon*, Nucl. Instrum. Methods Phys. Res. A **476(3)**, 645 (2002), proceedings of the 3rd International Conference on Radiation Effects on Semiconductor Materials, Detectors and Devices